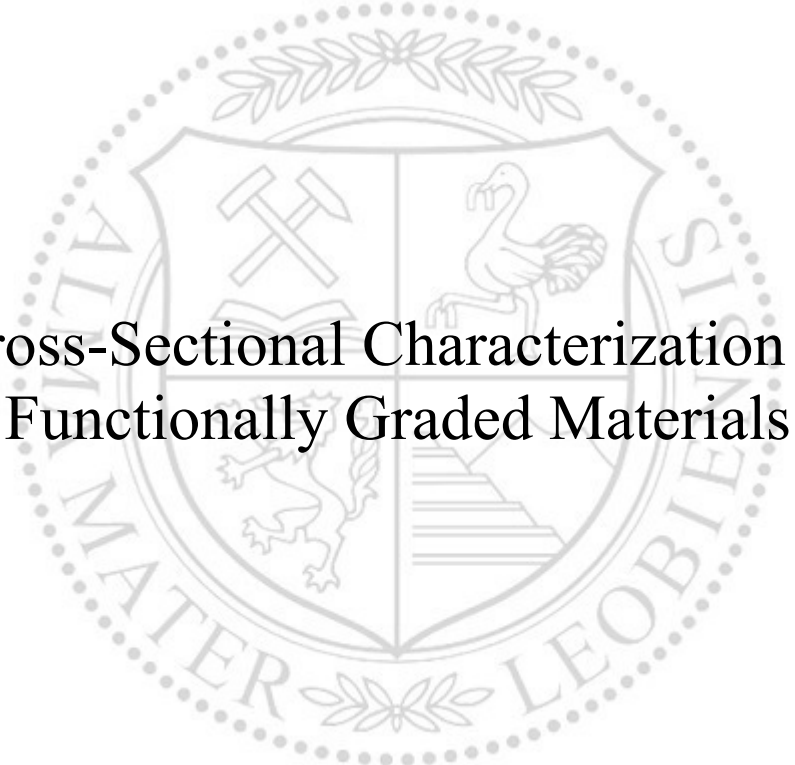




Chair of Materials Physics

Doctoral Thesis



Cross-Sectional Characterization of  
Functionally Graded Materials

Dipl.-Ing. Sabine Carmen Bodner, BSc

December 2022

2022 – Sabine C. BODNER

Montanuniversität Leoben

Department of Materials Science

*Jahnstraße 12*

*8700 Leoben*

AUSTRIA



**EIDESSTÄTLICHE ERKLÄRUNG**

Ich erkläre an Eides statt, dass ich diese Arbeit selbständig verfasst, andere als die angegebenen Quellen und Hilfsmittel nicht benutzt, und mich auch sonst keiner unerlaubten Hilfsmittel bedient habe.

Ich erkläre, dass ich die Richtlinien des Senats der Montanuniversität Leoben zu "Gute wissenschaftliche Praxis" gelesen, verstanden und befolgt habe.

Weiters erkläre ich, dass die elektronische und gedruckte Version der eingereichten wissenschaftlichen Abschlussarbeit formal und inhaltlich identisch sind.

Datum 20.12.2022

---

Unterschrift Verfasser/in  
Sabine Carmen Bodner



## Danksagung

Ich möchte mich an dieser Stelle bei all jenen Menschen bedanken, die mich in den vergangenen Jahren während meiner Zeit als Doktorandin begleitet haben.

Besonderer Dank gilt an dieser Stelle Univ. Prof. Dr. Jozef Kečkéš, der sich Zeit für unzählige Gespräche und Diskussionen genommen hat, mich fachlich und persönlich begleitet und meine Ideen unterstützt hat. Die Erfahrung von Jozef verbunden mit Denkanstößen und Einwänden zum jeweils richtigen Zeitpunkt haben wesentlich zum Abschluss und Gelingen dieser Arbeit beigetragen. Die Bezeichnung „Doktorvater“ könnte nicht treffender und bezeichnender sein.

Ausdrücklich bedanke ich mich ebenfalls bei meinem Mentor Univ. Prof. Dipl.-Ing. Dr. mont. Ronald Schnitzer. Jede Zusammenarbeit und Interaktion habe ich als äußerst positiv und bereichernd empfunden.

Mein Dank gilt an dieser Stelle meinen Co-Autoren und Kollegen am Lehrstuhl für Materialphysik, anderen Lehrstühlen und Instituten des Departments Werkstoffwissenschaft in Leoben, anderen Universitäten und Forschungseinrichtungen in Österreich, Deutschland und der Tschechischen Republik, sowie Industriepartnern in Österreich, Deutschland und den Niederlanden. Die Aktivitäten und Bemühungen haben zu einer Reihe gemeinsamer Publikationen geführt, die von vielen guten und für mich bereichernden Stunden und Gesprächen begleitet waren. Besonders hervorheben möchte ich hier die Zusammenarbeit mit Dr. Michael Meindlhumer, mit Dr. Juraj Todt, Dipl.-Ing. Nicole Käfer, Kevin Kutleša BSc., Dr. Oliver Renk, Dipl.-Ing. Michael Zawodski, Dr. Patrice Kreiml, Philipp Höbenreich, Dipl. Ing. Daniela Kečkéšova, Marco Reiter und Dipl. Ing. Peter Kutleša am ESI in Leoben. Weiters bedanke ich mich bei Ing. Gerald Resch, Florian Resch (beide Fa. Resch GmbH), Dipl.-Ing. Christoph Schindelbacher, Dipl.-Ing. Christian Brandstätter, Haiko Winklmayer, Peter Platzer, Dipl.-Ing. Marco Votruba, Dr. Thomas Hatzenbichler (alle Fa. Pankl Racing AG), Dipl.-Ing. Bernd Rübig (Fa. Rübig GmbH), Bart van de Vorst (TNO), Jaco Saurwalt (Admatec BV), MSc. Marc André Nielsen, Dr. Emad Maawad und Dr. Norbert Schell (Helmholtz Zentrum Hereon). Die Zeit während der Dissertation ist begleitet von Höhen und Tiefen, die ohne Freunde nicht dieselbe Freude bringen oder mit derselben Leichtigkeit durchschritten werden könnten. Ich bedanke mich bei meinen Freundinnen und Freunden, die mich teilweise schon seit meiner Kindheit und Jugend kennen und bei den lieben Menschen, die ich während des Studierens in Leoben und an der FH in Kapfenberg kennen lernen durfte. Nicht zuletzt, sondern vor allem bedanke ich mich aber bei allen Menschen, die ich zu meiner Familie zähle. Ich wurde in den Jahren meines gesamten Studiums von ihnen

## Danksagung

---

immer unterstützt. Besonders danke ich dafür Sonja, Markus und meiner Tochter Elena. Ihr möchte ich diese Arbeit widmen.

Die vorliegende Arbeit wurde finanziell durch öffentliche Mittel unterstützt, die von der Österreichischen Forschungsförderungsgesellschaft mbH für zwei Projekte mit den Akronymen „*CrossSurfaceMech*“ (Projektnummer: 861496) und „AMnonWeldSuperAlloys“ (Projektnummer: FO999888151) zur Verfügung gestellt wurden. Weiterer finanzieller Support wurde durch die Bundesministerien für Verkehr, Innovation und Technologie (BMVIT) und durch die Länder Tirol und Steiermark gewährt.

Darüber hinaus wurde die Nutzung des Synchrotrons an der P07B des PETRAIII Speicherrings am Deutschen Elektronensynchrotron (DESY) in Hamburg ermöglicht.

Für einzelne Experimente dieser Arbeit wurde darüber hinaus Infrastruktur von CEITEC Nano in Brünn (Tschechische Republik) genutzt.

## Kurzfassung

Gradientenwerkstoffe (FGMs) sind Werkstoffe mit örtlich variierenden, funktionalen Eigenschaften, die auf eine graduelle Änderung der chemische Zusammensetzung, der Dichte (Poren) und/oder des Gefüges zurück zu führen sind. Der optimierten Reaktion eines bestimmten FGMs liegt eine örtlich angepasste Struktur-Eigenschafts-Beziehung zu Grunde, welche sich auf unterschiedlichen Längenskalen und hierarchischen Ebenen äußert. Um ein Verständnis für diese sich räumlich verändernden Reaktionen erlangen zu können, müssen FGMs mit geeigneten Methoden auf der Makro-, der Mikro- und der Nanoskala untersucht werden.

Methodisch liegt der Schwerpunkt dieser Arbeit auf der experimentellen Charakterisierung von Eigenschaften des Grundmaterials und gezielt veränderten Gradientenbereichen nahe der Probenoberflächen metallischer FGMs, die mittels Röntgenbeugung am Querschnitt (CSmicroXRD) unter der Verwendung hochenergetischer Synchrotronröntgenstrahlung untersucht wurden. Die Ergebnisse wurden durch weitere Mikro- und Nanohärteprüfserien, verschiedene Mikroskopietechniken und chemische Analysen ergänzt und verifiziert. Diese Arbeit stellt insgesamt sechs verschiedene Anwendungsfälle der Charakterisierung von Eigenschaften am Querschnitt vor, welche durch den Einsatz der eben beschriebenen Methoden untersucht wurden. Es handelt sich dabei um drei FGMs, deren Gradienten mechanisch oder thermochemisch erzeugt wurden und drei weitere Fälle, in denen FGMs über das Laserstrahlschmelzverfahren (PBF-LB) hergestellt wurden. Es zeigt sich, dass die entwickelte Herangehensweise der Charakterisierung ein geeigneter Ansatz ist, um die räumlichen Variationen der Gefügeeigenschaften, Eigenspannungen, Kornmorphologien, Phasen- und chemischen Gradienten lokal zu untersuchen und in weiterer Folge mit den verwendeten Prozessparametern zu korrelieren.

Der zweite Schwerpunkt der vorliegenden Arbeit liegt auf der Anwendung des entwickelten Charakterisierungsansatzes. Konkret wurden Multi-Metall-Hybridstrukturen untersucht, welche durch ein schlickerbasiertes Laserstrahlschmelzverfahren additiv hergestellt wurden. Der experimentelle Teil der Arbeit konzentriert sich dabei auf die Analyse der Variation der strukturellen und mechanischen Eigenschaften in einer einzelnen Lage und in Baurichtung, wobei besonderes Augenmerk auf das Verständnis (i) der kontinuierlichen Entwicklung von Eigenspannungen im additiven Prozess und (ii) des Einflusses von Grenzflächen zwischen den verschiedenen Metalllegierungen gelegt wurde.

Die Ergebnisse der Untersuchungen wurden in vier Publikationen veröffentlicht die hier kurz beschrieben sind:

- Die Eigenschaften eines niederdruckaufgekohlten Einsatzstahls 18CrNiMo7-6, eines plasmanitrierten Warmarbeitsstahls W300 und eines kugelbestrahlten, hochfesten Stahls 300M wurden an der Beamline P07 des Speicherrings PETRAIII in Hamburg untersucht. Ermittelte Eigenspannungsverläufe konnten erfolgreich mit gemessenen Härtegradienten, chemischen Gradienten, Phasenverteilung und Korngröße) und den ursprünglich verwendeten Prozessparametern in Zusammenhang gebracht werden.
- Zylinderförmige Proben aus der korrosionsbeständigen S316L Stahllegierung wurden mittels Laserstrahlschmelzens im Pulverbett unter Anwendung von drei verschiedenen Laserscanstrategien hergestellt. CSmicroXRD und verschiedene Mikroskopiemethoden zeigen den Zusammenhang der verwendeten Prozessparameter mit der Ausbildung von Texturen im Material. Diese Publikation dokumentiert, wie FGMs in einem konventionellen PBF-LB Prozess nur durch die Adaption der Prozessparameter hergestellt werden können.
- Schlickerbasiertes Laserstrahlschmelzen wurde zur Herstellung einer Multimetall-Hybridstruktur verwendet, die aus S316L und der Nickelbasis-Superlegierung IN625 besteht. Beide Legierungen wurden entlang der Baurichtung (*interlayer* Variation) mehrere Duzend Male variiert. Die entstandene Struktur wurde in mehreren Größenskalen bis in den Nanometerbereich untersucht, wobei insbesondere die Entwicklung der Eigenspannung entlang der Bauhöhe durch das periodische Wechseln von S316L und IN625 komplex beeinflusst wurde. Im Gefüge vorhandene, kugelförmige Ausscheidungen konnten als Si- und Nb-reiche CrMO<sub>x</sub> Partikel identifiziert werden. Die Ausscheidung dieser Oxide im Prozess zeigt die Möglichkeit auf, FGMs mit einem hierarchischen Aufbau direkt herzustellen.
- Auf Basis der erzielten Ergebnisse des eben beschriebenen Anwendungsfalls wurde eine zweite S316-IN625 Gradientenprobe hergestellt, wobei die beiden Legierungen nun sowohl in Baurichtung (*interlayer*- ) als auch innerhalb einer einzelnen Schicht (*intralayer* Variation) variiert wurden. Der gesamte Querschnitt der erzeugten Struktur wurde mittels CSmicroXRD abgerastert. Die Ergebnisse zeigen, dass schlickerbasiertes Laserstrahlschmelzen die Erzeugung biomimetischer Multimetall-Materialien ermöglicht, in denen sich das Rissausbreitungsverhalten günstig beeinflussen lässt.

**Schlagwörter:** Gradientenwerkstoffe; 3D Multi-Material; Hybride Strukturen; Additive Manufacturing; Generative Fertigung; Powder Bed Fusion; Laserstrahlschmelzen; Gefüge und Eigenspannungen; Multi-Metall Material; Querschnittsanalyse; Synchrotron Mikro-XRD; Einflusszone; Oberflächennahe Analyse;



## Abstract

Functionally graded materials (FGMs) represent a type of material with spatially varying functional properties in one or more directions, which stem from internal gradients of chemical composition, phases, pores and/or microstructure. The optimized functional response of a particular FGM is triggered by a locally-tailored structure-property relationship, which is a result of the multi-scale material response, often encompassing several length scales and hierarchical levels. There is a need to apply advanced characterization approaches operating at the macro-, micro and nano-scale in order to understand the correlation between process parameters used to fabricate FGMs, their internal structural, chemical and morphological gradients and the spatially varying functional response.

The methodological focus of this thesis lies on the experimental characterization of near-surface and bulk properties of metallic FGMs using newly-introduced high-energy synchrotron cross-sectional synchrotron X-ray micro-diffraction (CSmicroXRD), which was complemented by micro- and nanohardness testing, optical characterization, electron microscopy and chemical analysis. The thesis presents three cases for the application of correlative cross-sectional analytics to characterize mechanically and thermo-chemically induced near-surface gradients, and further three cases of laser-based powder bed-fused samples. Correlative characterization is used to assess spatial variations of structural properties, residual stresses, grain morphology, phase and chemical gradients and local mechanical properties. The obtained results are correlated with the applied process parameters.

The second focus is to apply the developed methodology, enabling the characterization of multi-metal hybrid structures produced by *liquid-dispersed metal powder bed fusion*. The experimental work concentrates on the analysis of the in-plane and out-of-plane variation of structural and mechanical properties with special attention on understanding the residual stress build-up, and on attributes and the role of interfaces between metallic alloys.

In particular, the following topics are covered in the thesis and in the attached four publications:

- Near-surface properties of a low-pressure carburized case hardening steel 18CrNiMo7-6, a plasma-nitrided hot work tool steel W300 and a shot-peened high-strength steel 300M are characterized at the high-energy materials science beamline P07 of the storage ring PETRAIII at Deutsches Elektronensynchrotron (DESY) in Hamburg using CSmicroXRD. The evaluated residual stresses distributions are correlated with gradients of hardness, phases, crystallite sizes,

chemical gradients and/or microstructural features as well as with the applied process conditions.

- Rod-like samples from stainless steel S316L are manufactured by powder bed fusion using three different hatch strategies. The samples are investigated by optical microscopy, CSmicroXRD and using tensile tests in order to understand the correlation between different crystallographic textures induced by the particular hatch strategies and the observed differences in the deformation behaviour. The study presents a strategy to design functionally graded materials with dedicated mechanical properties by laser-based powder bed fusion.
- Liquid-dispersed metal powder bed fusion is used for the production of a multi-metal hybrid structure consisting of stainless steel S316L and the nickel-based superalloy IN625 with an alloy variation along the build direction. The process allows to fabricate different sub-regions and morphologically sharp interfaces between the two alloys, which are characterized with nanoscale spatial resolution. The periodic occurrence of S316L and IN625 with different crystallographic textures results in a complex distribution of residual stresses along the sample's build direction. Moreover, the formation of spherical  $\text{CrMO}_x$  precipitates enriched with Si and Nb during the build process indicates the possibility for a hierarchical design of FGMs by *reactive additive manufacturing*. This study is the first step in confirming that liquid-dispersed metal powder bed fusion is an effective tool that allows to fabricate unique hierarchical microstructures consisting of two alloys.
- Based on results revealed in the application case above, another S316L-IN625 FGM with an inter-, as well as an intralayer variation of the two metal alloys is designed and analysed on its cross-section. CSmicroXRD mapping is used to assess the distribution of phases, texture and residual stresses on the entire cross-section of the sample. The results reveal the sharpness of in-plane and out-of-plane-oriented interfaces between the alloys and allow to assess the possibility to design truly biomimetic structures with alternating metallic alloys, which can be used to alter crack propagation behaviour in multi-metal materials prepared by laser-based powder bed fusion.

**Keywords:** Functionally Graded Material; 3D Multi-Material Structure; Cross-sectional Gradient Materials; Hybrid Structures; Additive Manufacturing; Powder Bed Fusion; Microstructure and Stress; Multi-Metal Material; Cross-section Analysis; Synchrotron Micro-XRD; Near-Surface Characterization;

---

**Content**

<b>Affidavit</b>	<b>III</b>
<b>Danksagung</b>	<b>V</b>
<b>Kurzfassung</b>	<b>VII</b>
<b>Abstract</b>	<b>IX</b>
<b>Abbreviations and Symbols</b>	<b>XV</b>
<b>1 Motivation and Aim of this Thesis</b>	<b>1</b>
<b>2 Theoretical Background</b>	<b>3</b>
2.1 Graded Materials .....	3
2.1.1 Classification and Production Methods of Functionally Graded Materials	3
2.1.2 Additive manufacturing .....	5
2.1.3 Laser-based powder bed fusion.....	7
2.1.3.1 Liquid-dispersed metal powder bed fusion .....	8
2.1.4 Thermally and thermochemically induced gradients .....	10
2.1.4.1 Carburizing .....	11
2.1.4.2 Nitriding .....	13
2.1.5 Mechanically induced gradients .....	15
2.1.5.1 Shot-peening.....	16
2.2 Multiscale Characterisation .....	19
2.2.1 Cross-sectional synchrotron X-ray micro diffraction.....	20
2.2.1.1 Analysis of the phase composition .....	21
2.2.1.2 Analysis of the crystallographic texture .....	26
2.2.1.3 Analysis of residual stresses .....	27
2.2.1.4 Derivation of the microstructural morphology.....	31

<b>3</b>	<b>Determined novel Features in Graded Materials and Conclusions</b>	<b>33</b>
3.1	Synthesis of FGMs by Liquid-Dispersed Metal Powder Bed Fusion . . . . .	33
3.2	Modification of crystallographic Texture by different Hatch Strategies . .	34
3.3	Reverted Austenite Formation at the Diffusion Front of a plasma-nitrided Hot-Work Steel W300 . . . . .	34
3.4	Dynamic Recrystallization and Texture Formation during High-Energy Shot peening of a 300M Steel . . . . .	35
<b>4</b>	<b>Outlook and Impulses for further Scientific Work</b>	<b>36</b>
<b>5</b>	<b>List of Appended Publications</b>	<b>45</b>
5.1	Further Publications, and co-authored Publications . . . . .	47
5.1.1	Accepted publications: . . . . .	47
5.1.2	Submitted publications . . . . .	48
5.2	Supported Thesis . . . . .	48
5.2.1	Bachelor Thesis . . . . .	48
5.2.2	Master Thesis . . . . .	48
<b>6</b>	<b>Paper I: Inconel-steel Multilayers by Liquid Dispersed Metal Powder Bed Fusion: Microstructure, Residual Stress and Property Gradients</b>	<b>49</b>
6.1	Introduction . . . . .	51
6.2	Materials and Methods . . . . .	53
6.3	Results . . . . .	57
6.3.1	Cross-sectional morphology. . . . .	57
6.3.2	CSmicroXRD analysis . . . . .	58
6.3.3	Local texture analysis . . . . .	61
6.3.4	Chemical analysis . . . . .	63
6.3.5	Mechanical characterization. . . . .	65
6.3.6	TEM characterization . . . . .	66
6.4	Discussion . . . . .	69
6.5	Conclusion . . . . .	71

---

<b>7</b>	<b>Paper II: Correlative Cross-Sectional Characterization of nitrided, carburized and shot peened Steels: Synchrotron Micro-X-Ray Diffraction Analysis of Stress, Microstructure and Phase Gradients</b>	<b>79</b>
7.1	Introduction.....	81
7.2	Materials and Methods .....	82
7.2.1	Sample preparation .....	82
7.2.2	Experimental methods .....	84
7.2.3	CSmicroXRD data evaluation procedure .....	86
7.2.4	FEM-modelling .....	88
7.3	Results .....	90
7.3.1	Case Study I: Low-Pressure Plasma Nitrided Hot Work Steel Sample .....	90
7.3.2	Case Study II: Low-Pressure Carburized Case-Hardening Steel Sample .....	96
7.3.3	Case Study III: Shot-Peened Martensitic Steel Sample .....	99
7.4	Discussion .....	102
7.5	Summary and Conclusions.....	105
<b>8</b>	<b>Paper III: Influence of Hatch Strategy on Crystallographic Texture Evolution, Mechanical Anisotropy of Laserbeam Powder Bed Fused S316L Steel</b>	<b>113</b>
8.1	Introduction.....	115
8.2	Experiments and Methods .....	117
8.2.1	Sample preparation by PBF-LB .....	117
8.2.2	Optical Microscopy.....	118
8.2.3	Scanning Electron Microscopy.....	119
8.2.4	Synchrotron Experiments.....	119
8.2.5	Tensile Tests.....	121
8.3	Results and Discussion .....	122
8.4	Conclusion.....	131

**9 Paper IV: Graded Inconel-Stainless Steel Multi-Material Structure by inter- and intralayer Variation of Metal Alloys 139**

9.1	Introduction .....	141
9.2	Materials and Methods .....	143
9.2.1	Metallographic characterization .....	145
9.2.2	Hardness profiling .....	145
9.2.3	Nanoindentation .....	145
9.2.4	Synchrotron X-ray Micro-Diffraction .....	145
9.3	Theory: Residual Stress Evaluation .....	147
9.3.1	Qualitative phase analysis .....	149
9.3.2	Peak broadening .....	149
9.4	Results and Discussion .....	150
9.4.1	Cross-sectional microstructure and mechanical properties .....	150
9.4.2	Residual stress distribution, texture and microstructure .....	155
9.5	Conclusions .....	158

**Abbreviations and Symbols**

2D	two dimensional
3D	three dimensional
AM	additive manufacturing
BD	build direction
CSmicroXRD	cross-sectional synchrotron X-ray micro diffraction
DED	directed energy deposition
EDS	energy dispersive spectroscopy
FGM	functionally graded material
FGS	functionally graded structures
<i>H</i>	hardness
<i>H<sub>o-p</sub></i>	nanohardness
IN625	Inconel625
LDM-PBF-LB	liquid dispersed metal powder bed fusion (using a laser energy source)
LMD	laser metal deposition
PBF	powder bed fusion
PBF-EB	electron-based powder bed fusion
PBF-LB	laser-based powder bed fusion
S316L	stainless steel 316L
SEM	scanning electron microscopy
WAAM	wire arc additive manufacturing
XEC	X-ray elastic constants





# 1 Motivation and Aim of this Thesis

Functionally graded materials (FGM) are advanced composites for engineering applications with locally optimized properties. The term *functionally graded material* was established in the 1980s in Japan to describe materials possessing spatially tailored chemical, biochemical, physical and/or mechanical properties due to an adapted layout, often encompassing several lengths scales [2]. Initially, the FGM concept was suggested to produce advanced thermal barrier materials to be applied in future space programs [3]. FGM's extraordinary performance can be adjusted and is attributed to a specific design of alternating materials, depth gradients (chemical, biochemical, physical and mechanical), as well as variable microstructures and densities (porosities) throughout their volume [4]. The concept of FGMs is very commonly found in nature and represents an optimization strategy, using a limited number of chemical elements only. Prominent biological FGMs, which also attracted the interest of the scientific community already in the early 1970s are for example plants, nacre, cuticle, bone, sponge spicules [5]. An outstanding feature of biological FGMs is that surfaces or, in particular, near-surface areas are spatially adapted in order to optimize interaction with surrounding media. One such example is the bark of trees, which surrounds the trunk and serves to protect the more sensitive areas that are responsible for nutrient supply from pests and the elements. It is beneficial for material scientists to look into the manifold solutions already provided by nature with the goal to abstract and transfer those principles to technical applications. Such efforts are grouped under the umbrella term *biomimetics*. Due to its inherent complexity, biomimetic research requires a certain amount of interdisciplinarity, transdisciplinarity and creativity [6]. In contrast to biological FGMs, artificially produced gradient structures could benefit from the fact that a much wider range of chemical elements, processing conditions, etc. can be applied to synthesize them.

Artificial FGMs are already being applied in aerospace, automotive [5], and defence applications, cutting tools (in the form of vapor-deposited thin films), in medicine [7], nuclear reactors, turbine blades, sports equipment as well as smart structures. Due to their enhanced performance compared to standard bulk materials, it is often possible to reduce the mass of components, which is particularly important in the case of moving parts. FGMs can be employed with both economic and/or ecological benefits [8]. Depending on the application, it is important that particular areas of components (*e.g.* those close to the surface) are adapted to meet different mechanical, physical and chemical challenges. It has to be stated, that the optimization of FGMs is generally complex and requires a detailed understanding of the underlying physical phenomena.

One of the central challenges in the optimization of FGMs is the limited possibility to simulate different types of FGMs. This is due to a lack of experimentally confirmed data describing mechanical properties, which need to be fed into different databases prior to analytical modelling and numerical simulation. On the one hand, state-of-the-art methods like hardness or tensile tests – which are also applied on an industrial scale – are by far too inaccurate to provide appropriate data. On the other hand, the spatial resolution of existing micro- and nano-characterization techniques [9–12], which have been developed within the last decades, is either too high or too low to for the mesoscopic range between 5 and 100  $\mu\text{m}$ . This results in a remarkable gap in the ability to characterize FGMs at this level, which is becoming ever more important with the increasing capabilities and industrial relevance of additive manufacturing (AM).

The unresolved issues of FGM research described above have led to the following questions defining the main goals of this dissertation:

- The first aim was to synthesize biomimetic FGMs by means of novel additive manufacturing methods. Particular attention was paid here to the possibility of manufacturing graded structures on a suitable length scale, namely the meso-scale, characterized by dimensions between 5 and 100  $\mu\text{m}$ .
- The second aim was to test and develop suitable methods for measuring various materials properties at the meso-scale. Since it is necessary to use analytical techniques, offering a spatial resolution in the appropriate length scale, standard tests have to be scaled up or down in order to meet the required scale of resolution. In particular, 2D-synchrotron X-ray diffraction scanning was employed to assess microstructural features and residual stress levels in FGMs. Results of the modified characterization methods could be used as experimental input for the simulation of the macroscopic performance of FGM parts.

This work consists of five main parts: Following a general introduction in Chapter 1, Chapter 2 presents the theoretical framework of FMGs, involving a more precise definition of graded materials and their characteristics, of possible manufacturing processes, as well as different characterization techniques for different length scales. Chapter 3 summarizes the major findings of this dissertation, highlighting major results and putting the appended scientific publications into the context of current FMG research. Finally, Chapter 4 constitutes the central part of this thesis and consists of four publications (Paper I–IV), written and published in peer-reviewed journals in the course of the development and deepening of the thesis' topic. In addition, further publications and contributions to international conferences are listed.

## 2 Theoretical Background

This chapter intends to briefly introduce a possible classification of graded materials concerning their types, characteristics, and applications. Furthermore, different methods of synthesis and their significance for the production of FGMs are outlined. The second part of this chapter presents different characterization methods, used to investigate FGMs on a multi-scale level.

### 2.1 Graded Materials

In general, FGMs encompass a wide range of materials, differing in their chemical compositions. In this work, however, the main focus was placed on the fabrication and characterization of metallic FGMs. Thus, certain aspects of other FGMs will be mentioned only where appropriate.

#### 2.1.1 Classification and production methods of functionally graded materials

FGMs can be classified using different classification criteria. El-Galy *et al.* introduced six different classifications according to

- (i) *the state during FGM processing*: solid state processes, liquid state processes and vapor deposition processes
- (ii) *FGM structure*: continuous and discontinuous graded material
- (iii) *the type of FGM gradient*: composition, microstructure and porosity gradients [7]
- (iv) *FGM scale and dimension*: thin films (5 to 500 nm), thick films (about 1 to 120  $\mu\text{m}$ ) and thick FGMs (5 to 350 mm). In general, only the area in which a gradient is present is considered relevant for the classification, while the actual component size is ignored.
- (v) *the nature of the FGM gradation process*: constructive (layer-by-layer construction) and transport processing (*e.g.* fluid flow, diffusion or heat conduction)

## Theoretical Background

- (vi) the *field of application*: e.g. heat exchangers, heat-resisting elements in spacecraft, fusion reactors, materials for aerospace, biomaterials, automotive parts, cutting tools, smart structures, etc.

Figure 1 illustrates the classification of FGMs in terms of scale, field of application and selected production routes. Technologies used to synthesize samples for this work are highlighted in green color.

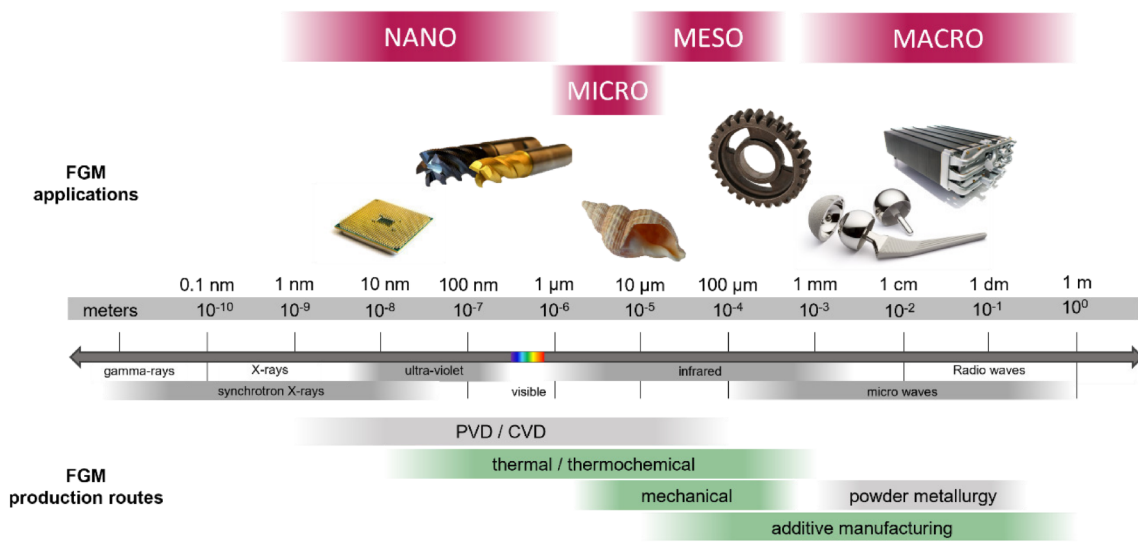


**Figure 1.** Schematic of the classification of functionally graded materials (FGM) and functionally graded structures (FGS) according to different length scales. In addition, potential selected areas of application are depicted and the electromagnetic spectrum is shown for scale reference. Also, selected manufacturing processes are listed. Processes that were used to manufacture graded structures within the scope of this theses are highlighted in green color.<sup>1</sup>

A category of materials closely related to FGMs is so-called *functionally graded structures* (FGSs). This term is commonly used when mechanical properties change spatially, and graded properties arise from geometrical parameters. This includes, for example, complex and adapted cellular materials, honeycombs and lattice structures where e.g. strut dimensions change as a function of location [13]. The term FGS is also used for components whose mechanical properties are adjusted by geometric or topological optimization. Possible applications for FGSs are light-weight components and energy absorbant components.

In the following subsections, the additive manufacturing, the thermal and thermochemical and the mechanical manufacturing production routes are described to provide a basic background for the technologies used in this work. Except for additive manufacturing (*cf.* section 2.1.2), the methods described below have in common that – like in biological

<sup>1</sup> Symbol images of FGM applications taken from pixabay.com. Access date: 22<sup>nd</sup> September, 2022.

FGMs – tailored gradients occur only in the near-surface region of the samples or components. AM was used to produce bio-inspired, graded materials and tailored microstructures in Paper I, Paper IV and Paper III, respectively. Thermochemical and mechanical processing were used to modify near-surface regions of three steel samples in Paper II.

### 2.1.2 Additive manufacturing

Within the last decade, AM technologies have become widely commercially available. The concept of building up a material layer by layer in principle provides all possibilities to produce FGMs and FGSs and in 2020 the term *functionally graded additive manufacturing* (FGAM) was introduced in the ISO/ASTM TR 52912 standard [14]. Possibilities to realize FGAM range from graded microstructures, graded composition (single material FGAM vs. multi-material FGAM) and porosity [7] to graded geometrical dimensions [13] (e.g. cell size or type in cellular structures [15]). Thus, FGAM enables design innovation by removing limitations for complex shape geometries that were previously subjected to the constraints of conventional subtractive processes. Moreover, and for the same reasons, FGAM is predestined to be used for synthesizing biomimetic structures. However, a key requirement for biomimetic FGAM is that sufficient spatial resolution can be achieved by the AM processes.

The currently available AM processes can be assigned to one of the following seven process categories:

1. *Material extrusion (ME)*: A thermoplastic filament extruded through a nozzle or extrusion head to be selectively dispersed onto a motorized ( $x$ - $y$  directions) build plate.
2. *Material jetting (MJ)*: Droplets of a feedstock material are selectively deposited by inkjet printing heads according to a layered<sup>2</sup> 3D model.
3. *Binder jetting (BJ)*: A binder material is selectively dropped onto a powder feedstock. The binder bonds the powder particles together to produce a 3D part. If colorized binders are used, this method allows for fully dyed, colored models.
4. *Sheet lamination (SL)*: Sheets of a material are bonded to form a part before the desired profile is cut in a second step by a laser or a mechanical cutting unit (tungsten carbide plate.)
5. *Vat photopolymerization (VP)*: A photosensitive resin is cured by ultraviolet laser light. The oldest AM process, stereolithography (SLA), can be assigned to this

---

<sup>2</sup> Each 3D-model needs to be virtually sliced into a stack of layers in order to provide suitable data for AM processing. The model is divided into the individual layers in the course of data preparation, using appropriate software.

category. A distinction is also made between systems, in which an entire layer is illuminated at one (pixel resolution) and systems in which a laser scans the area to be exposed in vector segments.

6. *Powder bed fusion (PBF)*: Thermal energy, provided by a laser or an electron beam is used to fuse powder particles layer-by-layer until a 3D component is built up.
7. *Directed energy deposition (DED)*: A powder or wire feedstock is molten by a focussed thermal energy (laser or electron beam source). The component is built up by the fused material as the motorized base plate moves in a way to follow the desired geometry.

Only categories (6) and (7) can be used to *directly* fabricate *metal* components. This means that no further debonding and sintering step is necessary to produce a final (FGM) part. Due to the limited resolution of DED, only powder-bed fusion (and its related processes) can reach a spatial resolution in finished parts that is sufficient for biomimetic FGAM.

In biomimetics, it is furthermore important to control (*e.g.* by adjusting process parameters) the microstructure, especially in case of materials that exhibit a strongly anisotropic mechanical behavior. This is possible by means of the solidification behavior of the molten material and can be controlled to a certain degree by adjusting the thermal gradient in the powder bed. Prominent examples for materials with a strong anisotropic behavior are composite materials. Various building strategies from nature, which were also listed in the introduction of Chapter 2 (*e.g.* nacre, wood, ivory etc.), teach us that that a material's properties can be optimized only through the variation and multiple stacking of individual materials possessing different mechanical properties.

Indeed, this is a problem for most of the AM techniques currently available, as the devices and processes are not conceptualized to provide easy and frequent feedstock changes. Unfortunately, the same is valid for laser-based powder bed fusion (PBF-LB) as a layer-wise variation of materials means either (i) that two powder reservoirs have to be available, each of them containing a different powder, or (ii) a second supplier (cylinder or hopper) has to provide another feedstock from top [16–21]. In all cases, the powders are mixed in the build volume.

In this thesis, a modified process, namely *liquid-dispersed metal powder bed fusion*, was applied to synthesize multi-metal materials (Paper I and Paper IV). Furthermore, the microstructure of stainless steel 316L was modified by applying different hatch strategies, *i.e.*, the arrangement and sequence of vectors which are traversed and molten by the laser in order to fuse the powder material to the underlying build-up over the entire surface.

The PBF-LB process will be described in the following subsection in more detail, followed by a description of liquid-dispersed metal powder bed fusion (LDM-PBF-LB).

### 2.1.3 Laser-based powder bed fusion

In case of PBF-LB, thermal energy is introduced into a powder bed via a laser, to selectively melt the metal powder layer by layer. Figure 2 shows a simplified and schematic illustration of the PBF-LB set-up. In a pre-processing step before printing, the 3D model is transformed into many individual 2D contours by *slicing* before the data is transferred to the printing device. During the printing process the following sequences are repeated until the entire 3D model is reconstructed: (i) The build plate moves incrementally down to set the desired layer height. (ii) The powder supply cylinder moves up to provide the powder feedstock. (iii) A recoating unit spreads the powder feedstock, provided by the powder supply, across the build plate. Excess powder is shifted to the powder overflow. Once powder is homogeneously spread across the powder bed, (iv) the focussed laser is guided into the process chamber and melts the respective contour selectively. In this process, the laser scans the areas to be melted by lining up many adjacent vectors. (v) Steps (i) to (iv) are repeated until the initially desired 3D geometry is reconstructed.

The whole process is carried out under a protective Ar or N atmosphere to prevent oxidation [22].

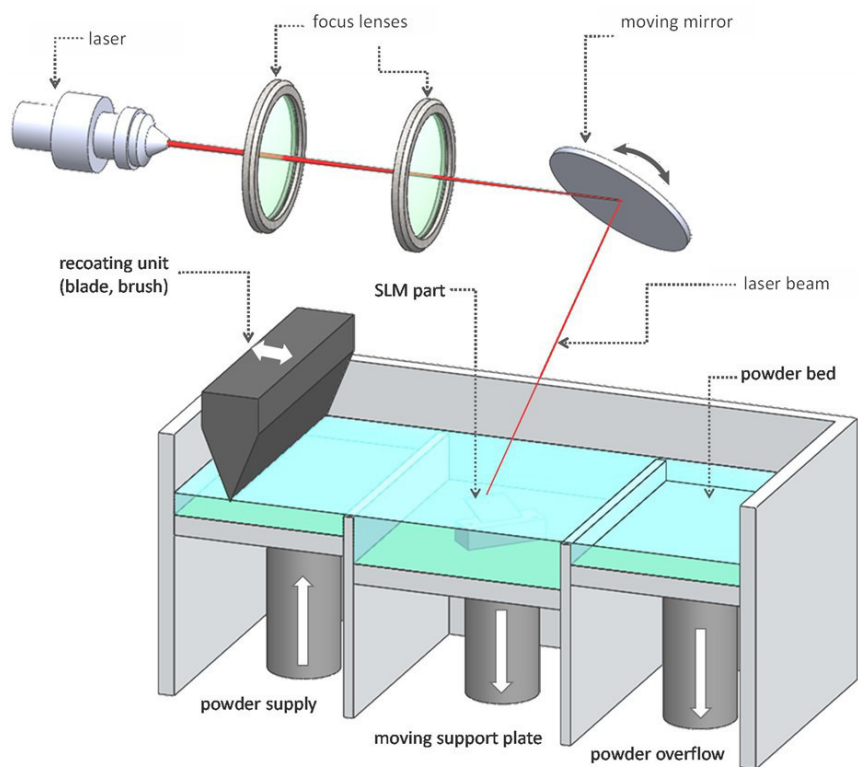


**Figure 2.** Illustration of the laser-based powder bed fusion setup (illustration taken from Ref. [23]).

Characteristics of the PBF-LB process are high solidification rates that can reach  $10^3$ - $10^6$  K/s [22] and result in very fine microstructures. The quality of the final parts strongly depends on the choice of well-suited process parameters. Otherwise, densities exceeding 99.5% cannot be reached due to lack of binding, and the formation of pores and cracks. A higher or different performance of densely printed materials compared to standard products of a similar chemical grade has been reported for Al-, Ti-, Ni- and Fe-based alloys [24–27]. The high cooling rates and thermal gradients within the build chamber lead to a directed solidification of the metal alloys and influence the morphology and feature size of the solidified microstructure. This results in a certain anisotropy of the microstructure and subsequently of physical and chemical properties. The expression of anisotropy in the printed part can be influenced by different process parameters, like energy input in general, applied hatch strategies and the orientation of the part within the build space. In the context of Paper III, the possibility of influencing microstructure and texture by three different hatch strategies and their effect on the deformation behavior was studied.

Currently, PBF-LB still has to deal with some disadvantages and obstacles. These are the size limitation of built parts, the low building rates resulting in a high production times, the poor availability of tailored alloys that are designed for PBF-LB and the high prices for devices and feedstock [22]. With regard to FGAM, classic PBF-LB has another significant disadvantage, which is the limitation in terms of the use of different materials. This is because it is currently not possible to produce FGMs using PBF-LB outside of an academic setting with a very limited sample size, *i.e.*, on an industrial scale.

At least the obstacle of an easy and frequent materials change can be overcome by the related and modified LDM-PBF-LB process.

### 2.1.3.1 Liquid-dispersed metal powder bed fusion

LDM-PBF-LB, initially developed between 2015 and 2017 at the Netherlands Organization of Applied Scientific Research (TNO), uses metal powder slurries instead of standard metal powders as feedstock. The process can be distinguished from all other AM processes as (i) metal powder is dispersed in a water-based binder and (ii) the process can still be attributed to direct metal AM processes, since the bonding between the individual layers happens in place and not in a downstream sintering process. Figure 3 presents a schematic sketch of the three most relevant process steps in which LDM-PBF-LB differs from the conventional PBF-LB. These are:

- (1) The *application of the feedstock*, in this case a metal powder suspension, by a pipetting system. The layer thickness is adjusted by a knife edge that spreads the metal suspension onto the build plate or underlying layers.



- (2) The *pre-drying step*, during which the liquid constituent of the water-based binder evaporates. At the same time, the powder bed densifies by about 5 to 10%.
- (3) In the third step, a laser beam hatches selectively across the powder bed and fuses the previously created “green layer” with the solid layers below.

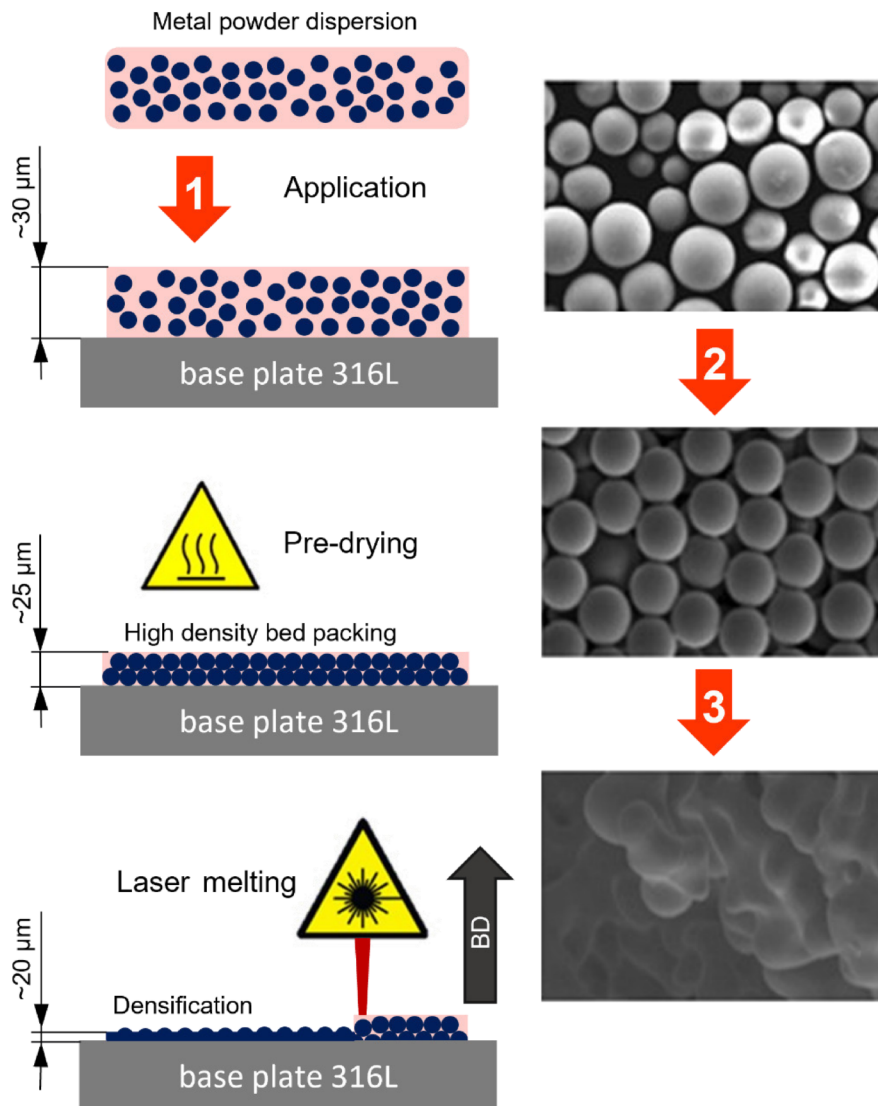


**Figure 3.** Schematic description of the liquid-dispersed metal powder bed fusion process. In a first step, a  $\sim 30\ \mu\text{m}$  thick layer of the metal suspension is applied on the base plate or the underlying, already densified layers. During the pre-drying step, the liquid fraction of the water-based binder is evaporated by a flow of nitrogen. The powder bed consequently densifies, resulting in a layer thickness of  $\sim 25\ \mu\text{m}$ . In a third step, the powder particles are molten by a laser beam to form a new metallic layer of  $\sim 20\ \mu\text{m}$  thickness. The black arrow *BD* denotes the build direction. (image modified from Ref. [28]).

Main advantages of this novel method are easier handling of the feedstock compared to dry metal powders, as the metal powder suspensions do not raise dust. In currently commercially available systems up to 20 different metal powder suspensions can be used during a single printing job. It is possible to stack different feedstocks and change materials layer by layer (*inter-layer* variation). Different metals can even be combined

within a single layer (*intra-layer* variation). Moreover, the binder system represents a further tuning parameter to favorably influence the printing and microstructural properties of the feedstock. Various additives that enable in-process alloying and improve the weldability of the metals can be added via the binder.

Thick FGM specimens produced for Paper I and Paper IV were designed and synthesized in a way to determine possibilities and limits of the LDM-PBF-LB process.

As illustrated in Figure 1, thin-film and thick-film FGMs can be produced by thermal, thermochemical and mechanical (surface) treatments. The production routes and evolution of gradients during these treatments are briefly described in the following sections.

### 2.1.4 Thermally- and thermochemically-induced gradients

*Thermally induced gradients* in steels are generated by a local austenitization followed by a subsequent oil or water quenching. These gradients can be induced in plain carbon or low alloy steels. The treatment is usually performed on parts with a finished or almost finished geometry. A high through-hardening ability of the used steels is not required. The local martensite formation leads to an increase of wear resistance and, due to the local increase of volume, to the appearance of a favorable residual stress distribution, exhibiting compressive residual stresses in the hardened zone. Hence, an increased fatigue strength is reached.

Processes applied to induce thermal gradients can be classified according to the different energy sources into (i) dip hardening, (ii) flame hardening, (iii) induction hardening, (iv) induction impulse hardening, (v) laser beam hardening and (vi) electron beam hardening. The power density and resulting energy input in the different processes differ greatly and only near-surface gradients with a limited extension can be realized.

In contrast to thermal processes, *thermochemical processes* are characterized by the fact that also the chemical composition in the near-surface region is altered. In this way, a chemical gradient develops in the material during the heat treatment. The chemical gradient is usually built up by the diffusion of interstitial elements such as C (carburizing, carbonitriding) and N (nitriding, nitrocarburizing). Examples of other processes, in which elements like B, V or Al are responsible for the formation of intermetallic phases to form a chemical gradient in the diffusion region are boronizing, vanadizing or aluminizing, respectively.

The mentioned thermochemical surface hardening methods have in common the aim to improve hardness, mechanical properties as well as wear and corrosion resistance [29], and can thus be classified as case-hardening treatments. Carburizing and nitriding are

---

described in more detail in the following sections, as both processes were used to modify samples in the context of this thesis.

#### 2.1.4.1 Carburizing

Carburizing describes a multi-step thermochemical process with the aim to harden a component's surface while the core of the material remains tough. In general, this approach is applied to workpieces with near-net-shape geometries. Typically, low carbon steels with a C-level below 0.2 wt.% are used.

In a first step, the component is heated up until the body-centered-cubic (bcc) ferrite phase changes to the face-centered-cubic (fcc) austenite. Typical temperatures are around or significantly above the  $A_{c3}$ <sup>3</sup> temperature. After that, in a second step, the temperature is held constant as C diffuses into the near-surface region of the workpiece. Thus, the C-content raises from initially < 0.2 to about 0.8 wt.%. Due to the C-enrichment, martensite transformation occurs if the critical cooling rate of the material is exceeded in a (third) quenching step.

Carburizing processes can be classified by the C-adsorbing atmosphere that decomposes at the metal surface and provides nascent C to the heated sample. Prominent processes and hardening agents used are:

- Pack carburizing (coke or charcoal pellets)
- Gas-carburizing (propane, methanol, methane)
- Low-pressure carburizing with or without plasma (methane, propane or acetylene)
- Salt bath carburizing (cyanides)

Important parameters for case-hardened samples by carburizing are surface hardness and case hardening depth (CHD). Starting at the component surface, the standardized CHD corresponds to the depth at which a hardness value of 550 HV<sub>1</sub><sup>4</sup> is determined.

In addition to the higher wear-resistance of the hardened component surface with simultaneous toughness of the core (due to the low C content), carburizing is – like other case hardening processes – primarily used to specifically introduce a residual stress gradient in the component. Compressive residual stresses are caused by the diffused carbon and local martensitic phase transformation in the carburized zone. This leads to an increased fatigue resistance of carburized components.

---

<sup>3</sup>  $A_{c3}$  denotes the temperature in steels at which the bcc ferrite lattice completely transforms into the fcc austenite lattice during heating. The index c denotes *heating* in French language (*chauffer*).

<sup>4</sup> HV denotes the hardness determination according to Vickers. The specimen is loaded with a defined force (in this case 9.81 N) transmitted by an indenter (diamond pyramid with an opening angle of 136°). The hardness of the material is determined from the size of the indentation.

Quenching and subsequent tempering can be applied (i) directly (direct hardening), (ii) in a separate process step (single quench hardening), (iii) with a temperature holding step (hardening with isothermal transformation), (iv) directly involving a second tempering and quenching step (double hardening) and (v) directly with an additional annealing step (single hardening with intermediate annealing) [30].

Direct hardening is the most cost-effective process and thus industrially applied for small parts in which grain growth during austenitizing does not occur due to the short holding time above  $A_{c3}$ .

*Single quench hardening* is applied for larger geometries and components which need to be machined before hardening. The components are cooled slowly after carburizing as the actual hardening takes place in a separate process step. The advantage of this temperature program is the second transformation from the ferrite to the austenite phase, which results in recrystallization and consequently grain refinement. The temperature during the second austenitization can either be chosen so that the phase transformation takes place only in the near-surface region, or high enough to austenitize the core of the component as well. The chosen temperature program influences the microstructure of the final part.

If the microstructure and properties of both, core and case, should be adjusted, *double quench hardening* can be applied. In that case, desired properties of the core are adjusted in a first tempering (temperature  $> A_{c3,core}$ ) and quenching. Thereafter, the components are reheated again to the (typically lower) austenitization temperature of the carburized surface layer and finally quenched.

*Low-pressure carburizing:* One of the samples investigated within the scope of this thesis was treated by low-pressure carburizing. This process is characterized by the use of methane ( $CH_4$ ), propane ( $C_3H_8$ ) or acetylene ( $C_2H_2$ ) as process gases at a typical pressure below 3 kPa, which enables high carburizing temperatures (900 to 1050°C) [31] and a high C-transfer due to the high decomposition rates under process conditions. The process results in surfaces entirely free of oxide. Compared to other carburizing methods, low-pressure carburizing is furthermore considered to be more environmentally friendly as a result of lower gas and energy consumption [32]. The different carburizing media possess particular properties, leading to different carburizing effects, applications, advantages and disadvantages. Acetylene has the best carburizing effect (*cf.* Table 1) and no plasma is necessary, contrary to the application of methane (plasma mandatory) and propane (plasma recommended) as carbon-releasing agents. Acetylene can therefore also be used to homogeneously carburize holes and small gaps in workpieces and is therefore widely used in industrial applications.

**Table 1:** Carburizing media used in low-pressure carburizing processes and the corresponding chemical reactions during the process.

	chemical formula	without plasma	with plasma
Methane	CH <sub>4</sub>	CH <sub>4</sub> → CH <sub>4</sub>	CH <sub>4</sub> → C + 2 H <sub>2</sub>
Propane	C <sub>3</sub> H <sub>8</sub>	C <sub>3</sub> H <sub>8</sub> → C + 2 CH <sub>4</sub>	C <sub>3</sub> H <sub>8</sub> → 3 C + 4 H <sub>2</sub>
Acetylene	C <sub>2</sub> H <sub>2</sub>	C <sub>2</sub> H <sub>2</sub> → 2 C + H <sub>2</sub>	-

After low-pressure carburizing, quenching is achieved with pressurized nitrogen or helium gas and pressures of 1 to 2 MPa. The substitution of oil-quenching by high-pressure gas quenching leads to less geometrical distortions of the components and higher surface qualities. Additionally, a downstream cleaning step in which the quenched components are cleaned from residual oil is avoided [31].

#### 2.1.4.2 Nitriding

Compared to the thermodynamic processes occurring during carburizing of ferritic steels, chemical processes during nitriding can be considered to be more complex, as published phase-diagrams do not represent the expected stable states that are a function of temperatures at a constant pressure. The solubility of nitrogen in ferrite, austenite and martensite is 0.4 (at 602°C), 10.3 (at 50°C) and up to 12 at.% (at room temperature), respectively. The entire process is very different from other typical heat treatment processes and takes place very far from thermodynamic equilibrium conditions [29]. Therefore, nitriding can be performed at lower temperatures that are typically below 600°C [33]. In contrast to standard heat treatment processes, the hardening effect does not result from a martensite transformation but from precipitation hardening of nitrides. This suggests that the alloying concept of the steels used must include strong nitride formers.

Depending on the process and atmosphere used during the nitriding of ferritic steel components, a compound layer can grow at the surface of the components. Due to its ceramic-like character and a brighter occurrence in metallurgically prepared cross-sections, which results from different etching behavior, the compound layer is often referred to as *white layer*. Compound layers locally exhibit a very high increase in wear resistance and, in addition, an increase in corrosion resistance. Like in the case of carburizing, a modified chemical composition and a compressive residual stress gradient are induced as a consequence of N diffusion in the near-surface region. Therefore, nitriding is also applied to components with an almost finished net-shape geometry.

## Theoretical Background

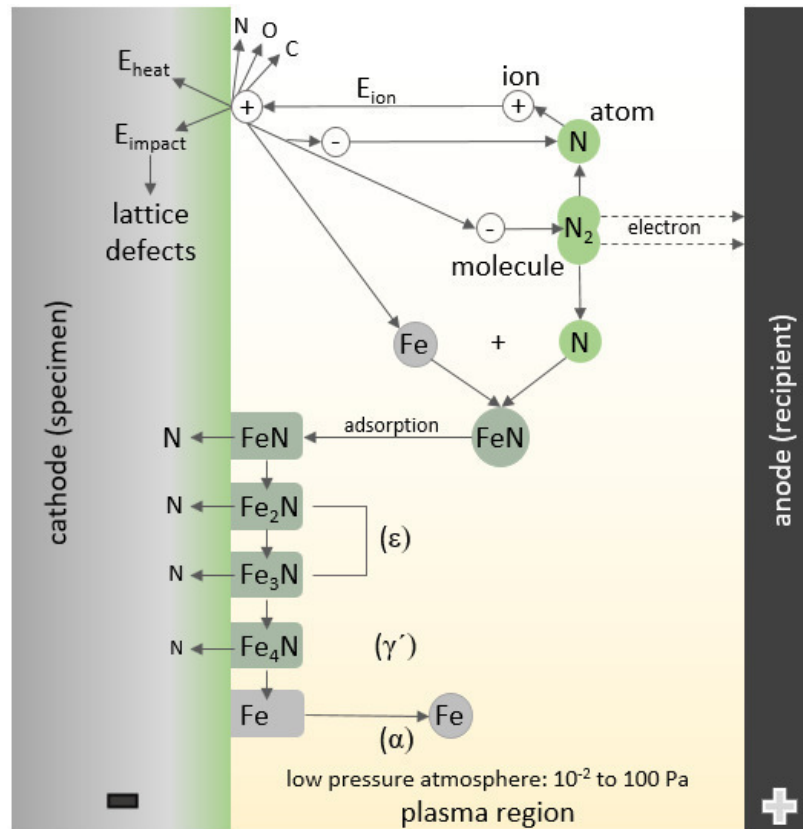
Prominent processes for nitriding are (i) gas nitriding, (ii) plasma nitriding and (iii) salt-bath nitriding. Table 2 lists the most important iron nitrides and their properties.

Table 2: Structure properties and characteristics of the most important iron nitrides [30,34].

phase	$\alpha$ -Fe	$\gamma'$ -nitride ( $\text{Fe}_4\text{N}$ )	$\varepsilon$ -nitride ( $\text{Fe}_x\text{N}$ ) $x = 2, 3$	$\zeta$ -nitride ( $\text{Fe}_2\text{N}$ )
space group	Im3m	Pm(3)m	P6 <sub>3</sub> 22	Pbcn
crystal structure	body-centered-cubic	face-centered-cubic (perovskite)	hexagonal	orthorombic
lattice parameters	$a = 2.87 \text{ \AA}$	$a = 3.80 \text{ \AA}$	$a = 4.60\text{-}4.79 \text{ \AA}$ $c = 4.34\text{-}4.42 \text{ \AA}$	$a = 4.44 \text{ \AA}$ $b = 5.54 \text{ \AA}$ $c = 4.84 \text{ \AA}$
wt.% of N	0	5.88	7.8 – 11.35	11.1 – 11.35

*Plasma nitriding* is described in more detail here, as some of the samples characterized in the context of this thesis were treated by this thermochemical process, during which pure nitrogen or ammonia is activated by applying a glow discharge. As a consequence, positively charged N-ions are accelerated in the low-pressure atmosphere of  $10^{-2}$  to 100 Pa towards the negatively charged workpiece surface. Figure 4 shows a simplified model representation of chemical reactions during plasma nitriding. The energy of the impacting ion is partly dissipated into heat, deformation and the surface being sputtered. [29]

Nitrogen and sputtered iron atoms form FeN which adsorbs at the surface. Nitrogen diffuses interstitially in the near-surface region due to a catalytic decay of FeN to Fe and causes the formation of nitrides in the diffusion zone. This leads to the development of a preferential residual stress state, exhibiting compressive residual stresses at the surface which increase the fatigue strength of the material. [30]



**Figure 4.** Simplified representation of surface reactions during plasma nitriding (modified illustration based on Ref. [35]).

Often, hydrogen is additionally present in the nitriding atmosphere. In this case, many parallel reactions take place. An increase of the hydrogen content can reduce the formation or composition of the compound layer to Fe<sub>4</sub>N. It is even possible to prevent the compound layer formation by adjusting the H<sub>2</sub> to N<sub>2</sub> ratio (8:1). [30]

### 2.1.5 Mechanically-induced gradients

Another possibility to enhance mechanical properties by inducing gradients in metal components are peening processes, which modify the microstructure, stress-state and dislocation density in the near-surface region. The following peening techniques are most widely used [36]:

- Shot peening,
- Ultrasonic Impact Peening,
- Laser Shock Peening,
- High-frequency hammer peening [37] and
- Rolling

where in the context of this work shot peening was applied to induce a gradient mechanically and will thus be described in more detail.

### 2.1.5.1 Shot peening

Shot peening is a process in which a blasting material accelerated by compressed air hits a target surface at high speed. The kinetic energy of one impacting particle, impinging with a high velocity causes an elasto-plastic deformation of the surface (Figure 5a). Due to the comparatively small contact area of the impinging particle, a dimple is created. Thus, the defect and dislocation densities in the bombarded material increase. The crystal lattice, which is located further away from the impact site, is elastically strained, thus (compressive) residual stresses are induced in the material. If not one but many (mostly spherical) blasting particles (further also denoted as *shot*) hit the surface, plastically and elastically deformed regions caused by the individual impacts overlap and interact with each other. This results in (i) work hardening, thus further increasing defect and dislocation densities in the severely plastically deformed regions which can even lead to recrystallization [36,38] and a gradual modification of the near-surface microstructure as well as (ii) a deformation front causing (compressively) strained region and a gradual modification of mechanical properties in the material.

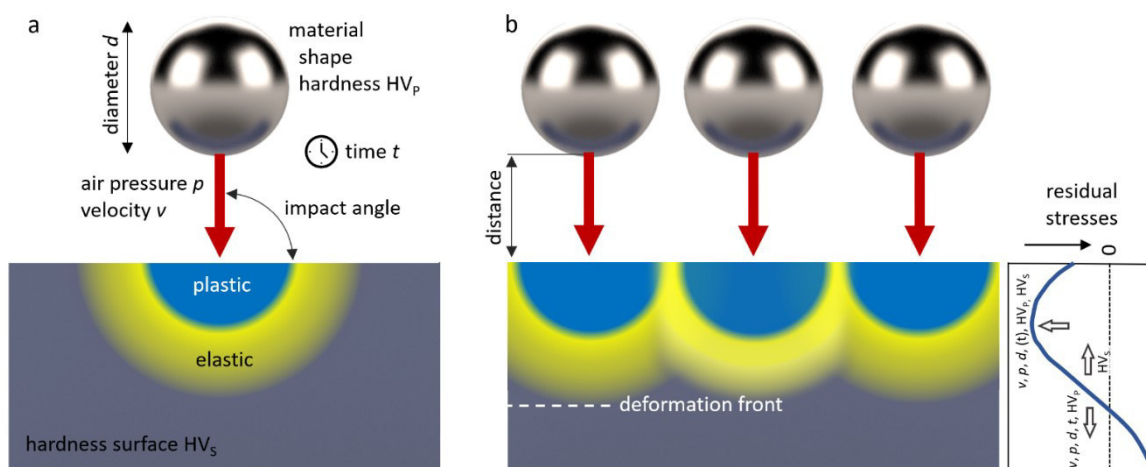


**Figure 5.** Schematic diagram of the particle-surface interaction as a result of a single impact (a) and factors influencing the shot peening process. During shot peening, multiple particles of the blasting medium hit the surface (b) and their plastically and elastically strained interaction zones interfere, causing a deformation front (dashed line), resulting in a gradual modification of the impacted material’s microstructure due to recrystallization and introduction of compressive residual stresses, respectively.

Several process parameters can be adjusted during shot peening [30,39,40], of which some are illustrated in Figure 5. These are

- (i) *Type, material, shape and hardness of the peening medium:* Spherical (martensitic) steel particles with a hardness  $HV_p$  in the range of 52 to 62 HRC are widely used. Also, larger-sized peening media are available. It should be



noted that also the shot is plastically deformed during shot peening and thus needs to be exchanged regularly [41]. In modern systems, media classification based on the shape of the particles is performed permanently during the process [42]. Other blasting media can be *e.g.* ceramic spheres, steel cylinders, etc.

- (ii) *Air pressure*: Compressed air is one way to accelerate the peening material onto specific surfaces to be treated. The pressure  $p$  used directly influences the velocity of the peening particles. Direct pressure systems are commonly used. Suction-style propulsion systems are used for lower peening intensities. In injector and injector-gravity systems, the peening material is also transported via an air stream. [30,39]

Other and airless possibilities to accelerate the peening media are wheel-blast machines, equipped with a centrifugal blast wheel. Wheel-blast peening is especially used in case of large production volumes without the need of masked areas. Nowadays, also hybrid devices are available. [42]

- (iii) *Nozzle (and jet) size*: The size and geometrical shape of the peening nozzle also influences the peening intensity. Straight bore or venturi style nozzles are commonly used for direct pressure peening. [42]
- (iv) *Stand-off distance*: The distance between the nozzle and the surface lies within the region of about 10 cm for severe shot peening treatments which are able to induce gradients in near-surface regions of a material. [38]
- (v) *Impact angle*. The angle of impact determines the percentage of energy adsorbed from the surface by the impact of the peening sphere. The maximum energy input therefor occurs at an angle of  $90^\circ$ .
- (vi) *Peening duration and surface coverage*: The peening duration influences exposure time  $t$  of the surfaces and thus the surface coverage. The speed of work determines these measures and both, a movement of the components and/or the nozzle can influence them. If every position on a surface is hit once by a peening particle, this corresponds to a coverage of 100%.

All mentioned parameters influence the energy transmitted to the near-surface region of the blasted material with a surface hardness  $HV_s$ . Thus, they directly influence the resulting elasto-plastic-deformation. Since the effects of a shot peening treatment on a material depends on these various variables and the blasted material often cannot be characterized with non-destructive methods, the so-called *Almen intensity* is alternatively used as an indicator in industrial practice [30,39]. The Almen intensity is a measure to directly compare different shot peening processes. Depending on the peening intensities (low, medium and high), three standardized Almen strip geometries (N, A and C, respectively) can be used to experimentally determine the shot peening impact [43]. Due

to the low thickness of Almen strips, the compensatory residual stresses introduced by the peening process result in a deformation of the strips. The deformation achieved can subsequently be used as a direct comparative value for processes with varying peening parameters.

FGMs produced by the above-described processes exhibit attractive functional properties resulting from effects that occur in the meso-scale (*cf.* Figure 1). Hence, it is important to use analytical techniques that enable characterization of the materials on the same scale. The following section describes selected characterization methods that were applied to analyze gradients of residual stresses, chemical gradient, gradual phase distributions and microstructural gradients.

## 2.2 Multiscale Characterization

Gradients in FGMs can span a wide range of length scales. An essential basic requirement that must be considered in the development and optimization of gradient materials is the correct application of their physical and chemical properties. These change spatially, which is why simulation of their behavior (biological and synthetically generated FGMs) is often very difficult, costly or simply too complex to be carried out with current methods and available computer performance. In contrast, experimental methods can provide direct insight into material gradients, and their results can subsequently also be fed into simulation databases. Figure 6 provides an overview of different microscopy techniques, mechanical tests and diffraction experiments that can be used to investigate the microstructural features present in FGMs and the structures produced by FGAM, respectively, across scales. The following section describes cross-sectional synchrotron X-ray micro diffraction (CSmicroXRD) – a method that was further developed and refined in this dissertation, with a particular focus on the characterization of mesoscale features.

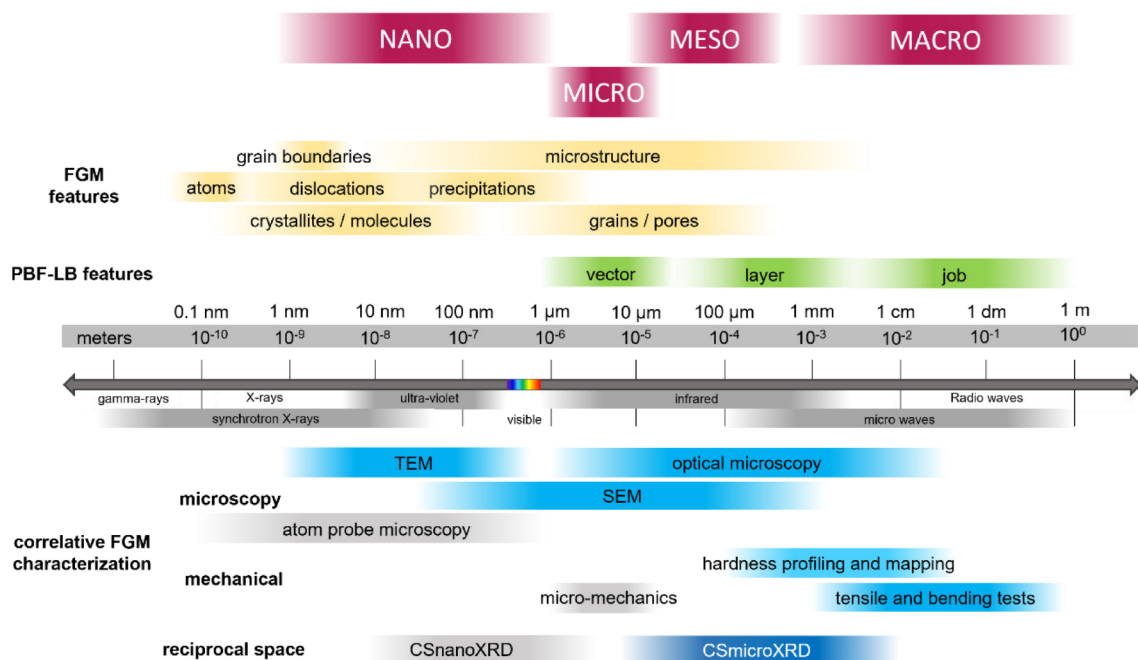


**Figure 6.** Schematic diagram of the classification of FGMs, different features in FGMs and materials synthesized by PBF-LB and a selection of characterization methods with reference to the scale range of the electromagnetic spectrum. Characterization methods that were employed within the scope of this work are highlighted in blue. Newly developed methods and/or methods that were significantly refined within the scope of this thesis are highlighted in dark blue.<sup>5</sup>

<sup>5</sup> Symbol images of FGM applications taken from pixabay.com. Access date: 22<sup>nd</sup> September, 2022.

### **2.2.1 Cross-sectional synchrotron X-ray micro-diffraction.**

As a further development of classical X-ray diffraction (XRD), cross-sectional XRD performed at large-scale research facilities (*i.e.*, synchrotrons) has been established as a powerful analytical method in materials research over the last ten years and is now indispensable. The major advantage in the use of synchrotron radiation sources is that X-rays of sufficiently high energy and brightness can be generated so that comparably thick samples can be penetrated and thus be investigated in transmission diffraction geometry. A schematic diagram of the experimental set-up used to characterize the three samples for Paper II is presented in Figure 7. A transmission diffraction geometry set-up for metals exceeding some microns in thickness is only possible at synchrotron sources, but not in in-house laboratory settings. This is due to the fact that only synchrotron sources provide sufficient photon energy, photon flux density, monochromaticity and beam parallelity. Depending on the type of sample to be investigated, the spatial resolution in the transmission set-up can reach the nanoscale [44–46] and nowadays even goes down to 30 nm and less in case of cross-sectional synchrotron X-ray nanodiffraction [47]. The method has been successfully employed to characterize (i) the phase composition, (ii) the crystallographic texture, (iii) the size of coherently scattering domains and (iv) residual strains of the 1<sup>st</sup>, the 2<sup>nd</sup> and the 3<sup>rd</sup> order. [12,44,45,47–52]

In the context of this thesis, the experimental conditions and evaluation methods were modified and further developed, respectively, in order to meet the requirements that the characterization of FGMs places on the methods. The following sections briefly describe some theoretical principles and the analyses applied.

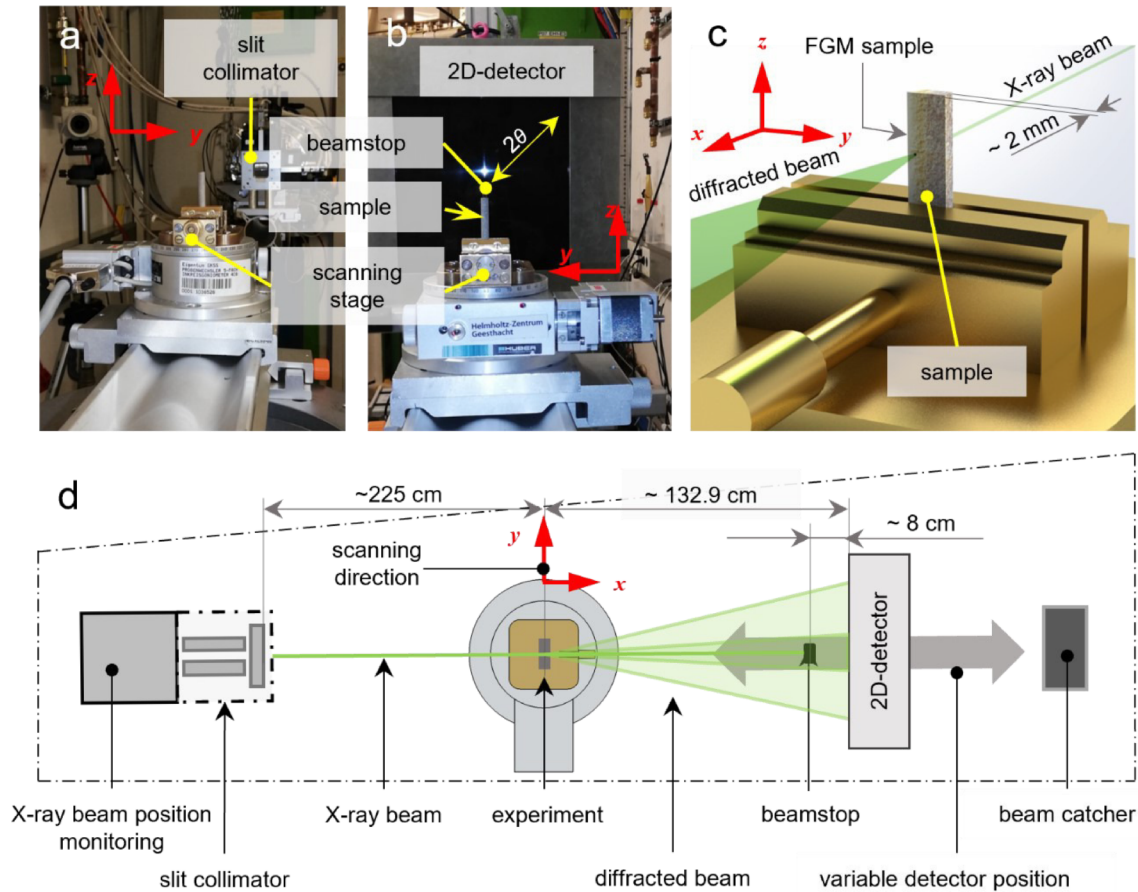


**Figure 7.** Set-up at the P07B experimental station at the storage ring PETRAIII of DESY, Hamburg, Germany. In the experiment graded material samples are placed in a way so that the collimated pencil beam penetrates the samples in transmission diffraction geometry along the  $x$ -axis (a,b). The samples are moved via a motorized stage along the  $y$  and  $z$  directions. A 2D X-ray-sensitive area detector acquires the diffraction signal at its intersection with the diffraction cones (c). The sample-to-detector distance can be adjusted by moving the detector along the  $x$ -axis; its exact position has to be calibrated. The incoming beam and the diffraction cones are indicated by a green line and green cones, respectively. A schematic overview of the experiment is given in (d). (Figure adapted from Ref. [53])

### 2.2.1.1 Analysis of the phase composition

Possessing a wavelength between  $10^{-3}$  and  $10^1$  nm, X-ray photons interact with matter and result in various absorption and scattering effects. In this context, coherent scattering, also known as Rayleigh scattering, describes the elastic interaction of high-energy photons with the electrons of atoms, surrounding their nuclei [48]. The photons scattered at the lattice planes in crystalline structures interfere in a constructive or destructive way as a consequence of the specific and periodic arrangement and spacing of the atoms. Constructive interference of two (and more) scattered waves results in a characteristic intensity signal that can be interpreted as “finger-print” of a crystalline phase. This phenomenon is called *diffraction* and is geometrically described by the *Bragg condition* [54] (Figure 8a),

$$2d_{hkl} \sin \theta_{hkl} = n\lambda \quad (1.1)$$

where  $d, \theta, n, \lambda$  and  $hkl$  represent the lattice plane spacing, the diffraction angle (also referred to as *Bragg angle*), the order of the diffraction peak, the wavelength of the incident X-rays and the Miller indices of the diffracting planes, respectively. The intensity of the diffraction signal of the respective  $hkl$  lattice plane family in a perfect crystal is proportional to the square of the crystallographic structure factor [55–57]

$$F_{hkl} = \sum_{j=1}^N f_j \cdot \exp(2\pi i(hx_j + ky_j + lz_j)) \quad (1.2)$$

where  $f_j$  and  $x, y, z$  denote the scattering factor of atom  $j$ , and the respective position of the atom in the unit cell, respectively.  $F_{hkl}$  describes the sum of all waves scattered in the specific  $hkl$  directions, where potentially a signal extinction can occur depending on the Bravais lattice and basis of the examined crystal structure. Thus,  $F_{hkl}$  must be non-zero for a diffracted intensity to be measured.

In polycrystalline materials with randomly oriented individual crystals, the sum of all crystals fulfilling Bragg's law for a fixed wavelength and incident X-ray direction results in the occurrence of diffraction cones. It follows from Eq. (1.1), that the use of monochromatic X-rays interacting with a polycrystalline material leads to a cone of diffracted intensity with a half opening angle  $2\theta$ . The corresponding signal can be recorded at the intersection of the diffraction cone with a 2D detector (Figure 7d). The intersection results in a diffraction pattern in the form of so-called *Debye-Scherrer rings* (Figure 9). The arrangement and angle at which these rings can be observed are again specific to the investigated crystalline phase.

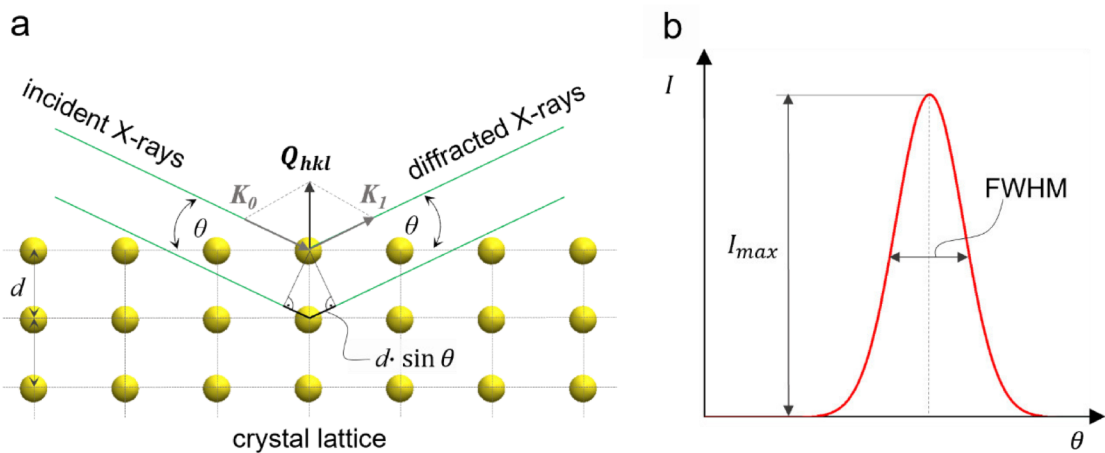


**Figure 8.** Geometrical visualization, showing the derivation of the Bragg condition. Incident X-rays are described by wave vector  $K_0$ , while scattered X-rays are represented by wave vector  $K_1$ . They interfere in a constructive manner if the phase shift between waves scattered at different lattice planes is a multiple of the incident wavelength  $\lambda$ . (a) The diffraction peak is observed at the Bragg angle  $\theta$  (b). Its full-width-at-half-maximum (FWHM) is influenced by several factors. Among them are the size of coherently scattering domains within the sample and lattice defects, as well as micro-strains. Figure adapted from Refs. [46,56–58].

From the azimuthal integration of the Debye-Scherrer rings, a plot of diffraction intensity  $I$  versus diffraction angle  $2\theta$  can be derived (Figure 8 and Figure 9). A correct calibration of the sample-to-detector distance, the beam center and the angular orientation of the detector with respect to the incident X-ray beam is essential to correctly determine the lattice parameters of the polycrystalline sample. Therefore, the diffraction pattern of a well-known calibration standard (*e.g.* lanthanum hexaboride – LaB<sub>6</sub>) is recorded and the listed parameters are determined by back-calculation.

The total peak intensity  $I_{hkl}$  and “shape” of the diffraction signal (*e.g.* its full-width-at-half-maximum value (FWHM) in Figure 8) for a lattice plane family in a real experiment with an existing (*i.e.*, non-ideal) crystal, depends on further contributions due to imperfections. Among these are absorption and polarization of the X-rays, the size of the coherently scattering domains, chemical inhomogeneity, residual stresses and crystal defects such as dislocations, stacking faults or twinning. In addition, there is an influence caused by the experimental set-up due to imperfections of the X-ray source, beam optics, detector, etc. [48,59]

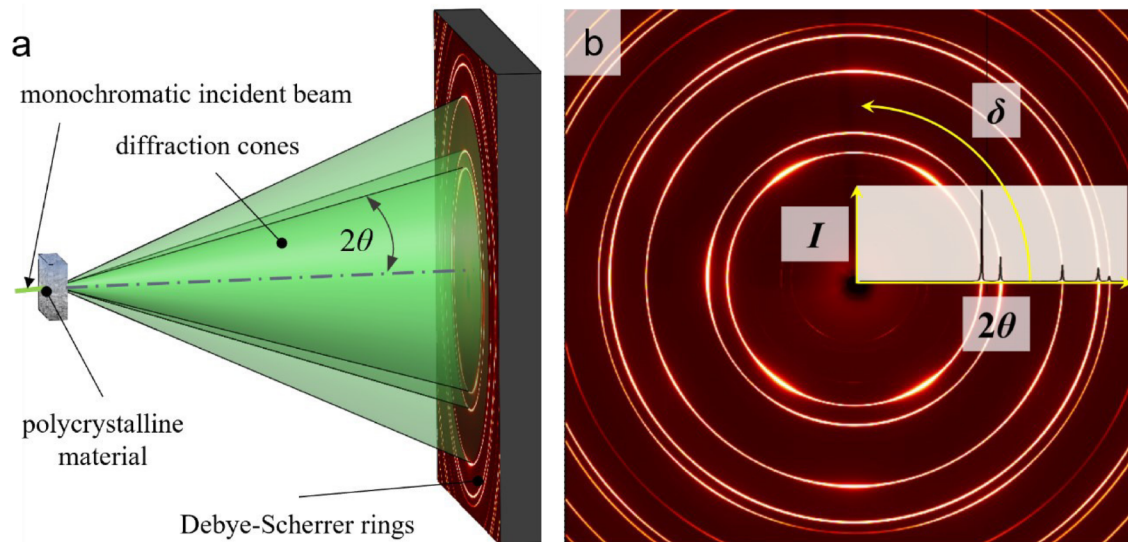


**Figure 9.** Schematic diagram of diffraction cones emanating from a polycrystalline sample investigated with a monochromatic beam (a). The illustrated 2D diffraction pattern with characteristic Debye-Scherrer rings represents the volume-averaged and orientation-dependent information from the irradiated gauge volume (b). An azimuthal integration along  $\delta$  around the beam center results in a  $I(2\theta)$  plot and is used for phase analysis. The inhomogeneous intensity distribution along  $\delta$  of specific rings is used to derive information about the crystallographic texture in the sample.

Integrated data from measured samples can be represented in different ways. In case of the investigation of FGMs, the representation in the form of phase plots has proven to be useful for simple scans during which diffractograms are acquired along a cross-sectional direction at different points. The distance between the individual positions and thus the step size usually corresponds to the geometric extension of the incident X-ray beam in this dimension. The processing and evaluation of the sizable amount of data generated in such experiments need to be handled in an automated fashion. The Python-language based package pyFAI [60] has the capability to evaluate such large amounts of data in a reasonable time on desktop computers. An in-house developed graphical user interface offers the possibility to load data into pyFAI in order to process them automatically with customized macros. Thus, the evaluation of phase ratios, texture and residual stresses can be handled efficiently.

### Evaluation of retained austenite contents in steels

The presence of retained austenite contents in martensitic steels strongly influences the mechanical properties of steel by reducing the hardness and strength of the material. An inhomogeneous distribution of interstitial carbon and nitrogen can lead to locally occurring retained or reverted austenite. The phase ratio of austenite in a steel can be derived from the integrated XRD data in different ways. Besides Rietveld analysis, the



comparison of integrated peaks intensities (*i.e.*, the area under the peak above the background) according to the ASTM E975-13[61] standard is widely used.

According to the ASTM standard the evaluation of the volume fraction  $V$  of austenite ( $\gamma$ ) in a two-phase material with the second phase being iron-ferrite ( $\alpha$ ) or martensite ( $\alpha'$ ) can be derived from the equalized intensities of  $p$  and  $q$  ferrite and martensite peaks, respectively, according to

$$V_{\gamma} = \frac{\frac{1}{q} \sum_{j=1}^q \frac{I_{\gamma,hkl}}{R_{\gamma,hkl}}}{\frac{1}{p} \sum_{i=1}^p \frac{I_{\alpha,hkl}}{R_{\alpha,hkl}} + \frac{1}{q} \sum_{j=1}^q \frac{I_{\gamma,hkl}}{R_{\gamma,hkl}}} \quad (1.3)$$

where  $I_{\gamma,hkl}$  and  $I_{\alpha,hkl}$  correspond to the integrated peak intensities. If further phases such as carbides are present in the material, the volume fraction of carbides must also be taken into account in order to reveal a correct volume fraction of austenite and ferrite.  $R_{hkl}$  values can be calculated for each phase to be

$$R_{hkl} = \frac{|F_{hkl}|^2 \cdot r \cdot L \cdot P \cdot \exp(-2(\sin \frac{\theta}{\lambda})^2 B)}{v^2} \quad (1.4)$$

where  $F_{hkl}$ ,  $r$ ,  $L$ ,  $\theta$ ,  $\lambda$ ,  $B$  and  $v$  are the structure factor, the multiplicity of the  $hkl$  lattice planes, the Lorentz factor, the Bragg angle, the wavelength of the X-rays, the Debye-Waller temperature factor and the volume of the crystal unit cell, respectively. The factor of the correction of the polarization  $P$  is

$$P = \frac{1 + \cos^2 2\theta}{2} \quad (1.5)$$

Various  $B$  factors, determined from the experimental phonon density of states are listed in Ref [62]. Room-temperature values of  $B_{\alpha} = 0.3250$  and  $B_{\gamma} = 0.5615$  are given and should be used in preference to the ASTM unified value (*i.e.*,  $B = 0.71$  for  $\alpha$  and  $\gamma$ ).

As the whole width of a Bragg reflex is recorded when a 2D detector is used, the Lorentz factor can be neglected if relative intensities equivalent to a conventional diffractometer are expected [57]. One further advantage resulting from the use of an area detector, is that the crystallographic texture, described in more detail in the following section, and its related intensity variations along the azimuth angle  $\delta$  do not strongly affect the result of the measurement.

### 2.2.1.1 Analysis of the crystallographic texture

Crystallites in a polycrystalline material are rarely distributed randomly, but possess a preferred orientation, also known as crystallographic texture [57]. XRD can be used to determine crystallographic textures, as the scattering signals of lattice planes in preferentially oriented crystallites cause an inhomogeneous intensity distribution along the azimuth direction  $\delta$  of Debye-Scherrer rings (Figure 9) due to orientation-dependent diffraction peak intensities. The orientation distribution of crystallites in the examined sample with a cubic crystal symmetry can be calculated, if the diffraction peak intensities of two or more non-parallel lattice plane families are measured.

In crystallography, so-called *pole figures* are useful and widely used as 2D representations of the 3D orientation distribution of lattice planes. In such representations, a *pole* is defined to be the point of intersection of the normal of a  $(hkl)$  lattice plane with a reference sphere (in 3D) with a unit radius  $r = 1$  residing around a crystal (Figure 10a). A pole figure then results from the projection of the poles of lattice planes in crystals of a polycrystalline sample onto an equatorial plane. The position of any (projected) pole can be described by the polar angle  $\alpha$  and a rotational angle  $\beta$ . The geometric correlation between the coordinates of a point at the pole figure centered on the cross-section-normal direction and the same point at the 2D-detector is given by

$$\sin \alpha = \sin \delta \cos \theta \quad (1.6)$$

and

$$\begin{aligned} \cos \beta = & + \sqrt{\frac{\cos^2 \delta \cos^2 \theta}{1 - \sin^2 \delta \cos^2 \theta}} \mid -90^\circ < \delta < 90^\circ, \\ & - \sqrt{\frac{\cos^2 \delta \cos^2 \theta}{1 - \sin^2 \delta \cos^2 \theta}} \mid +90^\circ < \delta < 270^\circ, \end{aligned} \quad (1.7)$$

where  $\alpha$ ,  $\beta$ ,  $\delta$  and  $\theta$  are the polar angle, the rotational angle, the detector's azimuthal angle and the diffraction angle of the 2D detector, respectively (*cf.* Figure 9).

A collection of preferentially oriented crystals in a polycrystalline sample results in a spatial concentration of  $hkl$  poles at the unit sphere (increased pole density). Consequently, the  $2\theta$  integrated intensity of Debye-Scherrer rings leads to  $\delta$ -dependent areas with intensity maxima (and minima) in the diffractogram (Figure 10b), according to the pole density of the corresponding crystallographic plane. It follows, that the derived intensity  $I_{hkl}$  for any  $\{hkl\}$  family of planes, diffracting at a Bragg angle  $\theta_{hkl}$ , in a polycrystalline, textured sample is a function of the sample orientation and the azimuth

angle of the detector (Figure 10). However, due to the experimental set-up and perpendicular alignment of the sample with respect to the incident synchrotron X-ray beam (*cf.* Figure 7), the number of sampled crystallite orientations is limited.

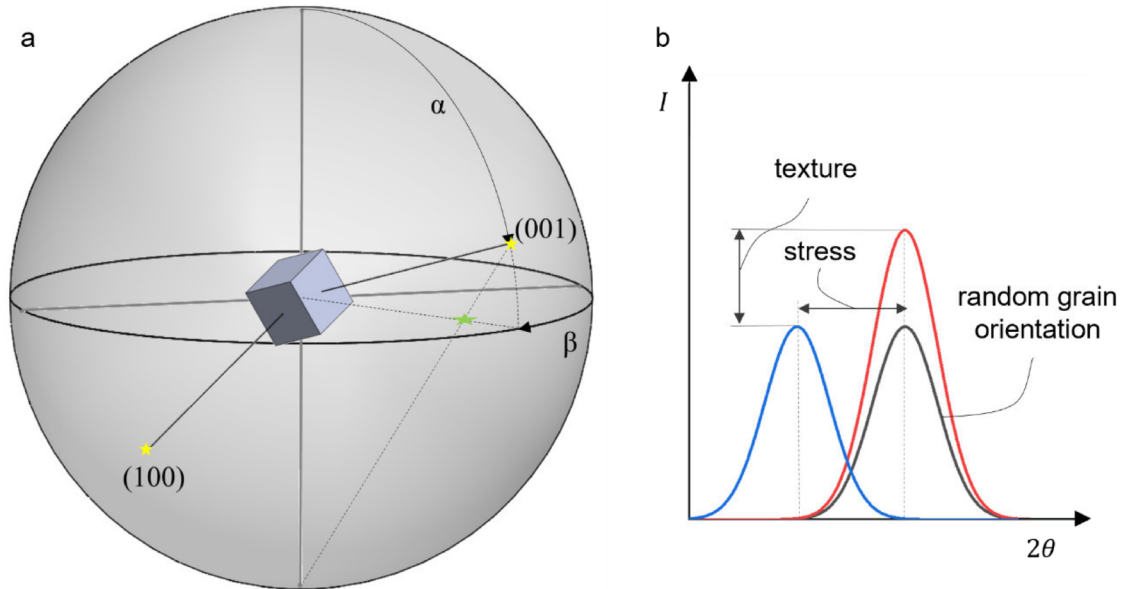


**Figure 10.** Orientation of the top plane (001) and the front plane (100) of a tilted cubic crystal surrounded by a unit sphere with a radius  $r = 1$ . The position of the 001 pole on the unit sphere with regard to an external reference frame is described by the polar and rotational angle  $\alpha$  and  $\beta$ , respectively (a). A collection of similarly oriented cubic crystals (in a textured, polycrystalline sample) leads to a concentration maximum of poles (indicated as yellow stars) and projected poles on the equator plane (green star). Thus, the orientation distribution of a textured sample exhibits intensity maxima (and minima) which can be determined also from the intensity of the integrated peaks in the corresponding diffractogram (b). (Residual) Stresses lead to a shift of peaks in a diffractogram due to an orientation-dependent change of the lattice spacing  $d$ .

As indicated in Figure 10b, the presence of (macroscopic) residual stresses in a sample does not influence the peak intensities but changes their position. The following section introduces the basics of residual stress analysis from XRD data.

### 2.2.1 Analysis of residual stresses

The gradual variation of physical and chemical properties in FGMs leads to the build-up of residual stresses, mainly in the gradient regions. First-order residual stresses encompass multiple grains in a polycrystalline sample and induce a proportional (elastic) lattice strain. This leads to an orientation-dependent change of the lattice spacing  $(d_{hkl})_{\phi\psi}$  that can be assessed by XRD experiments through *Bragg's law* (Eq. 1.1). Diffraction cones are generated from the stressed samples which are similar to the diffraction cones from an unstressed sample (Figure 9). However, the cones of stressed samples are elliptically distorted so that  $2\theta_{hkl}$  becomes a function of the azimuth angle  $\delta$  of the Debye-Scherrer ring. [57]

Generally, it is essential to know the unstrained lattice parameter  $d_0$  in order to calculate the lattice strain [46,57,58,63,64],

$$(\varepsilon'_{hkl})_{\phi\psi} = \frac{(d_{hkl})_{\phi\psi} - d_0}{d_0} \quad (1.8)$$

where  $\phi$  and  $\psi$  are rotation angles that relate the sample coordinate system to the coordinate system of the experimental (laboratory) set-up. For the XRD set-up in synchrotron experiments, it is more expedient to use detector coordinates  $\theta$  and  $\delta$  that can be linked to the sample rotation angle  $\psi$  using the following transformation which can be derived also from Heidelbach *et al.* [51]:

$$\cos \psi = \cos \theta \cos \delta \quad (1.9)$$

The experimentally determined and direction-dependent X-ray elastic strain  $(\varepsilon'_{hkl})_{\phi\psi}$  in the sample coordinate system can be related to the general triaxial stress state by a tensor transformation using the direction cosine matrix

$$a_{ik} = \begin{bmatrix} \cos \phi \cos \psi & \sin \phi \cos \psi & -\sin \psi \\ -\sin \phi & \cos \phi & 0 \\ \cos \phi \sin \psi & \sin \phi \sin \psi & \cos \psi \end{bmatrix} \quad (1.9)$$

As a consequence, the fundamental equation of X-ray strain determination [63] results in

$$\begin{aligned} (\varepsilon'_{hkl})_{\theta\delta} = & \varepsilon_{11} \sin^2 \theta - \varepsilon_{12} \sin 2\theta \sin \delta + \varepsilon_{22} \cos^2 \theta \sin^2 \delta \\ & + \varepsilon_{33} \cos^2 \theta \cos^2 \delta - \varepsilon_{13} \sin 2\theta \cos \delta + \varepsilon_{23} \cos^2 \theta \sin 2\delta \end{aligned} \quad (1.10)$$

where  $\varepsilon_{11}$  represents the normal strains oriented parallel to the incident X-ray beam and  $\varepsilon_{22}$  and  $\varepsilon_{33}$  represent the normal strains in-plane and the out-of-plane, respectively, with respect to the examined sample surface. Additionally, shear stresses  $\varepsilon_{ij}$  also contribute terms to the equation.

The stress state within the material can be related to the strain state by the fundamental theory of elasticity which is *Hooke's law*[55,57],

$$\sigma_{ij} = \sum_{k,l=1}^3 c_{ijkl} \varepsilon_{kl} \quad (1.11)$$

where  $\sigma_{ij}$ ,  $c_{ijkl}$  and  $\varepsilon_{kl}$  are the stress, the stiffness and the strain tensors, respectively.

In case of macroscopic elastically isotropic behavior of the investigated homogenous material, only two elasticity constants are independent from each other. These are *Young's modulus*  $E$  and *Poisson's ratio*  $\nu$ . With

$$s_{1,hkl} = \frac{-\nu}{E} \quad (1.12)$$

and

$$\frac{1}{2} s_{2,hkl} = \frac{1 + \nu}{E} \quad (1.13)$$

Combination of Eqs. (1.10) to (1.13) thus yields

$$\begin{aligned} (\varepsilon'_{hkl})_{\theta\delta} &= s_{1,hkl} (\sigma_{11} + \sigma_{22} + \sigma_{33}) \\ &+ \frac{1}{2} s_{2,hkl} (\sigma_{11} \sin^2 \theta + \sigma_{22} \cos^2 \theta \sin^2 \delta + \sigma_{33} \cos^2 \theta \cos^2 \delta) \\ &+ \frac{1}{2} s_{2,hkl} (-\sigma_{13} \sin^2 \theta + \sigma_{23} \cos^2 \theta \sin 2\delta + \sigma_{12} \sin 2\theta \sin \delta) \end{aligned} \quad (1.14)$$

as the inverse of the elastic stiffness tensor  $c_{ijkl}^{-1}$  is the elastic compliance tensor  $s_{ijkl}$ .

In Eq. 1.13,  $s_{1,hkl}$  and  $\frac{1}{2} s_{2,hkl}$  are the  $hkl$ -dependent X-ray elastic constants (XECs) of the investigated material, derived from different grain interaction models [55].

Considerations of the stress states that are actually present in materials in practical applications result often in certain boundary conditions. They lead to the possibility of equating several components of the stress matrix or setting them to zero in many cases. One example are thin films, where the normal stress component  $\sigma_{33}$  acting on the sample surface is negligible.[46,58] If furthermore (i) the presence of shear stresses can be excluded ( $\sigma_{ij} = 0$ ) and (ii) an equi-biaxial stress state with  $\sigma_{11} = \sigma_{22}$  can be assumed, Eq. 1.10 can be simplified as follows:

$$\begin{aligned} (\varepsilon'_{hkl})_{\theta\delta} &= \frac{(d_{hkl})_{\theta\delta} - d_0}{d_0} = s_{1,hkl} 2\sigma_{22} \\ &+ \frac{1}{2} s_{2,hkl} (\sigma_{22} \sin^2 \theta + \sigma_{22} \cos^2 \theta \sin^2 \delta) \end{aligned} \quad (1.15)$$

Similar to the  $\sin^2\psi$ -method, a linear relationship between  $(d_{hkl})_{\theta\delta}$  and  $\sin^2 \delta$  results in this case as well. Thus,  $\sigma_{22}$  can be assessed by a linear regression of the  $(d_{hkl})_{\theta\delta}$  vs.  $\sin^2 \delta$  distribution. In case of FGMs, the normal stress component  $\sigma_{33}$  in the out-of-plane direction cannot be assumed to be zero and the linear regression results in a difference of present stresses between the in-plane and the out-of-plane direction  $\sigma_{22} - \sigma_{33}$ .

This approach cannot be used for more complex stress conditions. In such a case, it is essential to know the unstressed lattice parameter  $d_0$  at each measurement point at the sample. This is a critical point especially for FGMs, since the changing chemical composition of the FGM results in a change of the unstressed lattice parameter as well. Furthermore, the influence of each normal stress component and the shear-stress components on the diffraction cones (and finally the Debye-Scherrer rings) need to be considered.

As  $\sigma_{11}$  is oriented parallel to the beam direction (Figure 7), this stress component cannot be assessed directly with sufficient sensitivity during a single CSmicroXRD experiment. To evaluate  $\sigma_{11}$  it is therefore necessary,

- (i) to rotate the sample  $90^\circ$  around  $z$  and repeat the measurement (if the sample geometry allows for it) or
- (ii) to assume some boundary conditions (*e.g.* due to sample symmetry or because the sample has a negligible extension along the  $x$  direction in contrast to the  $y$  and  $z$  directions) or
- (iii) to consider several Debye-Scherrer rings simultaneously for the evaluation of stresses. In this case, the Debye-Scherrer rings should cover as large a  $\theta$ -range as possible.

Contributions of the normal stress components  $\sigma_{22}$  and  $\sigma_{33}$  which are parallel to  $y$  and  $z$  (Figure 7), lead to an elliptical distortion of the Debye-Scherrer rings along its in-plane and out-of-plane dimensions, respectively. A further elliptical deformation of the Debye-Scherrer rings can be caused by the shear stress component  $\sigma_{23}$ . In contrast to the elliptical deformation due to  $\sigma_{22}$  and  $\sigma_{33}$ , the principal axes are oriented at an azimuth angle of  $45^\circ$  in this case.[46]

The shear stress components  $\sigma_{12}$  and  $\sigma_{13}$  have an effect similar to a poorly adjusted beam center – they cause a vertical or horizontal displacement of the entire Debye-Scherrer rings along the horizontal or vertical direction. It follows, that the initial translational and rotational detector alignment is essential as a poor alignment would be misinterpreted as elastic strain.

Complex stress states can finally be determined by solving a linear system of equations with up to six unknowns which can be derived from Eq. 1.13. The corresponding XECs are determined from databases or using grain interaction models. Since X-ray elastic strain values  $(\varepsilon'_{hkl})_\theta$  can be determined for several azimuth directions  $\delta$  by peak fitting, the unknown stress components can be derived numerically by least-squares fitting of the over-determined system of equations applying matrix algebra [46,58]. It follows, that the 2D diffraction pattern must not only be azimuthally integrated in the range of  $0 < d < 360^\circ$ , but in  $n$  azimuthal sectors *e.g.* of  $5$  or  $10^\circ$  in width are considered as integration boundaries. This results in a set of *e.g.*  $n = 72$  (or  $36$ )  $I(2\theta, \delta)$  profiles which can subsequently be used for the  $\delta$ -angle dependent peak fitting. [46,58]

A useful approach to fit the functions of the peak-profiles is the so-called *pseudo-Voigt* function which is a linear superposition of *Gaussian* and *Lorentzian* peak functions formulated with diffraction-related quantities and can be expressed through

$$I(2\theta, \delta) = \mu \frac{I_0}{1 + \left(\frac{2\theta - 2\theta_0}{\frac{1}{2}\beta}\right)^2} + (1 + \mu) I_0 \exp \left[ -\ln 2 \left( \frac{2\theta - 2\theta_0}{\frac{1}{2}\beta} \right)^2 \right] \quad (1.15)$$

where  $I(2\theta, \delta)$ ,  $I_0$ ,  $2\theta_0$ ,  $\beta$ ,  $\mu$  and  $2\theta$  are the angle-dependent intensity, the maximal peak intensity, the XRD peak's center position, the FWHM of the peak, the ratio of Lorentzian over Gaussian proportion to the peak function and the considered diffraction angle, respectively. The main results of the peak fit that are used also for further evaluations are  $2\theta_0$  and  $\beta$ .

Again, it should be noted that the evaluation described above is capable of determining only first-order, *i.e.*, macroscopic residual stresses. The presence of residual stresses of second and third order (*i.e.*, micro-stresses) contributes to the broadening of the peak instead. Other factors also contribute to peak broadening. One of them is the size of coherently diffracting domains. The following section deals with the interpretation of the microstructure morphology from the orientation-dependent peak width.

### 2.2.1 Derivation of the microstructural morphology

As mentioned on page 24, the size of coherently scattering domains influences the width of diffraction peaks, and thus also the width of the corresponding *hkl* Debye-Scherrer rings. This relationship was first reported by Scherrer [65] and is known as the *Scherrer equation*, which reads

$$D = \frac{K \lambda}{\beta \cos \theta} \quad (1.16)$$

where  $D$  is the size of coherently scattering domains and is often referred to as *particle size*. The variables  $\lambda$ ,  $\beta$  and  $\theta$  denote the wavelength of the X-rays, the FWHM of the *hkl* peak and the Bragg angle (Figure 9), respectively.  $K$  is a dimensionless factor that depends on the crystallite shape (globular or angular) and typically lies in the range between 0.9 to 1.0 [46,57]. It follows, that smaller grains result in a larger FWHM and vice versa. According to the underlying theory, the signal of a perfect crystal lattice of infinite extent would lead to an infinitely sharp diffraction peak and, in conclusion any deviation from the perfect crystal lattice must result in a broadening of the peak. As mentioned, several other factors (micro-strains/stresses, crystallographic defects, diffractometer optics) as well contribute to peak broadening and need to be considered and subtracted in order to minimize the evaluation error. [57]

In CSmicroXRD experiments performed with area detectors,  $\beta_{hkl}(\delta)$  which is the FWHM of different Debye-Scherrer rings in arbitrary  $\delta$ -directions, can be used to derive

## Theoretical Background

---

the size of coherently scattering domains that are oriented in different directions within the  $y$ - $z$ -plane of the polycrystalline sample. Due to the direction-dependent broadening of peaks, the morphological orientation of non-equiaxed grains can be assessed. Moreover, it is possible to distinguish globular from columnar or acicular grain shapes. [46]



### 3 Determined Novel Features in Graded Materials and Conclusions

This doctoral thesis deals with the fabrication of different FGMs by advanced production methods and a length-scale adapted characterization of these materials. The main objectives were to develop new methods (i) which are suitable for the fabrication of multi-metal materials with high spatial resolution, and (ii) that enable cross-scale studies in different FGMs to obtain results that accelerate their development and optimization. Results were verified by various standard analytical methods and correlated with their results. This section summarizes major findings which could not be assessed by other characterization methods and puts these results in context with the state of the art.

#### 3.1 Synthesis of FGMs by Liquid-dispersed Metal Powder Bed Fusion

The production of thick FGMs by AM is currently a topic which is intensively studied in the AM community.[1,21] In this thesis, LDM-PBF-LB was applied and further developed to synthesize metal-based FGAMs for the first time by combining two alloys. The first sample (extensively characterized and discussed in the context of Paper I) was designed in order to evaluate the spatial resolution in out-of-plane direction which is the direction parallel to the AM build direction (*cf.* Figure 3). This so-called *inter-layer* resolution was determined to be about 60  $\mu\text{m}$ . In a second sample, the two metal alloys were also varied within individual layers achieving a spatial resolution of about 1 mm (*intra-layer* resolution). The characterization of the latter sample was the subject of Paper IV.

Apart from the novel approach of using metallic slurries as feedstock for a powder bed-based process, LDM-PBF-LB with a comparatively high resolution limit was found to be a potential method for fabricating bio-inspired thick FGAMs.

The characterization of the microstructure using high-resolution characterization methods such as STEM and TEM-EDX led to the identification of homogeneously distributed, nano-scaled oxides that are able to enhance the mechanical strength of metal alloys. Oxides are formed through *reactive additive manufacturing* during the LDM-PBF-LB process as oxygen is provided by the water-based binder system. Hence, the binder system can be used as another influencing factor for tailoring chemical and mechanical properties during the build process.

The application of CSmicroXRD 2D-mapping contributed to the understanding of the evolution of residual stresses in AM specimens and, in particular, in the interfacial regions of the two processed metal alloys 316L and IN625 (*cf.* Paper IV). The entire sample cross-section of the multi-metal sample was scanned in the  $y$ - and  $z$ -directions and the distribution of phases, textures, microstructure morphology and residual stresses were investigated. The determined distribution of residual stresses on the sample cross-section explains, in particular, the origin of delamination effects at the sample edge and the occurrence of micro-cracking with a crack progression parallel to the build direction in the sample interior.

### **3.2 Modification of Crystallographic Texture by Different Hatch Strategies**

Stainless steel 316L produced by different AM methods is already a well-studied metal alloy and different influencing factors on the evolution of the microstructure have been intensively studied [66]. In this thesis, the influence of different hatch strategies in a standard PBF-LB process on the development of crystallographic textures was investigated as subject of Paper III. A novel result obtained is the correlation between the applied hatch strategies and the deformation mechanisms observed under uniaxial loading. While uniform deformation of the specimen cross-section was documented in two of three differently manufactured specimen sets, the third set showed a pronounced flow behavior of the material transverse to the loading direction. This effect could be explained by micro-twinning which was not observed in case of the other specimen sets. Moreover, a delayed work hardening was reported in case of the samples that exhibited micro-twinning.

### **3.3 Reverted Austenite Formation at the Diffusion Front of a Plasma-nitrided Hot-work Steel W300**

The interstitial diffusion of nitrogen during nitriding leads to the displacement of free carbon to greater depths. CSmicroXRD revealed the formation of an austenite phase ahead of the nitrogen diffusion front. The presence of austenite prior to the low-pressure plasma nitriding treatment can be excluded as otherwise, homogeneously distributed (retained) austenite would have been found also at greater sample depths. Hence, it has to be concluded, that a local phase transformation from martensite to (reverted) austenite took place during nitriding even though this effect had not yet been reported for a steel

with a nominal chemical composition of 0.39C-0.97Si-0.43Mn-0.21Ni-5.0Cr-1.14Mo-0.35V.

In addition, the variation of chemistry and phases along the sample's cross-section led to the evolution of a complex residual stress distribution, exhibiting two compressive residual stress peaks – one close to the sample surface and a second one at the interface between the diffusion zone and the core material which was also found to be the position with the maximal austenite content.

Current state-of-the-art standard characterization performed by laboratory XRD would not be able to detect the presence of the austenite phase as the experimental setup (reflection geometry) allows only for a very small penetration depth of the X-rays [46].

### **3.4 Dynamic Recrystallization and Texture Formation During High-energy Shot Peening of a 300M Steel**

Shot peening applying high energies at the surface of a heat-treated 300M steel led to a significant grain refinement (represented in CSmicroXRD through the size of coherently scattering domains) of the microstructure within the first ~20  $\mu\text{m}$  of the influenced region. Furthermore,  $\{110\}$  lattice planes of the bcc-crystal structure were found to exhibit a preferential orientation perpendicular to the sample's surface normal vector in the same region. Moreover, the mechanical surface-treatment of the low-alloy steel with a nominal chemical composition of 0.42C-1.65Si-0.80Mn-1.8Ni-0.80Cr-0.30Mo-0.80V induced a transformation of retained austenite to martensite that contributed (additionally to the peening treatment) to the evolution of compressive residual stresses due to volume expansion at depths smaller than 20  $\mu\text{m}$ .

The results of this application example show the easy transferability of CSmicroXRD to the analysis of FGMs, whose gradients were generated by different methods. Furthermore, results from CSmicroXRD experiments correlate with results from various standard characterization methods. Thus, these findings contribute to the use of experimentally determined values in database models in the future, for example to simulate residual stress curves based on measured hardness profiles on the cross-section.

## 4 Outlook and Impulses for Further Scientific Work

The successful application of CSmicroXRD for the advanced characterization of FGMs and FGAMs was demonstrated by selected examples. These results were correlated with the results of standard characterization methods like optical microscopy, scanning and transmission electron microscopy, hardness and tensile tests.

In addition to the results summarized and discussed in the four attached publications, the following new questions and impulses emerged that might be investigated in further scientific work.

- a) The transferability of CSmicroXRD characterization and its relevance to other biological FGMs (wood) [67] and homogenous PBF-LB fabricated samples has been demonstrated in further co-authored papers. Similar to the results presented in Paper II, it was shown that first-order residual stresses can be simultaneously determined in the martensite and austenite phases of a tool steel. [68]  
Regarding the cross-sectional characterization of FGMs and FGAMs using CSmicroXRD, it is important to continue working on solutions to determine correct values of unstrained lattice parameters and XECs which is especially demanding for interface regions between two or more different materials. However, a similar approach as in case of the aforementioned tool steel could be applied here.
- b) The selection of shot peening parameters based on Almen intensities is a common method in industrial practice. However, so far, no studies relate the introduced residual stresses to the deformations of the Almen platelets. Now that the material and geometry of the platelets used have been standardized, the comparison of the deformation with the introduced residual stresses lends itself to this method. In a next step with relevant industrial application, the correlation of the introduced residual stresses with the mechanical properties of the Almen platelets and the actually irradiated materials could be worked out.
- c) A broad scientific and industrial application of *reactive additive manufacturing* requires to influence the oxides formed during the AM process in terms of their size, shape, distribution, morphology and chemical composition. Thus, further studies on the influence of process parameters, alloy and binder design are needed to deepen this understanding. Another impulse is to provide tiny ceramic particles via the feedstock or as additives in the binder. These ceramic particles could serve as nucleation sites for the formation of reinforcing particles during the printing process.

- d) In case of multi-metal materials, the *inter-layer* spatial resolution (*i.e.*, parallel to the build direction during PBF) was determined to be sufficient for a further application in the synthesis of biomimetic FGAM samples. However, the *intra-layer* spatial resolution (*i.e.*, perpendicular to the build direction during PBF) needs to be improved further. It is important that a scale is reached, which is sufficient for exceptional mechanical behavior in biological structures (typically below 100  $\mu\text{m}$ ).
- e) The consolidation of ceramic particles to solid parts depends on temperature (high enough to enable diffusion) and time (long enough to enable sufficient diffusion). Even though in LD-PBF-LB the temperatures to sinter ceramic particles are reached, the diffusion time during the process is too short to reach a consolidation of the material. However, it could still be possible to fabricate metal-ceramic composites using this method. Preferably, a metal alloy that has to be heat-treated in a downstream process anyway (for example to form precipitates) is selected. In the course of this heat treatment, it could then also be possible to consolidate the ceramic part of the FGAM multi-material during the longer holding time at elevated temperatures.
- f) Since PBF-LB process parameters must be optimized for individual metal alloys, it is important that individual areas within the powder bed, containing one type of alloy, are melted with the specific process parameters. This is not trivial by default. A conceivable solution would be to use a combination of different process monitoring solutions (*e.g.* pyrometry, high-speed monitoring, and acoustic diagnostic) and feedback their signals in-situ to a process optimization algorithm which can regulate the parameters during printing within certain limits. The basic requirements for this are, on the one hand, the simultaneous processing of several input signals via a suitable high-throughput artificial intelligence software and, on the other hand, the availability of hardware that allows sufficiently high data transmission and computing speeds.

## References

- [1] Y. Li, Z. Feng, L. Hao, L. Huang, C. Xin, Y. Wang, E. Bilotti, K. Essa, H. Zhang, Z. Li, F. Yan, T. Peijs, A Review on Functionally Graded Materials and Structures via Additive Manufacturing: From Multi-Scale Design to Versatile Functional Properties, *Advanced Materials Technologies*. 5 (2020). doi: [10.1002/admt.201900981](https://doi.org/10.1002/admt.201900981).
- [2] Y. Miyamoti, W.A. Kaysser, H. Rabin, A. Kawasaki, G.F. Reneé, *Functionally Graded Materials - Design, Processing and Applications*, 1<sup>st</sup> ed., Springer New York, NY, New York, 1999.
- [3] M. Koizumi, FGM Activities in Japan, *Composites Part B*. 28B (1997) 1–4. doi: [10.1016/S1359-8368\(96\)00016-9](https://doi.org/10.1016/S1359-8368(96)00016-9).
- [4] A. Kawasaki, R. Watanabe, Concept and P/M fabrication of functionally gradient materials, *Ceramics International*. 23 (1995) 73–83. doi: [10.1016/0272-8842\(95\)00143-3](https://doi.org/10.1016/0272-8842(95)00143-3).
- [5] I.M. El-Galy, B.I. Saleh, M.H. Ahmed, Functionally graded materials classifications and development trends from industrial point of view, *SN Applied Sciences*. 1 (2019) 1–23. doi: [10.1007/s42452-019-1413-4](https://doi.org/10.1007/s42452-019-1413-4).
- [6] I.C. Gebeshuber, Biomimetics — Prospects and Developments, *Biomimetics*. 7 (2022). doi: [10.3390/biomimetics7010029](https://doi.org/10.3390/biomimetics7010029).
- [7] D. Mahmoud, M.A. Elbestawi, Lattice structures and functionally graded materials applications in additive manufacturing of orthopedic implants: A review, *Journal of Manufacturing and Materials Processing*. 1 (2017) 1–19. doi: [10.3390/jmmp1020013](https://doi.org/10.3390/jmmp1020013).
- [8] M. Naebe, K. Shirvanimoghaddam, Functionally graded materials: A review of fabrication and properties, *Applied Materials Today*. 5 (2016) 223–245. doi: [10.1016/j.apmt.2016.10.001](https://doi.org/10.1016/j.apmt.2016.10.001).
- [9] M.J. Pfeifenberger, M. Mangang, S. Wurster, J. Reiser, A. Hohenwarter, W. Pfleging, D. Kiener, R. Pippan, The use of femtosecond laser ablation as a novel tool for rapid micro-mechanical sample preparation, *Materials and Design*. 121 (2017) 109–118. doi: [10.1016/j.matdes.2017.02.012](https://doi.org/10.1016/j.matdes.2017.02.012).
- [10] G.B. Rathmayr, A. Bachmaier, R. Pippan, Development of a new testing procedure for performing tensile tests on specimens with sub-millimetre dimensions, *Journal of Testing and Evaluation*. 41 (2013) 1–12.

- doi:10.1520/JTE20120175.
- [11] D.S. Gianola, C. Eberl, Micro- and nanoscale tensile testing of materials, *Jom*. 61 (2009) 24–35. doi:10.1007/s11837-009-0037-3.
- [12] M. Bartosik, R. Daniel, C. Mitterer, I. Matko, M. Burghammer, P.H. Mayrhofer, J. Keckes, Cross-sectional X-ray nanobeam diffraction analysis of a compositionally graded CrN x thin film, 542 (2013) 1–4. doi:10.1016/j.tsf.2013.05.102.
- [13] F. Xu, X. Zhang, H. Zhang, A review on functionally graded structures and materials for energy absorption, *Engineering Structures*. 171 (2018) 309–325. doi:10.1016/j.engstruct.2018.05.094.
- [14] ISO/ASTM International, ISO / ASTM TR 52912:2020 Additive manufacturing — Design — Functionally graded additive manufacturing, 2020.
- [15] C. Yan, L. Hao, A. Hussein, P. Young, D. Raymont, Advanced lightweight 316L stainless steel cellular lattice structures fabricated via selective laser melting, *Materials & Design*. 55 (2014) 533–541. doi:10.1016/j.matdes.2013.10.027.
- [16] C. Wei, Z. Sun, Q. Chen, Z. Liu, L. Li, Additive Manufacturing of Horizontal and 3D Functionally Graded 316L/Cu10Sn Components via Multiple Material Selective Laser Melting, *Journal of Manufacturing Science and Engineering, Transactions of the ASME*. 141 (2019) 1–8. doi:10.1115/1.4043983.
- [17] C. Wei, H. Gu, Q. Li, Z. Sun, Y. hui Chueh, Z. Liu, L. Li, Understanding of process and material behaviours in additive manufacturing of Invar36/Cu10Sn multiple material components via laser-based powder bed fusion, *Additive Manufacturing*. 37 (2021) 101683. doi:10.1016/j.addma.2020.101683.
- [18] D. Wang, G.W. Deng, Y. qiang Yang, J. Chen, W. hui Wu, H. liang Wang, C. lin Tan, Interfacial microstructure and mechanical properties of selective laser melted multilayer functionally graded materials, *Journal of Central South University*. 28 (2021) 1155–1169. doi:10.1007/s11771-021-4687-9.
- [19] V.K. Nadimpalli, E. Hørdum, T. Dahmen, E.H. Valente, S. Mohanty, Multi-material additive manufacturing of steels using laser powder bed fusion eu s pen ' s 19 th International Conference & Exhibition , Bilbao , ES , June 2019 Multi-material additive manufacturing of steels using laser powder bed fusion, (2019). <https://backend.orbit.dtu.dk/ws/portalfiles/portal/192242879/ICE19230.pdf>.
- [20] E. Bleck, Wolfgang; Moeller, Handbuch Stahl, Carl Hanser Verlag, München, 2017. doi:10.3139/9783446449626.

## References

---

- [21] C. Wei, L. Li, Recent progress and scientific challenges in multi-material additive manufacturing via laser-based powder bed fusion, *Virtual and Physical Prototyping*. 16 (2021) 347–371. doi:10.1080/17452759.2021.1928520.
- [22] S.R. Narasimharaju, W. Zeng, T.L. See, Z. Zhu, P. Scott, X. Jiang, S. Lou, A comprehensive review on laser powder bed fusion of steels: Processing, microstructure, defects and control methods, mechanical properties, current challenges and future trends, *Journal of Manufacturing Processes*. 75 (2022) 375–414. doi:10.1016/j.jmapro.2021.12.033.
- [23] S. Bodner, Combinatorial study of process parameters, microstructure and mechanical properties in Inconel 718 parts produced by additive manufacturing, Montanuniversity Leoben, 2018.
- [24] K. Kempen, L. Thijs, J. Van Humbeeck, J.P. Kruth, Mechanical Properties of AlSi10Mg Produced by Selective Laser Melting, *Physics Procedia*. 39 (2012) 439–446. doi:10.1016/j.phpro.2012.10.059.
- [25] F. Bartolomeu, M. Gasik, F.S. Silva, G. Miranda, Mechanical Properties of Ti6Al4V Fabricated by Laser Powder Bed Fusion: A Review Focused on the Processing and Microstructural Parameters Influence on the Final Properties, *Metals*. 12 (2022). doi:10.3390/met12060986.
- [26] A. Marques, Â. Cunha, M.R. Silva, M.I. Osendi, F.S. Silva, Ó. Carvalho, F. Bartolomeu, Inconel 718 produced by laser powder bed fusion: an overview of the influence of processing parameters on microstructural and mechanical properties, *International Journal of Advanced Manufacturing Technology*. 121 (2022) 5651–5675. doi:10.1007/s00170-022-09693-0.
- [27] E. Liverani, S. Toschi, L. Ceschini, A. Fortunato, Effect of selective laser melting (SLM) process parameters on microstructure and mechanical properties of 316L austenitic stainless steel, *Journal of Materials Processing Technology*. 249 (2017) 255–263. doi:10.1016/j.jmatprotec.2017.05.042.
- [28] S.C. Bodner, L.T.G. van de Vorst, J. Zalesak, J. Todt, J.F. Keckes, V. Maier-Kiener, B. Sartory, N. Schell, J.W. Hooijmans, J.J. Saurwalt, J. Keckes, Inconel-steel multilayers by liquid dispersed metal powder bed fusion: Microstructure, residual stress and property gradients, *Additive Manufacturing*. 32 (2020). doi:10.1016/j.addma.2019.101027.
- [29] P. Schaaf, Laser Nitriding in Materials, *Progress in Materials Science*. 47 (2002) 1–161.
- [30] H.-W. [VerfasserIn] Zoch, G. [VerfasserIn] Spur, *Handbuch Wärmebehandeln*



- und Beschichten, Oxford, UK : Carl Hanser Verlag, 2015.
- [31] H. Altena, F. Schrank, Low Pressure Carburizing with High Pressure Gas Quenching, *Gear Technology*. 21 (2004) 27–32.
- [32] S. Bruce, V. Cheetham, P.F. Stratton, Low-pressure carburising systems: A review of current technology, *Berg- Und Hüttenmännisches Magazin*. 151 (2006) 8–14. doi:10.1007/bf03165206.
- [33] E.J. Mittemeijer, M.A.J. Somers, Thermodynamics, kinetics, and process control of nitriding, *Surface Engineering*. 13 (1997) 483–497. doi:10.1179/sur.1997.13.6.483.
- [34] P. Wojciechowski, M. Lewandowski, Iron Nitride Thin Films: Growth, Structure, and Properties, *Crystal Growth and Design*. 22 (2022) 4618–4639. doi:10.1021/acs.cgd.1c01528.
- [35] L. T, Young Poong Heat Treatment Co., Plasma Nitriding, (2022). <http://eng.heat-treatment.co.kr/theme/ins/html/business/05.php> (accessed September 23, 2022).
- [36] M. John, R. Rao Kavala, M. Misra, P.L. Menezes, Peening Techniques for Surface Modification: Processes, Properties and Applications, *Materials*. 14 (2021). doi: 10.3390/ma14143841.
- [37] W.L. Chan, H.K.F. Cheng, Hammer peening technology—the past, present, and future, *International Journal of Advanced Manufacturing Technology*. 118 (2022) 683–701. doi:10.1007/s00170-021-07993-5.
- [38] E. Maleki, S. Bagherifard, O. Unal, M. Bandini, G.H. Farrahi, M. Guagliano, Introducing gradient severe shot peening as a novel mechanical surface treatment, *Scientific Reports*. 11 (2021) 1–13. doi:10.1038/s41598-021-01152-2.
- [39] V. Schulze, J. Hoffmeister, Mechanische Randschichtverfestigungsverfahren – Verfahren, in: *Handbuch Wärmebehandeln Und Beschichten*, Edition Ha, Oxford, UK : Carl Hanser Verlag, 2015: pp. 593–609. <https://permalink.obvsg.at/mul/LG00006616>.
- [40] B. Scholtes, O. Vöhringer, Ursachen, Ermittlung und Bewertung von Randschichtveränderungen durch Kugelstrahlen, *Materialwissenschaft Und Werkstofftechnik*. (1993). doi:10.1002/mawe.19930241206.
- [41] SAE International, AMS2431TM/8 Peening Media - Conditioned Carbon Steel Cut Wire Shot , High Hardness, (2019) 1–6.
- [42] K. Balan, Air or Wheel Peening? An Application-Based Analysis, *The Shot*

## References

---

- Peener. Fall (2013) 18–20.
- [43] J. Champaigne, Shot Peening Intensity Measurement, *The Shot Peener*. 6 (1992) 1–6.
- [44] A. Zeilinger, J. Todt, C. Krywka, M. Müller, W. Ecker, B. Sartory, M. Meindlhumer, M. Stefanelli, R. Daniel, C. Mitterer, J. Keckes, In-situ Observation of Cross-Sectional Microstructural Changes and Stress Distributions in Fracturing TiN Thin Film during Nanoindentation, *Scientific Reports*. 6 (2016). doi:10.1038/srep22670.
- [45] M. Stefanelli, R. Daniel, W. Ecker, D. Kiener, J. Todt, A. Zeilinger, C. Mitterer, M. Burghammer, J. Keckes, X-ray nanodiffraction reveals stress distribution across an indented multilayered CrN-Cr thin film, *Acta Materialia*. 85 (2015) 24–31. doi:10.1016/j.actamat.2014.11.011.
- [46] J. Todt, Nanoscale Investigation of Performance-critical Regions in Non-homogenous Metallic and Ceramic Thin Films, Montanuniversität Leoben, 2016.
- [47] J. Keckes, R. Daniel, J. Todt, J. Zalesak, B. Sartory, S. Braun, J. Gluch, M. Rosenthal, M. Burghammer, C. Mitterer, S. Niese, A. Kubec, 30 nm X-ray focusing correlates oscillatory stress, texture and structural defect gradients across multilayered TiN-SiO<sub>x</sub> thin film, *Acta Materialia*. 144 (2018) 862–873. doi:10.1016/j.actamat.2017.11.049.
- [48] J. Epp, X-Ray Diffraction (XRD) Techniques for Materials Characterization, Elsevier Ltd, 2016. doi:10.1016/B978-0-08-100040-3.00004-3.
- [49] J. Todt, H. Hammer, B. Sartory, M. Burghammer, J. Kraft, R. Daniel, J. Keckes, S. Defregger, X-ray nanodiffraction analysis of stress oscillations in a W thin film on through-silicon via, *Journal of Applied Crystallography*. (2016). doi:10.1107/S1600576715023419.
- [50] J. Keckes, M. Bartosik, R. Daniel, C. Mitterer, G. Maier, W. Ecker, J. Vila-Comamala, C. David, S. Schoeder, M. Burghammer, X-ray nanodiffraction reveals strain and microstructure evolution in nanocrystalline thin films, *Scripta Materialia*. (2012). doi:10.1016/j.scriptamat.2012.07.034.
- [51] M. Stefanelli, J. Todt, A. Riedl, W. Ecker, T. Müller, R. Daniel, M. Burghammer, J. Keckes, X-ray analysis of residual stress gradients in TiN coatings by a Laplace space approach and cross-sectional nanodiffraction: A critical comparison, *Journal of Applied Crystallography*. 46 (2013) 1378–1385. doi:10.1107/S0021889813019535.

- 
- [52] M. Meindlhumer, N. Jäger, S. Spor, M. Rosenthal, J.F. Keckes, H. Hruby, C. Mitterer, R. Daniel, J. Keckes, J. Todt, Nanoscale residual stress and microstructure gradients across the cutting edge area of a TiN coating on WC[ $\text{sbnd}$ ]Co, *Scripta Materialia*. 182 (2020) 11–15. doi:[10.1016/j.scriptamat.2020.02.031](https://doi.org/10.1016/j.scriptamat.2020.02.031).
- [53] S.C. Bodner, M. Meindlhumer, T. Ziegelwanger, H. Winklmayr, T. Hatzenbichler, C. Schindelbacher, B. Sartory, M. Krobath, W. Ecker, N. Schell, J. Keckes, Correlative cross-sectional characterization of nitrided, carburized and shot-peened steels: synchrotron micro-X-ray diffraction analysis of stress, microstructure and phase gradients, *Journal of Materials Research and Technology*. 11 (2021) 1396–1410. doi: [10.1016/j.jmrt.2021.01.099](https://doi.org/10.1016/j.jmrt.2021.01.099).
- [54] W.L. Bragg, The diffraction of short electromagnetic Waves by a Crystal, *Proceedings of the Cambridge Philosophical Society*. 17 (1913) 43–57.
- [55] M. Birkholz, A Practical Guide to X-Ray Crystallography of Biomacromolecules Surface and Thin Film Analysis Electron Accelerators as X-Ray Sources Microscopic X-Ray Fluorescence Analysis X-Ray Spectrometry X-ray Characterization of Materials, WILEY-VCH Verlag GmbH & Co., 2006.
- [56] O. Engler, V. Randle, Introduction to Texture Analysis: Macrotecture, Microtexture, and Orientation Mapping, Second Edition, CRC Press/Taylor & Francis Group, 2009. doi:[10.1201/9781420063660](https://doi.org/10.1201/9781420063660).
- [57] B.B. He, Two-Dimensional X-Ray Diffraction, John Wiley & Sons, Inc., New Jersey, 2009.
- [58] M. Meindlhumer, Cross-sectional and High-Temperature Structure-Property Relationships in Nanocrystalline Thin Films, Montanuniversität Leoben, 2020.
- [59] I.C. Noyan, J.B. Cohen, Determination of Strain and Stress Fields by Diffraction Methods, *Residual Stress*. (1987) 117–163. doi: [10.1007/978-1-4613-9570-6\\_5](https://doi.org/10.1007/978-1-4613-9570-6_5).
- [60] J. Kieffer, D. Karkoulis, PyFAI, a versatile library for azimuthal regrouping, *Journal of Physics: Conference Series*. 425 (2013). doi: [10.1088/1742-6596/425/20/202012](https://doi.org/10.1088/1742-6596/425/20/202012).
- [61] ASTM International, Standard Practice for X-Ray Determination of Retained Austenite in Steel with Near Random Crystallographic Orientation 1, Astm. (2009). doi: [10.1520/E0975-13](https://doi.org/10.1520/E0975-13).
- [62] L.M. Peng, G. Ren, S.L. Dudarev, M.J. Whelan, Debye-Waller factors and absorptive scattering factors of elemental crystals, *Acta Crystallographica*

## References

---

- Section A: Foundations of Crystallography. 52 (1996) 456–470.  
doi:[10.1107/S010876739600089X](https://doi.org/10.1107/S010876739600089X).
- [63] I.C. Noyan, J.B. Cohen, Residual stress – measurement by diffraction and interpretation., 1<sup>st</sup> ed., Springer-Verlag New York Inc., New York, 1987.  
doi: [10.1007/978-1-4613-9570-6](https://doi.org/10.1007/978-1-4613-9570-6).
- [64] G.S. Schajer, Practical Residual Stress Measurement Methods, 2013. doi:  
[10.1002/9781118402832](https://doi.org/10.1002/9781118402832).
- [65] P. Scherrer, Bestimmung der Größe und der inneren Struktur von Kolloidteilchen mittels Röntgenstrahlen, Nachrichten von Der Gesellschaft Der Wissenschaften Zu Göttingen, Mathematisch-Physikalische Klasse. 2 (1918) 98–100.  
doi:[10.1007/978-3-662-33915-2](https://doi.org/10.1007/978-3-662-33915-2).
- [66] N. Ahmed, I. Barsoum, G. Haidemenopoulos, R.K.A. Al-Rub, Process parameter selection and optimization of laser powder bed fusion for 316L stainless steel: A review, Journal of Manufacturing Processes. 75 (2022) 415–434.  
doi: [10.1016/j.jmapro.2021.12.064](https://doi.org/10.1016/j.jmapro.2021.12.064).
- [67] M. Pramreiter, S.C. Bodner, J. Keckes, A. Stadlmann, F. Feist, G. Baumann, E. Maawad, U. Müller, Predicting strength of Finnish birch veneers based on three different failure criteria, Holzforschung. 75 (2021) 847–856.  
doi: [10.1515/hf-2020-0209](https://doi.org/10.1515/hf-2020-0209).
- [68] J. Platl, S. Bodner, C. Hofer, A. Landefeld, H. Leitner, C. Turk, M.A. Nielsen, A.G. Demir, B. Previtali, J. Keckes, R. Schnitzer, Cracking mechanism in a laser powder bed fused cold-work tool steel: The role of residual stresses, microstructure and local elemental concentrations, Acta Materialia. 225 (2022) 117570. doi:[10.1016/j.actamat.2021.117570](https://doi.org/10.1016/j.actamat.2021.117570).

## 5 List of Appended Publications

In this chapter, four publications published during the dissertation period are listed chronologically (Papers I–IV).

In addition, and for the sake of completeness, all other publications are listed which were either not predominantly conceptualized by the author of this dissertation or which topic were out of scope of the topic of this thesis.

### *Appended peer-reviewed papers*

**Paper I:** S. C. Bodner, L. T. G. van de Vorst, J. Zalesak, J. Todt, J. F. Keckes, V. Maier-Kiener, B. Sartory, N. Schell, J. W. Hooijmans, J. J. Saurwalt, J. Keckes,  
*Inconel-Steel Multilayers by Liquid Dispersed Metal Powder Bed Fusion: Microstructure, Residual Stress and Property Gradients*  
Additive Manufacturing - Volume 32, March 2020, 101027;  
DOI: [doi.org/10.1016/j.addma.2019.101027](https://doi.org/10.1016/j.addma.2019.101027)

**Paper II:** S. C. Bodner, M. Meindlhumer, T. Ziegelwanger, H. Winklmayr, T. Hatzenbichler, C. Schindelbacher, B. Sartory, M. Krobath, W. Ecker, N. Schell, J. Keckes  
*Correlative Cross-Sectional Characterization of Nitrided, Carburized and Shot-Peened Steels: Synchrotron Micro-X-Ray Diffraction Analysis of Stress, Microstructure and Phase Gradients*

Journal of Materials Research and Technology - Volume 11, March–April 2021, Pages 1396-1410

DOI: [doi.org/10.1016/j.jmrt.2021.01.099](https://doi.org/10.1016/j.jmrt.2021.01.099)

**Paper III:** S. C. Bodner, K. Hlushko, K. Kutleša, J. Todt, O. Renk, M. Meindlhumer, F. Resch, M. A. Nielsen, J. Keckes, J. Eckert

*Influence of Hatch Strategy on Crystallographic Texture Evolution, Mechanical Anisotropy of Laserbeam Powder Bed Fused S316L Steel*

Advanced Engineering Materials – 220052, 2022, Pages 1 - 12

DOI: [doi.org/10.1002/adem.202200524](https://doi.org/10.1002/adem.202200524)

## List of Appended Publications

---

**Paper IV:** S. C. Bodner, K. Hlushko, L. T. G. van de Vorst, M. Meindlhumer, J. Todt, M. A. Nielsen, J. W. Hooijmans, J. J. Saurwalt, S. Mirzaei, J. Keckes

*Graded Inconel-Stainless Steel Multi-Material Structure by Inter- and Intralayer Variation of Metal Alloys*

Journal of Materials Research and Technology - Volume 21, November-December 2022, Pages 4846-4859

DOI: [doi.org/10.1016/j.jmrt.2022.11.064](https://doi.org/10.1016/j.jmrt.2022.11.064)

*Contributions of the author to the papers:* The author of this thesis is responsible for the main conceptualization of the appended papers as well as for the corresponding planning, predominant execution of the experiments, data analysis and interpretation. Publications listed were mainly conceptualized by the author of this dissertation. Percentage values of the authors contributions are listed in Table 3.

Table 3: Contribution of the author to the appended publications in percent

Paper/Article	Conception and planning	Experiments	Analysis and interpretation	Manuscript preparation
I	90	70	70	50
II	90	90	90	90
III	100	90	80	90
IV	100	90	90	90

## 5.1 Further publications, and co-authored publications

### 5.1.1 Accepted publications:

- S.C. Bodner, T. Ziegelwanger, M. Meindlhumer, J. Holcova, J. Todt, N. Schell, J. Keckes, Cross-sectional gradients of residual stresses, microstructure and phases in a nitrided steel revealed by 20µm synchrotron X-ray diffraction, *Metallurgia Italiana*. 111 (2019).
- M. Pramreiter, S.C. Bodner, J. Keckes, A. Stadlmann, C. Kumpenza, U. Müller, Influence of fiber deviation on strength of thin birch (*Betula pendula* Roth.) veneers, *Materials*. 13 (2020). doi:10.3390/ma13071484.
- W. Gindl-Altmatter, I. Czabany, C. Unterweger, N. Gierlinger, N. Xiao, S.C. Bodner & J. Keckes, (2020). Structure and electrical resistivity of individual carbonised natural and man-made cellulose fibres. *Journal of materials science*, 55.2020(23), 10271-10280. <https://doi.org/10.1007/s10853-020-04743-y>
- M. Pramreiter, S.C. Bodner, J. Keckes, A. Stadlmann, F. Feist, G. Baumann, E. Maawad, U. Müller, Predicting strength of Finnish birch veneers based on three different failure criteria, *Holzforschung*. (2021). doi:10.1515/hf-2020-0209.
- J. Platl, S. Bodner, C. Hofer, A. Landefeld, H. Leitner, C. Turk, M.A. Nielsen, A.G. Demir, B. Previtali, J. Keckes, R. Schnitzer, Cracking mechanism in a laser powder bed fused cold-work tool steel: The role of residual stresses, microstructure and local elemental concentrations, *Acta Materialia*. 225 (2022) 117570. doi:10.1016/j.actamat.2021.117570.
- M. Pramreiter, S.C. Bodner, J. Keckes, A. Stadlmann, J. Konnerth, F. Feist, G. Baumann, C. Huber, U. Müller, Zerstörungsfreie Charakterisierung von Furnieren für strukturelle Verbundwerkstoffe, *Holztechnologie*. 62 (2021) 5–18.
- B. Ungerer, I. Sulaeva, S.C. Bodner, A. Potthast, J. Keckes, U. Müller, S. Veigel, Degradation of regenerated cellulose filaments by hydrogen chloride under aqueous and non-aqueous conditions, *Carbohydrate Polymer Technologies and Applications*. 4 (2022) 100238. doi:10.1016/j.carpta.2022.100238.
- J. Platl, S.C. Bodner, H. Leitner, C. Turk, M.A. Nielsen, J. Keckes, R. Schnitzer, Local microstructural evolution and the role of residual stresses in the phase stability of a laser powder bed fused cold-work tool steel Jan, *Materials Characterization*. (2022) 112505. doi:10.1016/j.matchar.2022.112318.

- M. Truschner; A. Janda; S.C. Bodner; A. Keplinger; G. Mori: Effect of deformation-induced twinning on the stress corrosion cracking resistance of a cold-drawn high-strength stainless steel wire, 2022. Submitted to Journal of Materials Science.

### **5.1.2 Submitted publications**

- F. Neudecker, M. Jakob, S.C. Bodner, J. Keckes, H. Buerstmayr, W. Gindl-Altmatter: Delignification and densification as a route to enable the use of wheat straw for structural materials, 2022. Submitted to Cellulose.

## **5.2 Supported thesis**

### **5.2.1 Bachelor Thesis**

- C. Weindl: Biegeanlage mit Drei- und Vier-Punkt-Biegewerkzeug zur In-Situ Untersuchung von miniaturisierten Biegeproben mittels Synchrotron-Röntgenstrahlung, 2019.
- K. Kutleša: Gradients of Microstructure and Mechanical Properties in and Additively Manufactured Case-Hardened Steel, 2022.

### **5.2.2 Master Thesis**

- N. Käfer: Additive Fertigung von Nickelbasissuperlegierungen – Rissbildung, Gefügeanalyse und Prozessoptimierung, 2022



# Inconel-Steel Multilayers by Liquid Dispersed Metal Powder Bed Fusion: Microstructure, Residual Stress and Property Gradients

S.C. Bodner<sup>a,\*</sup>, Bart van de Vorst<sup>c</sup>, J. Zalesak<sup>b</sup>, J. Todt<sup>b</sup>, J.F. Keckes<sup>b</sup>, V. Maier-Kiener<sup>d</sup>, B. Sartory<sup>e</sup>, N. Schell<sup>f</sup>, J.W. Hooijmans<sup>g</sup>, J.J. Saurwalt<sup>g</sup> and J. Keckes<sup>a</sup>

<sup>a</sup> Department of Materials Science - Chair of Materials Physics, Montanuniversität Leoben, A-8700 Leoben, Austria

<sup>b</sup> Erich Schmid Institute of Materials Science, Austrian Academy of Sciences, A-8700 Leoben, Austria

<sup>c</sup> TNO, 5656 AE Eindhoven, the Netherlands

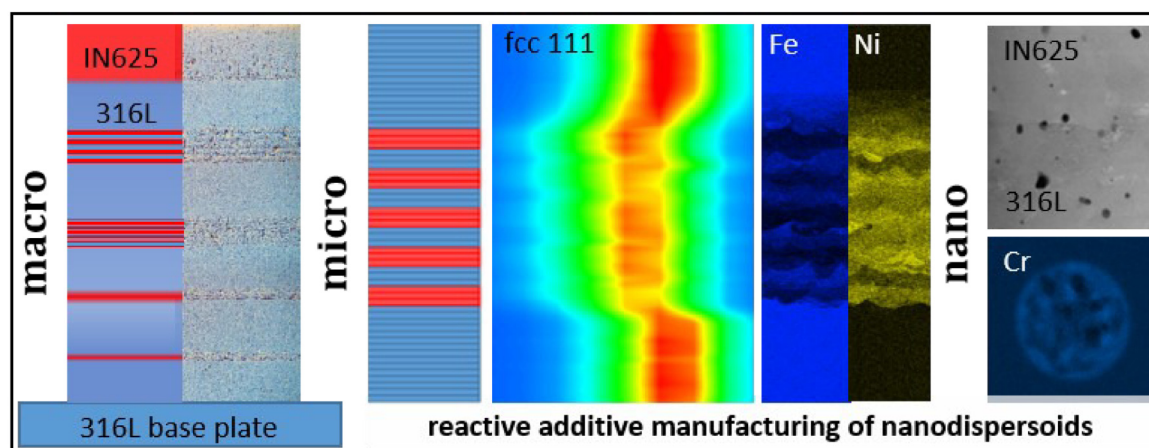
<sup>d</sup> Department of Materials Science, Chair of Physical Metallurgy and Materials Testing, Montanuniversität Leoben, A-8700 Leoben, Austria

<sup>e</sup> Materials Center Leoben GmbH, A-8700 Leoben, Austria

<sup>f</sup> Helmholtz Zentrum Geesthacht, Centre for Materials and Coastal Research, D-21502 Geesthacht, Germany

<sup>g</sup> Admatec Europe BV, 5051 DV Goirle, the Netherlands

## Graphical Abstract



## Abstract

Synthesis of multi-metal hybrid structures with narrow heat affected zones, limited residual stresses and secondary phase occurrence represents a serious scientific and technological challenge. In this work, *liquid dispersed metal powder bed fusion* was used to additively manufacture a multilayered structure based on alternating Inconel 625 alloy (IN625) and 316L stainless steel (316L) layers on a 316L base plate. Analytical scanning and transmission electron microscopies, high-energy synchrotron X-ray diffraction and nanoindentation analysis reveal sharp compositional, structural and microstructural boundaries between alternating 60  $\mu\text{m}$  thick alloys' sub-regions and unique microstructures at macro-, micro- and nano-scales. The periodic occurrence of IN625 and 316L sub-regions is correlated with a cross-sectional hardness increase and decrease and compressive stress decrease and increase, respectively. The laser scanning strategy induced a growth of elongated grains separated by zig-zag low-angle grain boundaries, which correlate with the occurrence of zig-zag cracks propagating in the growth direction. A sharp  $\langle 110 \rangle$  fiber texture within the 316L regions turns gradually into a  $\langle 100 \rangle$  fiber texture in the IN625 regions. The occurrence of the C-like stress gradient with a pronounced surface tensile stress of about 500 MPa is interpreted by the temperature gradient mechanism model. Chemical analysis indicates a formation of reinforcing spherical chromium-metal-oxide nano-dispersoids and demonstrates a possibility for *reactive additive manufacturing and microstructural design* at the nanoscale, as a remarkable attribute of the deposition process. Finally, the study shows that the novel approach represents an effective tool to combine dissimilar metallic alloys into unique bionic hierarchical microstructures with possible synergetic properties.

**Keywords:** Powder Bed Fusion; Microstructure and Stress; Multi-Metal Material; Stainless Steel; Inconel

## 6.1 Introduction

Multi-material hybrid structures in nature and technology combine properties of their individual constituents throughout complex microstructures to achieve synergistic effects, like improved mechanical properties and oxidation resistance, which go beyond the properties of their monophasic counterparts [1-3]. Typically, multilayered, composite and hierarchical microstructures are used to achieve improved functionality by combining materials with different physical properties [2,4-7]. Similarly, functionally graded materials (FGMs) are designed to comply with spatially variable functional requirements like strength, oxidation resistance or toughness by adopting gradients of dissimilar phases, microstructure and/or residual stresses [8-10]. However, joining of metals into multi-metal hybrid structures with diffuse or abrupt interfaces between the individual phases or alloys and narrow heat affected zones resulting in limited the first-order residual stress, macroscopic distortion and secondary phase formation represents still a serious technological challenge [11].

By their principle of a sequential layer-by-layer deposition, additive manufacturing technologies (AM) are ideally suited to manufacture parts with complex external and internal geometries [3,12-14]. Additionally, powder and wire feed material supplies have been known to allow for an adjustment of volume fraction of metallic components [15-17]. In particular, the directed energy deposition (DED) approach, in which powder is fed into the melt-zone and molten at every layer by a laser, can be used to fabricate components with a variable layer-by-layer composition and unique microstructures [18]. Within this contribution, however, a novel laser powder bed fusion-related technology, based on *liquid dispersed metal powder*, is used to produce a multi-metal hybrid structure. The fabrication of FGMs using AM technologies allows for generating property-specific part areas by matching the process parameters to the localized functionality [19]. It is however common that combining dissimilar metals using AM technology may result in the formation of compositional and microstructural inhomogeneities as well as in secondary phases and stress concentrations, which may decisively deteriorate part's functional properties [20-22].

A significant effort has been devoted to the development of multi-material additive manufacturing (MM-AM) of hybrid structures, reviewed recently in Ref. [3]. Exemplary AM systems equipped with *several powder feeders* were used to prepare graded Ti-V [23][24], Ti-Mo [24], V-Ti6Al4V alloy [25], stainless steel-Ti6Al4V alloy [26] and Ti-6Al-4V/Ti-6.5Al-3.5Mo-1.5Zr-0.3Si [27] materials with novel refined microstructural features, aiming at aircraft and aero-engine applications. Similarly, *bimetallic structures* like Inconel 718-copper alloy GRCo-84 [28] and stainless steel

304L-Invar 36 [25] as well as *gradient structures* like Ti–TiO<sub>2</sub> [29] and yttria-stabilized zirconia-steel [30] were fabricated.

In the field of nuclear and steam power plants, aerospace and/or repair applications, especially high strength, corrosion and oxidation resistance and/or creep and fatigue resistance are required [31,32]. For this reason, MM-AM of stainless steel (SS) and Inconel have been extensively explored [33,34]. Carroll *et al.* [35] reported on fabrication of Inconel-steel FGM with *diffuse* compositional, structural and microstructural boundaries by applying gradually varying mixtures of Inconel 625 and grade 304L SS powders. The observed formation of cracks with a length of several hundred microns in a region with 79 wt% SS 304L and 21 wt% IN625 was attributed to the presence of secondary phases of transition metal carbides in the form of (Mo,Nb)C. Similarly, aiming at nuclear fission reactor applications, Hinojos *et al.* [36] studied the joinability of Inconel 718 and 316L SS and vice versa utilizing electron beam melting (EBM) and reported *abrupt* compositional, structural and microstructural boundaries as well as low concentration of typical welding features. Cracking observed at the 316L/IN718 interface was attributed to the deformation constraints imposed by IN718. Additionally, using finite-element numerical analysis, Hofmann *et al.* [9] showed that a gradient transition from SS 304L to IN625 across an automobile valve stem are expected to exhibit ten times lower stress at the transitioning zone at 1000 K compared to a friction stir-welded joint of the same materials.

In general, all previous studies on FGMs combining nickel-based alloys and steel indicated complex process-microstructure-stress-properties relationships [35,36]. Additionally, FGMs produced with diffuse and abrupt interfaces comprise usually unique microstructures with secondary phases and precipitates like (Mo,Nb)C, M<sub>23</sub>C<sub>6</sub>, NbC [35,36] *etc.* and there were cracks with lengths up to several 100 μm observed systematically in the transition regions [35]. These findings indicate that there is a significant potential to further optimize the functional properties of the particular nickel-based alloys-steel FGMs by knowledge-based microstructural design, including a development of novel deposition routes and recipes.

For this work, the non-precipitation hardening alloy Inconel 625 (IN625) and stainless steel grade 316L (316L) are selected to fabricate a multi-metal hybrid structure. A relatively novel deposition technique based on *liquid dispersed metal powder bed fusion* is used to form a complex microstructure with multilayered morphology, zig-zag grain boundaries, multiscale interfaces and ceramic nanoparticle reinforcement. The three-fold work objectives encompass (i) exploring the possibilities and advantages of the liquid powder bed fusion technology, (ii) analyzing gradients of phases, microstructure, composition and mechanical properties at multiple length-scales using correlative cross-sectional micro-analytics and (iii) additive manufacturing of multi-metal hybrid

materials. Additionally, reactive additive manufacturing as an integral part of the liquid dispersed metal powder bed fusion process is introduced in order to indicate the possibility to tailor mechanical properties of the grown structures by integrating homogeneously dispersed nanoparticles.

## 6.2 Materials and methods

For the synthesis of a multi-layered IN625–316L structure on a 3 mm thick 316L stainless steel base plate, a prototype system *LASERFLEX Conflux* based on liquid dispersed metal powder bed fusion (Fig. 1) was used. As input material, AISI 316L (specified with ~[65, 12, 18, 2] % of Fe, Ni, Cr and Mo, respectively, as well as other balancing elements with less than ~1 % concentration) and IN625 (specified with ~[58, 20, 8, 4] % of Ni, Cr, Mo, Fe and Nb, respectively, as well as other balancing elements with less than ~1 % concentration) metal particles with  $d_{50}$ -diameters of ~4.2 and ~3.4  $\mu\text{m}$ , respectively, were applied. In order to produce two powder suspensions, the particles were dispersed in an aqueous solution enriched with an ethanol-based micropolymer glue. Individual IN625 and 316L layers were produced by (i) lowering the building platform by ~30  $\mu\text{m}$ , (ii) depositing the particular suspension, (iii) wiping the metal suspension across the building platform, (iv) waiting for a few seconds in order to dry and densify the liquid powder bed in the inert nitrogen atmosphere and (v) melting the dried metal powder in the nitrogen atmosphere, using a laser source (*cf.* Fig. 1). The laser system and its optics provides radiation with a wavelength of 1064 nm and a spot size of ~12  $\mu\text{m}$ . A laser power of 137 W, a scan speed of 500 mm/s, a hatch distance of 90  $\mu\text{m}$  and a hatch rotation angle of 66 degrees between the layers were used. These process parameters were identical for both alloys. The temperature of the base plate was kept at ~25°C. After the laser melting the described procedure from (i) to (v) was repeated to produce the next layer. For further microscopy analysis, the structure's cross-section was mechanically polished using a standard colloidal silica polishing suspension by Struers with a particle size of 0.04  $\mu\text{m}$  (O-PS polishing suspension).

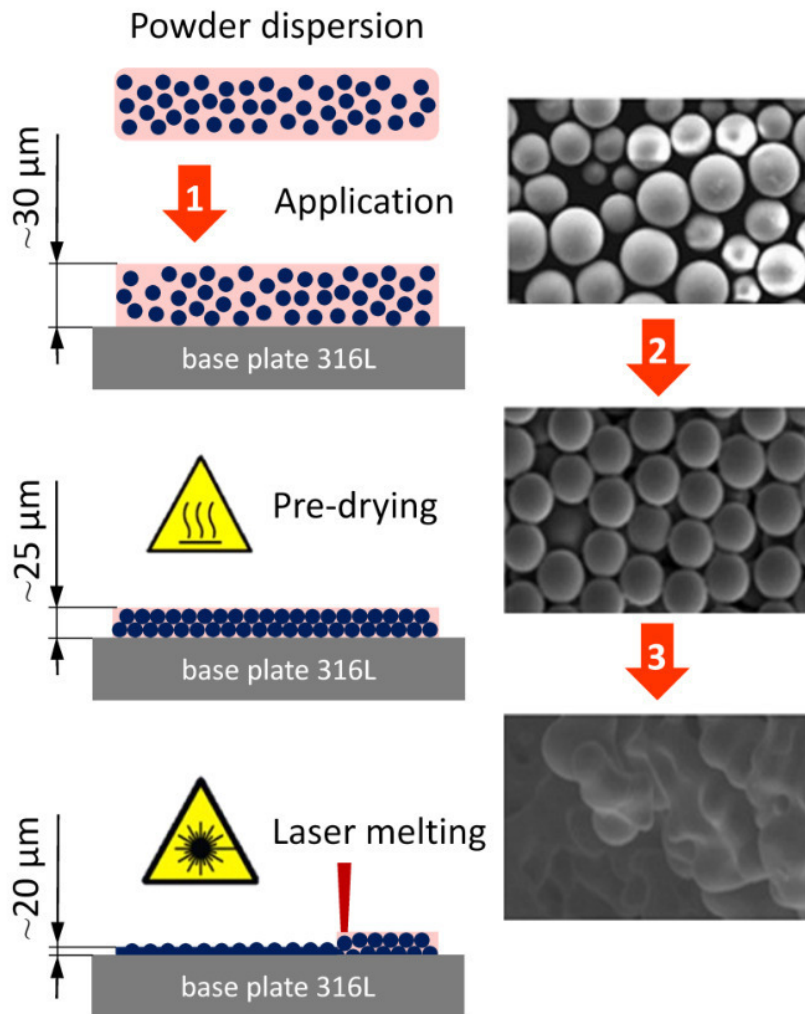


**Figure 1.** A schematic description of the liquid dispersed metal powder bed fusion process. Within the first step, a suspension layer with a thickness of  $\sim 30\ \mu\text{m}$  containing metallic 316L or IN625 particles is applied on the 316L base plate or on already existing build-up. Then, the suspension dries in a nitrogen flow and densifies to a thickness of  $\sim 25\ \mu\text{m}$ . Finally, a laser source is used to fuse the particles together and to produce a new metallic layer of  $\sim 20\ \mu\text{m}$  in thickness, which is reinforced with dispersed nanoceramic particles (*cf.* Sec. 3.6).

The approach from Fig. 1 was used to grow two multi-layered IN625-316L plate structures, identical in their morphology, with overall dimensions of  $\sim(15\times 2\times 7)\ \text{mm}^3$  each, on a 316L SS base plate with dimensions of  $\sim(40\times 40\times 3)\ \text{mm}^3$  (Fig. 2a). Both structures possessed a complex irregular cross-sectional morphology introduced in Fig. 2b. The aim behind selecting this specific morphology was primarily to evaluate the accuracy of the deposition approach to fabricate relatively thin mono-alloy layers, to obtain information on the intermixing of IN625 and 316L alloys, to analyze microstructural evolution at and near inter-alloy interfaces and to evaluate cross-sectional residual strain across the structure. Further on, experimental results obtained only from one structure will be presented.

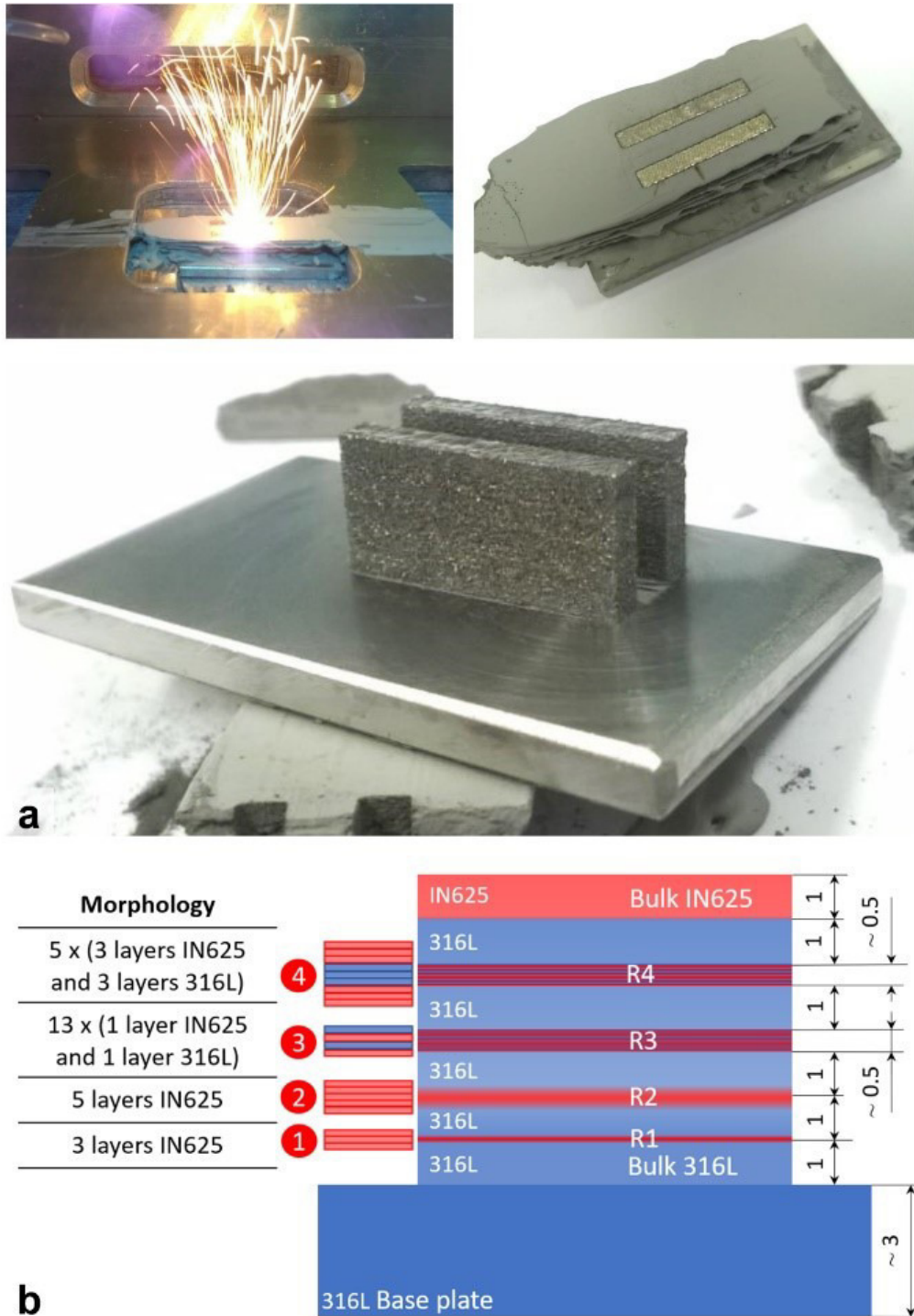


**Figure 2.** Synthesis and geometry of the IN625-316L structure. (a) Various stages of the fabrication process to produce two identical multilayered plates. (b) On a 316L base plate, ~1 mm thick layer of 316L was grown followed by four regions R1-R4 including IN625, which are always separated by ~1 mm of 316L. The deposition was finalized by ~1 mm of IN625 on top. As indicated in (b) left, the R1-R4 regions consist of 3 (R1) and 5 (R2) layers of IN625, alternating IN625 and 316L layers in R3 and alternating groups of three IN625 and three 316L layers (R4). The thickness of every individual layer was set to ~20  $\mu\text{m}$  (*cf.* Fig. 1).

Optical microscopy (OM) characterization was performed using an Olympus BX51 system. Scanning electron microscopy (SEM), electron backscatter diffraction (EBSD) and energy dispersive X-ray analysis (EDX) were performed using a Gemini SEM 450 and an AURIGA CrossBeam systems from Carl Zeiss. A cross-sectional transmission electron microscopy (TEM) lamella with a thickness of  $\sim 50$  nm was fabricated using focused ion beam (FIB) machining within the Zeiss Auriga system by applying an acceleration voltage of 30 kV and currents in the range from 20 nA to 50 pA. The lamella was extracted from a sample region containing an interface between the two alloys. Microstructural and chemical characterization of the lamella was performed using scanning TEM (STEM) mode in a probe-corrected FEI Titan Themis platform operated at 200kV and equipped with a Gatan Enfium ER spectrometer as well as FEI Super-X EDX four quadrant detectors. The collected EDX signal was treated using Bruker Esprit software applying built-in standards.

Nanoindentation experiments were conducted using a platform Nanoindenter G200 with a Berkovich diamond tip in strain-rate controlled mode. A sinusoidal load signal was superimposed during the continuous sample loading in order to record the contact stiffness. Tip shape and frame stiffness calibrations were performed on a regular base according the Oliver and Pharr method [37]. Arrays of indents with an indentation depth of  $\sim 1$   $\mu\text{m}$  and a minimum distance of  $\sim 20$   $\mu\text{m}$  between the indents were positioned over the R1-R4 regions. Hardness and indentation moduli were evaluated for the four regions as well as for bulk IN625 and 316L.

Synchrotron characterization of the multi-layered sample was performed at the high energy materials science (HEMS) beamline P07B of PETRA III at DESY in Hamburg, which is operated by Helmholtz Zentrum Geesthacht. The experimental setup is presented schematically in supplementary data. The sample characterization was performed using a monochromatic beam of 87.1 keV photon energy and a cross-section of  $\sim 20 \times 500$   $\mu\text{m}$ , which was directed approximately parallel to the interfaces between IN625 and 316L. To perform a scanning cross-sectional X-ray micro-diffraction experiment (CSmicroXRD), the sample was moved along the growth direction with an increment of 20  $\mu\text{m}$ . Almost 400 diffraction patterns, each with multiple Debye-Scherrer (DS) rings, were recorded from the sample's cross-section in transmission geometry using a Perkin Elmer two-dimensional (2D) flat panel detector of  $2048 \times 2048$  pixels with a pixel pitch of 200  $\mu\text{m}$ . The sample-detector distance was set to  $\sim 1.3$  m. A dark current correction was applied to each exposure. The exact geometry and distance of the detector with respect to the sample's position was determined using a  $\text{LaB}_6$  calibration standard powder. Diffraction data were treated using the *pyFAI* software package developed at the European Synchrotron Radiation Facility [38] and evaluated using custom scripts written in Python.



## 6.3 Results

### 6.3.1 Cross-sectional morphology

The morphology of the polished IN625–316L structure cross-section was analysed using OM and SEM. The OM micrograph in Fig. 3 shows the base plate, the five ~1 mm thick regions of 316L, the regions R1-R4 and a ~1 mm thick IN625 region on top (*cf.* also Fig. 2b). The interfaces between the layers appear to propagate parallel to the base plate surface and indicate that the microstructure is laterally homogeneous. The interface between the multi-layered structure and the base plate does not show any features of intermixing or dilution.

A variety of cracks were found at the structure's cross-section with a very typical *zig-zag morphology*. A representative example of one zig-zag crack is shown in the inset of Fig. 3 (*cf.* also OM and SEM micrographs in supplementary data). Comparable zig-zag cracks were found in the regions R1-R4 as well as in the top-most ~1 mm thick IN625 region. Their occurrence can be correlated with the presence of IN625. The cracks propagated across the layers of both alloys within regions R1-R4 and approximately in the structure's growth direction, their origins will be discussed in Secs. C.2 and 3.

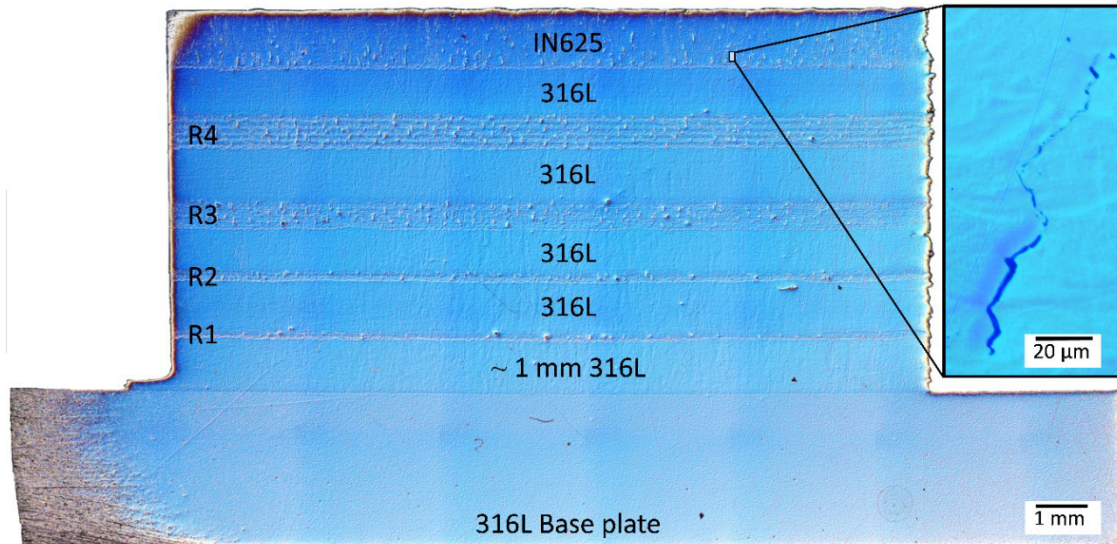


**Figure 3.** OM micrograph showing the multi-layered IN625-316L structure cross-section with ~3 mm base plate, five ~1 mm thick 316L regions separated by the regions R1-R4 with IN625 layers and layer-groups, respectively, and an IN625 region on top. The base plate's surface exhibits a concave bending. The inset at the right shows the cross-sectional morphology of a typical crack (*cf.* supplementary data).

The OM micrograph in Fig. 3 shows that the upper surface of the base plate shows a slight concave bending, which indicates the presence of compressive and tensile residual stress

states within the top and bottom regions of the plate, respectively [39]. Consequently, it can be expected that the near-base plate region of the structure possesses tensile stresses which change gradually into compressive at the structure's surface. The stress formation is a result of the structure fabrication and its origins will be discussed in the next section. Fig. 3 as well as all SEM and TEM micrographs presented along the text are shown in full resolution in supplementary material.

### 6.3.2 CSmicroXRD analysis

In order to obtain grain-averaged information on the cross-sectional distribution of crystalline phases, texture and strain across the multi-layered structure, CSmicroXRD was carried out and volume-averaged data from the 2 mm thick sample (Fig. 2a) (along the X-ray beam direction) were collected. XRD data obtained by an azimuthal integration of the complete Debye-Scherrer rings in Figs. 4a and b show a cross-sectional evolution of IN625 and 316L reflections. Since both alloys possess face-centered cubic (fcc) lattice and lattice parameters of stress-relieved IN625 matrix and 316L steel differ only a few percent (depending on the actual alloy composition), fcc reflection positions (modified by the residual stress gradient) in Fig. 4a vary only marginally. Moreover, no other reflections from secondary intermetallic phases like  $\gamma'$ ,  $\gamma''$  and  $\delta$  in IN625 [40] or ferrite and carbide phases in 316L [41] can be identified in this phase plot. It should be however noted that quantitative XRD analysis is not sensitive to secondary phases with volume fractions smaller than 3-10 %, depending on the crystallite size. The evolution of IN625 and 316L 311-reflections in Fig. 4b reveals also the presence of the individual R1-R4 layers, the top IN625 region as well as the base plate. The data in Fig. 4b allowed resolving also the presence of five groups of layers within region R4, which correlate with the multiple alternation of three IN625 and three 316L layers.

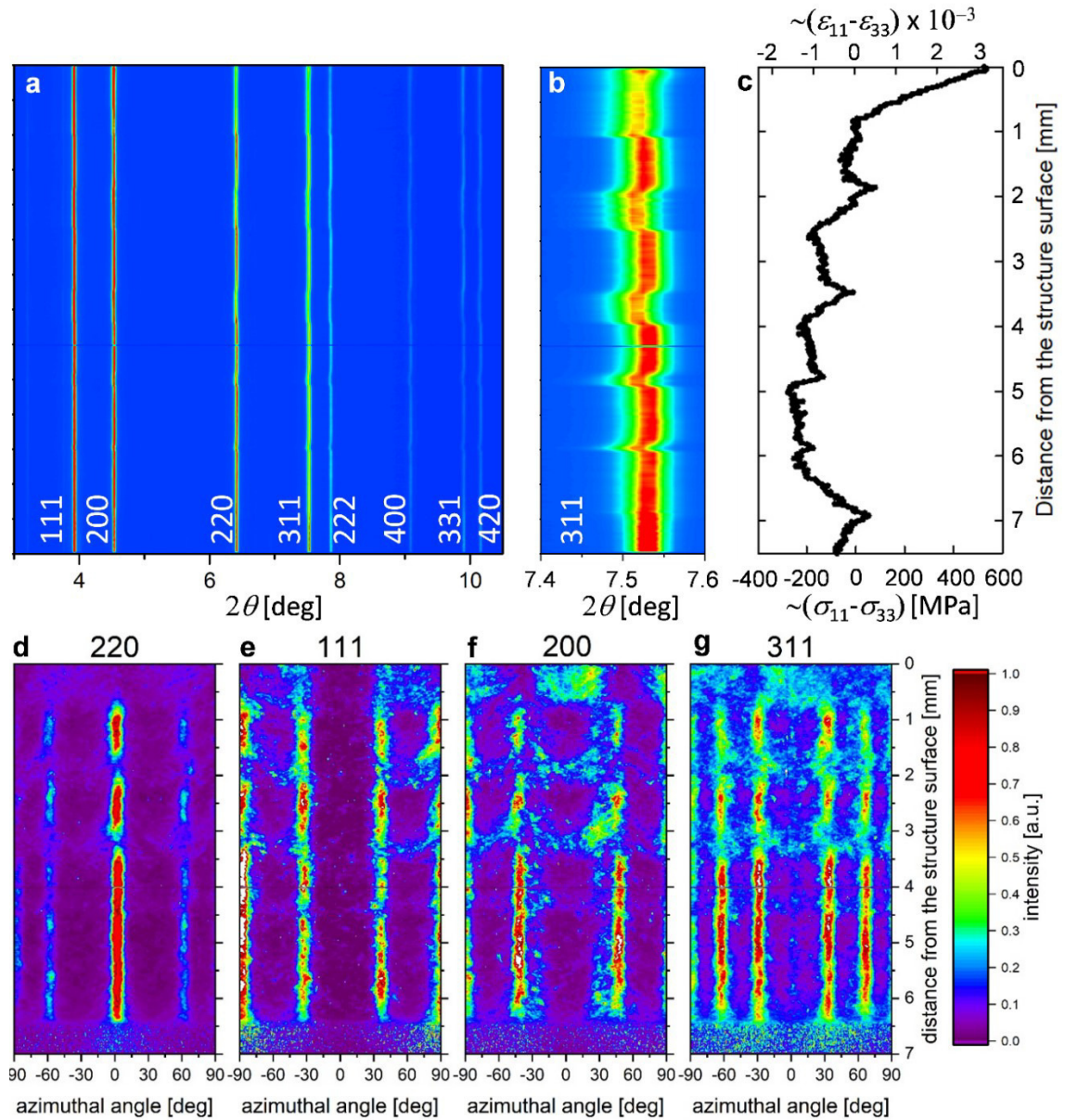


**Figure 4.** Results from CSmicroXRD on the multi-layered structure. (a) The phase plot reveals only the presence of fcc reflections of IN625 and 316L alloys with very similar lattice parameters. (b) The evolution of IN625 and 316L 311 reflections shows the positions of R1-R4 regions, the top IN625 layer and the base plate. (c) The strain/stress plot indicates a dominant C-shaped stress depth dependence with compressive stress relaxations at the positions of R1-R4 regions. (d-g) The texture plots show the distributions of diffraction intensities along Debye-Scherrer rings for IN625 and 316L 220, 111, 200 and 311 reflections.

The layer-by-layer laser melting process, which is accompanied by the generation of localized high thermal loads during the metal powder bed fusion (Fig. 1), results in the formation of complex multi-axial residual stress distributions [42] whose tensile stress concentrations may significantly influence the mechanical stability of the fabricated parts.

In the case of multi-metal hybrid structures like in Fig. 3, (i) thermal stresses are expected to be formed as a result of the mismatch of respective coefficients of thermal expansion (CTEs) of  $\sim 15 \times 10^{-6} \text{K}^{-1}$  [43] and  $\sim 18 \times 10^{-6} \text{K}^{-1}$  [44] at  $100^\circ\text{C}$  between IN625 and 316L regions. Additionally, (ii) growth stresses are formed as a result of complex cross-sectional microstructure and stress evolution during the fabrication process accompanied by cyclic elasto-plastic deformation. As the presence of residual stress was indicated by the base plate's bending (Fig. 3), scanning CSmicroXRD was used to assess cross-sectional strain-stress distributions in the structure. The motivation was to obtain qualitative data and assess the role of particular microstructural features in the formation of stress. IN625 and 316L 311-Debye-Scherrer rings collected from the individual cross-sectional structure positions were evaluated with regard to their ellipticity. The obtained data were used to estimate depth gradients of X-ray elastic strains and residual stresses. For the evaluation, it was supposed that the shear X-ray elastic strains  $\varepsilon_{ij}^{311}$  and shear residual stresses  $\sigma_{ij}$  can be neglected for simplicity. In this case, the measured ellipticity is proportional to the difference of in-plane and out-of-plane residual stresses of  $\sigma_{11} - \sigma_{33}$  and X-ray elastic strains  $\varepsilon_{11}^{311} - \varepsilon_{33}^{311}$ , which were evaluated using the *Hill* grain interaction model applying appropriate X-ray elastic constants [45,46]. Since the out-of-plane stresses  $\sigma_{33}$  can be supposed to be relatively small, due to the free sample surface, the evaluated  $\sigma_{11} - \sigma_{33}$  values from Fig. 4c can be therefore used to describe an evolution of the in-plane stresses  $\sigma_{11}$  across the structure's cross-section.

The surface region of the base plate is in compression [39] and the stress profile across the multi-layered structure exhibits a complex oscillatory stresses behaviour, which is superimposed on a dominant C-shaped stress depth dependence (Fig. 4c). According to the temperature gradient mechanism (TGM) model [39,42,47], the C-shaped stress profile across the multi-layered structure can be interpreted by the effect of the cyclic heating of the mechanically restrained preceding metallic layers, which results in the formation of compressive stresses and material plastification. During cooling down, tensile stresses are formed in the plastified surface zone (like in the top-most  $\sim 1$  mm thick IN625 region in Fig. 4c), which are balanced by compressive stresses in the build-up zone beneath and in the base plate. Additionally, the oscillatory stress behaviour in Fig. 4c indicates that the growth of 316L layers results systematically in an increase of compressive stresses at all five cross-sectional positions in the structure. Conversely, the deposition of IN625 results in a systematic relaxation of compressive stresses. The resulting compressive stress oscillations can be interpreted by a higher degree of plastic strain generation in 316L compared to IN625, which is due to a lower yield strength of 316L, as well as by a stress relaxation in IN625 manifested by the formation of zig-zag cracks, as visible in Fig. 3. It is clear, however, that this qualitative explanation of the stress gradient formation is very simplified and the formation depends on a variety of process and material parameters like

heat source path and heat transfer to the underlying layers, temperature distributions, local thermal conductivity, local yield strength and local CTEs. Moreover, due to their unique microstructures, materials' parameters are temperature- and , thus, laser power-dependent [17].

The plots in Figs. 4d-g show azimuthal distributions of diffraction intensities along IN625 and 316L 220, 200, 111 and 311 Debye-Scherrer rings and document thus a qualitative evolution of crystallographic texture across the structure. Since the angle 0 and 90 degrees in Figs. 4d-g correspond to the out-of-plane and in-plane orientations of the diffraction vectors, respectively, the results indicate the presence of  $\langle 110 \rangle$  fibre texture, which evolves gradually in the first 316L layer and saturates within  $\sim 0.4$  mm above the base plate. Thereafter, it is preserved in all subsequent 316L layers (Fig. 3d). This is documented for instance by the strong azimuthal maxima of 220, 200 and 111 reflections at  $\sim 0^\circ$ ,  $\sim 45^\circ$  and  $\sim 35^\circ$ , respectively. These maxima correspond to the angles of  $\sim 45^\circ$  and  $\sim 35^\circ$  between (110) and (100) as well as (110) and (111) crystallographic planes, respectively. The occurrence of azimuthal maxima broadening at the positions of R2, R3 and R4 regions indicates that the addition of IN625 weakens the  $\langle 110 \rangle$  fibre texture, which practically disappears or even turns into a  $\langle 100 \rangle$  fibre texture within the top IN625 sublayer. The results also reveal that the base plate is not free from texture, but there is a certain type of a weak biaxial texture. This is represented in Figs. 4d,e by the occurrence of weak maxima at  $\sim 0$  and  $\sim 90$  degrees for 220 and 111 reflections, respectively.

### 6.3.3 Local texture analysis

In Fig. 5, EBSD micrographs show the cross-sectional evolution of crystallite orientations and microtexture along the in-plane and out-of-plane sample axes [100] and [001], respectively, at the interface between the base plate and the first 316L layer (Fig. 5e,f) and across the regions R1 (Fig. 5c,d) as well as R4 (Fig. 5a,b). The data in Fig. 5e document that the apparently homogenous microstructure of the base plate with globular grains with an average size of  $\sim 12 \mu\text{m}$  in diameter rapidly turns into a textured microstructure with elongated grains and an average grain length of  $\sim 108 \mu\text{m}$  within the first 316L layers. In case of all five  $\sim 1$  mm thick 316L layers, the EBSD data indicate the presence of a relatively pronounced  $\langle 110 \rangle$  fibre texture with random in-plane crystallite orientations (*e.g.* along [100] and sample direction), in agreement with the data from Figs. 4d-g.

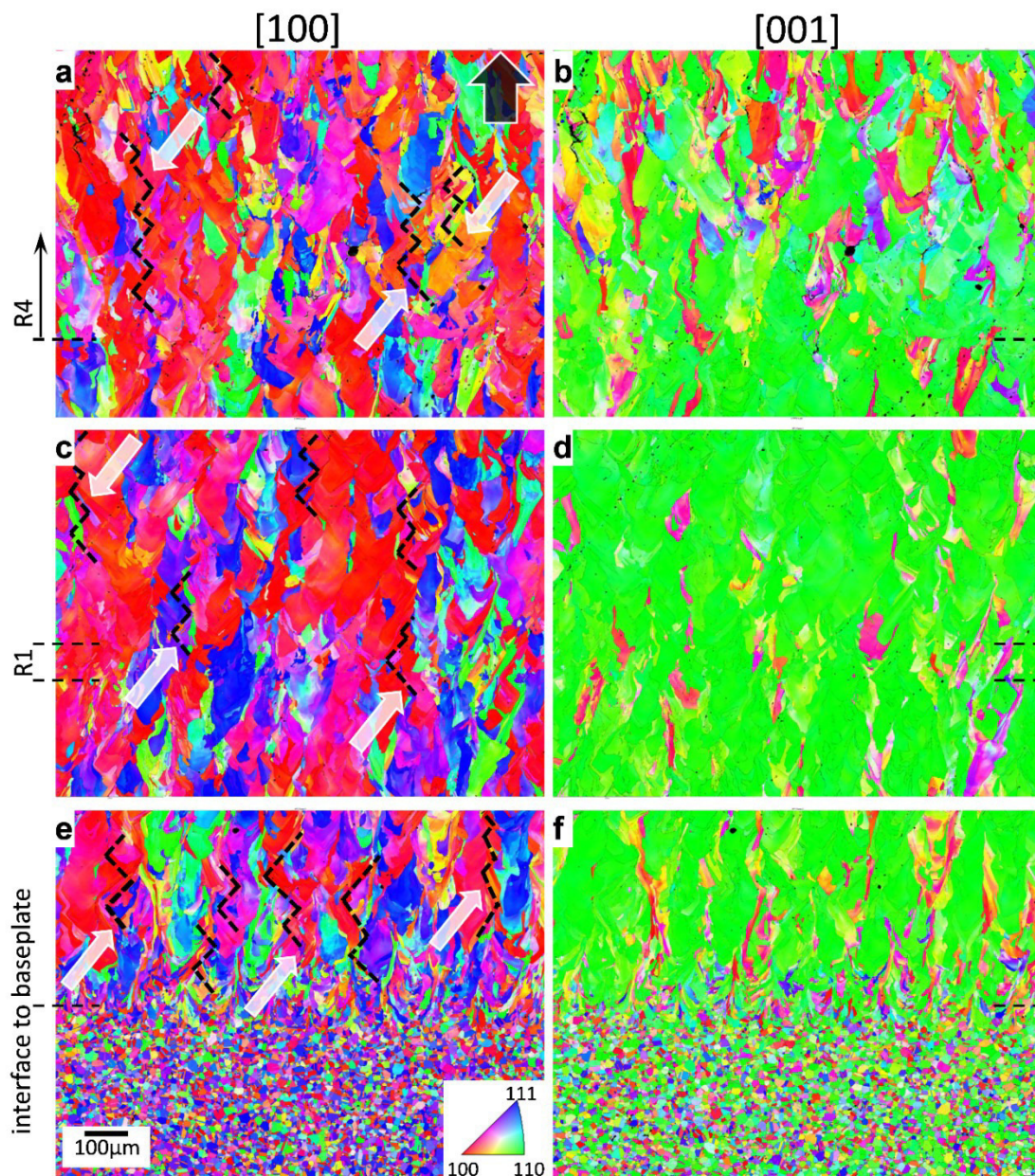


**Figure 5.** EBSD data show the orientation of the crystallites with respect to the in-plane and out-of-plane sample axes  $[100]$  and  $[001]$ , respectively, at the interface between the base plate and the first 316L layer (e,f) and across the regions R1 (c,d) as well as R4 (a,b). These microtexture data indicate the presence of a columnar grain morphology and a  $\langle 110 \rangle$  fibre texture in both alloys (*cf.* also supplementary data). The zig-zag patterns in the microstructure are indicated by black, dotted lines and white arrows (a, c d). The dark arrow in (a) indicates the growth direction.

The region R1 (Figs. 5 c,d) shows a very localized grain refinement and a small change in the crystallite orientation, which however seemingly does not influence the cross-sectional microstructure significantly. In other words, the insertion of the three IN625 layers (*cf.* Figs. 2b,3) did not influence the epitaxial overgrowth of the individual layers resulting in the preservation of the columnar grain microstructure as well as texture. This

is in agreement with the XRD results from Figs. 4d-g, where also no significant texture disruption was observed within the region R1. The behaviour of the preserved crystallite microtexture can be interpreted by very similar lattice parameters of both alloys, differing only a few percent, which clearly promoted a heteroepitaxial overgrowth.

The EBSD data from the region R4, however, indicate changes in the crystallite orientation (Figs. 5a,b) caused by the addition of IN625 sublayers, namely the  $\langle 110 \rangle$  fibre texture was gradually disrupted as can be seen especially in Fig. 5b. This observation is in agreement with the XRD data from Figs. 3d-g, which also showed that the deposition of multiple IN625 layers induces a gradual texture randomization.

Moreover, the EBSD results from Fig. 5 document a zig-zag cross-sectional morphology of elongated grains (and low-angle grain boundaries with a misorientation angle less than about 15 degrees), which is obtained as a result of the applied scanning strategy. Grain-boundary maps are also presented in the supplementary material. This zig-zag morphology can be correlated to the zig-zag cracks patterns observed using SEM and OM especially at the cross-sectional positions of the regions R1-R4 (*cf.* inset in Fig. 3). The zig-zag cracks are expected to originate from the particular shape of the grain boundaries and/or in-plane residual stresses induced by CTEs mismatch between the sublayers.

#### 6.3.4 Chemical analysis

SEM and EDX analyses were performed in order to characterize microstructure and chemistry of both alloys within the individual layers. The results indicate a homogenous distribution of elements in both phases and, additionally, no *microscopic precipitation* resulting in a localized elemental enrichment or depletion, in agreement with the CSmicroXRD data (Fig. 4). Moreover, no formation of *microscopic dendritic* regions was observed at the microscale. This is in contrast to the results from similar studies on the IN718–304L systems, where the formation of microscopic enrichments in Nb and Mo, with a few shared areas containing C, was observed inter- and intra-granularly in IN718 and IN625 [35,36]. This discrepancy can be interpreted by the different thermal treatments applied in Refs. [35,36] and in the present process.

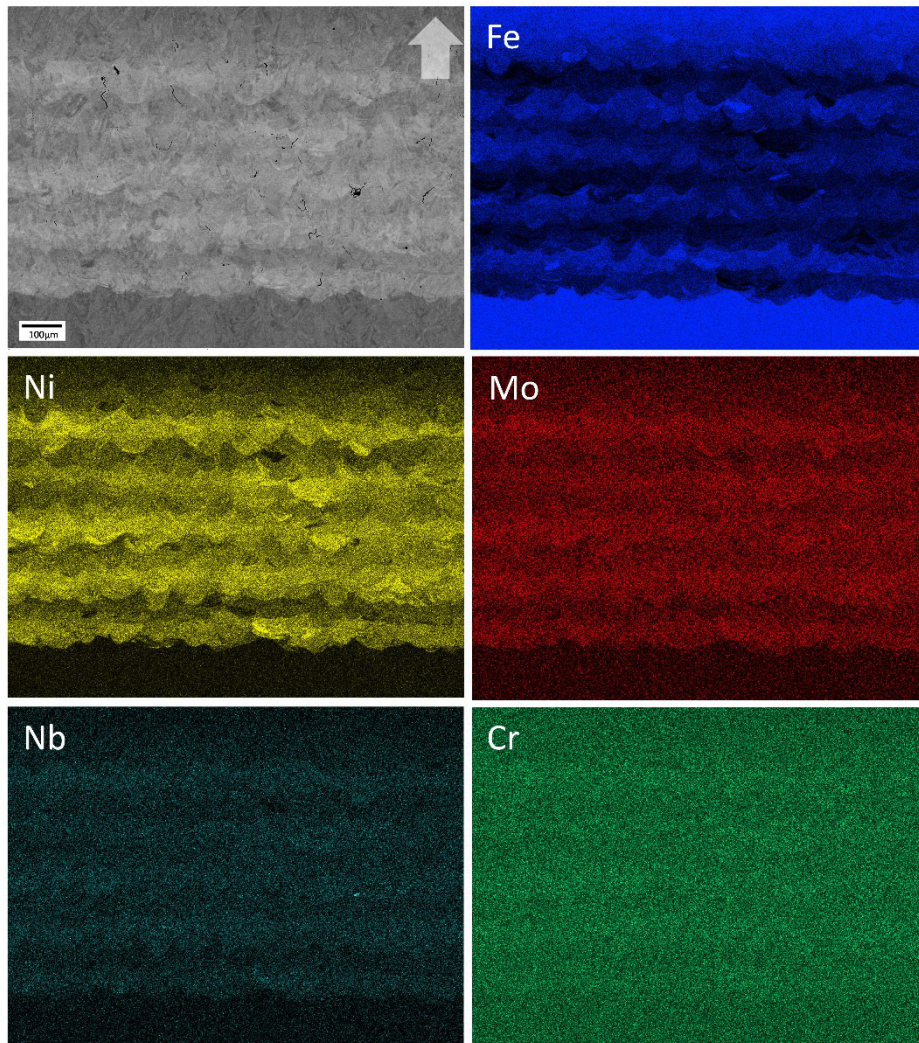


**Figure 6.** EDX concentrations maps show the distribution of elements in the area of region R4. The arrow in the SEM micrograph indicates the building direction.

EDX concentration mapping of the region R4 was performed to examine the intermixing of the elements between IN625 and 316L sub-regions during the multilayer structure fabrication. In Fig. 6, distributions of major elements indicate the presence of ten sub-regions, each consisting of three layers of IN625 or 316L. Both deposited alloys contain Fe, Ni, Cr and Mo elements, whereas Nb is initially present only in IN625. In the Nb concentration map in Fig. 6, it is possible to resolve five Nb-rich sub-regions representing IN625 and four 316L sub-regions with a smaller amount of Nb. Moreover, there is evidence of a higher concentration of Nb in the ~1 mm thick 316L region above region R4, compared to the Nb (EDX background) concentration level in the ~1 mm thick 316L region, below region R4. These observations indicate that after the deposition of IN625 layers, the elements of this alloy were distributed along the growth direction upwards as



a result of out-diffusion into the melt-pool. Probably, the concentration of the IN625 alloying elements decreases exponentially with distance from IN625 layers.

The Ni and Fe concentration maps in Fig. 6 indicate very clearly the presence of five IN625 and five 316L layer-groups in region R4. In both types of sub-regions a simultaneous occurrence of Fe and Ni was evaluated. This effect can be attributed to an intermixing of the two elements between the deposited sub-regions and to the (intrinsic) simultaneous occurrence of the elements in both alloys. The following effects are remarkable however: The top-most sub-region of three layers of 316L in region R4 (*cf.* Fig. 2b) shows lower and higher concentrations of Fe and Ni, respectively, compared to the neighbouring top-most ~1 mm thick 316L region (Fig. 6). Similarly, also the bottom-most sub-region of three 316L layers in region R4 (following the first IN625 layer, *cf.* Fig. 2b) shows lower and higher concentrations of Fe and Ni, respectively, compared to the underlying ~1 mm thick 316L region, which appears to be almost free of Ni (Fig. 6). These observations also indicate that growth of the IN625 and 316L sub-regions was accompanied by cyclic remelting of the alloys and an intermixing of the elements between the layer being deposited and preceding layers.

Since IN625 contains an amount of Mo that is approximately two times higher than that in 316L steel, Mo enrichments in the concentration map in Fig. 6 can be correlated with the occurrence of IN625 layers in region R4. The homogenous distribution of Cr across the region R4 (Fig. 6) correlates well with ~20 % amount of Cr in both alloys (*cf.* also Sec. C.5).

An attempt was made to relate the occurrence of the cross-sectional cracks (Fig. 3) with the chemical gradients across the multilayered sample [35], but no such correlation was observed. In other words, a local fluctuation of the elemental concentrations was not found to be responsible for the zig-zag crack growth behaviour, in contrast to the results of Carroll *et al.* [35], where microscopic Nb- and Mo- enrichment was observed within the cracked regions in IN625–304L system.

### 6.3.5 Mechanical characterization

Nanoindentation measurements were performed across the R4 region in order to evaluate the spatial distribution of hardness and reduced elastic modulus (the latter is presented in supplementary material). In Fig. 7, the cross-sectional distribution of hardness in the range of ~(3–4) GPa is superimposed on an occurrence of Ni determined using EDX analysis (from Fig. 6). The data indicates that the multiple hardness increase can be correlated with the occurrence of Ni within the five groups of IN625 layers. In four sub-regions, each consisting of three 316L layers, as well as on the borders of region R4, the

hardness decreases systematically. The regions R1-R3 showed the same behavior, where the insertion of IN625 interlayers caused an increase in hardness.

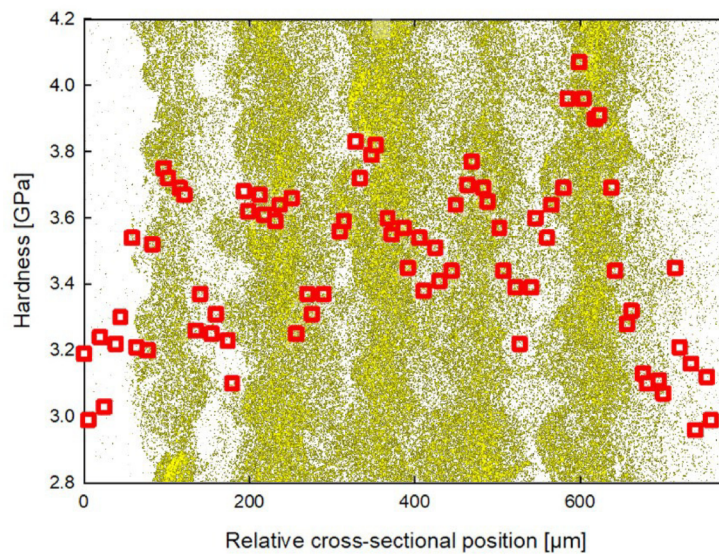


**Figure 7.** Cross-sectional distribution of hardness across the region R4 superimposed on the elemental distribution of Ni from Fig. 6. The hardness increase correlates with the positions of five IN625 sub-regions.

Hardness measurements were performed also on the sample (bulk) regions which consist exclusively of IN625 and 316L, where hardness values of  $3.95 \pm 0.08$  and  $2.81 \pm 0.08$  GPa were found, respectively, in relatively good agreement with the literature values of  $\sim 4.3$  [48] and  $\sim 3.5$  GPa [49]. This means that the bulk IN625 and 316L regions possess lower and higher hardness than the IN625 and 316L sub-regions in region R4, respectively. This finding can be interpreted by the elemental intermixing (*cf.* Fig. 6) and/or by different chemical compositions of  $\text{CrMO}_x$  dispersoids formed within region R4 (*cf.* Sec. 3.6.).

### 6.3.6 TEM characterization

TEM characterization was performed in order to analyze the local microstructure and chemical composition across an exemplary interface, between the upper part of the  $\sim 1$  mm thick 316L region and the topmost IN625 region (Figs. 2b, 3). Bright field and high-angle annular dark-field (HAADF) micrographs revealed the presence of morphologically sharp interface between both alloys with a large amount of spherical nanodispersoids distributed throughout the interface region and an occurrence of heavy elements primarily at the IN625 grain boundaries, as documented by the HAADF micrograph in Fig. 8.

However, EDX analysis of the interface indicated gradual changes in the concentrations of Fe and Ni at a length scale of several  $\sim 100$  nm across the interface (Fig. 8). At the IN625 side, grain boundaries were revealed to contain enrichments of Nb, Mo and C as result of nano-segregation, which is usually observed after thermal treatments of Inconel alloys [39]. At the 316L side, the segregation of Nb, Mo and C at the grain boundaries was observed to a much smaller extent and Nb as well as Si enrichments within the dispersoids were detected (*cf.* Fig. 8).

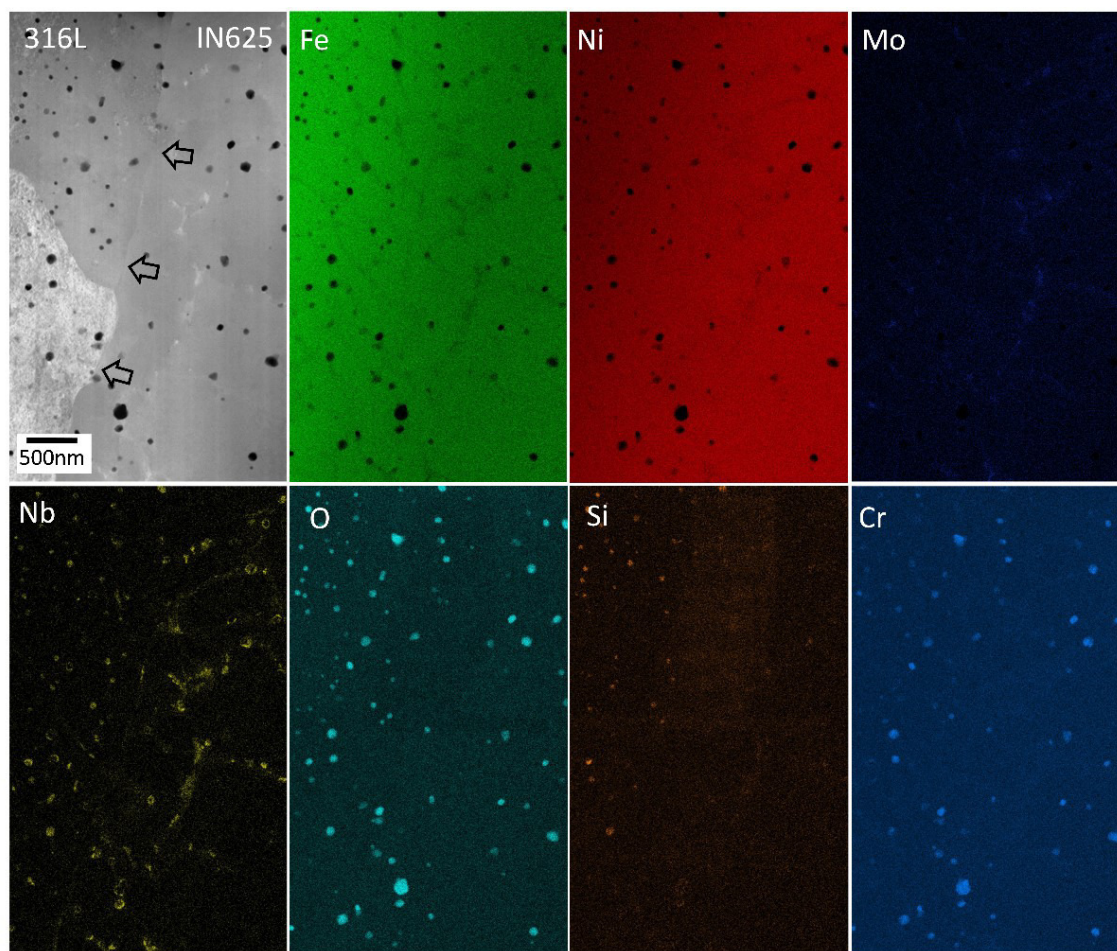


**Figure 8.** EDX concentration maps show distributions of elements at the interface between 316L and IN625 alloys, which is indicated by arrows in the HAADF micrograph. Besides gradual changes in Fe and Ni concentrations and in the composition of  $\text{CrMO}_x$  dispersions, Nb-rich precipitates change their shape as a function of the Nb-content in the base material.

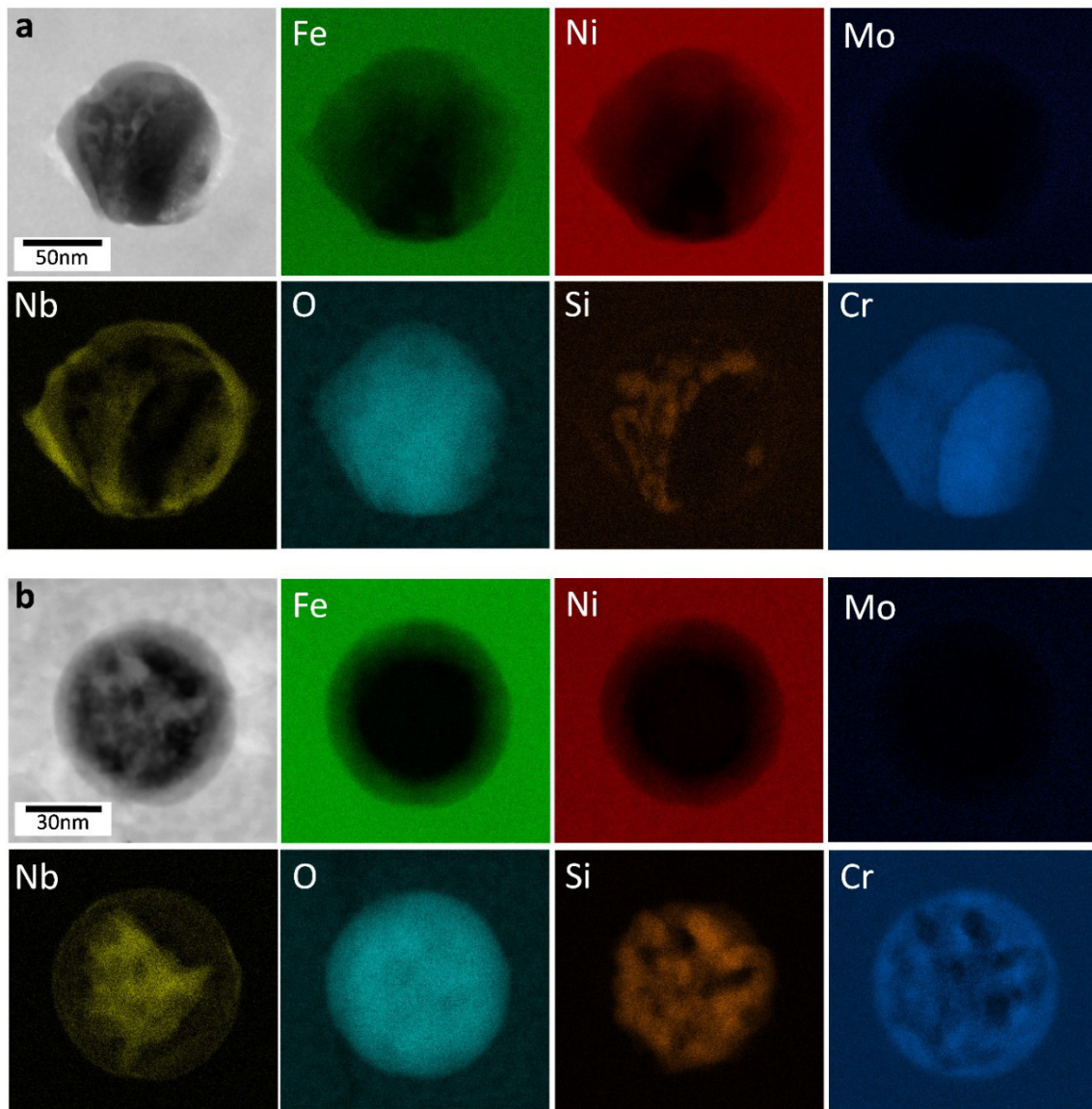


**Figure 9.** EDX concentration maps show distributions of elements within representative dispersoids in IN625 (a) and 316L (b) alloys near the interface shown in Fig. 8. The spherical  $\text{CrMO}_x$  nano-dispersoids possess Nb-rich shells and Si concentration appears to depend on the matrix alloy (*cf.* also Fig. 8).

Also a detailed EDX analysis of the spherical dispersoids with a diameter of  $\sim 20$ - $100$  nm was performed (Fig. 9) at both sides of the interface. As documented by EDX maps in Fig. 9, the dispersoids were identified to be chromium-metal-oxide nanoparticles  $\text{CrMO}_x$  enriched with Si and exhibiting Nb-rich shells. Generally, the dispersoids were found in both alloys across the whole structure at high concentrations and their actual composition depends on the chemistry of the particular alloy's matrix. This indicates that the dispersoid's formation is a characteristic attribute of the particular fusion process and resembles the formation of protective oxide scale rich in Cr in stainless steels with a relatively large fraction of Cr [50]. In other words, the liquid dispersed metal powder bed

fusion induces an oxidation of Cr present in both alloys, resulting in the formation of dispersoids with some traces of Si and Nb (Fig. 9). This phenomenon will be denoted as *reactive additive manufacturing*. The ceramic dispersoids represent nanoscopic alloy reinforcements, which are expected to be favorable for the mechanical properties of the structure. Therefore reactive additive manufacturing as a part of the liquid dispersed metal powder bed fusion can be used as an effective tool to homogeneously incorporate nanoscopic particles across deposited structures in order to tailor mechanical properties.

## 6.4 Discussion

This study demonstrates the feasibility of fabricating multi-layered IN625–316L structures (Figs. 2b,3) with sharp structural and microstructural boundaries between the two alloys, deposited using liquid dispersed metal powder bed fusion (Fig. 1), where the alloys alternation was achieved at meso- and micro-scales (Figs. 3,6). The implementation of regions with periodically varying mechanical properties is expected to hinder crack propagation and may results in the synthesis of damage-resistant materials [51,52]. Due to the out-diffusion of alloying elements in the growth direction, however, an elemental intermixing was observed at length scales of several 100 nm (Fig. 8). The results from the multilayered region R4 (Figs. 3-6) document that the approach allows for the deposition of spatially alternating alloys with the resolution of  $\sim 60 \mu\text{m}$  in the growth direction, which consequently exhibits an oscillating hardness depth profile with a period of  $\sim 100 \mu\text{m}$  (Fig. 7).

The 316L layers possess a  $\langle 110 \rangle$  fiber texture, which saturates already in the first  $\sim 1$  mm thick 316L region at a distance of  $\sim 0.4$  mm (Fig. 4e) above the base plate. However, the deposition of IN625 alloy induces a gradual disruption of the  $\langle 110 \rangle$  texture and the formation of a much weaker  $\langle 100 \rangle$  fiber texture like in Ref. [36], which is present especially in the top-most IN625 sublayer (Figs. 4d-g). The deposition of IN625 induces moreover a refinement of the microstructure, which is visible already in region R1 (Figs. 5c,d).

The occurrence of a C-shaped stress gradient with a negligible near-base plate stress, the oscillating compressive stresses at a level of  $\sim -150$  MPa and the pronounced surface tensile stress of  $\sim 500$  MPa (Fig. 3c) are interpreted by means of the TGM model [39, 42,47], supposing cyclic material plastification and densification during the additive deposition. The C-shaped stress profile is a result of the mechanical equilibrium achieved after cooling down from the process temperature of compressively and tensilely stressed and mutually restrained surface and underlying bulk structure regions, respectively, whose stress signs are expected to almost reverse at room temperature. The deposition of IN625 layers results in the relaxation of compressive residual stresses (Fig. 3c), as a result

of the supposed lower degree of plastic strain generation in IN625 and zig-zag cracking, which penetrates layers of both alloys (*cf.* inset in Fig. 3 and supplementary data) along zig-zag low-angle-grain boundaries. This effect is denoted as “ductility dip cracking” and appears as a result of IN625’s ductility decrease during cooling down from the process temperature at straight or non-tortuous boundaries [36,53].

EDX analysis in SEM (Fig. 6) indicated the absence of *microscopic* dendrites or precipitates with metallic enrichments/depletions zones in both alloys, in agreement with the CSmicroXRD data (Fig. 4a). Also no cracks were observed, which could be correlated with localized elemental enrichment or depletion. This is different from the results of Hinjos *et al.* [36] and Carroll *et al.* [35], where microscopic precipitates and features were reported in the same and/or similar alloys and which were correlated also with the occurrence of microscopic cracks. At the nanoscale, however, the EDX analysis performed in TEM indicated the presence of Nb, Mo and C enrichments caused by nano-segregation at IN625 grain boundaries (Fig. 8). These observations indicate that the liquid dispersed metal powder bed fusion process is favorable for the deposition of complex alloys because it is possible to suppress the formation of secondary phases at the microscale. Probably, due to the shorter diffusion lengths predefined by the particular laser design, the segregation of elements was limited and occurred only to a very small extent at the grain boundaries of IN625, as shown in Fig. 8.

IN625 regions and the top layer showed the presence of undesirable zig-zag cracks (Fig. 3), which may obviously negatively influence mechanical stability of the IN625-SS316L build-up. Therefore a further optimization of the process is needed. The possibilities are to include additives into the powder suspension that will help to reduce solidification cracking. Another approach would be to increase the lasers pulse frequency, inspired by the results of Patterson *et al.* [54].

A large concentration of spherical dispersoids with a diameter of ~20-100 nm, existing across the whole structure, was identified as a remarkable attribute of the liquid dispersed metal powder bed fusion process, which therefore includes also reactive additive manufacturing of ceramic nanodispersoids. The dispersoids could be found in both alloys and were identified mainly as CrMO<sub>x</sub> precipitates, enriched with Si and Nb, depending on the local alloy matrix chemistry. Their complex internal morphology is presented in Fig. 9. The dispersoid’s formation is interpreted by the oxidation of Cr and other elements and resembles the formation of protective Cr<sub>2</sub>O<sub>3</sub> oxide layers in Cr-rich stainless steels [50]. The dispersoids represent another hierarchical level within the alloy’s microstructure and actually provide structural reinforcement. Their formation indicates another interesting feature of AM technologies, namely the possibility to perform *reactive additive manufacturing and microstructural design at the nanoscale*. In other words, the deliberate formation of oxide nanoparticles during the liquid dispersed metal powder bed

fusion can be used as an effective tool to tune mechanical properties of AM-prepared alloys.

The multilayered structure (Fig. 3) exhibits a variety of bio-inspired attributes. The hatch strategy was selected to deposit microstructure with elongated grains and zig-zag low-angle grain boundaries (Fig. 5). Zig-zagging interfaces between crystallites and microstructural features are very common in natural materials and serve to enhance fracture toughness while preserving strength, for instance in *Saxidomus purpurata* shells with zig-zag oriented aragonite platelets. The deposition of the alternating alloys at meso- (Fig. 3) and micro-scales (Fig. 6a) with different mechanical properties and oscillating stress gradients [51] at the cross-section (Fig. 3) resembles a nacre-like microstructure [55] and has been known to improve the mechanical properties of hybrid-materials. Even though the mismatch in mechanical properties of IN625 and 316L is not sufficiently high, this work shows the possibility to tailor multilayer materials using the liquid dispersed metal powder bed fusion approach. Additionally, the incorporation of ceramic nano-dispersoids (Figs. 8,9) based on Cr oxides can be used as an effective tool to tune the mechanical properties of the AM structure by nanoscale design.

In summary, the liquid dispersed metal powder bed fusion approach offers the possibility to produce hierarchical microstructures based on meso- and micro-scale multilayers, grain boundaries of zig-zag shape, gradually changing textures, oscillatory stress concentrations and nanoscopic reinforcements, which together comprise a variety of multi-scale interfaces and can be used to tailor mechanical properties of AM structures.

## 6.5 Conclusions

This study demonstrates the feasibility of synthesizing a multi-metal hybrid structure based on IN625 and 316L, featuring unique multilayered microstructures at meso- and micro-scales, zig-zag shaped elongated grains and grain boundaries, regularly distributed nanoscopic dispersoids, complex texture evolution with gradual transitions, oscillating cross-sectional residual stresses and abrupt variation of mechanical properties across the multilayer. The zig-zag cracking correlated with the occurrence of IN625 (Fig. 2) as well as the pronounced C-shaped residual stress gradient (Fig. 3c), however, indicate the importance of process optimization in the fabrication of multi-metal hybrid materials with crack-free microstructures.

Although the synthesis of the multilayered structure (Fig. 3) was inspired by the architectural principles observed in biological materials [56] and the structure possesses a variety of interesting bionic microstructural features, the hardness values of IN625 and 316L do not differ significantly. Thus, effects like crack deflection toughening (observed in nacre) at the interfaces between IN625 and 316L layers and regions could not be

achieved here. The fabrication of hybrid systems consisting of materials with significantly different intrinsic mechanical properties like metal-ceramic composites has future potential to design multi-material structures with superior mechanical properties like high strength and toughness.

Finally, the presence of unique microstructures at meso-, micro- and nano-scales observed within the IN625–316L multilayer (Fig. 2) indicates the necessity of using cutting edge analytical techniques operating at multiple length scale in order to reveal the very particular process-microstructure-stress-property relationships in AM structures.

## **Acknowledgments**

A part of this work was supported by Österreichische Forschungsförderungsgesellschaft mbH (FFG), Project No. 861496, “CrossSurfaceMech”. Financial support by the Austrian Federal Government (in particular from Bundesministerium für Verkehr, Innovation und Technologie and Bundesministerium für Wissenschaft, Forschung und Wirtschaft) represented by Österreichische Forschungsförderungsgesellschaft mbH and the Styrian and the Tyrolean Provincial Government, represented by Steirische Wirtschaftsförderungsgesellschaft mbH and Standortagentur Tirol, within the framework of the COMET Funding Programme is gratefully acknowledged. Part of the research leading to this result has been supported by the project CALIPSOplus under the Grant Agreement 730872 from the EU Framework Programme for Research and Innovation HORIZON 2020. Another part of this work was carried out with the support of CEITEC Nano Research Infrastructure (ID LM2015041, MEYS CR, 2016–2019), CEITEC Brno University of Technology.



---

## References

- [1] K. Martinsen, S.J. Hu, B.E. Carlson, Joining of dissimilar materials, *CIRP Ann. Manuf. Technol.* 64 (2015) 679–699. doi:10.1016/j.cirp.2015.05.006.
- [2] P. Fratzl, R. Weinkamer, Nature's hierarchical materials, *Prog. Mater. Sci.* 52 (2007) 1263–1334. doi:10.1016/J.PMATSCI.2007.06.001.
- [3] A. Bandyopadhyay, B. Heer, Additive manufacturing of multi-material structures, *Mater. Sci. Eng. R Rep.* 129 (2018) 1–16. doi:10.1016/j.mser.2018.04.001.
- [4] W.J. Clegg, K. Kendall, N.M. Alford, T.W. Button, J.D. Birchall, A simple way to make tough ceramics, *Nature*. 347 (1990) 455–457. doi:10.1038/347455a0.
- [5] J.W.C. Dunlop, P. Fratzl, Biological composites, *Annu. Rev. Mater. Res.* 40 (2010) 1–24. doi:10.1146/annurev-matsci-070909-104421.
- [6] R. Hahn, M. Bartosik, R. Soler, C. Kirchlechner, G. Dehm, P.H. Mayrhofer, Superlattice effect for enhanced fracture toughness of hard coatings, *Scr. Mater.* 124 (2016) 67–70. doi:10.1016/j.scriptamat.2016.06.030.
- [7] Y.M. Wang, T. Voisin, J.T. McKeown, J. Ye, N.P. Calta, Z. Li, Z. Zeng, Y. Zhang, W. Chen, T.T. Roehling, R.T. Ott, M.K. Santala, P.J. Depond, M.J. Matthews, A. V. Hamza, T. Zhu, Additively manufactured hierarchical stainless steels with high strength and ductility, *Nat. Mater.* 17 (2018) 63–71. doi:10.1038/nmat5021.
- [8] A. Mortensen, S. Suresh, Functionally graded metals and metal-ceramic composites: part 1 Processing, *Int. Mater. Rev.* 40 (1995) 239–265. doi:10.1179/imr.1995.40.6.239.
- [9] D.C. Hofmann, J. Kolodziejska, S. Roberts, R. Otis, R.P. Dillon, J.-O. Suh, Z.-K. Liu, J.-P. Borgogna, Compositionally graded metals: a new frontier of additive manufacturing, *J. Mater. Res.* 29 (2014) 1899–1910. doi:10.1557/jmr.2014.208.
- [10] Y. Liu, F. Weng, G. Bi, Y. Chew, S. Liu, G. Ma, S.K. Moon, Characterization of wear properties of the functionally graded material deposited on cast iron by laser-aided additive manufacturing, *Int. J. Adv. Manuf. Technol.* (2019) 1–9. doi:10.1007/s00170-019-03414-w.

- [11] Z. Sun, R. Karppi, The application of electron beam welding for the joining of dissimilar metals: an overview, *J. Mater. Process. Technol.* 59 (1996) 257–267. doi:10.1016/0924-0136(95)02150-7.
- [12] D. Herzog, V. Seyda, E. Wycisk, C. Emmelmann, Additive manufacturing of metals, *Acta Mater.* 117 (2016) 371–392. doi:10.1016/J.ACTAMAT.2016.07.019.
- [13] C. Körner, Additive manufacturing of metallic components by selective electron beam melting — a review, *Int. Mater. Rev.* 61 (2016) 361–377. doi:10.1080/09506608.2016.1176289.
- [14] D.D. Gu, W. Meiners, K. Wissenbach, R. Poprawe, Laser additive manufacturing of metallic components: materials, processes and mechanisms, *Int. Mater. Rev.* 57 (2012) 133–164. doi:10.1179/1743280411Y.0000000014.
- [15] W.E. Frazier, Metal additive manufacturing: a review, *J. Mater. Eng. Perform.* 23 (2014) 1917–1928. doi:10.1007/s11665-014-0958-z.
- [16] D. Ding, Z. Pan, D. Cuiuri, H. Li, Wire-feed additive manufacturing of metal components: technologies, developments and future interests, *Int. J. Adv. Manuf. Technol.* 81 (2015) 465–481. doi:10.1007/s00170-015-7077-3.
- [17] M. Yakout, M.A. Elbestawi, S.C. Veldhuis, A review of metal additive manufacturing Technologies, *Solid State Phenom.* 278 (2018) 1–14. doi:10.4028/www.scientific.net/SSP.278.1.
- [18] T. DebRoy, H.L. Wei, J.S. Zuback, T. Mukherjee, J.W. Elmer, J.O. Milewski, A.M. Beese, A. Wilson-Heid, A. De, W. Zhang, Additive manufacturing of metallic components – process, structure and properties, *Prog. Mater. Sci.* 92 (2018) 112–224. doi:10.1016/j.pmatsci.2017.10.001.
- [19] J.J. Lewandowski, M. Seifi, Metal additive manufacturing: a review of mechanical properties, *Annu. Rev. Mater. Res.* 46 (2016) 151–186. doi:10.1146/annurev-matsci-070115-032024.
- [20] J.J. Sobczak, L. Drenchev, Metallic functionally graded materials: a specific class of advanced composites, *J. Mater. Sci. Technol.* 29 (2013) 297–316. doi:10.1016/J.JMST.2013.02.006.
- [21] C. Jang, J. Lee, J. Sung Kim, T. Eun Jin, Mechanical property variation within Inconel 82/182 dissimilar metal weld between low alloy steel and 316 stainless steel, *Int. J. Press. Vessel. Pip.* 85 (2008) 635–646. doi:10.1016/J.IJPVP.2007.08.004.

- [22] T. Mukherjee, W. Zhang, T. DebRoy, An improved prediction of residual stresses and distortion in additive manufacturing, *Comput. Mater. Sci.* 126 (2017) 360–372. doi:10.1016/J.COMMATSCI.2016.10.003.
- [23] R. Banerjee, P. Collins, D. Bhattacharyya, S. Banerjee, H. Fraser, Microstructural evolution in laser deposited compositionally graded  $\alpha/\beta$  titanium-vanadium alloys, *Acta Mater.* 51 (2003) 3277–3292. doi:10.1016/S1359-6454(03)00158-7.
- [24] P.C. Collins, R. Banerjee, S. Banerjee, H.L. Fraser, Laser deposition of compositionally graded titanium–vanadium and titanium–molybdenum alloys, *Mater. Sci. Eng. A.* 352 (2003) 118–128. doi:10.1016/S0921-5093(02)00909-7.
- [25] D.C. Hofmann, S. Roberts, R. Otis, J. Kolodziejska, R.P. Dillon, J. Suh, A.A. Shapiro, Z.-K. Liu, J.-P. Borgonia, Developing gradient metal alloys through radial deposition additive manufacturing, *Sci. Rep.* 4 (2015) 5357. doi:10.1038/srep05357.
- [26] H. Sahasrabudhe, R. Harrison, C. Carpenter, A. Bandyopadhyay, Stainless steel to titanium bimetallic structure using LENS<sup>TM</sup>, *Addit. Manuf.* 5 (2015) 1–8. doi:10.1016/J.ADDMA.2014.10.002.
- [27] S.Q. Wang, J.H. Liu, D.L. Chen, Tensile and fatigue properties of electron beam welded dissimilar joints between Ti–6Al–4V and BT9 titanium alloys, *Mater. Sci. Eng. A.* 584 (2013) 47–56. doi:10.1016/j.msea.2013.07.009.
- [28] B. Onuikwe, B. Heer, A. Bandyopadhyay, Additive manufacturing of Inconel 718–Copper alloy bimetallic structure using laser engineered net shaping (LENS<sup>TM</sup>), *Addit. Manuf.* 21 (2018) 133–140. doi:10.1016/J.ADDMA.2018.02.007.
- [29] V.K. Balla, P.D. DeVasConCellos, W. Xue, S. Bose, A. Bandyopadhyay, Fabrication of compositionally and structurally graded Ti–TiO<sub>2</sub> structures using laser engineered net shaping (LENS), *Acta Biomater.* 5 (2009) 1831–1837. doi:10.1016/j.actbio.2009.01.011.
- [30] V.K. Balla, P.P. Bandyopadhyay, S. Bose, A. Bandyopadhyay, Compositionally graded yttria-stabilized zirconia coating on stainless steel using laser engineered net shaping (LENS<sup>TM</sup>), *Scr. Mater.* 57 (2007) 861–864. doi:10.1016/J.SCRIPTAMAT.2007.06.055.
- [31] G.A. Knorovsky, M.J. Cieslak, T.J. Headley, A.D. Romig, W.F. Hammett, INCONEL 718: a solidification diagram, *Metall. Trans. A.* 20 (1989) 2149–2158. doi:10.1007/BF02650300.

- [32] N. Nadammal, S. Cabeza, T. Mishurova, T. Thiede, A. Kromm, C. Seyfert, L. Farahbod, C. Haberland, J.A. Schneider, P.D. Portella, G. Bruno, Effect of hatch length on the development of microstructure, texture and residual stresses in selective laser melted superalloy Inconel 718, *Mater. Des.* 134 (2017) 139–150. doi:10.1016/J.MATDES.2017.08.049.
- [33] S.J. Wolff, Z. Gan, S. Lin, J.L. Bennett, W. Yan, G. Hyatt, K.F. Ehmann, G.J. Wagner, W.K. Liu, J. Cao, Experimentally validated predictions of thermal history and microhardness in laser-deposited Inconel 718 on carbon steel, *Addit. Manuf.* 27 (2019) 540–551. doi:10.1016/J.ADDMA.2019.03.019.
- [34] K. Shah, I. ul Haq, A. Khan, S.A. Shah, M. Khan, A.J. Pinkerton, Parametric study of development of Inconel-steel functionally graded materials by laser direct metal deposition, *Mater. Des.* 54 (2014) 531–538. doi:10.1016/J.MATDES.2013.08.079.
- [35] B.E. Carroll, R.A. Otis, J.P. Borgonia, J. Suh, R.P. Dillon, A.A. Shapiro, D.C. Hofmann, Z.-K. Liu, A.M. Beese, Functionally graded material of 304L stainless steel and Inconel 625 fabricated by directed energy deposition: Characterization and thermodynamic modeling, *Acta Mater.* 108 (2016) 46–54. doi:10.1016/J.ACTAMAT.2016.02.019.
- [36] A. Hinojos, J. Mireles, A. Reichardt, P. Frigola, P. Hosemann, L.E. Murr, R.B. Wicker, Joining of Inconel 718 and 316 stainless steel using electron beam melting additive manufacturing technology, *Mater. Des.* 94 (2016) 17–27. doi:10.1016/J.MATDES.2016.01.041.
- [37] W.C. Oliver, G.M. Pharr, An improved technique for determining hardness and elastic modulus using load and displacement sensing indentation experiments, *J. Mater. Res.* 7 (1992) 1564–1583. doi:10.1557/JMR.1992.1564.
- [38] J. Kieffer, D. Karkoulis, PyFAI, a versatile library for azimuthal regrouping, in: *J. Phys. Conf. Ser.* 425 (2013) 202012. doi:10.1088/1742-6596/425/20/202012.
- [39] S. Timoshenko, Analysis of bi-metal thermostats, *J. Opt. Soc. Am. A.* 11 (1925) 233–255. doi:10.1364/JOSA.11.000233.
- [40] S.K. Rai, A. Kumar, V. Shankar, T. Jayakumar, K. Bhanu Sankara Rao, B. Raj, Characterization of microstructures in Inconel 625 using X-ray diffraction peak broadening and lattice parameter measurements, *Scr. Mater.* 51 (2004) 59–63. doi:10.1016/j.scriptamat.2004.03.017.

- [41] C. Yan, L. Hao, A. Hussein, P. Young, D. Raymont, Advanced lightweight 316L stainless steel cellular lattice structures fabricated via selective laser melting, *Mater. Des.* 55 (2014) 533–541. doi:10.1016/j.matdes.2013.10.027.
- [42] C. Li, Z.Y. Liu, X.Y. Fang, Y.B. Guo, Residual stress in metal additive manufacturing, *Procedia CIRP*. 71 (2018) 348–353. doi:10.1016/J.PROCIR.2018.05.039.
- [43] D. Seo, M. Sayar, K. Ogawa, SiO<sub>2</sub> and MoSi<sub>2</sub> formation on Inconel 625 surface via SiC coating deposited by cold spray, *Surf. Coatings Technol.* 206 (2012) 2851–2858. doi:10.1016/j.surfcoat.2011.12.010.
- [44] M. Yakout, M.A. Elbestawi, S.C. Veldhuis, A study of thermal expansion coefficients and microstructure during selective laser melting of Invar 36 and stainless steel 316L, *Addit. Manuf.* 24 (2018) 405–418. doi:10.1016/j.addma.2018.09.035.
- [45] P. Van Houtte, L. De Buyser, The influence of crystallographic texture on diffraction measurements of residual stress, *Acta Metall. Mater.* 41 (1993) 323–336. doi:10.1016/0956-7151(93)90063-X.
- [46] Z. Wang, E. Denlinger, P. Michaleris, A.D. Stoica, D. Ma, A.M. Beese, Residual stress mapping in Inconel 625 fabricated through additive manufacturing: method for neutron diffraction measurements to validate thermomechanical model predictions, *Mater. Des.* 113 (2017) 169–177. doi:10.1016/J.MATDES.2016.10.003.
- [47] P. Mercelis, J. Kruth, Residual stresses in selective laser sintering and selective laser melting, *Rapid Prototyp. J.* 12 (2006) 254–265. doi:10.1108/13552540610707013.
- [48] T. Dai, J. Lippold, Characterization of the interface of an alloy 625 overlay on steels using nanoindentation, *J. Mater. Eng. Perform.* 27 (2018) 3411–3418. doi:10.1007/s11665-018-3444-1.
- [49] C. Tromas, J.C. Stinville, C. Templier, P. Villechaise, Hardness and elastic modulus gradients in plasma-nitrided 316L polycrystalline stainless steel investigated by nanoindentation tomography, *Acta Mater.* 60 (2012) 1965–1973. doi:10.1016/j.actamat.2011.12.012.
- [50] T. Jonsson, S. Karlsson, H. Hooshyar, M. Sattari, J. Liske, J.-E. Svensson, L.-G. Johansson, Oxidation after breakdown of the chromium-rich scale on stainless steels at high temperature: internal oxidation, *Oxid. Met.* 85 (2016) 509–536. doi:10.1007/s11085-016-9610-7.

- [51] O. Kolednik, J. Predan, F.D. Fischer, P. Fratzl, Bioinspired design criteria for damage-resistant materials with periodically varying microstructure, *Adv. Funct. Mater.* 21 (2011) 3634–3641. doi:10.1002/adfm.201100443.
- [52] P. Fratzl, H.S. Gupta, F.D. Fischer, O. Kolednik, Hindered crack propagation in materials with periodically varying young's modulus - Lessons from biological materials, *Adv. Mater.* 19 (2007) 2657–2661. doi:10.1002/adma.200602394.
- [53] J.N. DuPont, J.C. Lippold, S.D. Kiser, *Welding metallurgy and weldability of Nickel-base alloys*, Wiley, 2009.
- [54] R.A. Patterson and J.O. Milewski, GTA weld cracking-alloy 625 to 304L. *Welding Res. Suppl.* 64 (1985) 227-231. [https://app.aws.org/wj/supplement/WJ\\_1985\\_08\\_s227.pdf](https://app.aws.org/wj/supplement/WJ_1985_08_s227.pdf)
- [55] F. Barthelat, C.M. Li, C. Comi, H.D. Espinosa, Mechanical properties of nacre constituents and their impact on mechanical performance, *J. Mater. Res.* 21 (2006) 1977–1986. doi:10.1557/jmr.2006.0239.
- [56] U.G.K. Wegst, H. Bai, E. Saiz, A.P. Tomsia, R.O. Ritchie, Bioinspired structural materials, *Nat. Mater.* 14 (2015) 23–36. doi:10.1038/nmat4089.

# Correlative Cross-Sectional Characterization of nitrided, carburized and shot peened Steels: Synchrotron Micro-X-Ray Diffraction Analysis of Stress, Microstructure and Phase Gradients

S. C. Bodner<sup>a\*</sup>, M. Meindlhumer<sup>b</sup>, T. Ziegelwanger<sup>a</sup>, H. Winklmayr<sup>c</sup>, T. Hatzenbichler<sup>c</sup>, C. Schindelbacher<sup>c</sup>, B. Sartory<sup>d</sup>, M. Krobath<sup>d</sup>, W. Ecker<sup>d</sup>, N. Schell<sup>e</sup> and J. Keckes<sup>a</sup>

<sup>a</sup> Department Materials Science, Chair of Materials Physics, Montanuniversität Leoben, Jahnstraße 12, Leoben, Styria, 8700, Austria

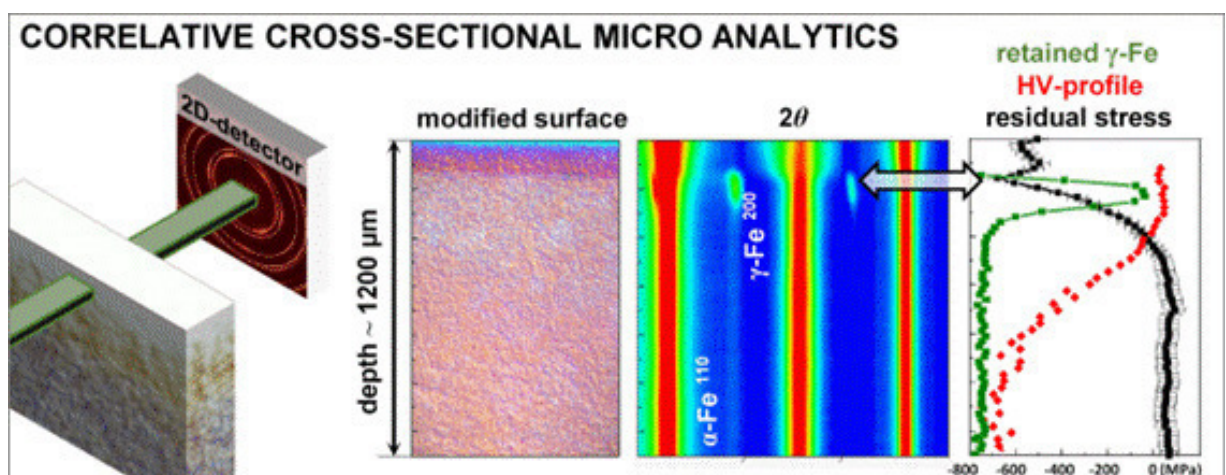
<sup>b</sup> Erich Schmid Institute of Materials Science, Austrian Academy of Sciences, A-8700 Leoben, Austria

<sup>c</sup> Pankl Racing Systems AG, Kapfenberg, Styria, 8610, Austria

<sup>d</sup> Materials Center Leoben, Roseggerstraße 15, Leoben, Styria, 8700, Austria

<sup>e</sup> Helmholtz Zentrum Geesthacht, Institute of Materials Research, GEMS, Notkestraße 85, Hamburg, 22607, Germany

## Graphical Abstract



## Abstract

Mechanical properties of case modified steels depend decisively on the near-surface gradients of residual stresses, microstructures, phases and chemical composition, which are generated by the empirically well-established case-hardening techniques. Currently, however, to obtain the correlation between near-surface structure-property gradients, applied hardening process parameters and steels' overall performance is a very challenging task. In this work, high-energy synchrotron cross-sectional X-ray diffraction (CSmicroXRD) using a pencil beam cross-section of  $20 \times 500 \mu\text{m}^2$  and complementary analytical techniques are used to characterize the surface-to-bulk gradient of (i) a plasma nitrided steel W300, (ii) a carburized case hardening steel (grade 18CrNiMo7-6) and (iii) a shot-peened high strength steel, type 300M. CSmicroXRD analysis reveals complex gradients of martensite and austenite phases, residual stresses in both phases, crystallographic texture and the evolution of diffraction peak broadening with a spatial resolution of  $\sim 20 \mu\text{m}$ . These parameters are correlated with the gradients of hardness, morphology-microstructure and with the changes in N and C concentrations and/or retained austenite formation/depletion in all three model samples. Finally, the correlative micro-analytics approach indicates the complexity of near surface structure-property relationships as well as the importance of innovative cross-sectional characterization, which allows for assessing gradual near-surface physical and/or chemical changes accompanying thermo-chemical and mechanical surface treatments.

**Keywords:** Cross-section Analysis; Synchrotron Micro-XRD; Near-Surface Characterization; Case-Hardening; Low-Pressure-Plasma Nitriding; Shot-Peening



## 7.1 Introduction

Advanced thermo-chemical surface treatments have been used to increase the mechanical performance of steel parts such as cam or ring gear, automotive components, drills and valves [1]. They provide these parts with a hard case and a tough core resulting in adequate fatigue strength and wear resistance, respectively, preventing brittle failure under high impact loads. Resulting functional aspects relevant to the industrial applications are in particular weight reductions due to topology optimization and/or an extended service life. Especially case-hardening technologies such as nitriding, carburizing, boronizing, nitrocarburizing and carbonitriding enhance the tooth root bending strength in gear components [2], the resistance against tensile and impact loads as well as alternating bending fatigue loading. Additional benefits are minimized distortion of the components due to the adaption of the residual stress state, the formation of microstructure depth gradients and the enhancement of corrosion and wear resistance in iron-based alloys [3,4].

Another possibility to enhance the mechanical properties of steels are mechanical surface modifications, like shot peening, which can even be applied to priorly thermally or thermo-chemically treated steels [5–7]. The surface plastification and work hardening is accompanied by the formation of compressive stress gradients, which favourably influence the fatigue resistance [8,9].

The common nitriding, carburizing and shot-peening treatments result in the formation of complex near surface depth gradients of microstructure, chemical composition, residual stress and/or crystalline phases, which, together with the alloying concept, decisively influence steel parts' mechanical properties. Currently, however, it is not trivial to correlate the applied surface treatment process parameters, the fabricated near-surface gradients and the parts' mechanical behaviour. The impact of the treatments at the micro, meso- and macroscale are usually assessed by (micro)hardness depth profiling [2,6,10], nanoindentation, optical and scanning electron microscopies (OM, SEM) and electron probe microanalysis [11]. In order to characterize microstructure, phase and stress gradients, X-ray and neutron diffraction [2,3,12] have been routinely applied (i) by analysing successively etched sample surfaces [13] and/or (ii) by using advanced grazing-incidence diffraction geometries, which require an inverse *Laplace transformation* of the data [14]. However, these techniques operating in *reflection diffraction geometries* provide structural data averaged across the respective X-ray or neutron beam penetration depths and their interpretation is therefore not always unambiguous [14–16].

A further development of the surface treatment technologies requires a comprehensive understanding of physical and chemical near-surface changes that take place during the

process with highest possible depth-resolution. The above mentioned surface treatments and corresponding recipes have been developed and used for decades. Although chemical gradients can nowadays be resolved on a nanoscale, there are several diffusion-induced phenomena within the parts' surfaces that have not been fully understood yet. These specifically include the incremental evolution and stabilization of phase gradients and their corresponding distributions of residual stresses as well as the microstructure within the individual phases, like in martensite and austenite [15,17].

This work focusses on the correlative cross-sectional characterization of exemplary (i) a low-pressure plasma nitrided hot-working steel, (ii) a low-pressure carburized case-hardening steel, and (iii) a shot-peened high performance steel grade. Results obtained from conventional laboratory experiments (OM, SEM, hardness profiling, electron microprobe analysis) and from scanning cross-sectional synchrotron high energy micro-X-ray diffraction (CSmicroXRD) with a spatial resolution of about  $\sim 20 \mu\text{m}$  are correlated. The novelty of the work resides (i) in introducing synchrotron CSmicroXRD methodology, based on *transmission diffraction geometry*, which allows for a simultaneous analysis of stress, microstructure and phase depth-gradients in the direct space, (ii) in applying robust complementary characterization approaches to assess cross-sectional structure-property relationships at the micro-scale and (iii) in observing cross-sectional correlations within the three different model sample systems. In contrast to previous studies dealing with relatively thin samples of  $\sim 50 \mu\text{m}$  in the X-ray beam direction

[18–20], the current work focuses on the simultaneous characterization of gradients of phases, residual stresses and microstructure in bulk samples with the thickness of  $\sim 2 \text{ mm}$ . Moreover, the three case hardened steel samples were selected without an additional intention to perform a further correlation between them.

## 7.2 Materials and Methods

### 7.2.1 Sample preparation

Three different martensitic steel samples were characterized in the present study: (i) a plasma-nitrided plate, (ii) a carburized cylinder and (iii) a shot-peened disc. The nominal compositions of the individual steel grades taken from [21–23] are given in Tab. 1. Each of the samples was surface modified as described below.

**Table 1** Nominal chemical compositions of steel grades used for gas-nitriding, carburizing and shot-peening according to references [21-23], respectively. The particular alloying contents are given in wt.%.

---

Process / Steel Grade	C	Si	Mn	Cr	Mo	Ni	V	other
Nitriding / X38CrMoV5-1 – W300	0.39	0.97	0.43	5.0	1.14	0.21	0.35	
Carburizing / 18CrNiMo7-6	0.17	0.25	0.50	1.65	0.3	1.55		Pb
Shot-Peening / 41SiNiCrMoV7-6 – 300M	0.42	1.65	0.8	0.8	0.3	1.8	0.8	

---

The *nitrided sample* was produced from a 30×30×10 mm<sup>3</sup> specimen of high alloy hot work steel type X38CrMoV5-1 (EN 1.2343 ESU – voestalpine Böhler Edelstahl GmbH, Kapfenberg, Austria) with a chromium content of 5%. The surface was modified by a long time low pressure plasma nitriding process. The sample was therefore kept in a process atmosphere of N<sub>2</sub>, H<sub>2</sub> and Ar gas mixture for 28 h at a temperature of 510 ±10°C. The base material was initially gas-quenched after austenitization at ~1010°C and tempered at 550, 530 and 520°C during the first tempering, the second tempering to working hardness and the third tempering for stress relief, respectively. The temperature was held for ~90 minutes during each tempering step before the material was cooled to ambient conditions.

The *carburized specimen*, a cylinder with a diameter of 40 mm and a height of 25mm of a low alloy case hardening steel type 18CrNiMo7-6 (EN 1.6857 – Deutsche Edelstahlwerke DEW, Witten, Germany), was case-hardened in an industrial vacuum furnace with dimensions of 0.6×0.75×1 m<sup>3</sup> by ALD Vacuum Technologies (Hanau, Germany). To enable the carbon enrichment in the near-surface region, the sample was low-pressure carburized for ~60 minutes in a hydrocarbon atmosphere (p=10 mbar) at a temperature of ~960°C. A martensitic microstructure was formed by high-pressure gas quenching using nitrogen with a pressure of ~10 bar. Finally, the sample was tempered at ~170°C for ~90 minutes.

The *shot-peened specimen* is a precipitation hardened, high strength heat treatable steel disc (similar to type 41SiNiCrMoV7-6 – EN 1.6928 – voestalpine Böhler Edelstahl GmbH, Kapfenberg, Austria) with a dimension of 50×7 mm<sup>2</sup> (diameter × height). Before the peening process, the sample was hardened at 870°C, quenched and double-tempered at 390 and 180°C for 60 and 180 minutes, respectively. The surface hardness of the steel disc before peening was determined to be 563 HV<sub>10</sub>. The specimen was shot-peened with an Almen-intensity of 0.2 ±0.05 mmA [24] in the next step. Spherical steel powder with

an initial diameter of  $\sim 0.35$  mm was used as blasting material. To end up in a smooth surface topology, the sample was furthermore fine-peened with an Almen-intensity of  $0.1 \pm 0.05$  mmA. The degree of coverage was 200 % in both peening-process steps.

## 7.2.2 Experimental methods

For the CSmicroXRD analysis, steel platelets of  $\sim (15 \times 5 \times 2)$  mm<sup>3</sup> were extracted from the three samples by precision cutting with an Accutom-5 (Struers, Germany) cutting machine, equipped with a diamond cutting wheel. A detailed analysis of near-surface residual stress relaxation caused by the sample cutting is discussed in Sec. 2.4 and in [18]. CSmicroXRD analysis was performed at the high energy materials science beamline P07B at the storage ring PETRAIII of DESY (German synchrotron) in Hamburg [25] in transmission diffraction geometry. The energy of the monochromatic beam was set to 87.1 keV which corresponds to a wavelength of 14.24 pm. Fig. 1 gives a schematic representation of the experimental set-up with the beam penetrating a sample in transmission diffraction geometry. An experimental protocol of the used set-up is presented in the supplementary data, Fig. S1. The near-surface regions of the three steel samples were scanned approximately at their centres by using a collimated pencil beam with a height and width of  $\sim 500$  and  $\sim 20$   $\mu$ m, respectively, oriented parallel to the sample's surfaces (*cf.* Fig. 1), using a scanning increment of  $\sim 10$   $\mu$ m. A two-dimensional (2D) amorphous silicon digital X ray detector (model XRD1621 by PerkinElmer) with  $2048 \times 2048$  pixels and a pixel pitch of 200  $\mu$ m was used to collect the diffracted signal. LaB<sub>6</sub> standard was used to determine the sample-to-detector distance of  $\sim 1329$  mm.

Each sample was aligned using a photo-sensitive diode and exact positions of the surfaces were determined in the same way.

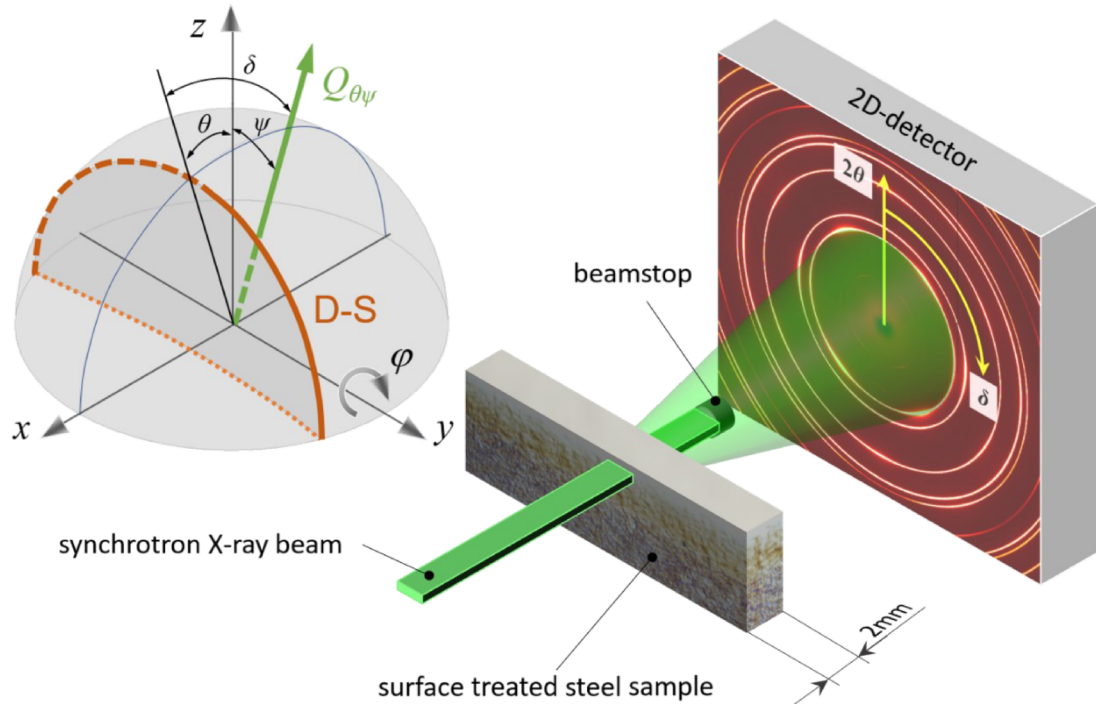


**Figure 1:** A schematic non-proportional drawing of the CSmicroXRD set-up at the PETRA III synchrotron. The steel sample with a thickness of  $\sim 2$  mm (in the beam direction) is moved along the  $z$ -direction in increments of  $\sim 20$   $\mu\text{m}$ . The sample surface is aligned parallel to the pencil beam by an  $\varphi$  rotation. The 2D detector collects a set of Debye-Scherrer (D-S) rings for each sample position using an acquisition rate of  $\sim 2$  s/frame. The stereographic projection illustrates the projection of one single D-S ring with a particular corresponding diffraction vector  $Q_{\theta\psi}$  schematically. The intensities of D-S rings at the azimuthal positions of  $\delta = 0^\circ$  and  $90^\circ$  represent diffraction on crystallographic planes oriented approximately parallel and perpendicular to the sample surface, respectively. The angle  $\psi$  denotes the angle between  $Q_{\theta\psi}$  and the normal of the surface of the sample  $z$ .

OM of all samples was performed using an Olympus BX51 microscope equipped with an Olympus digital camera.

SEM images were recorded with a Gemini field-emission SEM equipped with double condenser optics (Carl Zeiss SMT, Oberkochen, Germany) operating at an accelerating voltages of 5 kV and a beam current of 10 nA. To secure a clean surface, the near-surface cross-section of the plasma-nitrided and carburized steel samples were, additionally to standard metallurgical preparation techniques (grinding, polishing), prepared by  $\text{Ar}^+$  ion slicing at an ion milling system IM4000 (Hitachi High-Tech Corporation, Tokyo, Japan) using an accelerating voltage of 6 kV. N and C gradients in the parabola-shaped polished cross-sections of the plasma nitrided and carburized sample, respectively, were characterized by electron probe micro analysis (EPMA) using a X-Max 20 silicon drift detector by Oxford Instruments, suited for energy dispersive X-ray spectroscopy (EDX). For the carburized sample, the cross-sectional C-profile was furthermore evaluated using an electron probe micro-analyser, type JEOL JXA-8200 “Superprobe”, equipped with a wavelength dispersive spectrometer (WD-S). The set-up was calibrated using a pure

graphite calibrant before the polished metallurgical cross-section of the carburized sample was scanned by an electron beam of 15 kV acceleration voltage and 10 nA beam current with steps of 10  $\mu\text{m}$ . The FWHM for each spot and the corresponding background were measured for 20 and 10 s, respectively.

Micro hardness measurement scans using a Vickers indenter were performed across the polished cross-sections using a Mitutoyo/Buehler Micromet 5104 testing device equipped with a digital camera and the commercial Buehler Omnimet analysing software. Test loads of 100 and 500 g<sub>f</sub>, corresponding to HV<sub>0.1</sub> and HV<sub>0.5</sub>, were used to indent the metallographic sections of the three samples at depths between 0 and 100  $\mu\text{m}$  and at greater depths, respectively. Hardness values were calculated by averaging the result of three indents at redundant depth positions. The experiments were performed following the guidelines of DIN EN ISO 6507 1:2006. Consequently, the minimum distance between two indents as well as minimum distances to borders were taken into account. To determine the depth that was influenced by the nitriding and carburizing process, experimental HV data was fitted using an exponential decay function for the data down to a depth position of 600  $\mu\text{m}$ . The core hardness value of the basic material was determined by averaging HV-values measured from 600 to 5000  $\mu\text{m}$ .

### 7.2.3 CSmicroXRD data evaluation procedure

2D diffraction data (Fig. 1) were processed using the Python software package *pyFAI* [26]. The diffraction vector  $\mathbf{Q}_{\theta\psi}$  orientation-dependent lattice spacings  $d_{\theta\delta}(z)$  were evaluated from *Debye-Scherrer* (D-S) rings recorded at particular Bragg's angles  $\theta$ , the azimuthal angle  $\delta$  and the samples' depths  $z$  (Fig. 1). To elucidate  $d_{\theta\delta}(z)$ -values, 36 D-S rings sections, each encompassing  $\sim 10^\circ$  azimuthal range, were integrated and then evaluated using the Bragg's law. In general, D-S rings contain information on the crystallographic texture, the apparent size of coherently diffracting domains convoluted with the strains of second and third order (micro-strains), X-ray elastic strain of the first order (macro-strain) and volume fractions of phases within the irradiated gauge volume. Exact positions of the reflections' maxima as well as peaks' widths were fitted using a Pseudo-Voigt function. The novelty of this work resides mainly in the simultaneous examination of all above mentioned parameters using high-energy CSmicroXRD in bulk samples with a thickness of several mm, compared to the microscopic samples analysed in our previous studies [18–20].

X-ray elastic residual strain gradients at the particular sample depths  $z$  (Fig. 1) were determined from the D-S rings' ellipticity as follows

$$\varepsilon_{\theta\delta}^{hkl}(z) = \frac{d_{\theta\delta}^{hkl}(z) - d_0}{d_0} \quad (1)$$

with  $d_{\theta\delta}^{hkl}(z)$  being the distorted lattice parameter due to elastic residual strains in the material and  $d_0$  denoting the unstressed lattice parameter. It was assumed, that the three surface treatments had a negligible impact on the Poisson's ratio of the impacted materials. Therefore, depth-dependent unstressed lattice parameters  $d_0(z)$  were calculated from the measured  $\theta_0^{hkl}(z)$  positions of the diffraction peaks, which were retrieved (for each particular sample) from D-S rings always at the same rings' azimuthal position  $\delta_0$ , representing the stress-free direction (*cf.* Fig. 1) [18,27].

Since the initial geometry of the samples was rotationally symmetric, it was approximated that in plane  $\varepsilon_{11}(z)=\varepsilon_{22}(z)=\varepsilon(z)$  and out of plane  $\varepsilon_{33}(z)$  strain components are dominant and the shear strain components  $\varepsilon_{ij}(z)$  can be neglected for simplicity [18,28].  $\varepsilon_{22}(z)$  and  $\varepsilon_{33}(z)$  components represent the strain along  $y$  and  $z$  axes, further denoted as "in-plane" and "out-of-plane" components, respectively.  $\varepsilon_{11}(z)$  denotes the strain component in  $x$  direction (Fig. 1).

According to [29], intensities  $I(\delta, z)$  recorded at particular D-S azimuthal positions  $\delta$  (Fig. 1) can be transformed to  $I(\psi, z)$  dependencies as follows

$$\cos \psi = \cos \delta \cos \theta \quad (2)$$

The linearity of experimentally determined  $d_{\theta\delta}^{hkl}$  as a function of  $\sin^2\psi$  values along the investigated depth was used to prove the validity of the applied evaluation method, especially the absence of shear strain and stress components [18]. Additionally, an equibiaxial stress state with  $\sigma_{11}(z) = \sigma_{22}(z)$ ,  $\sigma_{12}(z) \cong 0$  and  $\sigma_{i3}(z) = 0$  ( $i = 1, 2, 3$ ) at the samples' free surfaces can be assumed, whereas at greater depths the out-of-plane residual stress component  $\sigma_{33}(z)$  cannot always be considered to be negligible [28,30,31]. Consequently, the distortion of the D-S rings as a function of the sample's depth can be generally expressed as follows

$$\frac{\partial d(\delta, z)}{\partial \sin^2 \delta} = [\sigma_{22}(z) - \sigma_{33}(z)] \frac{1}{2} S_2^{hkl} d_0(z) \quad (3)$$

where  $\frac{1}{2} S_2^{hkl}$  represents an X-ray elastic constant and  $d_0$  the unstrained lattice parameter [18,32]. In the case of martensite ( $\alpha'$ -Fe) and retained austenite ( $\gamma$ -Fe), X-ray elastic constants  $\frac{1}{2} S_2^{211} = 6.304 \times 10^{-6}$  and  $\frac{1}{2} S_2^{311} = 6.535 \times 10^{-6} \text{ MPa}^{-1}$ , respectively, were estimated using the *Kroener* grain interaction model [28,33]. In other words, knowing the X-ray elastic constants of a material, one can determine the actual experimental (*Exp*) (residual) stress  $\sigma_{22}(z) - \sigma_{33}(z)$  within the gauge volume from the slope of the linear regression in the  $d_{\theta\delta}^{hkl}$ - $\sin^2\psi$  diagram, Eq. (3), as derived in [28]. Additionally, unstressed lattice parameters  $d_0(z)$  can be simultaneously determined from the same system of linear equations in Eq. (3), considering the stress free direction defined by the azimuthal

angle  $\delta_0$  [27,28]. In contrast to the experiments performed in laboratory conditions,  $d_0$  and stresses can thus be elucidated directly from the D-S rings for every particular gauge volume without a previous knowledge of  $d_0(z)$ , as generally accepted. A detailed derivation of the stress evaluation procedure from two-dimensional synchrotron XRD data is presented elsewhere [18,20,27].

The actual angular resolution of the used set-up is predetermined by the pixel size of 200  $\mu\text{m}$  of the 2D detector, which corresponds to a  $2\theta$  angular range of  $\sim 0.0104$  degrees at  $2\theta = 5$  degrees and at the sample-detector distance of 1329 mm. Exact positions of the diffraction angles in the three experiments were determined by a fitting algorithm in pyFAI. Peak widths (full-width-at-half-maximum (FWHM) values) were extracted from these fits. Deviations for strain (and stress) were calculated based on a Gaussian error propagation.

The volume fraction of  $\gamma$ -Fe within the  $\alpha'$ -Fe matrix was determined by following an approach based on the ASTM practice E975-13 [34]. Accordingly,  $\alpha'$ -Fe 200/002 and 112/211 doublets and the 200 and 220 reflections from  $\gamma$ -Fe were azimuthally integrated from  $0 < \delta < 360^\circ$ . The presence of a crystallographic texture of the samples was assessed by evaluating the azimuthal distributions of the diffraction intensities  $I(\delta, z)$  of the particular D-S-rings, as presented in the supplementary data (Figs. S3, S9, S12).

#### 7.2.4 FEM-modelling

A finite elements model (FEM) was developed to reconstruct the original stress gradients within the three samples before cutting. As input parameters, the stress profiles  $\sigma_{22}(z) - \sigma_{33}(z)$  in Eq. (3) determined experimentally by CSmicroXRD, samples' elastic constants and geometry were used. For this reason, a linear elastic material model using the pairs of Young's moduli and Poisson's ratios of 215 GPa and 0.3, 190 GPa and 0.29 and 205 GPa and 0.28 was applied to the nitrided, carburized and shot-peened steels, respectively. Depending on the shape and dimensions of the three investigated samples, between 270000 and 660000 hexahedron elements with linear shape functions and reduced integration were used. In the samples' regions with stress gradients, structured meshes with element sizes of about 10  $\mu\text{m}$  were built. Towards the outer region of the specimens the mesh size increased gradually up to an element size of about 3 mm. The model's symmetry was used to reduce the number of elements. The independence of the results on mesh size and element's aspect ratio was verified in a mesh convergence study. In order to reconstruct the residual stress gradients across the uncut specimens a reverse engineering process was implemented. An initial stress state was therefore applied on the whole specimen, the cut was simulated by an element deletion of all elements except for the remaining sample geometry. The relaxed stresses of the simulated samples were



---

analysed at the centre of the samples with respect to its  $x$ -dimension (Fig. 1). A mean stress throughout the sample's thickness was then calculated for each depth position and sample [18]. Finally, the modelled stress profiles  $\sigma_{22}(z) - \sigma_{33}(z)$  denoted further as "FEM" stresses were optimized to fit the measured stress profiles from Eq. (3), further denoted as "Exp" stresses. The modelled residual stress gradients are presented together with the experimental results in Figs. 3-5 for comparison. Sample images with calculated stress distributions  $\sigma_{22}(z) - \sigma_{33}(z)$  and stress relaxation tendencies are presented in the supplementary data (Figs. S7, S11, S13). The above residual stress reconstruction procedure was applied only to the stress profiles obtained from  $\alpha'$ -Fe phase. For the  $\gamma$ -Fe phase, the approach was not applied because of the large standard deviations obtained for the experimental residual stress data.

## 7.3 Results

Cross-sectional data are presented on the basis of three case studies, each one for (i) the plasma nitriding, (ii) the carburizing and (iii) the shot-peening sample treatment.

### 7.3.1 Case Study I: Low-Pressure Plasma Nitrided Hot Work Steel Sample

OM and SEM analyses were used to characterize cross-sectional microstructure of the plasma-nitrided X38CrMoV5-1 steel (type W300). The near-surface diffusion zone and the martensitic core material are presented in the cross-sectional SEM micrograph of Fig. 2a. The presence of a thin, discontinuous compound layer with an average thickness of less than 100 nm can be identified at the surface in Fig. 2c. The diffusion zone encompasses  $\sim 80 \mu\text{m}$ . The steel microstructure and the morphology of the precipitates change gradually across this region. Fig. 2b indicates the homogenous distribution of equiaxed dispersoids with a size of several tens of nanometres at the martensite interlath positions within the diffusion zone. Further SEM micrographs with different magnifications are presented in the supplementary data (Figs. S4, S5, S6). The analysis revealed that additional larger precipitates are present, out of which some are globular and others are elongated in shape.

The formation of the *nanoscopic precipitates* in Fig. 2b can be interpreted by transformation kinetics as discussed in [35–37]. Lerchbacher *et al.* [35] reported on the formation of retained  $\gamma$ -Fe films in quenched W300 hot work steel at martensite interlath boundaries. Mesquita *et al.* [36] investigated carbide precipitation as a function of various silicon contents in similarly alloyed hot work tool steels. Investigated alloy compositions, comparable to the steel grade of the present work, exhibited a formation of chromium-rich  $\text{M}_7\text{C}_3$  coarser carbides, containing proportions of iron, molybdenum and vanadium that were also concentrated along martensite laths and packages boundaries. Michaud *et al.* [37] studied carbide formation in differently alloyed 5% Cr martensitic steels and observed the interlath precipitation of vanadium MC-carbides, chromium  $\text{M}_7\text{C}_3$ - and  $\text{M}_{23}\text{C}_6$  carbides as well as iron  $\text{M}_3\text{C}$  carbides during tempering. Considering the findings from [35–37], it is assumed that the precipitates within the diffusion zone in Fig. 2b are mainly nitrides and carbonitrides formed at martensite interlath positions and former boundaries of austenite grains. Furthermore, carbo-nitro precipitates, visible in Fig. 2c (and in the supplementary data Fig. S3 – S5) as equiaxed and elongated dark spots, are secondary carbides precipitated from the tetragonally distorted as-quenched  $\alpha'$ -Fe during the tempering treatments as well as carbides which had not been fully dissolved during austenitization.

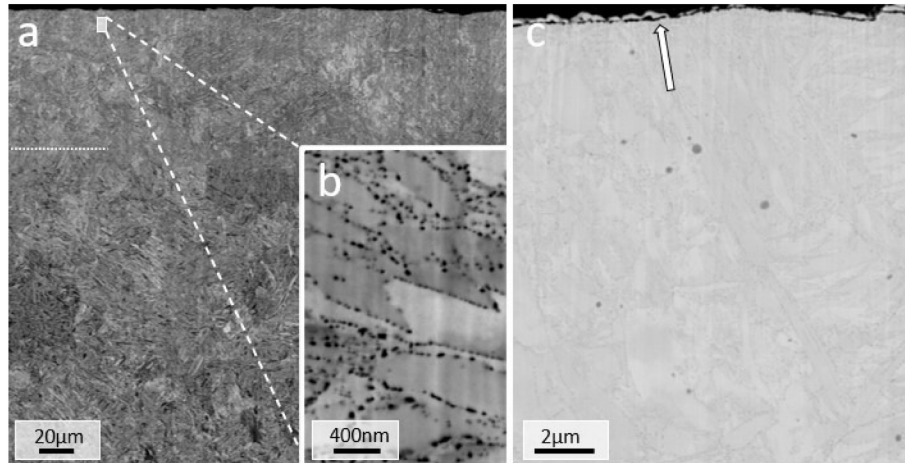


**Figure 2:** SEM-micrograph of the plasma-nitrided steel sample (a). The diffusion zone extends to a depth of  $\sim 80 \mu\text{m}$  (indicated by a white dotted line). The morphology of the precipitates is different in the diffusion zone and in the unnitrided core material. In the diffusion zone equiaxed interlath precipitates with a size of several tens of nanometers can be resolved (b) [36,37]. The presence of a discontinuous compound layer with a thickness of some tens of nanometers is indicated by an arrow and microscopic carbo-nitro precipitates are visible as equiaxed dark spots (c).

In Fig. 3, cumulative results obtained using cross-sectional experimental techniques are presented. A depth profile of the Vickers hardness (superimposed on an OM micrograph in Fig. 3a) indicates a steep hardness decrease from  $\sim 1054$  to a core hardness of  $\sim 589 \text{HV}_{0.5}$ , which is a typical value for this type of quenched and multiple-tempered steel grade [21]. The effective hardening depth can be determined at  $\sim 190 \mu\text{m}$ , meaning that the Vickers hardness at this position is 50 HV higher than the core hardness value.

CSmicroXRD analysis revealed austenite reflections, denoted as  $\gamma\text{-Fe } hkl$ , besides a dominant occurrence of martensite with pronounced  $\alpha'\text{-Fe } hkl$  reflections, which are indexed as doublets in Fig. 3b. A formation of a thin compound layer with a thickness of less than 100 nm at the sample's surface (*cf.* Fig. 2c) could not be resolved by CSmicroXRD. Additionally, no diffraction signals from nitride and carbide precipitates could be observed within the diffusion zone and within the core material, respectively. The very weak signals at  $2\theta$  positions of  $4.9$ ,  $5.3$ ,  $5.7^\circ$  and  $6.4$  and  $6.7^\circ$  visible in Fig. 2b (logarithmic scale) can be attributed to  $\alpha'\text{-Fe}$  and  $\gamma\text{-Fe}$  reflections, respectively, caused by high order harmonics of the synchrotron beam. If the synchrotron beam-energy is set by a crystal monochromator and no harmonic rejection optics is installed (like in the optics hutch at P07B), higher harmonics of the wavelength fulfilling Bragg's law with a higher order reflection, can pass through the crystal monochromator. Thus, additional peaks can appear in the XRD patterns, like in Fig. 2b.

In Figs. 3e and f, depth-dependent evolutions of the  $\alpha'\text{-Fe } 112/211$  reflection doublet for in-plane and out-of-plane diffraction vector orientations, respectively, are presented in detail. In general, one can observe an increase in the FWHMs at depths of 0-80  $\mu\text{m}$ , which

can be interpreted as the presence of micro-strain as well as by the crystallite size refinement induced by the increased N-concentration, as disclosed in Fig. 3d. The depth-dependent differences in the positions of the  $\alpha'$ -Fe 112/211 doublet for in-plane and out-of-plane diffraction vector orientations (Figs. 3e,f) are, however, correlated to both, the crystal lattice expansion as well as by the presence of a residual stress gradient (Fig. 3c). The  $\gamma$ -Fe reflections can be observed up to a depth of  $\sim 90 \mu\text{m}$  and a quantitative depth distribution of  $\gamma$ -Fe, estimated according to [34], is presented in Fig. 3d. The volume fraction of  $\gamma$ -Fe increases from 0 to  $\sim 9.58 \%$  within  $\sim 25 \mu\text{m}$ , starting  $\sim 65 \mu\text{m}$  below the surface and reaches a maximum of  $\sim 10.0\%$  at a depth of  $\sim 110 \mu\text{m}$ .

In Fig. 3c, a FWHM evolution of the  $\alpha'$ -Fe 202/220 reflection as a function of the diffraction vector orientation  $\psi$  from the range of  $\sim (2.8 - 90)^\circ$  (*cf.* Fig. 1) and the sample depth  $z$  is presented. The  $\psi$  angles of 2.8 and 90 degrees represent approximately in-plane and out-of-plane orientations of the diffraction vector  $\mathbf{Q}_{\theta\psi}$ , respectively (Fig. 1). Additional information on the evolutions of  $\alpha'$ -Fe FWHM as a function of sample's depth positions for the 101/110, the 002/200 and the 112/211 reflections are presented in the supplementary data (Fig. S2). In agreement with the data from Fig. 3e,f, the near-surface  $\alpha'$ -Fe 202/220 reflection broadening in Fig. 3c can be correlated with the domain size and micro-strain increase [38], which can be further correlated with the presence of the N-diffusion zone visible in Fig. 3d.

Superimposed on the FWHM map in Fig. 3c, experimental and modelled residual stress gradient data differing up to 20% are presented. In  $\alpha'$ -Fe, two compressive (FEM) stress maxima of  $\sim -765$  and  $\sim -841$  MPa at depths of  $\sim 10$  and  $\sim 80 \mu\text{m}$  can be identified, respectively. A steep stress relaxation can further be observed at a depth of  $\sim 230 \mu\text{m}$ . The high near-surface stresses are obviously mechanically balanced by low tensile stresses, which are present at larger sample depths. Fig. 3c also shows the stress distribution within the  $\gamma$ -Fe phase, which correlates well with the level of the  $\alpha'$ -Fe. Since the corresponding measurement errors of the evaluated stresses for the  $\gamma$ -Fe phase are inversely proportional to its volume fractions, they can be effectively compared with those from  $\alpha$ -Fe only at the depth of 80-150  $\mu\text{m}$ , where the  $\gamma$ -Fe concentration is relatively high. The origins of the compressive stress maxima in both phases are discussed below.

Residual stress profiles in  $\alpha'$ -Fe and  $\gamma$ -Fe can be correlated to the depth distributions of N and C in the near-surface region (Fig. 3d) as well as with the microstructural refinement manifested by the FWHM increase (Figs. 3c, e, f), the phase evolution and here, particularly, the local occurrence of  $\gamma$ -Fe (Fig. 3b). Within the first  $\sim 4 \mu\text{m}$  below the surface, N- and C- contents are complementary reduced and elevated, respectively. Below, they remain relatively stable and further decrease to zero and slightly increase, respectively, at the depth of 83  $\mu\text{m}$ , the edge of the diffusion zone.

The chemical composition profile of carbon can be used to interpret the formation of two compressive residual stress peaks in Fig. 3c. During plasma-nitriding, N diffuses into the near-surface area and causes a redistribution of the C throughout and also underneath the diffusion zone. Furthermore, C is firstly being partially exchanged by nitrogen in precipitates, especially in Cr,  $M_7C_3$ -type carbides and secondly being redistributed throughout the diffusion zone. The formation of a compound layer at the surface is documented to act as a diffusion barrier for C [39]. As a result of the C-diffusion, the EPMA-profile (Fig. 3d) exhibits a C-peak at a depth of  $\sim 5 \mu\text{m}$  and a C-enriched zone at the edge of the diffusion zone. Comparable results during plasma nitriding of steel are presented and discussed in [39,40]. The localized increase in the concentrations of N and C is assumed to expand the  $\alpha'$ -Fe lattice, which results in a formation of stress at a depth of  $\sim 83 \mu\text{m}$ .

Additionally, the increased C content at the front of the N-diffusion zone, which is the interface between the diffusion zone and the unnitrided core material (Fig. 3d), is assumed not only to contribute to a localized stabilisation of the  $\gamma$ -Fe phase but also to a localized reversion of  $\alpha'$ -Fe to  $\gamma$ -Fe during the long-term plasma nitriding. To the best authors knowledge, this effect has not been reported before on a W300 steel grade. Typically, austenite reverse transformation can be observed in quench and partitioning (Q&P) steels [41]. Raabe *et al.* [42] documented on a phase transformation of  $\alpha'$ -Fe to  $\gamma$ -Fe at grain boundaries in a Fe-9 at.% Mn and a Fe-12 at.% Mn maraging steel during aging at  $450^\circ\text{C}$ . In that case, the localized reversion of  $\alpha'$ -Fe to  $\gamma$ -Fe was correlated with the segregation of Mn at  $\alpha'$ -Fe interlath boundaries. Jegou *et al.* [43] determined a coarsening of pre-existing carbides in a ferrite matrix at the nitriding front in differently nitrided Fe-3.5Cr-0.35C (wt.%) model-steel but no reversion of  $\alpha'$ -Fe to  $\gamma$ -Fe in their samples. No coarsening of pre-existing carbides could be documented in this sample (supplementary data, Fig. S6). Thus, we assume that not the locally elevated C content itself but the combination of a locally elevated C content, the  $\alpha'$ -Fe matrix and the simultaneous presence of Si in the W300 causes the localized reversion of  $\alpha'$ -Fe to  $\gamma$ -Fe.

The exact origin, the formation kinetics and the character of the reverted  $\gamma$ -Fe build up (Fig. 3b) in the nitrided W300 steel however needs to be further investigated.

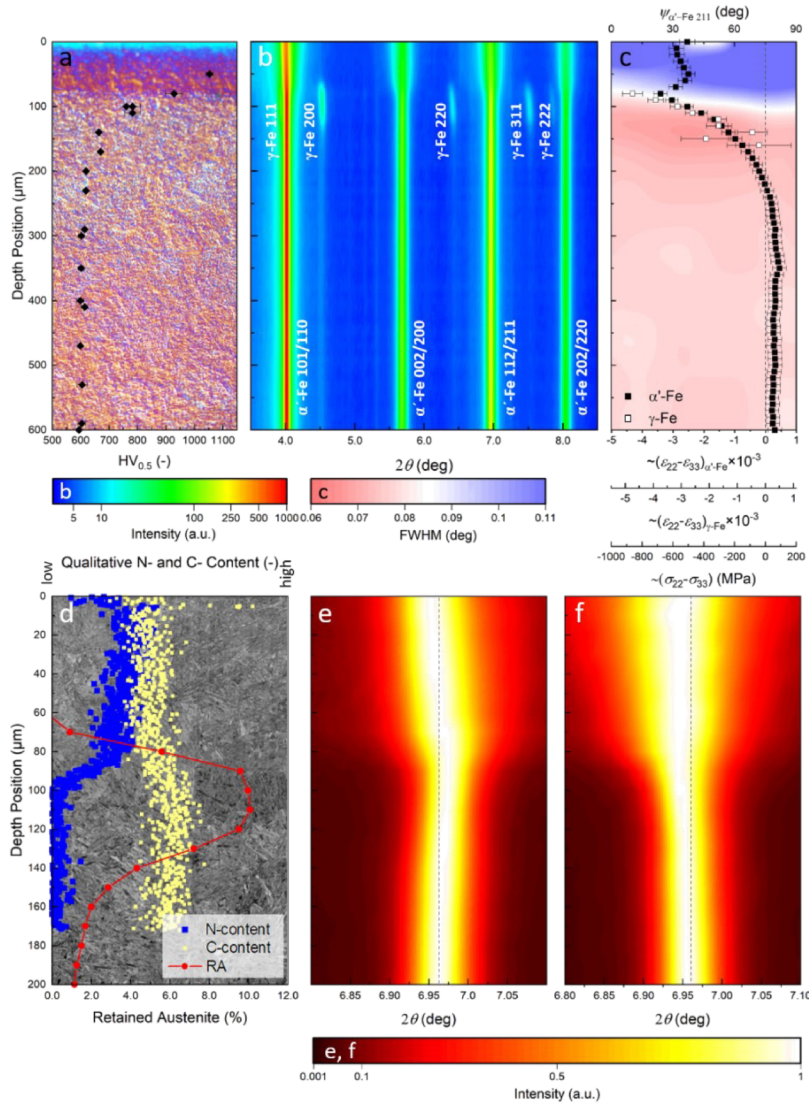


**Figure 3:** Correlative cross-sectional analysis of the low-pressure plasma nitrided steel sample. As indicated in the OM micrograph (a), the Vickers hardness decrease across the N-diffusion zone correlates with a gradual change in the near-surface martensitic microstructure (*cf.* also Fig. 2). The CSmicroXRD phase plot (b) indicates the presence of  $\alpha'$ -Fe matrix and reverted  $\gamma$ -Fe at the interface between the N-diffusion zone and the martensitic core material. Not indexed, weak reflections at  $2\theta$  positions of 4.9, 5.3, 5.7° and 6.4 and 6.7° are  $\alpha'$ -Fe and  $\gamma$ -Fe reflections, respectively, of higher order harmonics. (c) Experimental (Exp) and modelled (FEM) residual stress data representing  $\sigma_{22}(z) - \sigma_{33}(z)$  stresses indicate compressive stress maxima at the edge of the diffusion zone in  $\alpha'$ -Fe and  $\gamma$ -Fe phases, which can be correlated with the occurrence of reverted  $\gamma$ -Fe. A superimposed 2D map in (c) shows the FWHM distribution of the  $\alpha'$ -Fe 220/202 reflection for various diffraction vector orientations  $\psi$  (*cf.* Fig. 1). The reverted  $\gamma$ -Fe occurrence at the bottom of the diffusion zone (d) correlates well with the C and N concentrations as well as the microstructure does. Gradual changes of FWHMs and positions of  $\alpha'$ -Fe 112/211 reflections for in-plane (e) and out-of-plane (f)  $Q_{\theta\psi}$  orientations originates from the presence of the residual stress gradient (c) and the modified microstructure (d).

Complementary experimental results from CSmicroXRD and other techniques presented in Figs. 2 and 3 can be correlated. The thickness of the diffusion zone revealed quantitatively by EDX (*cf.* Fig. 3d) correlates (i) with the morphological changes in the microstructure in Fig. 2, (ii) with the broadening of martensite reflections from Figs.

3b,c,e,f and (iii) with the presence of compressive stresses in Fig. 3c. Additionally, two compressive residual stress maxima in Fig. 3c can be correlated with the increased concentration of N and C interstitial atoms (*cf.* Fig. 3d) and also with the local occurrence of reverted  $\gamma$ -Fe at the depth of  $\sim 80 \mu\text{m}$  (Fig. 3a). At greater depths, residual stress distribution can be correlated also with the hardness profile in Fig. 3a: compressive stress relaxes at  $\sim 230 \mu\text{m}$ , which is the same position where the value of the core hardness was measured.

There were several attempts to assess cross-sectional structure-property relationships in plasma-nitrided W300 steel samples. Leskovsek *et al.* [10] studied the correlation of residual stress (assessed by the hole drilling method) and micro-hardness gradients within eight differently plasma nitrided W300 samples. Similar to the results of the present work, they reported on the correlation between residual stress and micro-hardness gradients and suggested a routine to estimate residual stresses from a hardness-related parameter. It is notable, that they could not observe the formation of a compound layer at plasma-nitriding temperatures of  $480^\circ$  but just  $60^\circ\text{C}$  above, at a temperature of  $540^\circ\text{C}$ , which is in contradiction with the compound layer build-up at  $510^\circ\text{C}$  in the present work. Remarkably, residual stress profiles obtained by hole drilling [10] are comparable to the results of the present work in terms of their shape and maximal compressive stresses of  $\sim -700$  to  $-850 \text{ MPa}$ . However, two stress maxima (Fig. 3c) as well as a coexistence of  $\alpha'$ -Fe and  $\gamma$ -Fe were not reported. Similar, Kurz *et al.* [3] reported on depth gradients of residual stresses, unstressed lattice parameters, microstructure and the N-diffusion during gas nitriding of Fe-M(= Al, V) specimens. High-energy synchrotron X-ray diffraction was employed to assess the spatially resolved stress state which was correlated to different precipitation mechanisms. Due to the small beam size of  $20 \times 5 \mu\text{m}^2$  (horizontal  $\times$  vertical) that was used in their setup, the nitrided samples were moved parallel to the cross-sectional surface along the  $y$ -direction to obtain more representative diffraction data at specific sample depths.

### 7.3.2 Case Study II: Low-Pressure Carburized Case-Hardening Steel Sample

The CSmicroXRD approach was additionally tested on a carburized case-hardened steel sample (Fig. 1). A SEM micrograph in Fig. 4a obtained from the cross-section of the carburized 18CrNiMo7-6 steel indicates a gradual morphological change across the martensite matrix and a decreasing volume fraction of the (brighter)  $\gamma$ -Fe phase as a function of the sample depth (also visible in the high-resolution SEM images presented in the supplementary data Fig. S8 ). For this sample, the cross-sectional changes in the microstructure (Fig. 4a) and phase (Fig. 4b) evolutions can be correlated as well with the distribution of C diffused into the near-surface region, as presented in Fig. 4d and in supplementary data Fig. S10b. Superimposed on the SEM micrograph, Fig. 4a also shows the hardness depth-profile across the diffusion zone and the core material. Vickers hardness measurements revealed a case hardness of  $711 \pm 5 \text{ HV}_{0.5}$ , which is almost constant down to the depth of  $\sim 275 \mu\text{m}$ . Further below, the hardness decreases gradually to a core hardness of  $\sim 431 \pm 13 \text{ HV}_{0.5}$  observed at a depth of  $\sim 800 \mu\text{m}$ . According to EN ISO 2639, the case hardening depth (CHD) of carburized samples is defined as the depth, at which the hardness reaches the limit of  $550 \text{ HV}_1$ . In this case, the CHD of the sample was determined for  $\sim 660 \mu\text{m}$  below the surface. The corresponding hardness profile is presented in the supplementary data (Fig. S10a).

The cross-sectional phase analysis indicates gradual changes in the volume fractions of the  $\alpha'$ -Fe matrix and the  $\gamma$ -Fe fraction (Fig. 4b), which were observed priorly by SEM (Fig. 4a). In the near surface area at a depth smaller than  $\sim 600 \mu\text{m}$ , broadened  $\alpha'$ -Fe  $hkl$  and retained  $\gamma$ -Fe  $hkl$  reflections are pronounced due to the high C-content (Fig. 4d). At depths greater than  $\sim 250 \mu\text{m}$ , the decreasing volume fraction of  $\gamma$ -Fe is reflected by a decreasing intensity of the  $\gamma$ -Fe reflections while the intensity of the martensite peaks increases and their FWHM decreases, because of the supposed ceasing tetragonal distortion of martensite.

The FWHM evolution of the  $\alpha'$ -Fe112/211 reflection as a function of the diffraction vector orientation  $\psi$  and the sample depth position is presented in Fig. 3c. A notable increase in martensite's FWHM down to a depth of  $\sim 580 \mu\text{m}$  (*cf.* Figs. 4e,f) correlates (i) with the observed  $\text{CHD}_{\text{HV}0.5}$  (using a test load  $500 \text{ gf}$  – *cf.* Fig. 4a) and (ii) with the maximum of the compressive residual stress of  $\sim -682 \text{ MPa}$  from the FEM model. In the carburized sample, the difference between experimental and modelled stresses is large (*cf.* Fig. 4c). This effect is caused by the comparable dimensions of the carburized sample depth of  $\sim 1 \text{ mm}$ , the stress-affected region of more than  $2 \text{ mm}$  and the sample thickness in the  $x$  direction of  $2 \text{ mm}$ . This effect was extensively discussed in [18]. The distribution



of the residual stresses and the reversal of compressive to tensile stresses at  $\sim 80 \mu\text{m}$  depth can again be correlated to the C-content and to the increasing volume fraction of  $\gamma\text{-Fe}$ . A second reversal in sign of the residual stresses occurs at a depth of  $\sim 1030 \mu\text{m}$ . As a consequence of mechanical equilibrium, tensile stresses are induced at depths above and below these positions, respectively. Residual stresses in  $\gamma\text{-Fe}$  are low compared to  $\alpha'\text{-Fe}$  (Fig. 4c) but display a significantly higher variance. Their nature down to a depth of  $\sim 300 \mu\text{m}$  is tensile. A similar observation for  $\gamma\text{-Fe}$  was also reported by Ericsson *et al.* [17]. In  $\alpha'\text{-Fe}$  phase, the stress profile originates from quenching and from martensite phase transformation hardening, the latter one depending strongly on the C-content. It should be noted that the martensite start temperature ( $M_s$ ) as well as the yield stress are being attained at different locations of the sample at different times during quenching [15,17]. The specific stress gradient formed during quenching in Fig. 4c can be interpreted by considering segments of the hardening process and their corresponding sample depth dependent transformation kinetics, described in detail in [15,17].

The gradual change of the martensite start (and finish) temperature as a function of the C-content furthermore affects the quantity of retained  $\gamma\text{-Fe}$ . Fig. 4d presents a quantitative depth distribution of the retained  $\gamma\text{-Fe}$ . Within the first  $100 \mu\text{m}$  below the surface, a high  $\gamma\text{-Fe}$  volume fraction of  $\sim 31.7 \%$  could be evaluated, which decreases gradually to the magnitude of  $2.8 \%$  within the core material at  $800 \mu\text{m}$  and below.

Figs. 4e and 4f show the  $\alpha'\text{-Fe}$  112/211 reflection evolution for  $Q_{\theta\psi}$  in-plane and out-of-plane orientation, respectively, down to the sample depth of  $1000 \mu\text{m}$ . The intensities occurring at both  $Q_{\theta\psi}$  orientations were normalized frame per frame to the individual maximal intensity of the reflection. The shift and the broadening of the reflections at depths of  $\sim (0-800) \mu\text{m}$  can be correlated to the compressive residual stress increase and to the unstressed lattice parameter increase, due to interstitially soluted C. The maximum peak shift can be observed at  $\sim 580 \mu\text{m}$  depth, which is the depth of the highest compressive stress magnitude (Fig. 4c) and the  $\text{CHD}_{\text{HV}0.5}$  that was determined with a test load of  $500 \text{ g}_f$  (Fig. 4a).

Correlative Cross-Sectional Characterization of nitrided, carburized and shot peened Steels:  
Synchrotron Micro-X-Ray Diffraction Analysis of Stress, Microstructure and Phase Gradients

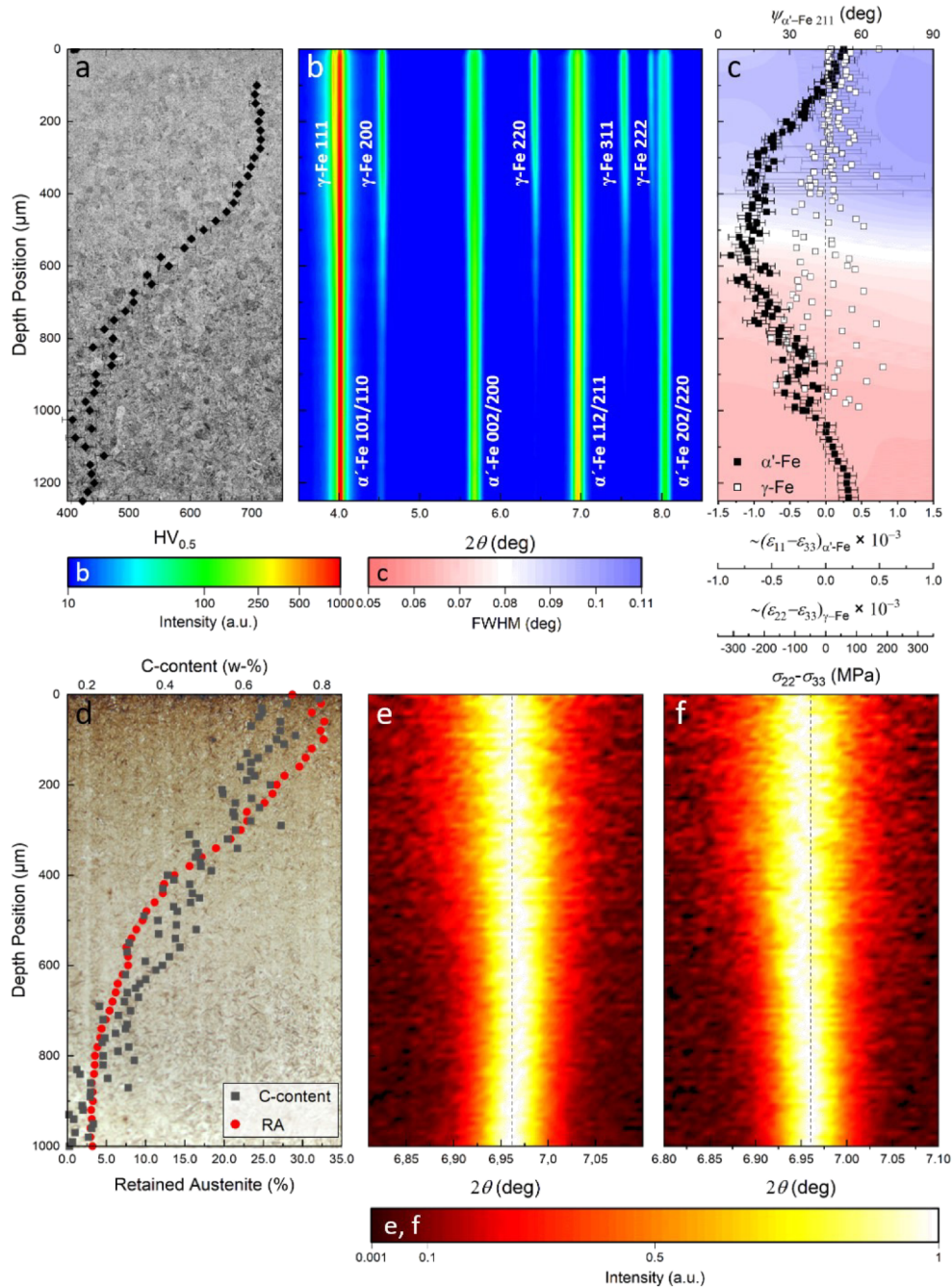


**Figure 4:** Cross-sectional analysis of the carburized steel sample. The analysis revealed a decreasing hardness and the gradient microstructure of the iron-martensite matrix along the sample's depth (a). The particular reflection intensities in the phase plot (b) indicate the presence of the dominant martensite matrix and a gradual decrease of retained  $\gamma$ -Fe volume fraction. The formation of residual stresses with a compressive stress peak of  $\sim -682$  MPa in  $\alpha'$ -Fe and negligible stresses in  $\gamma$ -Fe phase are visible in the modelled and experimental stress data in (c). Quantitative retained  $\gamma$ -Fe analysis correlates with the distribution of C down to the 1000  $\mu\text{m}$  depth, which are shown in (d), together with the optical micrograph of the etched sample cross-section. The positions and FWHMs of  $\alpha'$ -Fe 112/211 reflections in for in-plane (e) and out-of-plane (f)  $Q_{0\psi}$  orientation change due to the compressive residual stress state in the carburized zone and microstructural refinement.

### 7.3.3 Case Study III: Shot-Peened Martensitic Steel Sample

The CSmicroXRD approach was additionally applied to a shot-peened martensitic steel. The microstructure, the hardness profile and the distributions of the phases and residual stresses of the shot-peened hardened and double-tempered 300M steel sample are presented in Fig. 5.

The darker appearance of the microstructure down to the depth of  $\sim 20 \mu\text{m}$  in the Nital-etched cross-section (Fig. 5a) is caused by the absence of retained  $\gamma$ -Fe in this area. In the same region, the shot peening treatment attained a strain induced phase transformation from  $\gamma$ -Fe to  $\alpha'$ -Fe. The effect of a strain-induced transformation of retained  $\gamma$ -Fe into  $\alpha'$ -Fe during shot-peening was documented also by Ebenau *et al* [8]. Their study reports that a shot-peening treatment of austempered nodular cast iron samples with high volume fractions of up to  $\sim 19$  and  $\sim 39\%$   $\gamma$ -Fe resulted in a significant reduction of the  $\gamma$ -Fe content and a formation of  $\alpha'$ -Fe at depths down to  $\sim 300 \mu\text{m}$ .

In Fig. 5, the microstructure changes gradually to the tempered  $\alpha'$ -Fe base material with increasing depth. In the uninfluenced core, a  $\gamma$ -Fe volume fraction of  $\sim 5\%$  could be evaluated (Fig. 5d), whereby Vicker's hardness values decrease simultaneously from  $\sim 694.5 \pm 5 \text{ HV}_{0.5}$  at  $\sim 50 \mu\text{m}$  to  $\sim 663 \pm 10 \text{ HV}_{0.5}$  at  $\sim 170 \mu\text{m}$  (Fig. 5a), which is the depth that corresponds to the uninfluenced base material.

CSmicroXRD indicates the presence of a dominant martensite matrix with a small volume fraction of  $\gamma$ -Fe in the unpeened base material (Fig. 5b). A quantitative  $\gamma$ -Fe analysis (Fig. 5d), revealed a steep  $\gamma$ -Fe decrease at depths smaller than  $\sim 50 \mu\text{m}$  whereas an amount of  $\sim 5\%$  could be determined in the unpeened material.

The decrease in the martensite's FWHM values in the deformed region for the  $\alpha'$ -Fe 112/211 reflection is presented in Fig. 5c and can be interpreted as follows: (i) due to the massive plastic deformation induced by the shot-peening process, grain orientations of the initially untextured material were rearranged in order to form a  $\langle 110 \rangle$ -fibre-texture within the influenced regions (*cf.* Fig 5d and Fig. S12 in the supplementary data) and (ii) the energy impact due to the shot-peening process was high enough to increase the size of the coherently scattering domains and to decrease micro-strains at depths smaller than  $\sim 20 \mu\text{m}$  due to an annealing effect (*cf.* [6,7]).

The applied shot-peening treatment induced high compressive (FEM) stresses of  $\sim 1371 \text{ MPa}$  at the depth of  $20 \mu\text{m}$  (Fig. 5c) in  $\alpha'$ -Fe. As a result, a pronounced peak shift of the  $\alpha'$ -Fe 211/112 doublet to higher and lower angles for in-plane and out-of-plane  $Q_{\theta\psi}$  orientations, respectively, can be observed in Figs. 5e and 5f. The reversal in sign of the compressive residual stresses occurs at a depth of  $\sim 105 \mu\text{m}$ . At greater depths, negligible tensile stresses could be evaluated. Due to the weak intensities of  $\gamma$ -Fe phase D-S rings,

the residual stress values in  $\gamma$ -Fe exhibit high standard-deviations, although the stress levels approach that of martensite (Fig. 5c).

The cumulative results in Fig. 5 obtained from various cross-sectional characterization techniques show remarkable correlations. At a depth of  $\sim 20 \mu\text{m}$ , down to which the modified microstructure due to deformation-induced phase transformation can be observed by OM (Fig. 5a),  $\langle 110 \rangle$  fibre-texture formation (Fig. 5d and supplementary data, Fig. S12), an abrupt change in the FWHM evolution (Fig. 5c) and the compressive residual stress peak (Fig. 5c) were observed.

Scholtes and Vöhringer [7] discussed the influence of shot-peening and the peening parameters on the near-surface regions they describe a strain-induced transformation of retained  $\gamma$ -Fe and the evolution of a  $\langle 110 \rangle$  fibre texture. Results obtained by CSmicroXRD in the present work coincide with these findings from hardened steels and document that the shot-peening process results not only in a surface plastification and stress formation but also in remarkable changes in the near-surface microstructure and the phase composition.

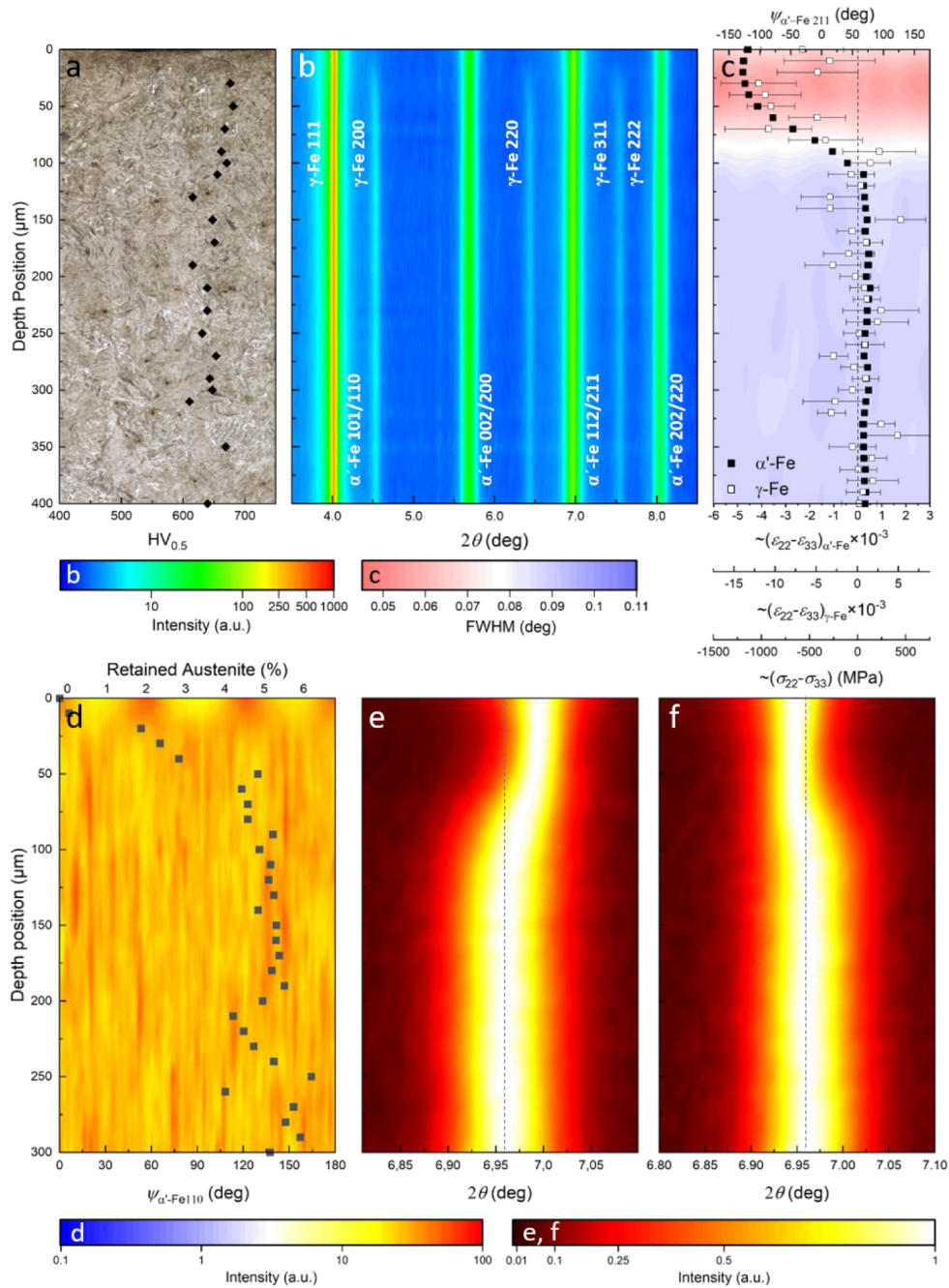


**Figure 5:** Cross-sectional analysis of the shot-peened sample. The investigations revealed a hardness increase toward the surface due to the work hardening effect that correlates well with the gradual change in the microstructure visible in the OM micrograph (a). The phase plot (b) confirms the presence of plastic strain induced phase transformation of the metastable  $\gamma$ -Fe to martensite in the shot-peening influenced near-surface region. A decrease in  $\alpha'$ -Fe 112/211 FWHMs within the near-surface region (c) indicates that the shot-peening induced a significant rearrangement of the microstructure with larger crystallites and/or a lower density of structural defects, in agreement with the  $\alpha'$ -Fe 112/211 profiles form (e) and (f) for in-plane and out-of-plane  $Q_{\theta\psi}$  orientations, respectively. The quantitative  $\gamma$ -Fe analysis (d) exhibits a significant drop in the deformed region down to  $\sim 50 \mu\text{m}$  depth. Furthermore, the influence of the shot-peening treatment is shown by a  $\langle 110 \rangle$  fibre texture formation down to  $\sim 20 \mu\text{m}$  depth in (d).

## 7.4 Discussion

This study demonstrates the advantages of applying synchrotron CSmicroXRD technique in conjunction with conventional laboratory techniques (like OM, SEM, EDX and micro-hardness profiling) to characterize gradients of residual stresses, microstructures, crystallites morphology, composition and hardness in surface treated steels. The main aim of the work is to show the possibilities of CSmicroXRD analysis on three different sample types, without any additional intention to carry out a further correlation between the samples and the results. The three samples were selected to test the CSmicroXRD approach. Consequently, hereafter methodological aspects of the results are discussed followed by only a few materials science related points.

In general, CSmicroXRD can be considered as an upscaling of X-ray nanodiffraction conducted using sub-50 nm X-ray beams usually on micro-lamellae of  $\sim 50 \mu\text{m}$  in thickness (in the X-ray beam direction) and of crystallite size of several tens of nanometers [19]. Due to the larger grain size of the steel samples (even in the micrometer range) and the larger depth of interest (in the millimeter range), it is reasonable to apply scanning high-energy X-ray microdiffraction (CSmicroXRD) to obtain both sufficient diffraction statistics and satisfactory depth resolution within relatively thick samples of several millimeters. Additionally, in comparison with the results presented in previous X-ray microdiffraction studies *e.g.* in [3], the present work indicates the possibility to evaluate not only residual stress gradients but also gradients of crystallographic texture, FWHM and crystalline phases from the 2D XRD data. In this way, complex correlations between the microstructure and stresses on one side and the applied process conditions as well as the functional properties, like gradients of hardness, on the other side can be deduced. It can be expected that the relatively simple CSmicroXRD set-up (Fig. 1) will be used in future to routinely investigate surface-treated bulk samples by high energy X-ray diffraction.

The comparison of the modelled and experimental stress dependencies in Figs. 3-5 indicates reasonable differences up to  $\sim 15\%$  in nitrided and shot-peened samples (Fig. 3c, and 5c), due to the relatively small affected depths of the samples by both processes. In the case of carburized sample, the (experimental) stresses relaxed nearly 50% in the cut sample (Fig. 4c). As already mentioned, this is caused by the comparable dimensions of the carburised sample depth of  $\sim 1 \text{ mm}$  and the sample thickness in the  $x$  direction of 2 mm. This effect was studied and discussed in [18].

It is obvious, that absolute magnitudes of the residual stresses (in Figs. 3c, 4c and 5c) obtained from the three investigated specimens cannot be directly compared due to the different alloying concepts and surface treatments of the steel grades. It follows, that the

use of particular X-ray elastic constant  $\frac{1}{2} S_2=(1+\nu)/E$  provide not absolute but just approximate residual stress values. An experimental study of Marion and Cohen [44] indicated, that individual X-ray elastic constants should be individually, experimentally determined in principle not only for different steel compositions but also for different grain sizes, microstructures, deformations and heat treatments. Consequently in the present case, X-ray elastic constants should be determined for every sample depth and the corresponding material composition and microstructure. This has not been done in this work, thus, resulting imprecisions were taken in account during the error determination. Therefore, the residual stress data in Figs. 3c, 4c and 5c are presented together with experimentally determined X-ray elastic strains.

The experimental results from the three different surface-treated steel samples (Figs. 3-5) allows to draw conclusions on the near-surface gradients and their correlations. However, since the steel grades used for the individual experiments differ one from another, it is not trivial or it could even be impossible to draw significant correlations between the experimental data from Figs. 3-5. In the low-pressure plasma-nitrided hot-work tool steel W300 (Fig. 3), a local occurrence of  $\gamma$ -Fe at depths greater than  $\sim 80 \mu\text{m}$  was detected by CSmicroXRD. On the one hand, the heat treatment introduced in [21] indicates a full transformation from retained  $\gamma$ -Fe to  $\alpha'$ -Fe during or after the three tempering cycles. Hence, the presence of  $\gamma$ -Fe prior to the nitriding process can be excluded in the present case. On the other hand, the Fe-C-N phase diagram indicates that the formation of  $\gamma$ -Fe below  $590^\circ\text{C}$  should not be possible, as well as during the nitriding process at  $510^\circ\text{C}$  in the present case. *Jegou et al.* [43] investigated the role of C-diffusion and its impact on the development of residual stresses in differently nitrided ferritic model alloy Fe-3Cr-0.35C (wt.%) samples. A growth of the carbide particles ahead of the nitriding front but no  $\alpha'$ -Fe-to  $\gamma$ -Fe reversion from was documented in their work. In contrast to the model alloy used in [43], W300 contains a significant higher content of  $\sim 1.1$  wt.% Si. [21]. Therefore, the origin of  $\gamma$ -Fe in Fig. 3 is assumed to be correlated with the segregation of  $\gamma$ -Fe stabilizing elements, probably C, at  $\alpha'$ -Fe interlath boundaries in combination with an increased Si-content during the 28 hours low-pressure plasma nitriding at  $510^\circ\text{C}$ . Due to a higher defect density in the (initial) martensitic microstructure of the W300, the diffusivity of interstitial elements is expected to be higher here compared to a ferrite. Additionally, it is worth mentioning that standard laboratory XRD investigations could easily miss the presence of this reverted  $\gamma$ -Fe phase as they are performed at the surface of the sample in reflexion geometry.

Based on the previous aspect, it should be noted, that the origins of  $\gamma$ -Fe formation in the plasma-nitrided W300 steel grade (section 3.1, Fig. 3) and in the low-pressure carburized case hardening steel 18CrNiMo7-6 (section 3.2, Fig. 4) are assumed not to be the same. The gradual formation of *retained*  $\gamma$ -Fe in the carburized case-hardened steel can be

attributed to the elemental C-profile in Fig. 4d and can be understood by the resulting time- and chemistry-dependent reception of the  $\alpha'$ -Fe temperature  $M_s$ . In contrast, in the nitrided sample both, mainly interstitial C and substitutional Mn, are assumed to contribute to the localized occurrence and stabilization of *reverted*  $\gamma$ -Fe.

In the carburized sample, however, a discrepancy in the macro-stress formation was observed for  $\alpha'$ -Fe and  $\gamma$ -Fe phases (Fig. 4c). This effect can be explained as follows: In contrast to the nitrided and the shot-peened samples – which do not exhibit a comparable discrepancy (*cf.* Fig. 3c and 5c) – the carburized sample was tempered at 170°C for ~90 minutes (section 2.1). During this additional tempering cycle  $\alpha'$ -Fe and  $\gamma$ -Fe phases were heated up and expanded. Taking in account a surface carbon content of ~0.67 at.% (Figs. 4d and S10b), linear thermal expansion coefficients for  $\gamma$ -Fe and  $\alpha'$ -Fe can be estimated according to [45], as  $\sim 24.6 \times 10^{-6}$  and  $13.6 \times 10^{-6} \text{ K}^{-1}$ , respectively. This means that the  $\gamma$ -Fe would expand almost twice as much as the  $\alpha'$ -Fe matrix but as the expansion is suppressed by the (harder) matrix,  $\gamma$ -Fe is compressively stressed. Once the yield strength of (the softer)  $\gamma$ -Fe is exceeded, the  $\gamma$ -Fe phase deforms plastically. Consequently, tensile stresses occur in the  $\gamma$ -Fe phase after the final cooling of the material.



## 7.5 Summary and Conclusions

This methodological study introduces correlative cross-sectional micro-analytics based primarily on the application of scanning high-energy synchrotron CSmicroXRD analysis of phases, residual stresses and microstructure, performed in combination with other conventional characterization technologies (like optical and electron microscopy, HV-analysis and electron probe microanalysis). The approach was used to reveal complex structure-property gradients in near-surface regions of three model surface-treated steels. In the technology of surface-treated steel products, the correlative approach and the possibilities of CSmicroXRD will represent an important tool to understand the complex correlations between the applied surface treatment process parameters, the fabricated near-surface gradients and the parts' overall mechanical properties.

This correlative approach was applied to three representative model sample systems. The particular materials science findings of the CSmicroXRD, OM, SEM, micro-HV-profiling and electron probe microanalyses are shortly summarized hereafter.

The near-surface diffusion of N into the plasma-nitrided W300 surface gives rise to a gradual distribution of nitrides and morphological changes in martensite matrix within the  $\sim 80 \mu\text{m}$  thick diffusion zone (Fig. 3). A residual stress profile with two local compressive maxima of  $\sim 765$  and  $\sim 841$  MPa was elucidated and correlates well with the N and C distributions as well as with the resulting width of the diffusion zone, the local occurrence of  $\gamma$ -Fe and the microstructural changes (Fig. 3). The second residual stress maximum can be correlated with the  $\gamma$ -Fe occurrence at the front of the N-diffusion zone. The case hardening depth in a low-pressure carburized 18CrNiMo7-6 steel sample could be correlated with the occurrence of a compressive residual stress peak of  $\sim 682$  MPa (Fig. 4). Again, the diffusion profile of C, obtained by wavelength dispersive X-ray spectroscopy, is related to the gradual change of the retained  $\gamma$ -Fe volume fraction in the near-surface region.

A massive plastic deformation induced by the shot-peening in the near-surface region down to  $\sim 25 \mu\text{m}$  caused a formation of a  $\langle 110 \rangle$ -fibre texture within an initially untextured quenched and tempered 300M steel (Fig. 5). Shot-peening furthermore led to a localized significant decrease in  $\gamma$ -Fe caused by a plastic-strain induced transformation into martensite as well as to the formation of high compressive residual stresses with a stress maximum of  $\sim 1371$  MPa  $\sim 25 \mu\text{m}$  below the surface.

Finally, the work shows that CSmicroXRD in combination with standard laboratory characterization techniques represent a powerful tool to determine complex structure-property correlations within the near-surface regions of mechanically and thermo-chemically treated steels. Cross-sectional investigation of the near-surface

Correlative Cross-Sectional Characterization of nitrided, carburized and shot peened Steels: Synchrotron Micro-X-Ray Diffraction Analysis of Stress, Microstructure and Phase Gradients

---

regions is essential for the understanding of the complex chemical and physical processes occurring in the steels during the surface treatments and can subsequently be used to optimize the particular process recipes.

## Acknowledgements

A part of this work was supported by Österreichische Forschungsförderungsgesellschaft mbH (FFG), Project No. 861496, “CrossSurfaceMech”. Financial support by the Austrian Federal Government (in particular from Bundesministerium für Verkehr, Innovation und Technologie and Bundesministerium für Wissenschaft, Forschung und Wirtschaft) represented by Österreichische Forschungsförderungsgesellschaft mbH and the Styrian and the Tyrolean Provincial Government, represented by Steirische Wirtschaftsförderungsgesellschaft mbH and Standortagentur Tirol, within the framework of the COMET Funding Programme is gratefully acknowledged. Part of the research leading to this result has been supported by the project CALIPSOplus under the Grant Agreement 730872 from the EU Framework Programme for Research and Innovation HORIZON 2020.

## Author's Contributions

S.C.B. performed the XRD experiments at DESY, analysed and interpreted the data from various experimental techniques, visualized the results and coordinated the experimental activities. M.M. supported the XRD experiments at DESY and contributed to the XRD data interpretation. T.Z. performed laboratory experiments on the carburized sample and interpreted these data. H.W. developed the thermo-chemical treatments of the low-pressure plasma nitrided and carburized steels and provided the samples. C.S. developed the peening process and provided the sample. T.H. established the funding of the collaborative research, contributed to the project conceptualization and the project administration. B.S. carried out the EDX analyses in the SEM. W.E. and M.K. developed and performed the FEM model simulation on residual stresses. N.S. developed the XRD set-up and supported the experiments at DESY. J.K. established the funding of the collaborative research, made the project conceptualization and the project administration, organized and coordinated resources and experimental activities. S.C.B. and J.K. wrote the original draft of the manuscript, reviewed and edited it and coordinated the contribution of all other authors.

---

## References

- [1] Schneider MJ, Company TT, Chatterjee MS. Introduction to Surface Hardening of Steels[1]. *Steel Heat Treating Fundamentals and Processes* 2018;4:389–98. <https://doi.org/10.31399/asm.hb.v04a.a0005771>.
- [2] Kratzer D, Dobler F, Tobie T, Hoja T, Steinbacher M, Stahl K. Effects of low-temperature treatments on surface hardness, retained austenite content, residual stress condition and the resulting tooth root bending strength of case-hardened 18CrNiMo7-6 gears. *Proceedings of the Institution of Mechanical Engineers, Part C: Journal of Mechanical Engineering Science* 2019;233:7350–7. <https://doi.org/10.1177/0954406219846160>.
- [3] Kurz SJB, Meka SR, Schell N, Ecker W, Keckes J, Mittemeijer EJ. Residual stress and microstructure depth gradients in nitrided iron-based alloys revealed by dynamical cross-sectional transmission X-ray microdiffraction. *Acta Materialia* 2015;87:100–10. <https://doi.org/10.1016/j.actamat.2014.12.048>.
- [4] Gibmeier J, Rebelo-Kornmeier J, Strauss T. Local Residual Stress Depth Distribution in the Inner Gearing of a Case Hardened Sliding Collar. *Materials Science Forum* 2016;879:601–6. <https://doi.org/10.4028/www.scientific.net/msf.879.601>.
- [5] Benedetti M, Fontanari V, Ho B. Influence of shot peening on bending tooth fatigue limit of case hardened gears. *International Journal of Fatigue* 2002;24:1127–36. [https://doi.org/10.1016/S0142-1123\(02\)00034-8](https://doi.org/10.1016/S0142-1123(02)00034-8).
- [6] Nordin E, Alfredsson B. Experimental Investigation of Shot Peening on Case Hardened SS2506 Gear Steel. *Experimental Techniques* 2017;41:433–51. <https://doi.org/10.1007/s40799-017-0183-4>.
- [7] Scholtes B, Vöhringer O. Ursachen, Ermittlung und Bewertung von Randschichtveränderungen durch Kugelstrahlen. *Materialwissenschaft Und Werkstofftechnik* 1993. <https://doi.org/10.1002/mawe.19930241206>.
- [8] Ebenau A, Lohe D, Vohringer O, Macherauch E. Influence of shot peening on the microstructure and the bending fatigue strength of bainitic-austenitic nodular cast iron. *ICSP 4, The Japan Society of Precision Engineering*; 1990, p. 389–98.
- [9] Merkel J, Schulze V, Vohringer O. The Effects of Shot Peening and Deep Rolling on the Surface Layer and the Mechanical Properties of Sintered Iron. *Icsp-9* 2005;3:241–6.

- [10] Leskovšek V, Podgornik B, Nolan D. Modelling of residual stress profiles in plasma nitrided tool steel. *Materials Characterization* 2008;59:454–61. <https://doi.org/10.1016/j.matchar.2007.03.009>.
- [11] Díaz-Guillén JC, Alvarez-Vera M, Díaz-Guillén JA, Acevedo-Davila JL, Naeem M, Hdz-García HM, et al. A Hybrid Plasma Treatment of H13 Tool Steel by Combining Plasma Nitriding and Post-Oxidation. *Journal of Materials Engineering and Performance* 2018;27:6118–26. <https://doi.org/10.1007/s11665-018-3669-z>.
- [12] Epp J, Hirsch T, Hunkel M, Wimpory RC. Combined Neutron and X-Ray Diffraction Analysis for the Characterization of a Case Hardened Disc. *Materials Science Forum* 2010;652:37–43. <https://doi.org/10.4028/www.scientific.net/msf.652.37>.
- [13] Díaz NEV, Schacherl RE, Zagonel LF, Mittemeijer EJ. Influence of the microstructure on the residual stresses of nitrided iron-chromium alloys. *Acta Materialia* 2008;56:1196–208. <https://doi.org/10.1016/j.actamat.2007.11.012>.
- [14] Christiansen T, Somers MAJ. Avoiding ghost stress on reconstruction of stress- and composition-depth profiles from destructive X-ray diffraction depth profiling. *Materials Science and Engineering A* 2006;424:181–9. <https://doi.org/10.1016/j.msea.2006.03.007>.
- [15] Ericsson T. Residual Stresses Produced by Quenching of Martensitic Steels. vol. 12. Elsevier; 2014. <https://doi.org/10.1016/B978-0-08-096532-1.01209-7>.
- [16] Prevéry PS. X-Ray Diffraction Characterization of Residual Stresses Produced By Shot Peening. *Shot Peening Theory and Application* 1990;c:81–93.
- [17] Ericsson T. Residual Stresses Caused By Thermal and Thermochemical Surface Treatment. 1987;2:31.
- [18] Stefenelli M, Todt J, Riedl A, Ecker W, Müller T, Daniel R, et al. X-ray analysis of residual stress gradients in TiN coatings by a Laplace space approach and cross-sectional nanodiffraction: A critical comparison. *Journal of Applied Crystallography* 2013;46:1378–85. <https://doi.org/10.1107/S0021889813019535>.
- [19] Stefenelli M, Daniel R, Ecker W, Kiener D, Todt J, Zeilinger A, et al. X-ray nanodiffraction reveals stress distribution across an indented multilayered CrN-Cr thin film. *Acta Materialia* 2015;85:24–31. <https://doi.org/10.1016/j.actamat.2014.11.011>.

- [20] Zeilinger A, Todt J, Krywka C, Müller M, Ecker W, Sartory B, et al. In-situ Observation of Cross-Sectional Microstructural Changes and Stress Distributions in Fracturing TiN Thin Film during Nanoindentation. *Scientific Reports* 2016;6. <https://doi.org/10.1038/srep22670>.
- [21] Medvedeva A, Andersson J, Robertsson R, Nilsson C, Ejnermark S. W300 - Hot work tool steel 2019:6.
- [22] Deutsche-Edelstahlwerke. Carbodur 6587 - Werkstoffdatenblatt 18CrNiMo7-6, 1.6587. 2016.
- [23] BÖHLER High Performance Metals International GmbH V. 300M - Böhler V132 data sheet 2020. [www.bohler.at/austria/de/products/v132/](http://www.bohler.at/austria/de/products/v132/) (accessed March 28, 2020).
- [24] Almen JO, Black PH. *Residual Stresses and Fatigue in Metals*. New York: McGraw-Hill; 1963.
- [25] Schell N, King A, Beckmann F, Ruhnau HU, Kirchhof R, Kiehn R, et al. The High Energy Materials Science Beamline (HEMS) at PETRA III. *AIP Conference Proceedings*, 2010. <https://doi.org/10.1063/1.3463221>.
- [26] Kieffer J, Karkoulis D. PyFAI, a versatile library for azimuthal regrouping. *Journal of Physics: Conference Series* 2013;425. <https://doi.org/10.1088/1742-6596/425/20/202012>.
- [27] Geandier G, Vautrot L, Denand B, Denis S. In situ stress tensor determination during phase transformation of a metal matrix composite by high-energy X-ray diffraction. *Materials* 2018;11:1–19. <https://doi.org/10.3390/ma11081415>.
- [28] Noyan IC, Cohen JB. *Residual Stress - Measurement by Diffraction and Interpretation*. 1987. <https://doi.org/10.1002/crat.2170240228>.
- [29] Heidelbach F, Riekkel C, Wenk HR. Quantitative texture analysis of small domains with synchrotron radiation X-rays. *Journal of Applied Crystallography* 1999;32:841–9. <https://doi.org/10.1107/S0021889899004999>.
- [30] Dölle H. The influence of multiaxial stress states, stress gradients and elastic anisotropy on the evaluation of (Residual) stresses by X-rays. *Journal of Applied Crystallography* 1979. <https://doi.org/10.1107/S0021889879013169>.
- [31] Renault PO, Le Bourhis E, Villain P, Goudeau P, Badawi KF, Faurie D. Measurement of the elastic constants of textured anisotropic thin films from x-ray diffraction data. *Applied Physics Letters* 2003;83:473–5. <https://doi.org/10.1063/1.1594280>.

- [32] Vermeulen AC. an Elastic Constants Database and Xec Calculator for Use in Xrd Residual Stress Analysis. *Advances in X-Ray Analysis* 2001;44:128–33.
- [33] Kim SA, Johnson WL. Elastic constants and internal friction of martensitic steel, ferritic-pearlitic steel, and  $\alpha$ -iron. *Materials Science and Engineering A* 2007;452–453:633–9. <https://doi.org/10.1016/j.msea.2006.11.147>.
- [34] ASTM International. Standard Practice for X-Ray Determination of Retained Austenite in Steel with Near Random Crystallographic Orientation 1. *Astm* 2009. <https://doi.org/10.1520/E0975-13>.
- [35] Lerchbacher C, Zinner S, Leitner H. Atom probe study of the carbon distribution in a hardened martensitic hot-work tool steel X38CrMoV5-1. *Micron* 2012;43:818–26. <https://doi.org/10.1016/j.micron.2012.02.005>.
- [36] Mesquita RA, Barbosa CA, Morales E V, Kestenbach H. Effect of Silicon on Carbide Precipitation after Tempering of H11 Hot Work Steels. *Metallurgical and Materials Transactions A* 2011;42:461–72. <https://doi.org/10.1007/s11661-010-0430-0>.
- [37] Michaud P, Delagnes D, Lamesle P, Mathon MH, Michaud P, Delagnes D, et al. The effect of the addition of alloying elements on carbide precipitation and mechanical properties in 5 % chromium martensitic steels To cite this version : HAL Id : hal-01715082 The effect of the addition of alloying elements on carbide precipitation a 2019.
- [38] Scherrer P. Bestimmung der Größe und der inneren Struktur von Kolloidteilchen mittels Röntgenstrahlen. *Nachrichten von Der Gesellschaft Der Wissenschaften Zu Göttingen, Mathematisch-Physikalische Klasse* 1918;2:98–100. <https://doi.org/10.1007/978-3-662-33915-2>.
- [39] Tier MA, Kieckow F, Strohaecker TR, Da Silva Rocha A, Bell T. A study of carbon redistribution during plasma nitriding of steel. “Proceedings - 15th IFHTSE - International Federation for Heat Treatment and Surface Engineering Congress 2006” 2006:193–9.
- [40] Barrallier L. Classical nitriding of heat treatable steel. Woodhead Publishing Limited; 2015. <https://doi.org/10.1533/9780857096524.3.393>.
- [41] Dieck S, Rosemann P, Kromm A, Halle T. Reversed austenite for enhancing ductility of martensitic stainless steel. *IOP Conference Series: Materials Science and Engineering* 2017;755. <https://doi.org/10.1088/1757-899X/181/1/012034>.

- 
- [42] Raabe D, Sandlöbes S, Millán J, Ponge D, Assadi H, Herbig M, et al. Segregation engineering enables nanoscale martensite to austenite phase transformation at grain boundaries: A pathway to ductile martensite. *Acta Materialia* 2013;61:6132–52. <https://doi.org/10.1016/j.actamat.2013.06.055>.
- [43] Jegou S, Barrallier L, Kubler R, Somers MAJ. Evolution of residual stress in the diffusion zone of a model Fe-Cr-C alloy during nitriding. *HTM - Haertereitechnische Mitteilungen* 2011;66:135–42. <https://doi.org/10.3139/105.110104>.
- [44] Marion RH, Cohen JB. The need for experimentally determined X-ray elastic constants. *Advances in X-Ray Analysis* 1976;20: Twenty:355–67. <https://doi.org/doi.org/10.1154/S0376030800011964>.
- [45] Lee SJ, Lusk MT, Lee YK. Conversional model of transformation strain to phase fraction in low alloy steels. *Acta Materialia* 2007;55:875–82. <https://doi.org/10.1016/j.actamat.2006.09.008>.





# Influence of Hatch Strategy on Crystallographic Texture Evolution, Mechanical Anisotropy of Laserbeam Powder Bed Fused S316L Steel

Sabine C. Bodner<sup>1,\*</sup>, Kostyantyn Hlushko<sup>1</sup>, Kevin Kutleša<sup>1</sup>, Juraj Todt<sup>1</sup>, Oliver Renk<sup>1,4</sup>, Michael Meindlhumer<sup>1</sup>, Florian Resch<sup>2</sup>, Marc-André Nielsen<sup>3</sup>, Jozef Keckes<sup>1</sup>, Jürgen Eckert<sup>1,4</sup>

<sup>1</sup> Montanuniversität Leoben, Department of Materials Science, Chair of Materials Physics, 8700 Leoben, Austria

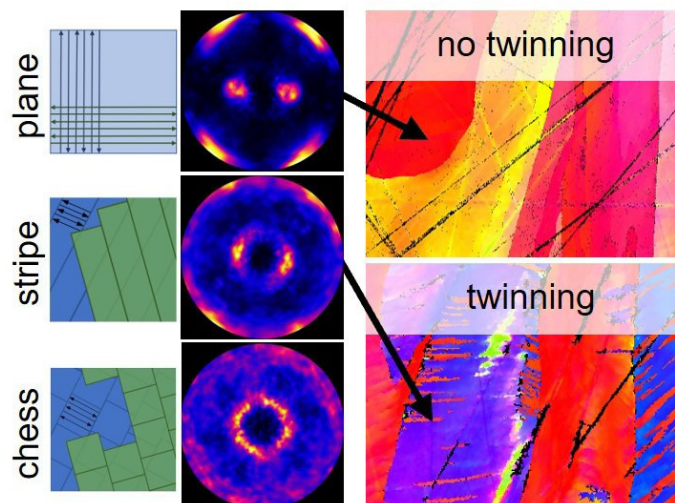
<sup>2</sup> Resch GmbH, 8421 Glojach, Austria

<sup>3</sup> Helmholtz-Zentrum Hereon GmbH, Outstation at DESY, 22607 Hamburg, Germany

<sup>4</sup> Erich Schmid Institute of Materials Science, Austrian Academy of Sciences, 8700 Leoben, Austria

## Graphical Abstract

S316L - Laserbeam Powder Bed Fusion  
Three hatch styles – different deformation



## Abstract

The correlations between process conditions, microstructure and mechanical properties of additively manufactured components are not fully understood yet. In this contribution, three different hatch strategies are used to fabricate rod-like samples from S316L stainless steel, which are further investigated using synchrotron diffraction, optical microscopy and tensile tests. The results indicate the presence of  $\langle 110 \rangle$  biaxial and fiber textures, whose sharpness depends on the applied hatch strategy. Mechanical tests reveal a strong correlation of the samples' response to the observed anisotropy in the plane perpendicular to the build direction. Even though the average yield and ultimate tensile strengths of around 475 and 500 MPa, respectively, do not differ significantly, the stress-strain behavior can be correlated to the observed in-plane anisotropy. Particularly, twinning induced plasticity, a distinct increase of the work hardening rate at larger strains and elliptical necking are observed in some samples with biaxial (Goss) texture. These findings indicate that texture design by means of applying dedicated hatch strategies can be used to effectively tune the multiaxial deformation behavior of components produced by laser powder bed fusion.

**Keywords:** additive manufacturing, powder bed fusion, hatch strategies, textures, TWIP, stainless steel, anisotropy

## 9.1 Introduction

S316L stainless steel with face-centered cubic crystal structure has been widely applied in aerospace, nuclear, medical and petroleum industries mainly due to its excellent corrosion resistance, high strength, good biocompatibility and weldability as well as excellent strength-ductility trade-off [1,2]. Various conventional production routes like casting, sintering and forging have been used to produce structural components, coronary stents, pipelines, marine applications *etc.* [1,3].

Due to its excellent processability, S316L austenitic steel has become also a popular material used in additive manufacturing technology, which provides a unique opportunity for designing complex structural components at minimal material consumption [4]. For this purpose, especially the laser powder bed fusion (PBF-LB) has been applied [5,6].

There have been numerous studies analyzing the correlations between applied PBF-LB process conditions, internal microstructure, residual stresses, corrosion behavior, fatigue properties and local as well as overall mechanical properties. Furthermore, different mathematical models have been established to predict the process conditions and simulate the influence of different laser spot sizes and laser power [7], scanning speed [8], defocus distances [9] and other. The simulations were validated also by experiments. The efforts have been motivated mainly by the fact that PBF-LB manufactured S316L parts exhibit better structural and functional properties like strength, toughness and corrosion resistance, than their conventionally produced counterparts [10]. It was observed that the local microstructure depends strongly on the energy delivered by the laser system, where high (typically 1000 W) or low (400 W) energies result in the formation of large elongated vs. small equiaxed grains, respectively [11]. Similarly, the application of various laser scanning modes, called *hatch strategies*, was found to influence the evolution of preferred  $\langle 100 \rangle$  and/or  $\langle 110 \rangle$  fibre textures and, consequently, also anisotropic mechanical properties. Kumar *et al.* [1] applied four different hatch styles, whose complexity scaled with increasing compressive strength, grain morphology and texture. Kurzynowski *et al.* [12] reported that the hatch strategy and laser power strongly affect the grain substructure of the austenite, the amount of ferrite and the crystallographic texture. Stress relieving experiments at 500°C induced changes in the microstructure, which resulted in decreased strength [12]. Similarly, Greco *et al.* [13] demonstrated that the input energy density alone is not enough as an indicator for the resulting work piece characteristics, but rather the ratio of scanning speed, layer thickness and hatch spacing to the laser power. Consequently, it was shown that smaller hatch spacings translated to a more homogeneous microstructure, and to some extent to a denser material [10,13]. Moreover, it was found that the hatch strategy has also a significant effect on the internal

porosity and surface quality [5,14–16], which correlate with the mechanical properties, especially the fatigue behaviour [6]. Larimian *et al.* [15] analysed the influence of three hatch strategies on the densification, microstructure and tensile properties of S316L and reported that the best mechanical properties (yield strength, ultimate tensile strength, and elongation as well as microhardness) were obtained for a hatch strategy with rectangular alternating hatches and a single pass of the laser beam.

To further enhance mechanical properties and materials' performance of S316L of the material, different metal-matrix composites were fabricated by PBF-LB and characterized. AlMangour *et al.* [17] investigated the influence of four different hatch strategies to tailor textures in LB-PB fused TiC/S316L composites. Interestingly, the analysis of texture coefficients in their study revealed a reduced, almost random crystal orientation when they applied a hatch strategy which is similar to the *plane* type used in the present study. In another study, AlMangour *et al.* [18] focussed on enhanced compressive mechanical properties of TiC reinforced S316L. They varied the size of the ceramic particles and revealed a significantly lower anisotropy in nano-TiC composites, where nanoscaled TiC led further to a grain refinement. In similar studies, Zhou *et al.* [16] showed that the tensile properties of the Ti–22Al–25Nb intermetallic compound depends decisively on the hatch distance selected from the range of 0.08 - 20 mm. Robinson *et al.* [19] performed an extensive analysis of the influence of hatch strategies on density, surface roughness, tensile strength and residual stress for pure titanium and indicated a strong dependence of the elongation-to-failure on the hatching angles between subsequent layers.

In general, the previous reports on the correlations between process conditions, internal microstructure and mechanical properties of S316L steel and other metallic systems indicate that the hatch strategy plays a crucial role in the compressive and tensile response of additively manufactured work pieces. Currently, the effect of the hatch style has still not been fully understood yet, especially due to (i) the large variability of possible hatch strategies (including the hatch distance  $h$ , laser movement vector and mutual lateral and vertical orientation of the neighbouring hatches), and (ii) a relatively large range of applicable laser energies ( $P$ ), speeds ( $s$ ) and the range of layer thicknesses  $t$ , which decisively influence the anisotropic mechanical response of the components nevertheless still leading to fully dense synthesized parts. Therefore, the volumetric energy density  $VED = P/(h \cdot s \cdot t)$  alone is not the sole parameter determining the mechanical behaviour of additively manufactured work pieces.

In this contribution, three hatch strategies were applied to fabricate S316L cylindrical samples while the VED was kept constant. Subsequently, synchrotron X-ray diffraction, tensile tests and scanning electron microscopy were used to obtain a correlation between the samples' texture and mechanical properties, respectively. The results indicate

complex process-microstructure-property correlations with both isotropic and anisotropic properties in the build plane of the samples.

## 9.2 Experiments and methods

### 9.2.1 Sample Preparation by PBF-LB

Two different geometries of steel rods with dimensions of about  $\varnothing 5 \times 40 \text{ mm}^2$  and  $\varnothing 9 \times 70 \text{ mm}^2$ , were synthesized using an EOS M290 (Krailling, Germany) PBF-LB device. Commercial 316L powder obtained from m4p material solutions GmbH (Feistritz, Austria), suitable for processing via PBF-LB (i.e. with a particle size distribution of about 15 to 45  $\mu\text{m}$ ) was used for the experiments. The samples were built using EOS standard parameters for laser power, scan speed, hatch distance and layer thickness under argon atmosphere. Three different hatch styles were applied, as indicated in Figure 1. The resulting hatch strategies will be further denoted as plane, stripe and chess. In total, three  $\varnothing 5 \text{ mm}$  cylinders (one for each hatch style) and nine  $\varnothing 9 \text{ mm}$  cylinders (three for each hatch style) were fabricated.

#### Plane Style

The powder was laser-melted across the whole cross-section using a bi-directional scanning strategy (Figure 1a). The angle between a subjacent layer  $n$  and the following layer  $n+1$  was chosen to be 90 degrees.

#### Stripe Style

The powder was laser-melted in a stripe-like pattern with a stripe width of about 5 mm and a length exceeding the respective cross-section of the sample (Figure 1d). The angle between a subjacent layer  $n$  and the following layer  $n+1$  was chosen to be 67 degrees and a bi-directional scanning strategy [20] was applied.

#### Chess Style

The powder was laser-melted in small islands, each  $3 \times 3 \text{ mm}^2$  in size. Within these squares, a bi-directional scanning strategy was applied (Figure 1g). The angle between a subjacent layer  $n$  and the following layer  $n+1$  was set to 67 degrees.

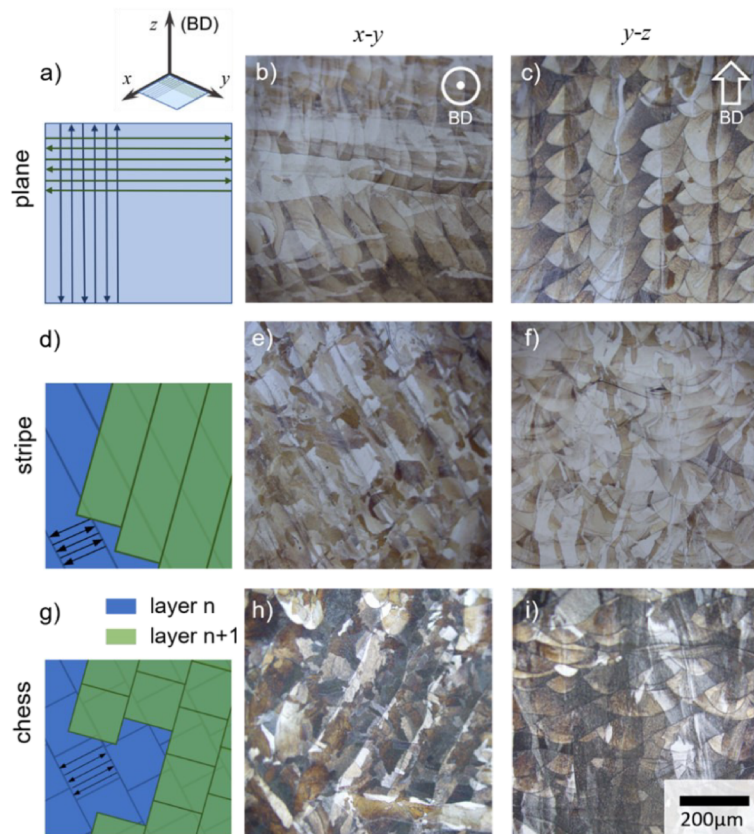


**Figure 1.** Schematic description of the three hatch strategies named *plane*, *stripe* and *chess* in the build plane ( $x$ - $y$ ), perpendicular to the build direction (BD) (a, d, g). The corresponding optical micrographs show the microstructure for *plane*, *stripe* and *chess* hatch strategies in the  $x$ - $y$  (b, e, h) and  $y$ - $z$  (c, f, i) planes, which are oriented perpendicular and parallel to the BD respectively.

## 9.2.2 Optical Microscopy

Cross-sections oriented perpendicular (Figure 1b, e, h) and parallel to the build direction (Figure 1c, f, i) were prepared for each of the three sample types. For this purpose, the specimens were cut in a first step using a precision cutting machine Secotom (Struers, Willich, Germany). Afterwards, the sample pieces were hot-embedded (15 bar, 180°C, 15 minutes) in a phenol resin, type Polyfast (Struers), ground and polished. The last polishing step was performed with a 0.04  $\mu\text{m}$  colloidal Si suspension (type OP-S, Struers). Subsequently, the V2A etched samples were examined by optical microscopy using an Olympus BX51, equipped with a Tango Desktop high resolution  $x$ - $y$ - $z$  stepper motor controller (Märzhausen-Wetzlar, Wetzlar, Germany) and an active vibration isolation desktop unit Halcyonics\_i4 (Accurion, Göttingen, Germany).

Porosities of the samples were determined at the metallurgical cross-sections. The size of the region of interest was set to 5 $\times$ 5 mm<sup>2</sup> and the area was scanned with a magnification

of 100. The porosity function of StreamMotion (Olympus) was used to evaluate the images.

### 9.2.3 Scanning Electron Microscopy

Unetched cross-sections and representative fracture surfaces of the tensile samples were investigated by scanning electron microscopy (SEM) for each sample type.

The microstructures and fracture surfaces of the specimens were examined using a Zeiss LEO 1525 SEM equipped with an in-lens, a secondary electron and a back-scattered electron (BSE) detector. Images of the cross-sections were recorded with the BSE detector. The acceleration voltage and the aperture width were set to 20 kV and 60  $\mu\text{m}$ , respectively.

Images of the fracture surfaces were acquired using the in-lens detector. The acceleration voltage and the aperture width were set to 5 kV and 30  $\mu\text{m}$ , respectively.

Electron backscatter diffraction (EBSD) investigations were performed using a Tescan Magna SEM (Tescan, Brno, Czech Republic), equipped with an eFlash FS detector (Bruker, Germany). The acceleration voltage of the electron gun and the probe current were set to 30 kV and 10 nA. The Bruker Esprit 2.3 software was used for post-processing of the EBSD data.

### 9.2.4 Synchrotron Experiments

Synchrotron experiments were performed at the high energy materials science (HEMS) beamline P07 [21] of the PETRA III storage ring at Deutsches Elektronensynchrotron (DESY, Hamburg). Figure 2 illustrates a simplified schematic experimental set-up. The highly brilliant synchrotron X-ray beam with an energy of 87.1 keV, corresponding to a wavelength of 14.25 pm, was collimated to  $0.7 \times 0.7 \text{ mm}^2$ . The as-built steel rods were scanned in transmission diffraction geometry with the X-ray beam oriented perpendicular to their cylinder axis. During the experiments, the  $\emptyset$  5 mm sample cylinders were rotated using an increment  $\Delta\omega$  of 2 degrees in the angular range of 0 to 180 degrees (Figure 2). At each sample position, a two-dimensional (2D) diffraction pattern was recorded by a Perkin Elmer XRD 1621 detector (Perkin Elmer, Waltham, USA) with a pixel pitch of 200  $\mu\text{m}$ . The distance between the sample and the detector of 1.3757 m was calibrated with a  $\text{LaB}_6$  powder standard.

## Texture Analysis

The collected data were further processed using the Python software package *pyFAI* [22]. Individual *hkl* Debye-Scherrer (D-S) rings 111, 200, 220 and 311 in every 2D pattern were radially integrated to obtain azimuthal angle  $\delta$  distributions of diffraction intensities  $I_{hkl}(\delta)$  with  $\Delta\delta$  steps of 1 degree. Subsequently, pole figures and inverse pole figures were generated from the integrated  $I_{hkl}(\delta)$  data by applying self-created MATLAB scripts for the MTEX software package [23].

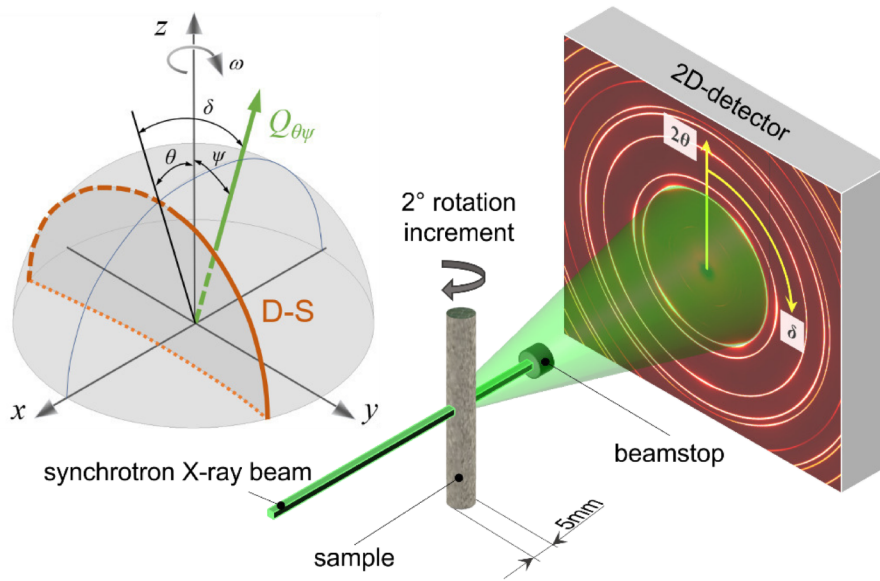


**Figure 2.** Non-proportional schematic description of the experimental setup used to analyse the texture in transmission diffraction geometry at the HEMS beamline and a 3D sketch showing the coordinate system and the orientation relations of a stereographic projection with an exemplary Debye-Scherrer ring (D-S). Steel rods with a diameter of 5 mm were rotated around the  $\omega$  axis using an increment of 2 degrees. At every sample position, 2D diffraction patterns were collected and further used to calculate pole figures by analysing diffraction intensities as a function of the azimuthal angle  $\delta$  of the particular D-Ss.  $\theta$  represents Bragg's diffraction angle and  $\psi$  represents the angle between the sample normal direction and the diffraction vector  $Q_{\theta\psi}$ .

## Residual Stresses

X-ray data were furthermore used to determine first-order residual strains in the samples. For this, the signal of the 311 D-S-ring of each sample and each pattern was azimuthally integrated in the range of  $0 < \delta < 360$  degrees in 36 sections, each of  $\Delta\delta = 10$  degrees in width. After fitting, orientation-dependent lattice parameters  $d_{\delta\theta}^{hkl}(y, z)$  and subsequently the residual strains prevailing in the samples were calculated by applying the  $\sin^2\psi$  method [24]. By using the X-ray elastic constant  $\frac{1}{2}S_2 = 6.701 \times 10^{-6} \text{ MPa}^{-1}$  - calculated by the applying the *Eshelby-Kröner* [25] model on the basis of Ref. [24] - residual stresses were estimated from the experimentally determined values in the next step. The method is described in detail in Refs. [26–29].



### 9.2.5 Tensile Tests

Tensile samples with a circular cross-section and a gauge volume according to DIN EN ISO 6892-1 ( $\varnothing 5 \times 25 \text{ mm}^3$ ) were fabricated from the  $\varnothing 9 \text{ mm}$  cylinders to further assess the mechanical properties, namely the yield strength  $R_{p0.2}$  and the ultimate tensile strength  $R_m$ . Classic quasi-static tensile tests were performed at room temperature using a Z100 AllroundLine testing device (ZwickRoell, Ulm, Germany). The device was equipped with an optical extensometer which allowed for contactless and precise measurement of the elongation. Constant strain rates of  $0.0025$  and  $0.006 \text{ s}^{-1}$  were applied in the elastic and plastic regions, respectively, for each type of hatch strategy. Further relevant test conditions were directly preset in the ZwickRoell standard test program textXpert. A self-created Python script was used to evaluate the data and derive the mechanical properties of the samples.

True stress and true strain values,  $\sigma_t$  and  $\varepsilon_t$ , respectively, were evaluated according to Ref. [30].

The fractured samples surfaces were further scanned using an Accura (Carl Zeiss, Oberkochen, Germany) coordinate measuring device, equipped with a LineScan 2-50 optical scanner and operated via the software package Calypso (Zeiss). The sensitivity was set to maximum, which allowed to determine the surface via a point cloud with an accuracy of  $20 \mu\text{m}$ .

### 9.3 Results and Discussion

Optical micrographs of the cross sections of the three sample types, oriented parallel ( $y$ - $z$  plane) and perpendicular ( $x$ - $y$  plane) to the build direction (BD), are presented in Figure 1. Optical micrographs with a higher magnification are provided in Figure S1 of the supplementary data. No significant microscopic defects like pores or cracks are visible.

The porosities of the *plane*, *stripe* and *chess* samples were evaluated to be 0.02, 0.03 and 0.02 %, respectively, and no correlation with the scan strategy could be determined. Similarly, we did not observe any differences in the oxides. The micrographs showing cross-sectional planes ( $y$ - $z$ ) exhibit regular melt-pool boundaries for the *plane* sample and a more random cross-sectional morphology for the other two types of samples. Similarly, the complementary micrographs from the  $x$ - $y$  plane indicate quite aligned grain microstructures of the top layer with individual melt-pool boundaries. The remarkable difference between the *plane* samples and the other two types of samples can be explained by the use of the non-orthogonal hatching modes in the case of *stripe* and *chess* samples (*cf.* Figure 1).

Differences in microstructural morphologies are further visible in the SEM images of Figure 3 for the as-built and deformed states of the *plane*, *stripe* and *chess* sample types. Images taken by the backscatter electron (BSE) detector, sensitive to  $Z$  and orientation contrast of the investigated area, indicate clear differences especially in the deformed microstructures (Figures 3b, d and f). Pronounced twinning induced by plastic deformation was observed in the *stripe* sample. We further used EBSD to investigate the deformed region of the *plane* and *stripe* samples. Inverse pole figure maps are presented in the supplementary data, Figure S3 and Figure S5, and underline the effect of deformation twinning in the *stripe* sample. This phenomenon was also reported by Pham *et al.* [31] for LB-PB fused 316L. The authors assumed that twinning occurred due to the fact that their samples were synthesized in a nitrogen atmosphere. Our present study, however, indicates that deformation twinning in 316L must have a different reason as, in contrast, the *plane* and *chess* samples exhibit a fine-grained microstructure and in case of the *plane* sample, a typical sub-grain cell structure could even be determined in the deformed region.

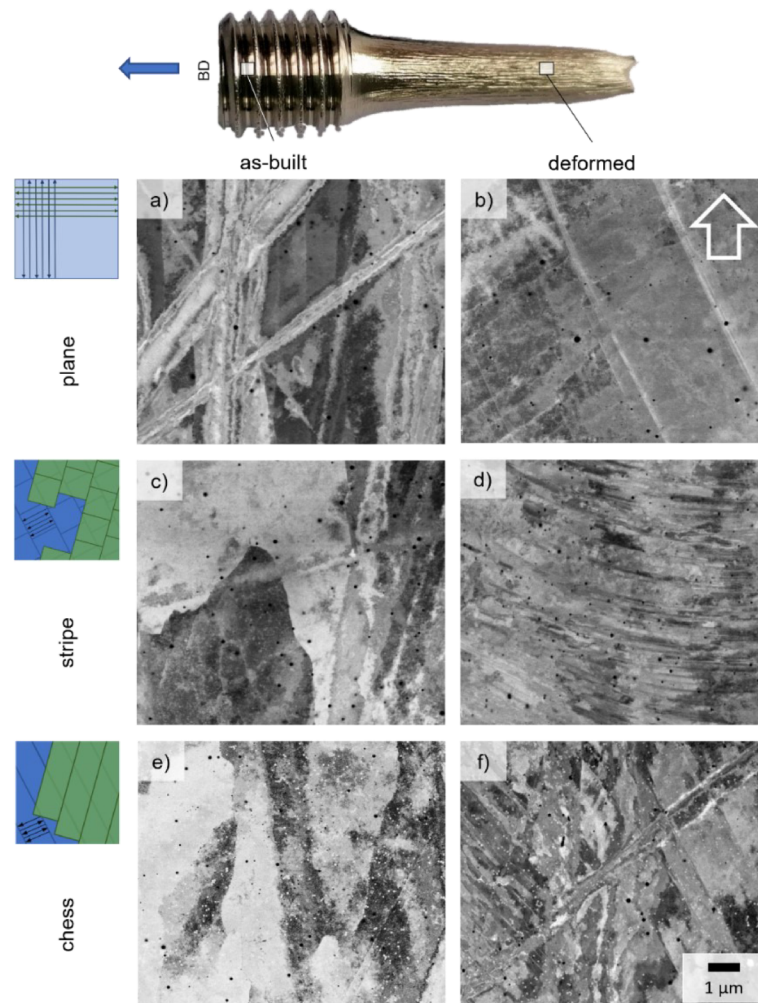


**Figure 3.** SEM-BSE images of the cross-sections in the as-built and deformed regions of the plane (a and b), stripe (c and d) and chess (e and f) samples indicate differences in the microstructures of the specimens. The white arrow in (b) indicates the building direction BD. The microstructure of the deformed region of stripe (d) and its comparison with the as-built state (c) indicates pronounced deformation twinning – an effect that was not observed for the plane and chess samples.

An average grain size of about 211, 158 and 185  $\mu\text{m}$  for the *plane*, stripe and chess samples was determined by EBSD. The corresponding IPF maps are presented in Figure S2, Figure S4 and Figure S6 in the supplementary data.

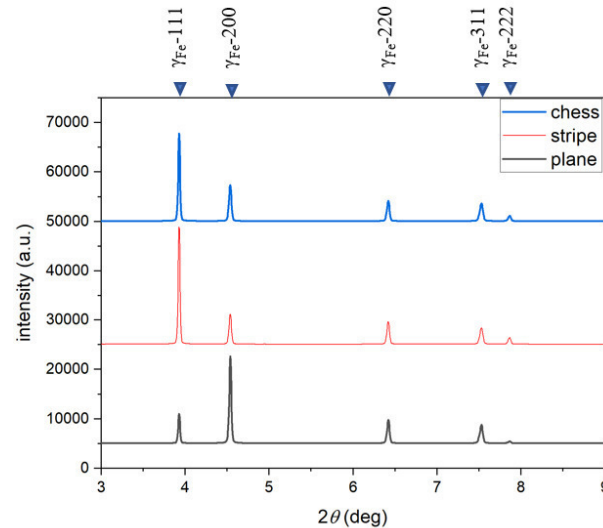


**Figure 4.** Integrated X-ray diffraction data obtained from the 2D diffraction patterns, indicating the presence of a face-centred cubic phase in the *plane*, *stripe* and *chess* style samples. The differences in the austenite peak intensities are caused by the sample's textures.

Figure 4 shows X-ray diffraction patterns obtained from the synchrotron 2D diffraction data. All three types of samples consist exclusively of iron austenite with a face-centered cubic crystal structure. The differences in the peak intensities can be mainly attributed to the expected crystallographic texture induced by the three different hatch strategies. As a measure of peak widths, the average FWHM of the 311 peak was evaluated for all sample types.

The analysis revealed the following results:  $FWHM_{\text{plane}}^{311} = 0.0385 \pm 0.011$  deg,  $FWHM_{\text{stripe}}^{311} = 0.0370 \pm 0.008$  deg,  $FWHM_{\text{chess}}^{311} = 0.0380 \pm 0.07$  deg. FWHM values can be used to estimate the size of coherently diffracting domains according to the Scherrer's equation [32]. Moreover, the peak width is influenced also by residual micro-stresses.

In general, residual stresses of first, second and third order influence the position and shape of diffraction peaks. First order residual stresses result in an elliptical deformation of Debye-Scherrer rings, recorded by the 2D detector. Therefore, the 360° azimuthal integration results in principle in a broadening of the peaks presented in Figure 4.

Residual stresses of second- and third-order (micro-stresses) and the change of the domain size of coherently diffracting domains also contribute to peak broadening. As a result of superposition of all these effects, micro-stresses cannot be reliably assessed from the presented data.

Residual stress analysis indicates the presence of first-order stresses of about  $184 \pm 79$  MPa for the *plane* sample whereas stresses in the *stripe* and *chess* samples are comparable with  $271 \pm 36$  and  $280 \pm 29$  MPa, respectively.

In Figure 5 and Figure 6, pole figures and inverse pole figures, respectively, generated from the synchrotron data are presented. The inverse pole figures in  $z$  direction document a preferred  $\langle 110 \rangle$  orientation of the crystallites with respect to the BD. This type of texture is very common in S316L parts and has been reported before [1,33]. Pole figures and inverse pole figures illustrate the orientation of crystallites in the plane ( $x$ - $y$ ) perpendicular to the BD (Figure 1). In the case of the *plane* sample, the two-fold symmetry of the pole figures correlates well with the applied hatch strategy (of two perpendicularly moving laser beams) and is usually denoted as Goss texture with the  $\{110\}$  planes lying in the sample's  $x$ - $y$  plane. This sample possessed the most pronounced out-of-plane orientation among the three sample types. For the *stripe* sample, the in-plane orientation of the crystallites is more random, compared to the *plane* samples, but still biaxial and more pronounced than in the out-of-plane orientation. In the *chess* samples, the preferred orientation appears as a nearly perfect fiber texture with a random in-plane orientation of the crystallites, again with the  $\{110\}$  planes lying in the sample  $x$ - $y$  plane. In general, the texture data presented in Figure 5 and Figure 6 document an anisotropy of the samples in the plane perpendicular to the BD for the *plane* and *stripe* samples.

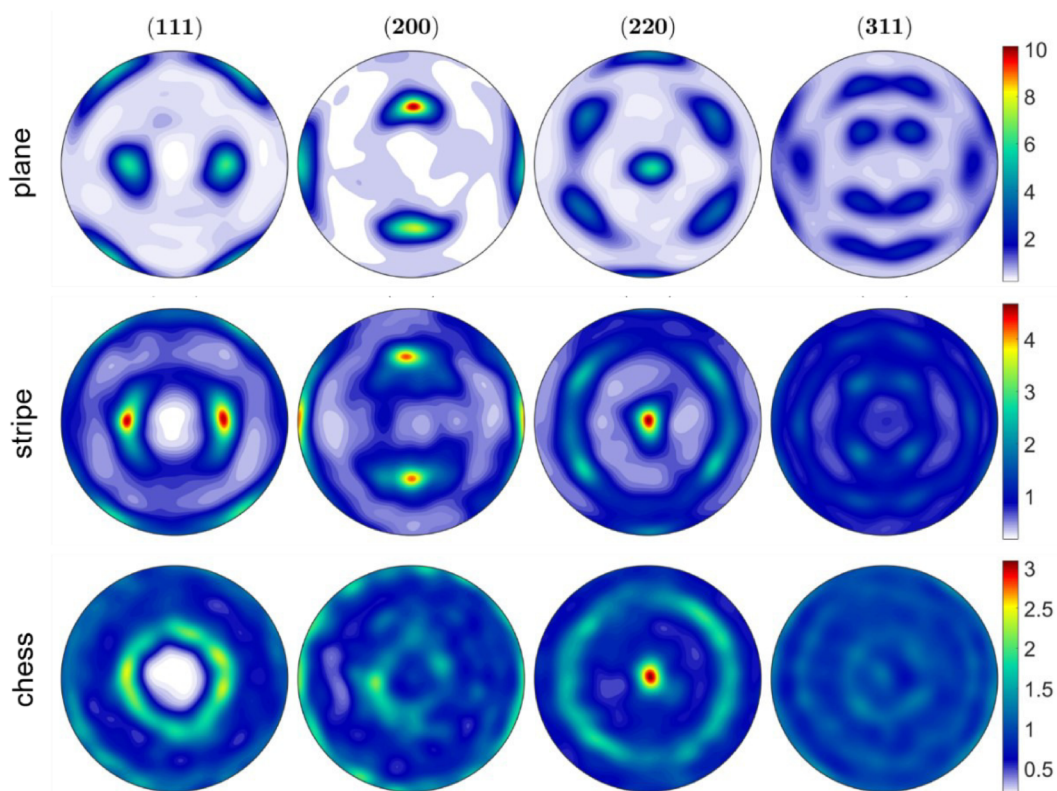


**Figure 5.** 111, 200, 220 and 311 pole figures evaluated from the synchrotron data of *plane*, *stripe* and *chess* samples, revealing a strong dependence of crystallographic textures of the different samples on the applied hatch strategy. Biaxial textures are observed for the *plane* and *stripe* hatching styles and a nearly perfect fibre texture is found for the *chess* type.

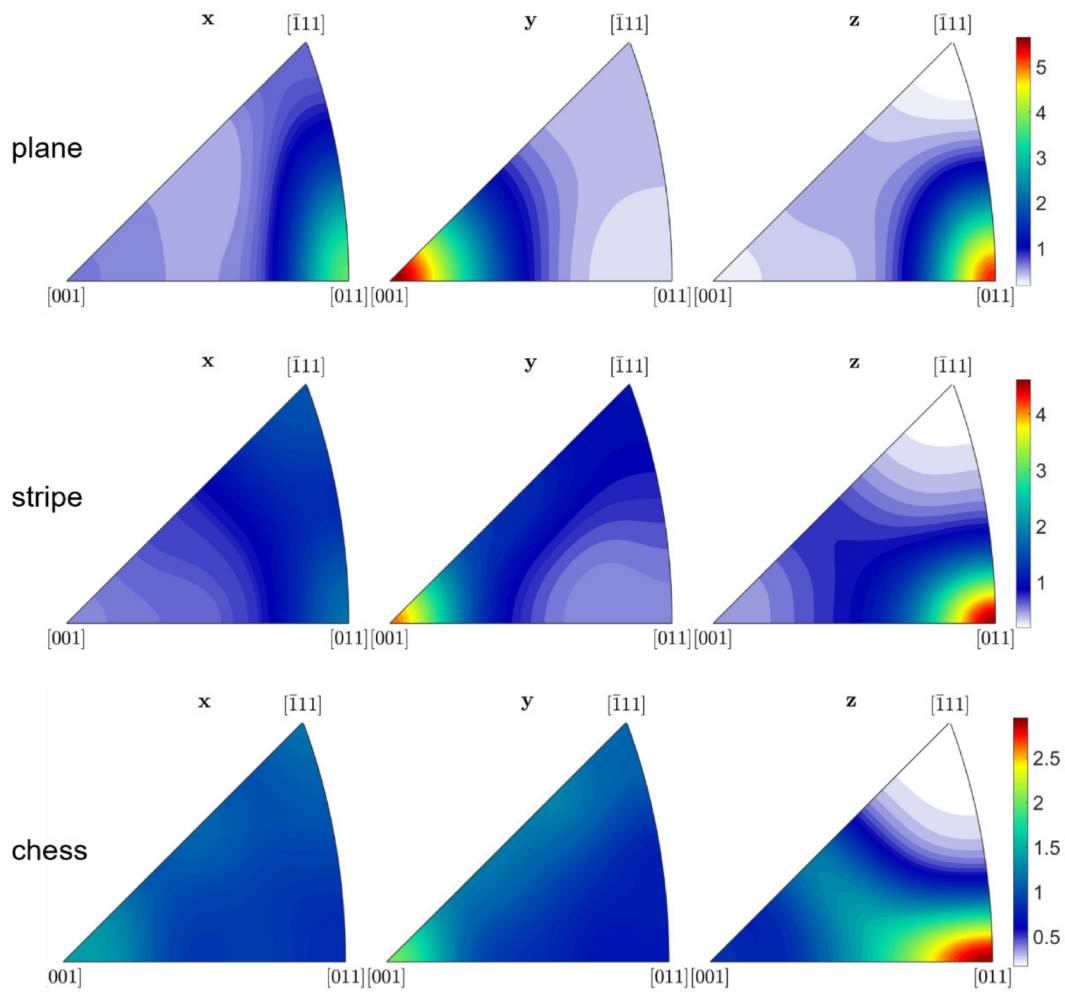


**Figure 6.** Inverse pole figures evaluated from the synchrotron data of *plane*, *stripe* and *chess* samples with respect to the samples' two in-plane directions ( $x$ ,  $y$ ) and the build direction ( $z$ ). The plots indicate a  $\langle 110 \rangle$  preferred orientation in all three types of samples with respect to the build direction  $z$ . The  $x$  and  $y$  inverse pole figures indicate a pronounced, a comparatively weaker and an almost random preferred orientation of crystallites in the  $x$ - $y$  plane for the *plane*, *stripe* and *chess* sample types, respectively.

Figure 7 shows representative stress-strain curves recorded during the tensile experiments for the *plane*, *stripe* and *chess* samples, respectively. A yield strength  $R_{p0.2}$  of about 475 MPa, and an ultimate tensile strength  $R_m$  of about 550 MPa can be deduced. These very similar yield strengths can be interpreted as indirect measure of a comparable initial dislocation density and/or comparable size of grains or cells within the grains whereas the individual influence cannot be estimated. The stress-strain behavior of the *stripe* samples is obviously different from the other two types (*plane* and *chess*, Figure 7a and Figure 7c, respectively). In particular, the *stripe* samples (Figure 7b) exhibit an increase of the work hardening rate starting at an engineering strain of about 40% and, consequently, a higher fracture strain. The plastic deformation of these samples occurs in two stages, which are discussed below. To understand the different deformation mechanisms within the sample, previously described results as well as the work hardening

curves, illustrated in Figure 8 must be taken into account. At first, the samples are deformed elliptically in the  $x$ - $y$  plane and subsequently elongated further and deformed plastically along the BD. During this stage, twinning is induced in the austenite grains (supplementary data, Figure S5) and is expected to be the dominant deformation mechanism. This phenomenon is known as transformation induced plasticity (TWIP-effect) [34–36], and leads to the possibility of extended plastic deformation in S316L [31]. Additionally, due to the  $\{110\}/[001]$  texture in the *stripe* sample,  $\{110\}$  and  $\{100\}$  lattice planes are oriented parallel and perpendicular to the loading direction which corresponds also to the BD. Due to the anisotropic stiffness and plastic deformation of the particular crystallographic planes, this leads to an inherent macroscopic elasto-plastic anisotropy in the respective sample directions. In other words, the uniaxially loaded *stripe* samples are about 30% stiffer in their out-of-plane direction (which is the BD in the present case) compared to their in-plane ( $x$ - $y$ ) direction. As a result, the initially circular cross-section deforms to an ellipse. Although this hypothesis could explain the anisotropic behavior, other reasons need to play an important role as well as otherwise, a similar ellipticity would be expected for the *plane* samples (as they possess an even more pronounced in-plane texture).

Mechanical twinning was reported to occur in fcc-alloys (especially in high Mn-steels) with a low stacking fault energy  $\gamma_{SF}$  of roughly  $18 \leq \gamma_{SF} \leq 45 \text{ mJ m}^{-2}$  [37]. Woo *et al.* [38] reported an average  $\gamma_{SF}$  of additively manufactured S316L of  $32.8 \text{ mJ m}^{-2}$  which could explain the observed twinning behavior of the *stripe* sample. A texture-dependent strain hardening in S316L and twinning was also reported by Kumar *et al.* [1] in compressively loaded specimen. Those samples were produced by other hatch strategies than in the present work. The authors reported heterogeneous deformation mechanisms such as slip lines, twins, bands for all hatch strategies whereas an enhanced twin density was reported for samples, possessing a combination of  $\langle 100 \rangle$  and  $\langle 110 \rangle$  textured with respect to the build and load directions. Furthermore, Sun *et al.* [39] documented enhanced mechanical properties in  $\langle 011 \rangle$  textured 316L samples due to deformation twinning during tensile loading. The authors showed that the melt pool geometry has a significant influence on texture's formation. Melt pool's width, depths and height were adjusted by the application of different laser powers. In comparable flat melt pools, adjusted by the use of a lower energy input, grains grow straight from bottom to top, inducing a  $\langle 001 \rangle$  preferred orientation of the crystals. In the deeper melt pools, adjusted by the use of a high energy input, equiaxed grains grow in the center of the melt pool, prevent columnar grains from further growth and lead to a  $\langle 011 \rangle$  preferred orientation of the crystals. In the present case, however, an influence of the melt pool geometry on texture formation can be excluded as the process parameters and conditions were identical except from the hatch strategies. Metelkova *et al.* [40] studied the influence of different process parameters on melt pool's

Influence of Hatch Strategy on Crystallographic Texture Evolution, Mechanical Anisotropy of Laserbeam Powder Bed Fused S316L Steel

geometries focusing on different melt pool morphologies set by a convergent or divergent laser beam. The results revealed by the authors suggest that also larger laser defocus values are suitable for targeting the formation of textures during the PBF-LB process.

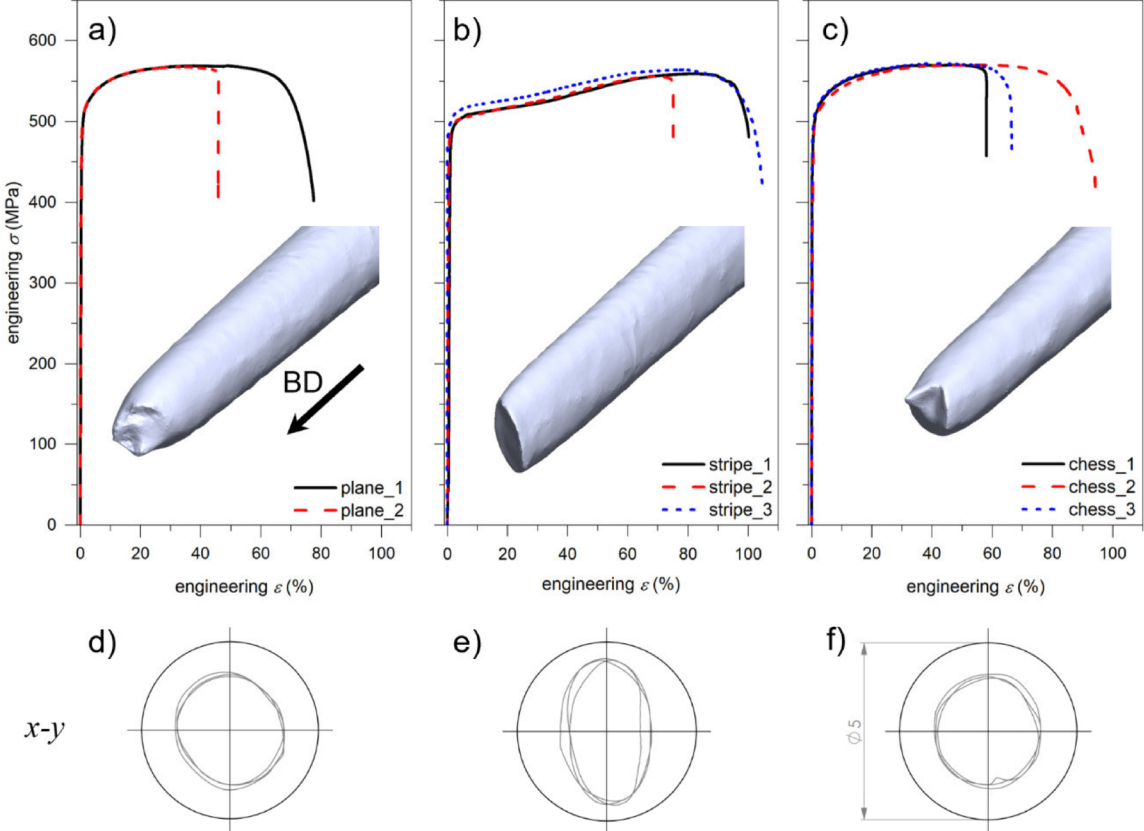


**Figure 7.** Representative tensile engineering stress-strain curves for the three different hatch styles *plane*, *stripe* and *chess*, respectively. The *stripe* samples (b) exhibit a higher ductility due to the increase work hardening at larger plastic strains, which is in contrast to the *plane* (a) and *chess* samples (c). The insets in each diagram represent the fracture surfaces of the samples, while the respective test cross-sections are presented in (d), (e) and (f). The *stripe* samples exhibit pronounced anisotropic x-y (in-plane) deformation leading to elliptical necking.



**Table 1.** Tensile properties of the *plane*, *stripe* and *chess* sample types.  $R_{p0.2}$  and  $R_m$  represent the yield strength and the ultimate tensile strength, respectively. In addition, the table includes the material properties determined by the equipment manufacturer EOS GmbH published in Ref. [41].

	EOS data sheet[41]	<i>plane</i>	<i>stripe</i>	<i>chess</i>
number of samples	-	2	3	3
$R_{p0.2}$ [MPa]	470 ± 90	477 ± 12	478 ± 12	475 ± 12
$R_m$ [MPa]	540 ± 55	569 ± 1	560 ± 5	571 ± 1

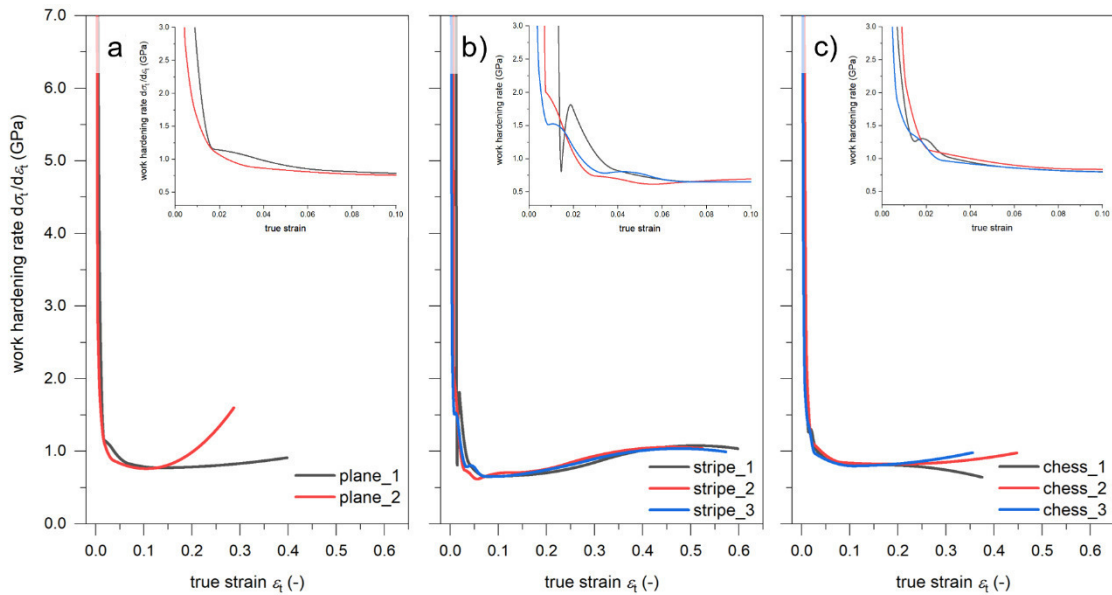


**Figure 8.** Representative work hardening curves of the three different hatch styles *plane*, *stripe* and *chess*, respectively. After the strong decay of the work hardening rates, the *stripe* samples (b) exhibit a higher ductility and a delayed work hardening in contrast to the *plane* (a) and *chess* samples (c).

Further deformation in a second step results in an increase of the dislocation density in the material leading to work hardening. Three-dimensional geometries of representative fracture surfaces from the three sample types are presented in Figure 7d-f. In case of the *stripe* sample, less pronounced necking was observed. Instead, the fractured surfaces are inclined by about 45 degrees with respect to the loading axis. This observation indicates that failure in the *stripe* samples occurs as a result of shear stress. SEM images of the fracture surfaces of three representative samples are provided in Figure S7 of the supplementary data. The averaged tensile properties of the samples are summarized in Table 1. In general, all three sample types' mechanical properties resemble those published by EOS GmbH [41] and are consistent with further benchmark values, as summarized by Sarafan *et al.* [42].

Shear failure in textured (high Mn-) TWIP steels was reported by Li *et al.* [37]. A Goss texture in those specimens was induced by a rolling process and resulted in a comparable stress-strain curve as well as shear fracture, similar to the present case.

Figure 8 shows a plot of the work hardening rate as a function of the true plastic strain  $\varepsilon_t$  for the three sample types. Assumptions on present deformations mechanisms are made on the basis of the findings of El-Danaf *et al.* [43] on uniaxially compressed low  $\gamma_{SF}$  fcc-alloys. All curves show a decreasing work hardening rate with increasing strain up to about 0.02 and the highest hardening rates are observed for the *plane* samples. The subsequent progression of the work hardening rate is significantly different for the specific sample types and is thus best described type-by-type. The *plane* samples (Figure 8a) exhibit a further (slight) decrease of the work hardening rate before the work hardening rises again. In case of two of the *stripe* samples (Figure 8b), the work hardening increases after the first decay and primary twinning is expected as reason for this. The rise is very pronounced for *stripe\_1*, exhibiting one maximum only. *Stripe\_2* and *stripe\_3* exhibit additionally a second maximum in the strain region up to  $\varepsilon_t = 0.1$  before the work hardening rate rises again in all *stripe* samples. Samples *chess\_1* and *chess\_2* show a more and a less pronounced maximum, respectively, as well, before the work hardening rate reaches a local minimum at about  $\varepsilon_t = 0.11$  before the work hardening decreases in *chess\_1* and rises in *chess\_2* and *chess\_3* until rupture.

Besides mechanical twinning, martensite formation was reported as another deformation mechanism for alloys with a  $\gamma_{SF} \leq 20 \text{ mJ m}^{-2}$  [37]. Kumar *et al.* [44] reported transformation-induced plasticity (TRIP) in S304L steel. However, Li *et al.* [45] documented a retarded TRIP effect and the presence of  $\delta$  ferrite in additively manufactured S316L. These contradictory results let us in the present case to investigate the presence of martensite using EBSD. Maps were recorded in the as-built and deformed regions (outside the neck region). EBSD analysis was not able to determine the presence of any other phase except the fcc crystal structure.

Additionally, we could not detect a pronounced ferromagnetic behavior in any of the fractured tensile specimens. Nevertheless, the formation of martensite during the tensile deformation cannot be totally excluded at this point but needs to be further investigated.

Previous results published by other authors [1,12,46] revealed complex correlations between different hatch strategies and the observed mechanical properties. The present careful analysis of the stress-strain behavior indicates that the hatch strategy (i) has a significant influence not only on the crystallographic texture of the samples, *i.e.*, especially on the anisotropy in the x-y plane perpendicular to the BD, but and furthermore (ii) results also in pronounced anisotropic deformation within the x-y (build) plane in the case of the stripe samples. However, as powder, gas atmosphere (thus the chemistry in the final samples) and energy input during sample production were identical, the change

of the deformation mechanism resulting in transformation induced plasticity in case of the stripe samples still cannot be solely explained by different textures. In particular, it is not clear, why *plane* samples, exhibiting the most pronounced (Goss) texture among the investigated sample types do not behave in a similar way as *stripe* samples. Thus, further studies need to address individual influences given by (i) the dislocation densities as well as residual second and third order stresses in the respective as-built states, (ii) differences in (sub)grain sizes and morphologies and (iii) the possible deformation induced martensite formation in the samples.

## 9.4 Conclusions

The aim of this work was to elucidate the role of three hatch strategies on the formation of crystallographic texture and mechanical response of S316L samples manufactured using PBF-LB. The experimental findings can be summarized as follows:

- Application of *plane*, *stripe* and *chess* hatch strategies induces the formation of a Goss-texture, a biaxial texture and a fiber-like texture, respectively.
- All observed textures exhibit a  $\langle 110 \rangle$  orientation of the crystallites, which is preferably oriented parallel to the build direction.
- The tensile behavior of the samples shows a correlation of deformation mechanisms to the texture formed during building. The presence of a biaxial-texture in the *stripe* style samples correlates with an elliptical deformation of the cross-section of the mechanically tested samples.
- The average yield and ultimate tensile strengths of the different samples of about 475 and 500 MPa, respectively, do not differ significantly between the differently hatched samples. However, twinning induced plasticity in the (low Mn-containing) 316L is observed in case of the biaxial-textured *stripe* samples.

These results document that the stress-strain response and deformation behavior during tensile loading of PBF-LB manufactured S316L samples can be tailored by using dedicated hatch strategies.

## Acknowledgments

Part of this work was supported by Österreichische Forschungsförderungsgesellschaft mbH (FFG), Project No. 861496, “CrossSurfaceMech” and Project No. FO999888151, “AMnonWeldAlloys”. Financial support by the Austrian Federal Government (in particular from Bundesministerium für Verkehr, Innovation und Technologie and Bundesministerium für Wissenschaft, Forschung und Wirtschaft) represented by Österreichische Forschungsförderungsgesellschaft mbH and the Styrian and the Tyrolean Provincial Government, represented by Steirische Wirtschaftsförderungsgesellschaft mbH and Standortagentur Tirol, within the framework of the COMET Funding Programme is gratefully acknowledged.

The support of the HEMS-beamline-team at DESY Hamburg is gratefully acknowledged.

## Author's contributions

S.C.B. – conceptualization, analysis and interpretation of the results, data visualization, coordination of experimental activities.

K.H. and M.-A.N - performance of XRD experiments at DESY.

K.K. - performance of tensile experiments and tensile data evaluation.

J.T. –XRD data evaluation in Mtex, script-programming and interpretation of the results.

O.R. – SEM analysis and data interpretation.

M.M. – SEM/EBSD analysis and data visualization and interpretation.

F.R. – additive manufacturing of the samples and 3D scanning of tensile samples post mortem.

J.K. - conceptual design, project coordination, data interpretation, establishment of funding and collaborative research, coordination of resources.

J.E. – conceptualization, project coordination, establishment of funding.

S.C.B and J.K. wrote the original draft of this manuscript, edited and prepared it for submission. All authors contributed equally in the further revision process.

---

## References

- [1] D. Kumar, G. Shankar, K.G. Prashanth, S. Suwas, Texture dependent strain hardening in additively manufactured stainless steel 316L, *Materials Science and Engineering A*. 820 (2021) 141483. doi: [10.1016/j.msea.2021.141483](https://doi.org/10.1016/j.msea.2021.141483).
- [2] S. Afkhami, M. Dabiri, H. Piili, T. Björk, Effects of manufacturing parameters and mechanical post-processing on stainless steel 316L processed by laser powder bed fusion, *Materials Science and Engineering A*. 802 (2021). doi: [10.1016/j.msea.2020.140660](https://doi.org/10.1016/j.msea.2020.140660).
- [3] Y. Zhong, L.E. Rännar, L. Liu, A. Koptuyg, S. Wikman, J. Olsen, D. Cui, Z. Shen, Additive manufacturing of 316L stainless steel by electron beam melting for nuclear fusion applications, *Journal of Nuclear Materials*. 486 (2017) 234–245. doi: [10.1016/j.jnucmat.2016.12.042](https://doi.org/10.1016/j.jnucmat.2016.12.042).
- [4] W.H. Kan, L.N.S. Chiu, C.V.S. Lim, Y. Zhu, Y. Tian, D. Jiang, A. Huang, A critical review on the effects of process-induced porosity on the mechanical properties of alloys fabricated by laser powder bed fusion, *Journal of Materials Science*. (2022). doi: [10.1007/s10853-022-06990-7](https://doi.org/10.1007/s10853-022-06990-7).
- [5] E. Ramirez-Cedillo, M.J. Uddin, J.A. Sandoval-Robles, R.A. Mirshams, L. Ruiz-Huerta, C.A. Rodriguez, H.R. Siller, Process planning of L-PBF of AISI 316L for improving surface quality and relating part integrity with microstructural characteristics, *Surface and Coatings Technology*. 396 (2020) 125956. doi: [10.1016/j.surfcoat.2020.125956](https://doi.org/10.1016/j.surfcoat.2020.125956).
- [6] O. Andreau, E. Pessard, I. Koutiri, P. Peyre, N. Saintier, Influence of the position and size of various deterministic defects on the high cycle fatigue resistance of a 316L steel manufactured by laser powder bed fusion, *International Journal of Fatigue*. 143 (2021) 105930. doi: [10.1016/j.ijfatigue.2020.105930](https://doi.org/10.1016/j.ijfatigue.2020.105930).
- [7] P. Ansari, A.U. Rehman, F. Pitir, S. Veziroglu, Y.K. Mishra, O.C. Aktas, M.U. Salamci, Selective laser melting of 316L austenitic stainless steel: Detailed process understanding using multiphysics simulation and experimentation, *Metals*. 11 (2021). doi: [10.3390/met11071076](https://doi.org/10.3390/met11071076).
- [8] S. Waqar, K. Guo, J. Sun, FEM analysis of thermal and residual stress profile in selective laser melting of 316L stainless steel, *Journal of Manufacturing Processes*. 66 (2021) 81–100. doi: [10.1016/j.jmapro.2021.03.040](https://doi.org/10.1016/j.jmapro.2021.03.040).
- [9] A. Aggarwal, S. Patel, A. Kumar, Selective Laser Melting of 316L Stainless

- Steel: Physics of Melting Mode Transition and Its Influence on Microstructural and Mechanical Behavior, *Jom.* 71 (2019) 1105–1116. doi: [10.1007/s11837-018-3271-8](https://doi.org/10.1007/s11837-018-3271-8).
- [10] T. Voisin, R. Shi, Y. Zhu, Z. Qi, M. Wu, S. Sen-Britain, Y. Zhang, S.R. Qiu, Y.M. Wang, S. Thomas, B.C. Wood, Pitting Corrosion in 316L Stainless Steel Fabricated by Laser Powder Bed Fusion Additive Manufacturing: A Review and Perspective, *Jom.* (2022). doi: [10.1007/s11837-022-05206-2](https://doi.org/10.1007/s11837-022-05206-2).
- [11] T. Niendorf, S. Leuders, A. Riemer, H.A. Richard, T. Tröster, D. Schwarze, Highly anisotropic steel processed by selective laser melting, *Metallurgical and Materials Transactions B: Process Metallurgy and Materials Processing Science.* 44 (2013) 794–796. doi: [10.1007/s11663-013-9875-z](https://doi.org/10.1007/s11663-013-9875-z).
- [12] T. Kurzynowski, K. Gruber, W. Stopyra, B. Kuźnicka, E. Chlebus, Correlation between process parameters, microstructure and properties of 316 L stainless steel processed by selective laser melting, *Materials Science and Engineering A.* 718 (2018) 64–73. doi: [10.1016/j.msea.2018.01.103](https://doi.org/10.1016/j.msea.2018.01.103).
- [13] S. Greco, K. Gutzeit, H. Hotz, B. Kirsch, J.C. Aurich, Selective laser melting (SLM) of AISI 316L—impact of laser power, layer thickness, and hatch spacing on roughness, density, and microhardness at constant input energy density, *International Journal of Advanced Manufacturing Technology.* 108 (2020) 1551–1562. doi: [10.1007/s00170-020-05510-8](https://doi.org/10.1007/s00170-020-05510-8).
- [14] C. Kamath, B. El-Dasher, G.F. Gallegos, W.E. King, A. Sisto, Density of additively-manufactured, 316L SS parts using laser powder-bed fusion at powers up to 400 W, *International Journal of Advanced Manufacturing Technology.* 74 (2014) 65–78. doi: [10.1007/s00170-014-5954-9](https://doi.org/10.1007/s00170-014-5954-9).
- [15] T. Larimian, M. Kannan, D. Grzesiak, B. AlMangour, T. Borkar, Effect of energy density and scanning strategy on densification, microstructure and mechanical properties of 316L stainless steel processed via selective laser melting, *Materials Science and Engineering A.* 770 (2020) 138455. doi: [10.1016/j.msea.2019.138455](https://doi.org/10.1016/j.msea.2019.138455).
- [16] Y.H. Zhou, W.P. Li, L. Zhang, S.Y. Zhou, X. Jia, D.W. Wang, M. Yan, Selective laser melting of Ti–22Al–25Nb intermetallic: Significant effects of hatch distance on microstructural features and mechanical properties, *Journal of Materials Processing Technology.* 276 (2020). doi: [10.1016/j.jmatprotec.2019.116398](https://doi.org/10.1016/j.jmatprotec.2019.116398).
- [17] B. AlMangour, D. Grzesiak, J.M. Yang, Scanning strategies for texture and

- anisotropy tailoring during selective laser melting of TiC/316L stainless steel nanocomposites, *Journal of Alloys and Compounds*. 728 (2017) 424–435. doi: [10.1016/j.jallcom.2017.08.022](https://doi.org/10.1016/j.jallcom.2017.08.022).
- [18] B. AlMangour, M.S. Baek, D. Grzesiak, K.A. Lee, Strengthening of stainless steel by titanium carbide addition and grain refinement during selective laser melting, *Materials Science and Engineering A*. 712 (2018) 812–818. doi: [10.1016/j.msea.2017.11.126](https://doi.org/10.1016/j.msea.2017.11.126).
- [19] J.H. Robinson, I.R.T. Ashton, E. Jones, P. Fox, C. Sutcliffe, The effect of hatch angle rotation on parts manufactured using selective laser melting, *Rapid Prototyping Journal*. 25 (2019) 289–298. doi: [10.1108/RPJ-06-2017-0111](https://doi.org/10.1108/RPJ-06-2017-0111).
- [20] H. Jia, H. Sun, H. Wang, Y. Wu, H. Wang, Scanning strategy in selective laser melting (SLM): a review, *International Journal of Advanced Manufacturing Technology*. 113 (2021) 2413–2435. doi: [10.1007/s00170-021-06810-3](https://doi.org/10.1007/s00170-021-06810-3).
- [21] N. Schell, A. King, F. Beckmann, H.U. Ruhnau, R. Kirchhof, R. Kiehn, M. Müller, A. Schreyer, The High Energy Materials Science Beamline (HEMS) at PETRA III, in: *AIP Conference Proceedings*, 2010. doi: [10.1063/1.3463221](https://doi.org/10.1063/1.3463221).
- [22] J. Kieffer, D. Karkoulis, PyFAI, a versatile library for azimuthal regrouping, *Journal of Physics: Conference Series*. 425 (2013). doi: [10.1088/1742-6596/425/20/202012](https://doi.org/10.1088/1742-6596/425/20/202012).
- [23] F. Bachmann, R. Hielscher, H. Schaeben, Texture analysis with MTEX- Free and open source software toolbox, *Solid State Phenomena*. 160 (2010) 63–68. doi: [10.4028/www.scientific.net/SSP.160.63](https://doi.org/10.4028/www.scientific.net/SSP.160.63).
- [24] I.C. Noyan, J.B. Cohen, *Residual stress – measurement by diffraction and interpretation.*, 1st ed., Springer-Verlag New York Inc., New York, 1987. doi: [10.1007/978-1-4613-9570-6](https://doi.org/10.1007/978-1-4613-9570-6).
- [25] E. Kröner, Berechnung der elastischen Konstanten des Vielkristalls aus den Konstanten des Einkristalls, *Zeitschrift Für Physik*. 151 (1958) 504–518. doi: [10.1007/BF01337948](https://doi.org/10.1007/BF01337948).
- [26] M. Stefanelli, J. Todt, A. Riedl, W. Ecker, T. Müller, R. Daniel, M. Burghammer, J. Keckes, X-ray analysis of residual stress gradients in TiN coatings by a Laplace space approach and cross-sectional nanodiffraction: A critical comparison, *Journal of Applied Crystallography*. 46 (2013) 1378–1385. doi: [10.1107/S0021889813019535](https://doi.org/10.1107/S0021889813019535).
- [27] A. Zeilinger, J. Todt, C. Krywka, M. Müller, W. Ecker, B. Sartory, M.

- Meindlhumer, M. Stefenelli, R. Daniel, C. Mitterer, J. Keckes, In-situ Observation of Cross-Sectional Microstructural Changes and Stress Distributions in Fracturing TiN Thin Film during Nanoindentation, *Scientific Reports*. 6 (2016). doi: [10.1038/srep22670](https://doi.org/10.1038/srep22670).
- [28] G. Geandier, L. Vautrot, B. Denand, S. Denis, In situ stress tensor determination during phase transformation of a metal matrix composite by high-energy X-ray diffraction, *Materials*. 11 (2018) 1–19. doi:[10.3390/ma11081415](https://doi.org/10.3390/ma11081415).
- [29] S.C. Bodner, M. Meindlhumer, T. Ziegelwanger, H. Winklmayr, T. Hatzenbichler, C. Schindelbacher, B. Sartory, M. Krobath, W. Ecker, N. Schell, J. Keckes, Correlative Cross-Sectional Characterization of Nitrided, Carburized and Shot-Peened Steels: Synchrotron Micro-X-Ray Diffraction Analysis of Stress, Microstructure and Phase Gradients, *Journal of Materials Research and Technology*. (2021). doi: [10.1016/j.jmrt.2021.01.099](https://doi.org/10.1016/j.jmrt.2021.01.099).
- [30] B. Heine, *Werkstoffprüfung*, 3rd Editio, Carl Hanser Verlag, München, 2015.
- [31] M.S. Pham, B. Dovgyy, P.A. Hooper, Twinning induced plasticity in austenitic stainless steel 316L made by additive manufacturing, *Materials Science and Engineering A*. 704 (2017) 102–111. doi: [10.1016/j.msea.2017.07.082](https://doi.org/10.1016/j.msea.2017.07.082).
- [32] P. Scherrer, Bestimmung der Größe und der inneren Struktur von Kolloidteilchen mittels Röntgenstrahlen, *Nachrichten von Der Gesellschaft Der Wissenschaften Zu Göttingen, Mathematisch-Physikalische Klasse*. 2 (1918) 98–100. doi: [10.1007/978-3-662-33915-2](https://doi.org/10.1007/978-3-662-33915-2).
- [33] A.K. Agrawal, G. Meric de Bellefon, D. Thoma, High-throughput experimentation for microstructural design in additively manufactured 316L stainless steel, *Materials Science and Engineering A*. 793 (2020) 139841. doi:[10.1016/j.msea.2020.139841](https://doi.org/10.1016/j.msea.2020.139841).
- [34] O. Grässel, G. Frommeyer, C. Derder, H. Hofmann, Phase transformations and mechanical properties of Fe-Mn-Si-Al TRIP-steels, *Journal De Physique. IV : JP*. 7 (1997) 1–6. doi: [10.1051/jp4:1997560](https://doi.org/10.1051/jp4:1997560).
- [35] O. Grässel, L. Krüger, G. Frommeyer, L.W. Meyer, High strength Fe-Mn-(Al, Si) TRIP/TWIP steels development - properties - application, *International Journal of Plasticity*. 16 (2000) 1391–1409. doi: [10.1016/S0749-6419\(00\)00015-2](https://doi.org/10.1016/S0749-6419(00)00015-2).
- [36] I. Gutierrez-Urrutia, D. Raabe, Dislocation and twin substructure evolution during strain hardening of an Fe-22 wt.% Mn-0.6 wt.% C TWIP steel observed by electron channeling contrast imaging, *Acta Materialia*. 59 (2011) 6449–6462. doi: [10.1016/j.actamat.2011.07.009](https://doi.org/10.1016/j.actamat.2011.07.009).



- [37] Y. Li, L. Zhu, Y. Liu, Y. Wei, Y. Wu, D. Tang, Z. Mi, On the strain hardening and texture evolution in high manganese steels: Experiments and numerical investigation, *Journal of the Mechanics and Physics of Solids*. 61 (2013) 2588–2604. doi: [10.1016/j.jmps.2013.08.007](https://doi.org/10.1016/j.jmps.2013.08.007).
- [38] W. Woo, J.S. Jeong, D.K. Kim, C.M. Lee, S.H. Choi, J.Y. Suh, S.Y. Lee, S. Harjo, T. Kawasaki, Stacking Fault Energy Analyses of Additively Manufactured Stainless Steel 316L and CrCoNi Medium Entropy Alloy Using In Situ Neutron Diffraction, *Scientific Reports*. 10 (2020) 2–4. doi: [10.1038/s41598-020-58273-3](https://doi.org/10.1038/s41598-020-58273-3).
- [39] Z. Sun, X. Tan, S.B. Tor, C.K. Chua, Simultaneously enhanced strength and ductility for 3D-printed stainless steel 316L by selective laser melting, *NPG Asia Materials*. 10 (2018) 127–136. doi: [10.1038/s41427-018-0018-5](https://doi.org/10.1038/s41427-018-0018-5).
- [40] J. Metelkova, Y. Kinds, K. Kempen, C. de Formanoir, A. Witvrouw, B. Van Hooreweder, On the influence of laser defocusing in Selective Laser Melting of 316L, *Additive Manufacturing*. 23 (2018) 161–169. doi: [10.1016/j.addma.2018.08.006](https://doi.org/10.1016/j.addma.2018.08.006).
- [41] EOS GmbH, Materialdatenblatt StainlessSteel 316L, Materialdatenblatt EOS GmbH Electro Optical System. 49 (2017) 1–5. [https://cdn0.scrvt.com/eos/ccaf69b7dbb3dc84/412597466f6c/EOS\\_StainlessSteel\\_316L.pdf](https://cdn0.scrvt.com/eos/ccaf69b7dbb3dc84/412597466f6c/EOS_StainlessSteel_316L.pdf).
- [42] S. Sarafan, P. Wanjara, J. Gholipour, F. Bernier, M. Osman, F. Sikan, Benchmarking of 316L Stainless Steel Manufactured by a Hybrid Additive / Subtractive Technology, (2022).
- [43] E. El-Danaf, S.R. Kalidindi, R.D. Doherty, Influence of deformation path on the strain hardening behavior and microstructure evolution in low SFE FCC metals, *International Journal of Plasticity*. 17 (2001) 1245–1265. doi: [10.1016/S0749-6419\(00\)00090-5](https://doi.org/10.1016/S0749-6419(00)00090-5).
- [44] P. Kumar, Z. Zhu, S.M.L. Nai, R.L. Narayan, U. Ramamurty, Fracture toughness of 304L austenitic stainless steel produced by laser powder bed fusion, *Scripta Materialia*. 202 (2021) 114002. doi: [10.1016/j.scriptamat.2021.114002](https://doi.org/10.1016/j.scriptamat.2021.114002).
- [45] V.K. Nadimpalli, E. Hørdum, T. Dahmen, E.H. Valente, S. Mohanty, Multi-material additive manufacturing of steels using laser powder bed fusion eu s pen ' s 1 9 th International Conference & Exhibition , Bilbao , ES , June 2019 Multi-material additive manufacturing of steels using laser powder bed fusion, (2019). <https://backend.orbit.dtu.dk/ws/portalfiles/portal/192242879/ICE19230.pdf>.

- [46] M. Avateffazeli, M. Haghshenas, Ultrasonic fatigue of laser beam powder bed fused metals: A state-of-the-art review, *Engineering Failure Analysis*. 134 (2022) 106015. doi:[10.1016/j.engfailanal.2021.106015](https://doi.org/10.1016/j.engfailanal.2021.106015).

## **Graded Inconel-Stainless Steel Multi-Material Structure by Inter- and Intralayer Variation of Metal Alloys**

**S.C. Bodner<sup>a,\*</sup>, K. Hlushko<sup>a</sup>, L.T.G. van de Vorst<sup>b</sup>, M. Meindlhuber<sup>a</sup>, J. Todt<sup>a</sup>, M.A. Nielsen<sup>c</sup>, J.W. Hooijmans<sup>d</sup>, J.J. Saurwalt<sup>d</sup>, S. Mirzaei<sup>e,f</sup>, J. Keckes<sup>a</sup>**

<sup>a</sup> Department of Materials Science - Chair of Materials Physics, Montanuniversität Leoben, A-8700 Leoben, Austria

<sup>b</sup> The Netherlands Organization for Applied Scientific Research TNO – Department Thin Films, 1755-LE Petten, Netherlands

<sup>c</sup> Helmholtz Zentrum Hereon, Institute of Materials Physics, D-21502 Geesthacht, Germany

<sup>d</sup> Admatec Europe BV, 5066 GJ Moergestel, Netherlands

<sup>e</sup> CEITEC BUT, Brno University of Technology, Purkynova 123, CZ- C61200, Czech Republic

<sup>f</sup> Fraunhofer Institute for Material and Beam Technology, Winterbergstraße 28, DE-01277 Dresden, Germany

## Abstract

Additively manufactured multi-metal hybrid structures can be designed as functionally graded materials providing an optimized response at specific positions for particular applications. In this study, *liquid dispersed metal powder bed fusion* is used to synthesize a multi-metal structure based on Inconel 625 (IN625) and stainless steel 316L (S316L) stainless steel regions, built on a S316L base plate. *Both alloys alternate several times along the build direction as well as within the individual sublayers.* The multi-metal sample was investigated by optical microscopy, scanning electron microscopy, microhardness measurements, nanoindentation and energy-dispersive X-ray spectroscopy. Cross-sectional synchrotron X-ray micro-diffraction 2D mapping was carried out at the high-energy material science beamline of the storage ring PETRAIII in Hamburg. Sharp morphological S316L-to-IN625 interfaces along the sample's build direction are observed on the micro- and nanoscale. A gradual phase transition encompassing about 1 mm is revealed in the transverse direction. Mechanical properties change gradually following abrupt or smooth phase transitions between the alloys where a higher strength is determined for the superalloy. The two-dimensional distribution of phases can be assessed indirectly as S316L and IN625 in this multi-metal sample possess a  $\langle 110 \rangle$  and a  $\langle 100 \rangle$  fiber crystallographic texture, respectively. Tensile residual stresses of  $\sim 900$  and  $\sim 800$  MPa in build direction and perpendicular to it, respectively, are evaluated from measured residual X-ray elastic strains. Generally, the study indicates possibilities and limitations of *liquid dispersed metal powder bed fusion* for additive manufacturing of functionally graded materials with unique synergetic properties and contributes to the understanding of optimization of structurally and functionally advanced composites.

**Keywords:** 3D multi-material structure; multi-metal material; liquid dispersed metal powder bed fusion; cross-sectional gradient materials; X-ray synchrotron characterization; hybrid structures;

## 9.1 Introduction

Additive manufacturing (AM) of metals is known as a novel production technology that is able to synthesize products of complex geometries for prototyping, mechanical engineering, medicine, automotive and aerospace applications [1]. Contrary to the original assumption that AM could replace a large part of traditional manufacturing processes, the latest developments show that AM will not displace subtractive processes in the future, but rather joins them as a complementary manufacturing technology. The unique advantage of AM technology resides in the ability to customize the shape and size of every individual component. Additionally, relatively recent developments in AM enable to fabricate components with spatially varying functional properties by combining different metals into one functionally graded material (FGM) and/or multi-material hybrid composites [2-5]. FGMs exhibit advantageous functionalities and physical properties, as special requirements like oxidation resistance, thermal strength or toughness can be tailored by optimizing the local use of different materials. In the following, this article refers exclusively to metallic FGMs produced by AM. Their synthetization still poses a particular challenge. This is (i) due to the sometimes very different physical properties of the metals such as the thermal expansion coefficient or the tendency to corrosion, (ii) due to the tendency to form intermetallic phases (depending on the metal combination selected) and (iii) due to the requirements placed on the synthesis process.

The possibility to combine different metal alloys into one workpiece was reported for directed energy deposition (DED) based processes where a layer-wise change or alternation of materials can be realized *e.g.* by wire arc additive manufacturing (WAAM) and laser metal deposition (LMD) [3,6]. The effort needed for a change of material is manageable using these synthetization methods as only the feedstock (wire or powder) has to be exchanged and fed via a coaxial feeding system to the source of energy [7]. An inherent flexibility is one key point for the production of FGMs. Major drawbacks of DED-based processes are however the limited spatial resolution and surface quality, in particular for small geometries, due to comparably thick layers.

Thus, powder bed fusion (PBF) based processes are regularly used for the production of parts with complex geometries and with higher demands on surface quality and geometric accuracy [4]. If a laser is used as energy source, the correct terminology according to ASTM 52900:2021-11 is laser based powder bed fusion (PBF-LB). Concerning the manufacturing of FGMs, the main drawback of commonly and industrially applied PBF-based processes is the limited flexibility when it comes to a change of the powder feedstock. A spatial variation of materials in state-of-the-art PBF-LB systems means in

practice either (i) the application of a printed metal being different from the base plate material [8], (ii) that the whole machine has to be cleaned, before the second (chemically different) powder can be spread over the build area [9] or, (iii) that, if available, a second supplier (cylinder or hopper [10-14]) provides another feedstock and both materials are varied and/or mixed in the build volume. Thus, differentiated process parameters or variations in part's densities (*e.g.* cellular structures) are rather used than different materials to synthesize FGMs by PBF-LB. Xiong *et al.* [15] studied mechanical properties of PB-fused TiAl6V4 with density changes due to pores and honeycomb structures which could be considered to be used in orthopedic applications. Ghorbanpour *et al.* [16] used a commercial available PBF-LB device and influenced the microstructure of the  $\gamma'$ -precipitating Inconel 718 Ni-base alloy by varying the laser powder in different regions along the build direction (BD) and perpendicular to it.

A PBF-LB related process, capable to produce FGMs is liquid dispersed metal powder bed fusion (LDM-PBF-LB). In a previous work [17], the strength and limitations of this relatively novel approach that uses a metal slurry feedstock was indicated. A multi-metal hybrid structure was synthesized, which consisted of five different regions, incorporating both sharp and gradual interfaces between the non-precipitation hardening Ni-base Inconel625 (IN625) alloy and a stainless steel stainless steel 316L (S316L) along the BD. Several transitions of both alloys were realized along the BD. Thus, according to Ref. [2] that sample can be categorized as 2D multi-material structure.

Different approaches to print 2D multi-material structures by PBF-LB were recently studied also by other scientific groups. Mao *et al.* [18] reported on the influence of process parameters on the formation of the interface in S316 L/CuCrZr FGMs and analyzed corresponding differences of mechanical properties. Chen *et al.* [19] printed Inconel 718 on a S316 substrate and studied the process-microstructure property relationship in-situ using high-speed synchrotron X-ray imaging. Demir *et al.* [20] used a prototype PBF-LB system, equipped with a double feeder powder system to fabricate a Fe/Al-12Si multi-material with three distinct regions: pure Fe, Fe/Al12Si blend and Al-12Si.

The variation of a material along a second dimension (*i.e.*, within an individual layer) significantly complicates the fabrication of FGMs using PBF-LB techniques. Thus, only a limited number of publications document the successful fabrication of PB-fused 3D multi-metal structures. Wei *et al.* used a PBF-LB system equipped with six single ultrasonic powder dispensers to produce complex shaped demonstrator parts with discrete and gradual S316 L/Cu10Sn material's variations along the BD and within individual layers. Preliminary results of S316 L/CuSn10 3D multi-metal sample fabricated using a semi-industrial PBF-LB equipment by Aconity 3D and Aerosint were revealed in their collaboration with the ETH Zürich and published in the context of a review on multi-material powder bed fusion techniques by Mehrpouya *et al.* [21] The system is equipped

with two patterning drums which allows for the simultaneous deposition of up to three materials [22] within an individual layer.

In this work, a 3D multi-metal structure produced by LDM PBF-LB is characterized. S316L and IN625 were alternated twelve times along the BD and more than a hundred times within individual layers (*i.e.*, perpendicular to the BD). An advanced analytical approach aimed at correlating the results of different microscopy methods, energy dispersive spectroscopy (EDS), 2D hardness mapping and cross-sectional synchrotron X-ray micro diffraction (CSmicroXRD). The methods were applied to evaluate the complex microstructure-property-relationship of the fabricated 3D multi-metal sample at different length-scales.

## 9.2 Materials and Methods

Two identical multi-material samples with dimensions of  $3 \times 15 \times 7 \text{ mm}^3$  ( $x \times y \times z$ ) were produced by LDM PBF-LB on a Laserflex Conflux system (Admatec Europe BV, The Netherlands). The system is equipped with a SPI RedPower Laser SP200C (wavelength = 1064 nm) and a galvoscaner-optics, resulting in a small spot size of 12  $\mu\text{m}$ . Gas-atomized Fe and Ni-based powders S316L (size PF-5K by Epson Admix Corp., Japan) and Inconel 625 (Sandvik Osprey, Sweden) with a  $d_{50}$  particle size of 4.18 and 3.40  $\mu\text{m}$ , respectively, were mixed with a water-based binder (Admatec Europe BV). The chemical composition was analyzed by EDS in an IntouchScope JSM-6010LA (JEOL, Japan) which was also used for scanning electron microscopy (SEM). Nominal and actual chemical compositions of the used alloys are given in Table 1.

**Table 1:** Nominal and actual chemical compositions of S316L and IN625 in ppm (O) and weight.-% (other elements).

S316L	Fe	C	Si	Mn	P	S	Ni	Cr	Mo	O (ppm)
nominal and maximal	balance	0.03	1.00	<2.00	0.045	0.03	12.0- 15.0	16.0- 18.0	2.0- 3.0	-
actual	balance	0.025	0.036	0.11	0.014	0.006	12.14	17.84	2.10	3.400
IN625	Ni	Cr	Mo	Nb	Fe	Al	Co	Ti	Si	Mn
nominal and maximal	balance	23.0	10.0	4.15	5.0	0.40	1.00	0.40	0.50	0.50
actual	balance	21.2	9.1	0.24	2.2	0.04	0.01	0.01	0.27	0.24

## Graded Inconel-Stainless Steel Multi-Material Structure by Inter- and Intralayer Variation of Metal Alloys

Both slurries were selectively applied to the building platform by a pipetting system (Figure 1b) and spread by a knife edge, resulting in a liquid metal-dispersed powder bed. After a drying step of some seconds, during which the liquid metal-dispersed powder bed densified (Figure 1b), the metal powders were selectively melted by the laser operated with a power of 137 W (Figure 1c) in a nitrogen gas atmosphere. The layer thickness, the scan speed, the hatch distance and the alternating angle were set to 20  $\mu\text{m}$ , 500 mm/s, 9  $\mu\text{m}$  and 66°, respectively.

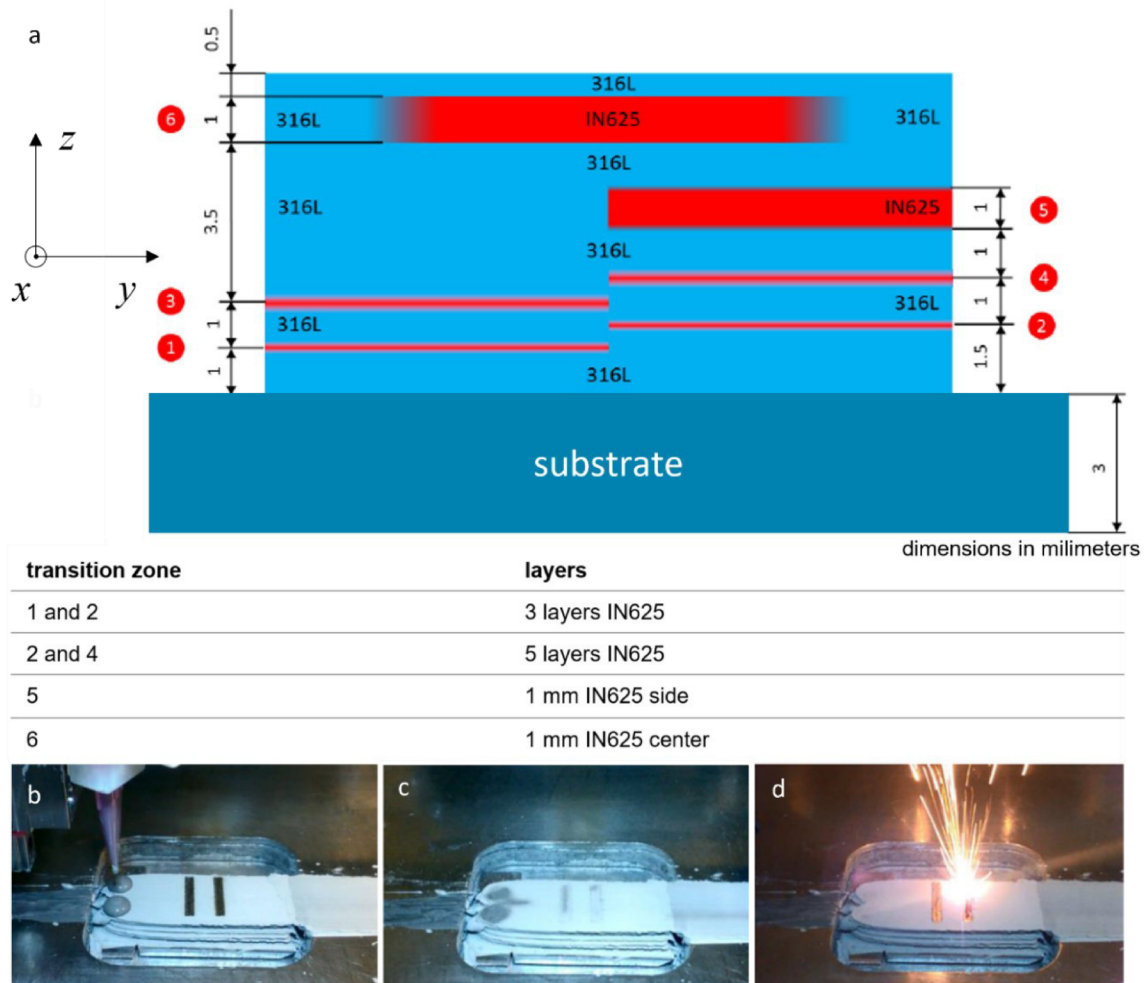


**Figure 1.** Two identical IN625 and S316L multi-material samples (a) were produced by liquid dispersed metal powder bed fusion. The slurries were selectively applied by an automated pipetting system (b), spread across the building platform, resulting in a liquid powder bed and let dry (c) before a laser beam was used to build up the desired geometries layer by layer (d).

The samples were cleaned from the powder cake and further analyzed by optical microscopy, hardness profiling and CSmicroXRD [17], as described below.



### 9.2.1 Metallographic Characterization

The specimen (see Figure 1) was hot-embedded in graphite-filled bakelite “PolyFast” (Struers, Germany). The metallurgical cross-section was prepared by grinding and polishing, finishing with a 1  $\mu\text{m}$  diamond suspension. Two-dimensional phase occurrence at the cross-section was assessed by confocal microscopy using a DCM 3D optical surface metrology system (Leica, Germany) at various magnifications. SEM was carried out on an IntouchScope JSM-6010LA (JEOL, Japan), at voltages of 5 and 15 kV.

### 9.2.2 Hardness Profiling

Vicker's microhardness measurements were performed across the polished sample cross-section to evaluate hardness gradients at the interfaces between S316L to IN625 in both  $y$  and  $z$  directions (see Figure 1). The pyramid-shaped diamond tip was loaded with a test force of 4.905 N, corresponding to  $\text{HV}_{0.5}$ , by a Mitutoyo-Bühler Micromet 5104 hardness-testing device. Distances between two single indents were set to 200 and 500  $\mu\text{m}$  in  $y$  and  $z$  directions, respectively, and minimum edge-distances were respected according to ASTM E384-99 [23].

### 9.2.3 Nanoindentation

Changes in mechanical properties within transition regions between S316L and IN625 were further assessed by a nanoindentation experiment using a Hysitron TI 950 Triboindenter equipped with a Berkovic indenter. The maximum load of 5 mN in the load-controlled regime was employed to prepare arrays of  $10 \times 10$  indents within two sample regions (comprising in-plane- and out-of-plane-oriented interfaces between S316L to IN625). The spacing between two adjacent indents was set to  $\sim 50 \mu\text{m}$  to map the mechanical properties within a larger area. The obtained data were evaluated in terms of hardness and reduced elastic modulus based on the Oliver and Pharr method [24].

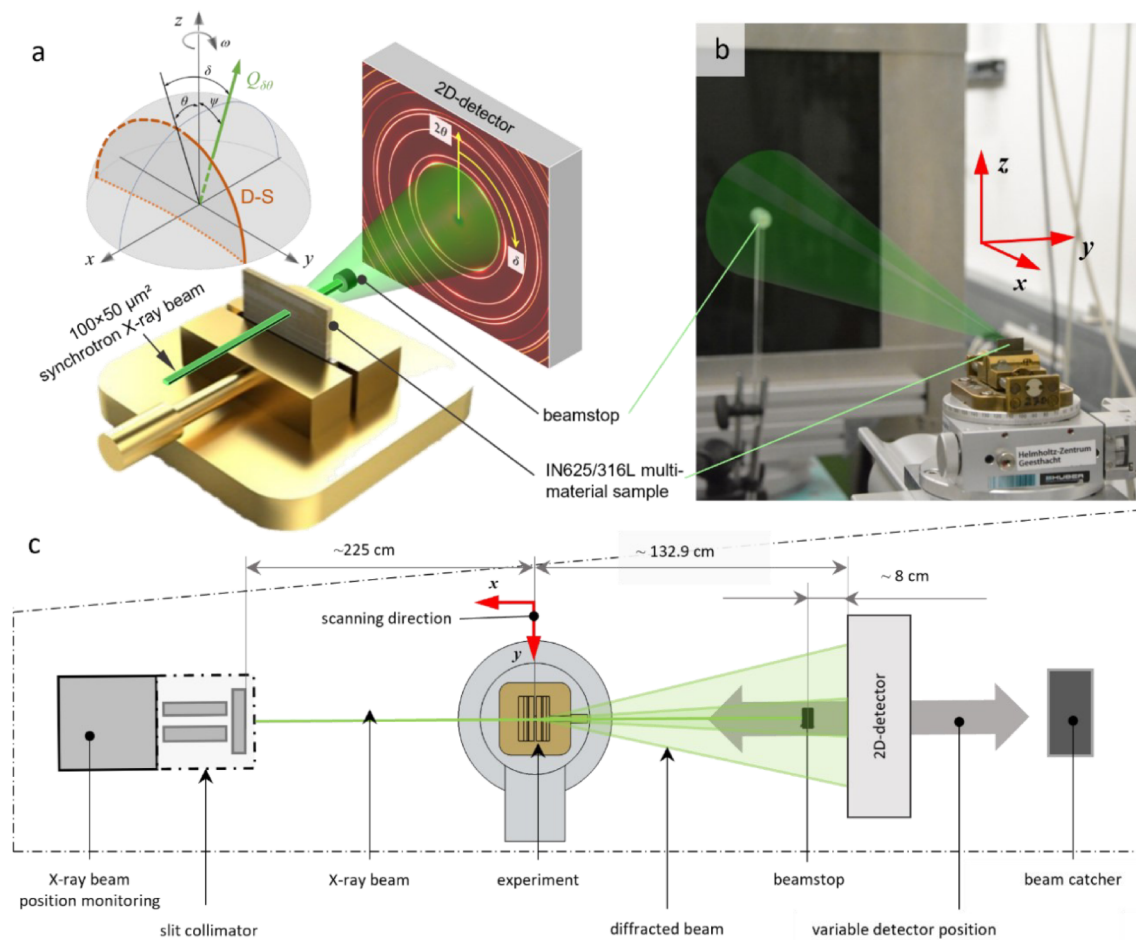
### 9.2.4 Synchrotron X-ray Micro-Diffraction

Figure 2 presents the experimental setup that was used to characterize the specimen by CSmicroXRD at the *Hereon* operated side-hutch P07B of the high-energy materials science (HEMS) beamline of the storage ring PETRA III at Deutsches Elektronen Synchrotron (DESY) in Hamburg, Germany [25]. The specimen (see Figure 1a) was scanned along  $y$  and  $z$  directions using a step size of 50 and 100  $\mu\text{m}$ , respectively, mapping the whole cross-section in transmission diffraction geometry using a beam size of

## Graded Inconel-Stainless Steel Multi-Material Structure by Inter- and Intralayer Variation of Metal Alloys

$50 \times 100 \mu\text{m}^2$  ( $y \times z$ ). The used photon energy of 87.1 keV corresponds to a wavelength of 0.1423 Å.

24,960 diffractograms were collected by a 2D digital X-ray flat panel detector, type XRD1621 (PerkinElmer, Waltham, USA), which has an array size and a pixel pitch of  $2048 \times 2048$  pixels and  $200 \mu\text{m}$ , respectively. The sample-to-detector distance, the rotation angle of the tilting plane and the angle of the detector tilt in-plane were calibrated using a  $\text{LaB}_6$  standard powder. This methodology named cross-sectional synchrotron X-ray micro-diffraction was introduced in our previous work [17].



**Figure 2.** Schematic (a, c) and actual (b) experimental setup with indicated X-ray beam and diffraction cone for the cross-sectional X-ray micro-diffraction (CSmicroXRD) [17] measurements at the side-hutch P07B of the HEMS-beamline at PETRA III. The Inconel-steel multi-material sample was mapped in transmission diffraction geometry by scanning the sample in the X-ray beam along  $y$  and  $z$  axes with increments of 100 and 50  $\mu\text{m}$ , respectively.

### 9.3 Theory: Residual Stress Evaluation

2D-XRD data were further processed using the python library *pyFAI* [26] to obtain information on the distribution of phases, microstructure (texture and crystallize size) and strain at the cross-section of the multi-metal sample (averaged along the beam directions) (Figure 1). Diffraction patterns were azimuthally integrated in the range of  $0 < \delta < 360^\circ$ , which was split into 36 segments, so-called “cakes”, each encompassing a  $\Delta\delta$  range of  $10^\circ$ . Lattice parameters of  $(hkl)$  crystallographic planes and the particular alloy were determined from the positions of 311 and the 222  $(hkl)$  reflections using Bragg's law. Each value represents the lattice parameter evaluated at the sample position, while the  $(hkl)$  lattice plane normal-direction was oriented parallel to the diffraction vector (*cf.* Figure 2a).

In the next step, the  $d_{\delta\theta}^{m,hkl}(y,z)$  data were used to obtain residual lattice strain  $\varepsilon_{\delta\theta}^{m,hkl}(y,z)$  along the direction of the diffraction vector  $\mathbf{Q}_{\delta\theta}$  as follows:

$$\varepsilon_{\delta\theta}^{m,hkl}(y,z) = \frac{d_{\delta\theta}^{m,hkl}(y,z) - d_0^{m,hkl}}{d_0^{m,hkl}} \quad (1)$$

where  $\delta$  and  $\theta$  represent the azimuthal position of the *Debye-Scherrer* (D-S) rings on the detector (Figure 2a) and the Bragg's angle, respectively, and is the unstressed lattice spacing for the crystallographic plane  $(hkl)$ .

A determination of the correct  $d_0^{m,hkl}$ -values in an additively manufactured multi-metal-material is not trivial, as neither the microstructure nor the chemical composition are homogenous within the sample. In this study, we determined the unstressed lattice parameter  $a_0^m$  for both fcc-alloys by fitting the 311 and 222 Debye-Scherrer (D-S) rings for IN625 as well as S316L at several measurement positions located directly next to the free surfaces of the sample, supposing a negligible perpendicular stress component. We obtained  $a_0^{IN625}$  and  $a_0^{316L}$  of 3.5952 and 3.5948 Å, respectively. These results are in accordance with those determined in [27] and [28], respectively.

Experimentally determined residual X-ray elastic strains  $\varepsilon_{\delta\theta}^{m,hkl}(y,z)$  were used to assess residual stress components  $\sigma_{i,j}(y,z)$ ; ( $i,j = x,y,z$ ), defined in the sample coordinate system with  $x,y$  and  $z$  axes, using the following approach:

$$\begin{aligned}
 \varepsilon_{\delta\theta}^{m,hkl}(y,z) = & \frac{1}{2}S_2^{m,hkl}[\sin^2\theta \sigma_{xx}(y,z) \\
 & + \cos^2\theta \sin^2\delta \sigma_{yy}(y,z) + \cos^2\theta \cos^2\delta \sigma_{zz}(y,z) \\
 & + \cos^2\theta \sin 2\delta \sigma_{yz}(y,z) - \sin 2\theta \cos\delta \sigma_{xz}(y,z) \\
 & - \sin 2\theta \sin\delta \sigma_{xy}(y,z)] \\
 & + S_1^{m,hkl}[\sigma_{xx}(y,z) + \sigma_{yy}(y,z) + \sigma_{zz}(y,z)]
 \end{aligned} \tag{2}$$

$S_1^{m,hkl} = (-\frac{\nu}{E})^{hkl}$  and  $\frac{1}{2}S_2^{m,hkl} = (\frac{1+\nu}{E})^{hkl}$  are the X-ray elastic constants (XEC) in Voigt's notation. Young's modulus and Poisson's ratio are expressed by  $E$  and  $\nu$ , respectively, which are  $hkl$  peak-specific due to single crystal anisotropy. Eq. (2) can be derived by applying *Hooke's law* for a quasi-isotropic material [29].

The *Eshelby-Kroener* grain-interaction model [30] was used to calculate XECs, using single-crystal elastic constants of Refs. [31,32], resulting in:

$$\begin{aligned}
 S_1^{IN625,311} &= -1.618 \times 10^{-6} \text{ MPa}^{-1}, \\
 \frac{1}{2}S_2^{IN625,311} &= 6.649 \times 10^{-6} \text{ MPa}^{-1}; S_1^{IN625,222} \\
 &= -1.108 \times 10^{-6} \text{ MPa}^{-1}, \\
 \frac{1}{2}S_2^{IN625,222} &= 5.121 \times 10^{-6} \text{ MPa}^{-1}; S_1^{316L,311} \\
 &= -1.378 \times 10^{-6} \text{ MPa}^{-1}, \\
 \frac{1}{2}S_2^{316L,311} &= 6.536 \times 10^{-6} \text{ MPa}^{-1}; S_1^{316L,222} \\
 &= -0.899 \times 10^{-6} \text{ MPa}^{-1}, \quad \frac{1}{2}S_2^{316L,222} = 5.098 \times 10^{-6} \text{ MPa}^{-1}
 \end{aligned}$$

Shear-stress components along planes parallel to the primary X-ray beam ( $x$ -direction) were assumed to be negligible ( $\sigma_{xy}^m(y,z) \cong 0$ ;  $\sigma_{xz}^m(y,z) \cong 0$ ). Due to (i) the comparatively small sample dimension in  $x$  and (ii) the fact, that the experimental geometry is insensitive to this stress component, calculations within this work are made on the assumption that the corresponding stress component  $\sigma_{xx}^m(y,z)$  is zero. Consequently, Eq. (2) can be transformed to

$$\begin{aligned}
 \varepsilon_{\delta\theta}^{m,hkl}(y,z) = & S_1^{m,hkl}[\sigma_{yy}(y,z) + \sigma_{zz}(y,z)] \\
 & + \frac{1}{2}S_2^{m,hkl}[\cos^2\theta \sin^2\delta \sigma_{yy}(y,z) \\
 & + \cos^2\theta \cos^2\delta \sigma_{zz}(y,z) + \cos^2\theta \sin 2\delta \sigma_{yz}(y,z)]
 \end{aligned} \tag{3}$$

which allows to determine the stress-state within the investigated area by least-squares fitting of an overdetermined system of 36 equations, based on experimentally determined

$\varepsilon_{\delta\theta}^{m,hkl}(y, z)$  [33]. In the following, results of  $\sigma_{yy}$ ,  $\sigma_{zz}$  and  $\sigma_{yz}$  are referred to as in-plane, out-of-plane and shear stresses.

### 9.3.1 Qualitative Phase Analysis

Since the steel S316L and IN625 exhibit relatively similar lattice parameters of 3.5948 and 3.5952 Å, respectively, it was not trivial to evaluate the spatial occurrence of both phases from the analysis of D-S rings' intensities. Our former study [17] on a comparable sample indicated that these alloys, printed with similar process parameters, usually possess different crystallographic textures, *i.e.*, a  $\langle 110 \rangle$  fibre texture for S316L and a  $\langle 100 \rangle$  fibre texture for IN625. Therefore, in order to qualitatively evaluate the spatial occurrence of the steel S316L and IN625 phases at the sample cross-section, different azimuthal 220 D-S ring intensity maxima within the azimuthal ranges of  $350 \leq \delta \leq 10$  and  $35 \leq \delta \leq 55$  deg were considered, respectively. Hereafter, the spatial occurrence of the steel S316L is presented, where the occurrence of the IN625 phase balances.

### 9.3.2 Peak broadening

Changes in diffraction peak widths are influenced by 2<sup>nd</sup> and 3<sup>rd</sup> order residual stresses, by gradients of 1<sup>st</sup> order stresses as well as by the size of coherently scattering domains. In the present case, full-width-at-half-maximum (FWHM) data were used to estimate the size of coherently scattering domains by using a very simplified approach based on the *Scherrer equation* [34]. For this study, we analyzed the 211<sub>S316L</sub> and the 311<sub>IN625</sub> peaks according to Eq. (4) which is a rearrangement of Scherrer's equation by Langford and Wilson [35]

$$p = K \cdot \varepsilon = K \cdot \frac{\lambda}{b \cdot \cos \theta} \quad (4)$$

where  $p$  is the 'true' size of the coherently scattering domains, defined as the cubic root of the crystallite volume.  $K$ ,  $\varepsilon$ ,  $\lambda$ ,  $b$  and  $\theta$  are the Scherrer constant, the apparent crystal size, the wavelength of the used radiation, the additional FWHM-broadening and the Bragg's angle, respectively.

## 9.4 Results and Discussion

### 9.4.1 Cross-sectional microstructure and mechanical properties

The cross-sectional microstructure of the multi-material sample was investigated by confocal laser scanning microscopy, SEM and EDX aiming to determine the distribution of the phases, the individual microstructures and chemical gradients in different regions actually achieved by LDM PBF-LB. The micrographs of the polished cross-section in Figure 3a,b indicate a clear separation of S316L and IN625 phases (Figure 3d) *along the BD* (further also denoted as the *out-of-plane direction*) with morphologically sharp and diffuse interfaces whenever the material changes from S316L to IN625 and from IN625 to S316L, respectively. Remarkably, the latter interface shows an intermixing of the phases with a transition region of  $\sim 200\ \mu\text{m}$ . This observation can be attributed to the fact that Ni face-centered crystal structure may solve up to about 50 weight.% of alloying elements [36].

*Perpendicular to the BD* (further also denoted as the *in-plane direction*), the interface region between the used alloys encompasses a width larger than 1 mm. Furthermore, structural defects due to a lack of binding can be observed here and for the same reason, the occurrence of micro-cracks propagating mainly along high-angle grain boundaries can be observed in IN625 (Figure 3c-e). Lack of binding in IN625 can be addressed to the same origin as the observed higher porosity IN625 region. The occurrence of both, lack of binding as well as a comparatively higher porosity result from the fact, that the process parameters used for both alloys were optimized for processing S316L. The shape of gas pores resulting from excessive energy input is round/spherical. However, the pores present in IN625 regions of the 3D multi-metal FGM have an irregular, angular shape. Therefore, it can be assumed that these pores were created by lack of fusion. Their angular surface morphology cause a notch effect and could be identified as the starting point for some high-angle grain boundary cracks. In conclusion, optimized processing of IN625 by LDM PBF-LB would require a higher energy input.

Bundles of oriented, columnar grains, visible in Figure 3e, originate from the scanning pattern of the laser. Grains grew in the direction of the thermal gradient ( $z$ -direction) and their length encompasses several melt pool boundaries. An out-of-plane preferred orientation of these epitaxially grown bundles can be identified in the micrographs. This behaviour has been known for IN625 built by a standard PBF-LB process [37] as well as by other metal AM processes and has also been documented in Ref. [38].

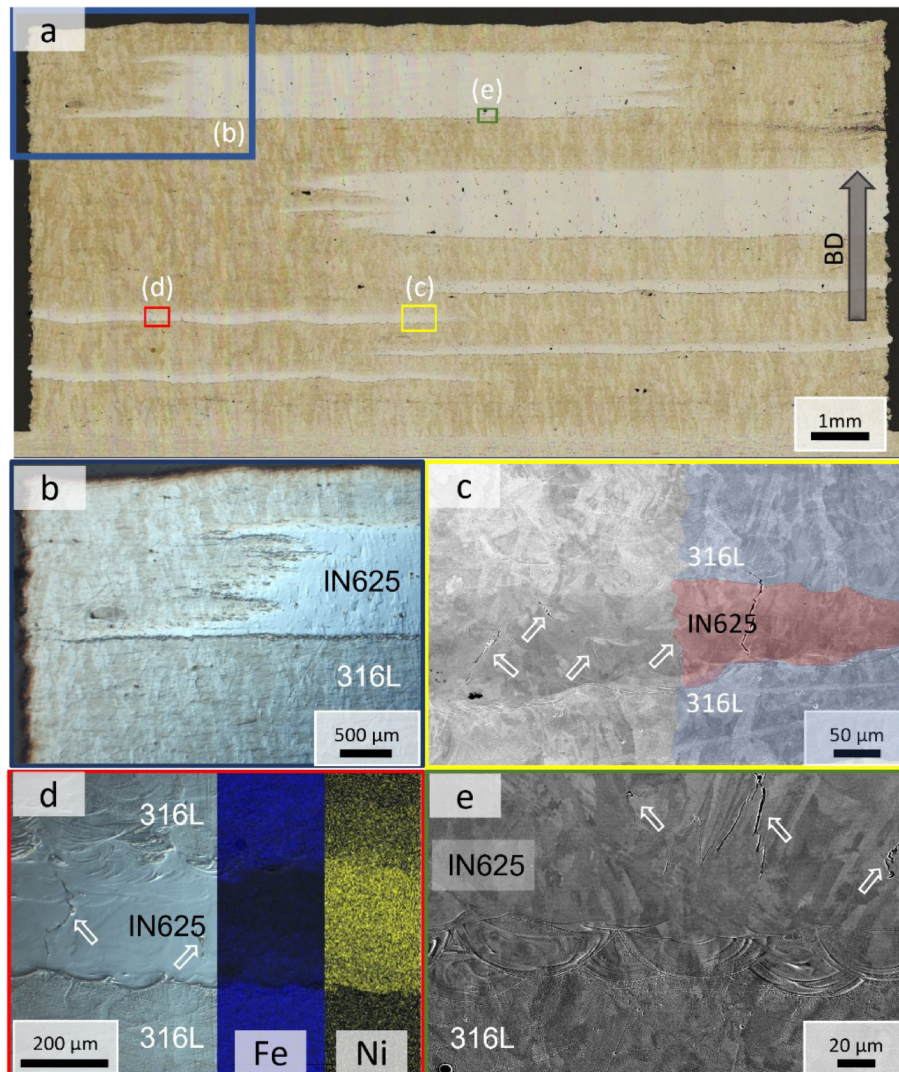


**Figure 3.** Cross-sectional micrographs, recorded using confocal laser scanning microscopy (a,b,d) and SEM (c,e) indicate the presence of micro-cracks in IN625 regions of the multi-metal sample. Each magnified area from (b) to (d) is highlighted in colour in (a). IN625 regions appear brighter in the overview (a) and the build-direction (BD) is indicated by an arrow. An additional chemical analysis by EDS (d) revealed a morphological sharp interface whenever IN625 was applied on S316L but a blurred interface when S316L was applied onto IN625. Perpendicular to the BD, an intermixing at the interface of  $\sim 1$  mm in width could be determined (b). Bundles of grains with a preferred orientation that correlates with the BD could be determined in the SEM images (c) and (e).

Cahoon *et al.* [39] indicated that the yield strength of materials can be related to hardness values for brass, steel and aluminium alloys. Thus, Vickers hardness profiling was used to characterize the gradual change of mechanical properties in particular interfacial areas (

Figure 4). Mean microhardness values ( $H$ ) of  $237 \pm 5$ ,  $285 \pm 5$  and  $168 \pm 11$  HV<sub>0.5</sub>, corresponding to  $2.32 \pm 0.05$ ,  $2.80 \pm 0.05$  and  $1.65 \pm 0.11$  GPa were determined for S316L, IN625 and the S316L base plate, respectively. Measurement points located in the transition area of the two materials were excluded from the evaluation of mean hardness

values. Microhardness values in in-plane oriented interface regions change gradually from bulk S316L to IN625 and vice versa within an intermixing zone that encompasses about 2 mm in width (

Figure 4c-d). The gradual change of microhardness values correlates to the width of the intermixing zone in which the chemical composition of both alloys change gradually from S316L to IN625.

Due to the higher spatial resolution needed in order to determine local mechanical properties nanoindentation mapping in an area of  $500 \times 500 \mu\text{m}^2$  at the top of the region 5 (*cf.* Figure 5) was conducted. Reduced moduli for S316L and IN625 were measured using nanoindentation and evaluated to be  $\sim 181$  and  $\sim 191$  GPa, respectively. Nanohardness values ( $H_{0-P}$ ), determined by the Oliver-Pharr method [24], increased from  $\sim 3.4 \pm 0.1$  GPa in S316L to  $\sim 4.7 \pm 0.1$  GPa in IN625. These values are obviously higher than the values determined by the microhardness measurements.

Even though the processing route of the multi-material sample investigated in this study differs from a standard PBF-LB process in industry (previously also known as laser melting process) [40–42], the determined hardness values for the S316L alloy can be compared with literature results [43] but are about  $\sim 7\%$  higher than the macro-hardness value of  $\sim 221$  HV<sub>10</sub> reported in Refs. [44,45]. Valente *et al.* [46] investigated the influence of different protective gas atmospheres used in PBF-LB and observed systematically higher hardness values for samples built in an N<sub>2</sub> atmosphere which was also the case in the present study. The authors explained their observation with a remarkable solubility of N in stainless steel while Ar as an inert gas is not soluble.

The determined hardness values of  $285 \pm 5$  HV<sub>0.5</sub> for IN625 were compared with results of macro- and microhardness measurements published in data sheets and literature [37,47–49]. SLM Solutions [47] provides slightly varying values of 291 to 310 HV<sub>10</sub> for the as-built condition, depending on the layer thickness that was used in their process. The reported tendency suggests that material's hardness decreases with an increasing layer thickness. Wong *et al.* [38] documented the dependence of hardness values on badly/well optimized parameters used during a multi-laser PBF-LB process. It can be concluded that the values reported here are in good accordance with results of (micro) hardness measurements on samples synthesized by standard PBF-LB processes.

A gradual adaptation in transition zones, comparable to the in-plane and out-of-plane oriented intermixing zones of this sample, has also been determined in the case of a S316L/Cu10Sn multi-metal system [50] as well as for a S316L/C184000 (Cu alloy) material combination [51].



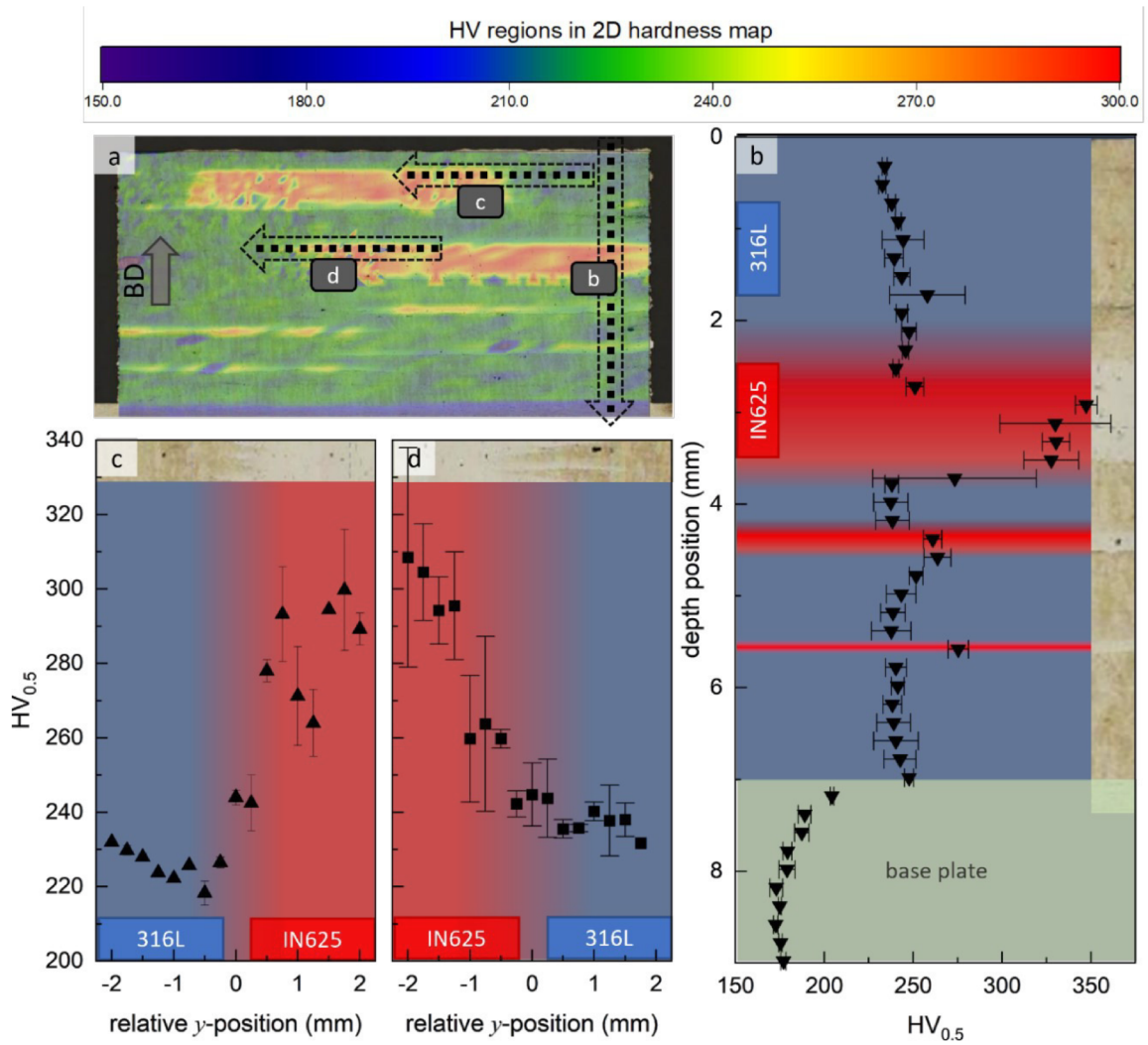


**Figure 4.** Overview optical micrograph with a superimposed 2D hardness chart (a) indicates approximate positions and directions of one vertical (b) and two horizontal (c,d) microhardness scans used to determine Vickers hardness across the S316L and IN625 interfaces. Error bars for each measurement position represent the standard deviation calculated from three measurement points at comparable spatial positions.

A similar behaviour was observed by Qian *et al.* [52] for five inorganic materials, including Cu and stainless steel 304. The authors report nanoindentation hardness to be 10-30% higher compared to microhardness. The deviation of results is explained with respect to differences in the applied methods. In the case of nanoindentation, hardness values are evaluated using the projected contact area at the full load, while in the case of microhardness experiments, values are post-experimentally determined from the residual projected area. Further deviations between the methods stem from indentation-size effects, among these are (i) disproportionately larger influences of pile-ups [24], (ii) dislocation density [53], (iii) volume deformation energy and (iv) free surface energy [54]. In the present work, ratios of  $H_{O-P}/H$  were calculated to be 0.68 and 0.60 for S316L and IN625, respectively. Thus, the deviation between nano- and microhardness values was found to be larger than in Ref. [52] where the experimental determined  $H_{O-P}/H$  ratio

## Graded Inconel-Stainless Steel Multi-Material Structure by Inter- and Intralayer Variation of Metal Alloys

for stainless steel 304 was determined to be 0.73. A possible explanation for the even larger deviation in the case of IN625 are microcracks and pores in the respective region. In nanoindentation experiments, the surrounding region that provides support for the plastically deformed area during indentation is relatively smaller than in microhardness testing. Consequently, with the increasing penetration depth and size of the indent, the probability increases that pores or microcracks are present in the surrounding region during microhardness measurements. Their influence results in lower experimentally determined hardness values.

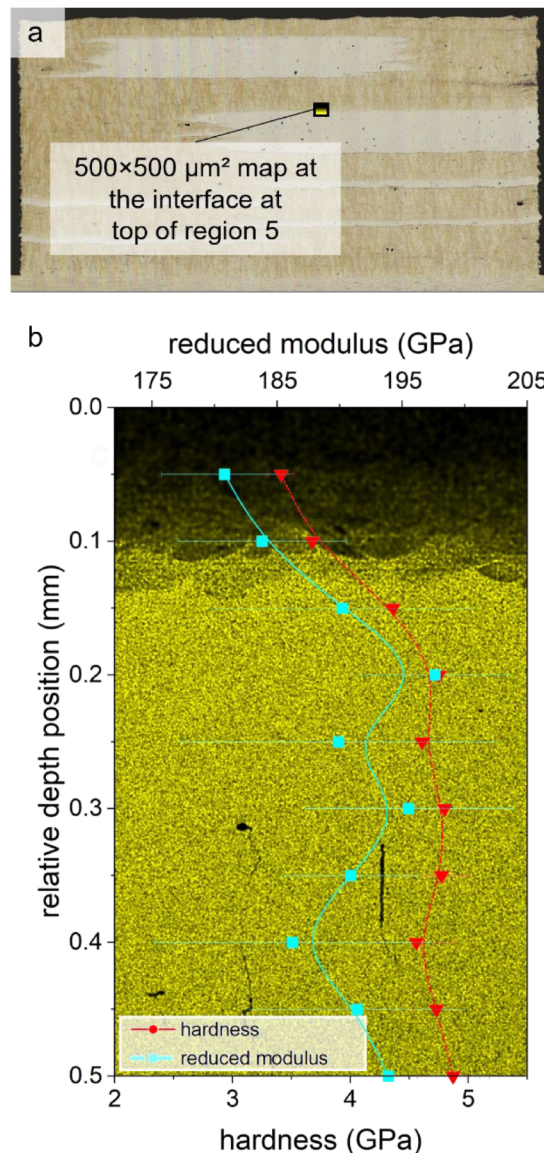


**Figure 5.** Local mechanical properties (hardness and reduced modulus) at the S316L/IN625 interface were determined by nanoindentation. Indentation was performed in a 500×500 μm large region which is marked in (a). The profiles of hardness and reduced modulus are shown across the SEM-EDX map of Ni in (b). Error bars for each measurement position represent the standard deviation calculated from ten indents at comparable spatial positions.

### 9.4.2 Residual stress distribution, texture and microstructure

CSmicroXRD was performed to assess the distribution of the stress state, the texture, phases and microstructural changes in the build up. The information was derived from 2D diffractograms which were used to quantify the residual strain state in the synthesized multi-material sample. In a next step, the residual stress distribution was calculated (Sec. 3) by using the corresponding XECs of both materials. As the XECs of the materials are different, residual stresses in IN625 and S316L were calculated separately. In-plane, out-of-plane and shear stresses, are illustrated in Figure 6 and 7a, b and c, respectively. The distribution of residual stresses in Figure 6 and Figure 7 correlates well with stress-formation models of Ref. [55] and helps to understand mechanisms affecting the crack initiation in AM materials. The in-plane stress distribution in Figure 7a in the uppermost layers shows maximal tensile stresses of approx. 400 MPa in the specimen's centre and reduced tensile stresses of approx. 50 MPa or nearly stress-free regions at the left and right edges of the specimen. As indicated in Figure 6c and Figure 7c, shear stresses in the respective area are negligible. In-plane residual stresses (Figure 6a and Figure 7a) in the topmost layer are thus relevant especially for solidification cracking and crack propagation parallel to the BD, which is the  $z$ -direction in this case. At greater depths of  $>1$  mm, in-plane residual stresses behave in the opposite way, exhibiting a (compressive) minimum in the sample's centre and moderate (tensile) maxima at the left and right edges. Furthermore the evaluation of experimental data exhibited stress concentrations in both phases whenever the printed material changed from IN625 to S316L. Maximal tensile stresses of approx. 800 MPa could be detected on top of sample region 6 due to the superposition of (i) the stress component given by the temperature gradient mechanism [56] and (ii) the stress component induced during the cool-down phase of the molten top layers.

In contrast, stresses in the out-of-plane orientation were determined to reach maximal levels of  $>900$  MPa at the left and right edges of the specimen (Figure 6(b) and 7(b)). Like the distribution of in-plane residual stresses, this correlates well with predicted results from simulations [55] and helps to understand the strong tendency for crack propagation perpendicular to the BD, starting at the sample's edges. This kind of crack propagation is often referred to as "delamination" and can be found in various PBF-LB materials [57–59]. It is important to notice that the evaluated stress levels correspond to stress components of the Cauchy stress tensor. These components can thus exceed the yield strength of the materials as the yield strength determined in uniaxial tensile tests does not represent the stress components but the yield criterion described *e.g.* by the maximum energy distortion criterion.

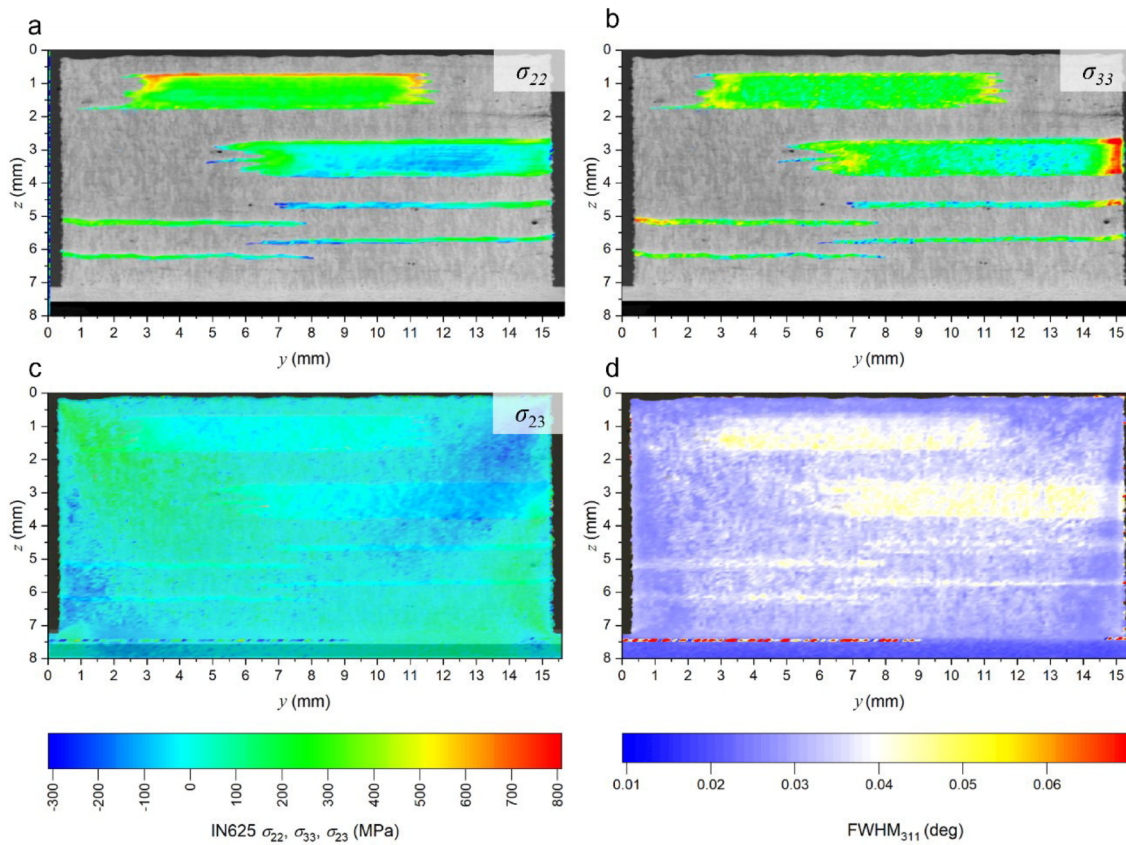


**Figure 6.** Stack of the optical micrographs of S316L and the 2D residual stress distributions in IN625. Residual stresses were calculated from the residual strain distribution in the sample for in-plane normal stresses (a), out-of-plane normal stresses (b) and shear stresses in (c). FWHM values of the 311 peak (d) indicate coarser grains in S316L compared to the brighter appearing areas of IN625.

Being aware of the fact, that the broadening of XRD peaks is influenced by micro strains, structural defects, temperature factors, stress gradients and the instrumental broadening, the FWHM data from Figure 6a were used to qualitatively estimate the size of coherently scattering domains across the specimen [35]. According to Scherrer's formula [34], a qualitative interpretation of the FWHM map thus suggests a smaller crystallite size in the IN625 areas compared to S316L.

Beside the crystallite size, also the spatial occurrence of the phases was evaluated from the D-S rings by considering the  $\langle 110 \rangle$  and  $\langle 100 \rangle$  fibre textures of S316L and IN625 phases. These two types of textures were identified already in our previous publication. Figure 7d shows the spatial occurrence of S316L phase, where the IN625 is given by the balance.

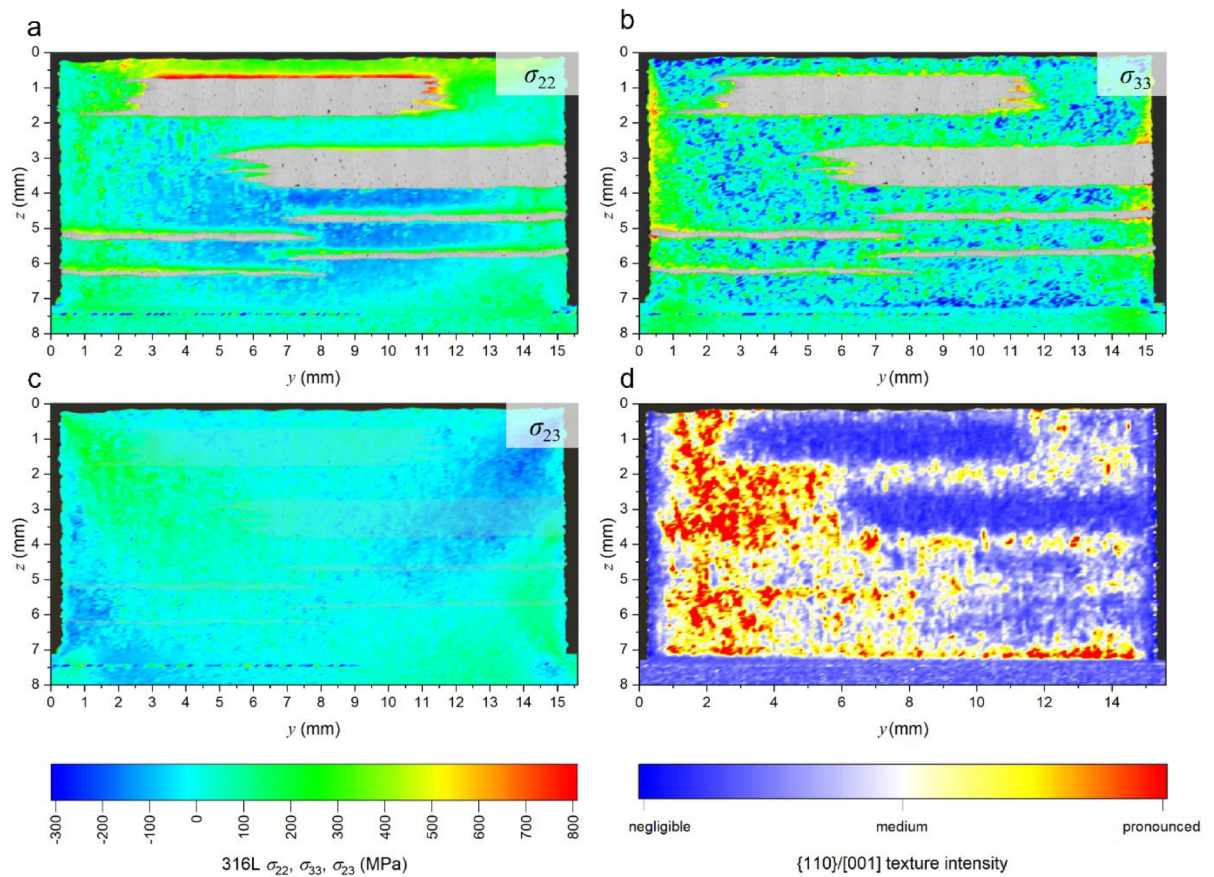


**Figure 7.** Stack of the optical micrograph of IN625 and the 2D residual stress distribution in S316L. Residual stresses were calculated from the residual strain distribution in the sample for in-plane normal stresses (a), out-of-plane normal stresses (b) and shear stresses in (c). The qualitative evaluation of crystallographic texture (d) in the sample indicates a pronounced  $\langle 110 \rangle$  texture in S316L. It has been known from a previous study that IN625 has a preferential orientation of the  $\langle 100 \rangle$ -lattice directions parallel to the BD.

The phase analysis did not exhibit the formation of intermetallic compounds at interface regions of the S316L/IN625 material. The intermixing of both alloys was studied intensively in a previous work [17].

## 9.5 Conclusions

The present work documents the application of correlative standard and advanced characterization methods to investigate the complex microstructure, mechanical properties and the distribution of residual stresses in a printed 3D multi-metal FGM. Two identical specimens were synthesized by LDM PBF-LB which represents a relatively novel technique based on the use of slurries instead of powders in a PBF-LB process. The samples' cross-sections were subjected to micro- and nanohardness tests and furthermore characterized by confocal microscopy and SEM, EDS and CSmicroXRD.

Results of this study indicated that:

- Stainless steel S316L and IN625 were successfully combined layer-by-layer (in build-direction  $z$ ) and within individual sub-layers ( $x$ - $y$  direction) with resolutions better than 200  $\mu\text{m}$  and of about 1 mm, respectively, to form solid 3D multi-metal FGMs.
- Nanohardness experiments revealed a gradual change of mechanical properties at interface regions of the build-up. Microhardness gradually changed from  $237\pm 5$  in the stainless steel to  $285\pm 5$  HV<sub>0.5</sub> in the Ni-base alloy at graded horizontal and morphological sharp vertical interfaces.
- Reduced moduli of  $\sim 181$  and  $\sim 191$  GPa for S316L and IN625, respectively, of the pure alloys and at one interface were assessed by nanoindentation mapping.
- CSmicroXRD mapping indicated the presence of significant residual stresses of approx. 800 MPa in the in-plane direction (*i.e.*, the  $y$ -direction, oriented perpendicular to the BD). Maximal residual stresses of  $>900$  MPa were determined in out-of-plane orientation (*i.e.*, the  $z$ -direction, oriented parallel to the BD). Shear components in these build-ups could be neglected due to their negligible degree of expression.

The experimentally assessed results of this work lead to a deeper understanding of an optimized design of multi-metal 3D FGMs synthesized by PBF-LB related AM technologies in terms of crack-initiation and crack-propagation.

## Acknowledgments

Financial support for this work was provided by Österreichische Forschungsförderungsgesellschaft mbH (FFG), project numbers FO999888151, “AMnonWeldSuperAlloys” and 861496, “CrossSurfaceMech”. Furthermore, financial support by the Austrian Federal Government (in particular from Bundesministerium für Verkehr, Innovation und Technologie and Bundesministerium für Wissenschaft, Forschung und Wirtschaft) represented by Österreichische Forschungsförderungsgesellschaft mbH and the Styrian and the Tyrolean Provincial Government, represented by Steirische Wirtschaftsförderungsgesellschaft mbH and Standortagentur Tirol, within the framework of the COMET Funding Programme is gratefully acknowledged. We acknowledge CzechNanoLab Research Infrastructure supported by LM2018110. The authors gratefully acknowledge the support of beamline scientists working at the HEMS beamline during synchrotron experiments at DESY

## Author’s contribution statement

S.C.B: conceptualization, data curation, investigation, methodology, project administration, validation, visualization, writing – original draft, writing – review & editing

K.H.: investigation

L.T.G.vdV.: investigation, methodology, visualization

M.M.: validation, visualization, writing – review & editing

J.T.: formal analysis, software, writing – review & editing

M.A.N.: investigation

S.M.: investigation, visualization

J.W.H.: methodology, resources

J.J.S.: methodology, resources

J.K.: funding acquisition, project administration, resources, supervision, validation, writing – review & editing

All authors contributed to the discussion and revision of the manuscript.

## References

- [1] Li C, Liu ZY, Fang XY, Guo YB. Residual Stress in Metal Additive Manufacturing. *Procedia CIRP* 2018;71:348–53. <https://doi.org/10.1016/J.PROCIR.2018.05.039>.
- [2] Schneck M, Horn M, Schmitt M, Seidel C, Schlick G, Reinhart G. Review on additive hybrid- and multi-material-manufacturing of metals by powder bed fusion: state of technology and development potential. *Progress in Additive Manufacturing* 2021;6:881–94. <https://doi.org/10.1007/s40964-021-00205-2>.
- [3] Li Y, Feng Z, Hao L, Huang L, Xin C, Wang Y, et al. A Review on Functionally Graded Materials and Structures via Additive Manufacturing: From Multi-Scale Design to Versatile Functional Properties. *Advanced Materials Technologies* 2020;5. <https://doi.org/10.1002/admt.201900981>.
- [4] Ghanavati R, Naffakh-Moosavy H. Additive manufacturing of functionally graded metallic materials: A review of experimental and numerical studies. *Journal of Materials Research and Technology* 2021;13:1628–64. <https://doi.org/10.1016/j.jmrt.2021.05.022>.
- [5] Balla VK, DeVasConCellos PD, Xue W, Bose S, Bandyopadhyay A. Fabrication of compositionally and structurally graded Ti–TiO<sub>2</sub> structures using laser engineered net shaping (LENS). *Acta Biomaterialia* 2009;5:1831–7. <https://doi.org/10.1016/j.actbio.2009.01.011>.
- [6] Carroll BE, Otis RA, Borgonia JP, Suh J, Dillon RP, Shapiro AA, et al. Functionally graded material of 304L stainless steel and inconel 625 fabricated by directed energy deposition: Characterization and thermodynamic modeling. *Acta Materialia* 2016;108:46–54. <https://doi.org/10.1016/J.ACTAMAT.2016.02.019>.
- [7] Schneck M, Horn M, Schindler M, Seidel C. Capability of multi-material laser-based powder bed fusion—development and analysis of a prototype large bore engine component. *Metals* 2022;12. <https://doi.org/10.3390/met12010044>.
- [8] Fox P, Pogson S, Sutcliffe CJ, Jones E. Interface interactions between porous titanium/tantalum coatings, produced by Selective Laser Melting (SLM), on a cobalt-chromium alloy. *Surface and Coatings Technology* 2008;202:5001–7. <https://doi.org/10.1016/j.surfcoat.2008.05.003>.



- [9] Borisov E, Polozov I, Starikov K, Popovich A, Suffiarov V. Structure and properties of Ti/Ti64 graded material manufactured by laser powder bed fusion. *Materials* 2021;14. <https://doi.org/10.3390/ma14206140>.
- [10] Wei C, Sun Z, Chen Q, Liu Z, Li L. Additive Manufacturing of Horizontal and 3D Functionally Graded 316L/Cu10Sn Components via Multiple Material Selective Laser Melting. *Journal of Manufacturing Science and Engineering, Transactions of the ASME* 2019;141:1–8. <https://doi.org/10.1115/1.4043983>.
- [11] Wei C, Gu H, Li Q, Sun Z, Chueh Y hui, Liu Z, et al. Understanding of process and material behaviours in additive manufacturing of Invar36/Cu10Sn multiple material components via laser-based powder bed fusion. *Additive Manufacturing* 2021;37:101683. <https://doi.org/10.1016/j.addma.2020.101683>.
- [12] Wang D, Deng GW, Yang Y qiang, Chen J, Wu W hui, Wang H liang, et al. Interfacial microstructure and mechanical properties of selective laser melted multilayer functionally graded materials. *Journal of Central South University* 2021;28:1155–69. <https://doi.org/10.1007/s11771-021-4687-9>.
- [13] Beal VE, Erasenthiran P, Ahrens CH, Dickens P. Evaluating the use of functionally graded materials inserts produced by selective laser melting on the injection moulding of plastics parts. *Proceedings of the Institution of Mechanical Engineers, Part B: Journal of Engineering Manufacture* 2007;221:945–54. <https://doi.org/10.1243/09544054JEM764>.
- [14] Nadimpalli VK, Hørdum E, Dahmen T, Valente EH, Mohanty S. Multi-material additive manufacturing of steels using laser powder bed fusion eu spen ' s 1 9 th International Conference & Exhibition , Bilbao , ES , June 2019 Multi-material additive manufacturing of steels using laser powder bed fusion 2019.
- [15] Xiong YZ, Gao RN, Zhang H, Dong LL, Li JT, Li X. Rationally designed functionally graded porous Ti6Al4V scaffolds with high strength and toughness built via selective laser melting for load-bearing orthopedic applications. *Journal of the Mechanical Behavior of Biomedical Materials* 2020;104:103673. <https://doi.org/10.1016/j.jmbbm.2020.103673>.
- [16] Ghorbanpour S, Deshmukh K, Sahu S, Riemslog T, Reinton E, Borisov E, et al. Additive manufacturing of functionally graded inconel 718: Effect of heat treatment and building orientation on microstructure and fatigue behaviour. *Journal of Materials Processing Technology* 2022;306:117573. <https://doi.org/10.1016/j.jmatprotec.2022.117573>.

- [17] Bodner SC, van de Vorst LTG, Zalesak J, Todt J, Keckes JF, Maier-Kiener V, et al. Inconel-steel multilayers by liquid dispersed metal powder bed fusion: Microstructure, residual stress and property gradients. *Additive Manufacturing* 2020;32. <https://doi.org/10.1016/j.addma.2019.101027>.
- [18] Mao S, Zhang DZ, Ren Z, Fu G, Ma X. Effects of process parameters on interfacial characterization and mechanical properties of 316L/CuCrZr functionally graded material by selective laser melting. *Journal of Alloys and Compounds* 2022;899:163256. <https://doi.org/10.1016/j.jallcom.2021.163256>.
- [19] Chen WY, Zhang X, Li M, Xu R, Zhao C, Sun T. Laser powder bed fusion of Inconel 718 on 316 stainless steel. *Additive Manufacturing* 2020;36:101500. <https://doi.org/10.1016/j.addma.2020.101500>.
- [20] Demir AG, Previtali B. Multi-material selective laser melting of Fe/Al-12Si components. *Manufacturing Letters* 2017;11:8–11. <https://doi.org/10.1016/j.mfglet.2017.01.002>.
- [21] Mehrpouya M, Tuma D, Vaneker T, Afrasiabi M, Bambach M, Gibson I. Multimaterial powder bed fusion techniques. *Rapid Prototyping Journal* 2022;28:1–19. <https://doi.org/https://doi.org/10.1108/RPJ-01-2022-0014>.
- [22] Aerosint. Multi-Material 3D Printing Bundle for Laser Powder Bed Fusion 2020. <https://aerosint.com/multi-material-3d-printing-bundle> (accessed November 3, 2022).
- [23] ASTM International. Standard Test Method for Microindentation Hardness of Materials. ASTM International; 2016.
- [24] Oliver WC, Pharr GM. An improved technique for determining hardness and elastic modulus using load and displacement sensing indentation experiments. *Journal of Materials Research* 1992;7:1564–83. <https://doi.org/10.1557/JMR.1992.1564>.
- [25] Schell N, King A, Beckmann F, Fischer T, Müller M, Schreyer A. The high energy materials science beamline (HEMS) at PETRA III. *Materials Science Forum* 2014;772:57–61. <https://doi.org/10.4028/www.scientific.net/MSF.772.57>.
- [26] Kieffer J, Karkoulis D. PyFAI, a versatile library for azimuthal regrouping. *Journal of Physics: Conference Series* 2013;425. <https://doi.org/10.1088/1742-6596/425/20/202012>.
- [27] Rai SK, Kumar A, Shankar V, Jayakumar T, Bhanu Sankara Rao K, Raj B. Characterization of microstructures in Inconel 625 using X-ray diffraction peak

- broadening and lattice parameter measurements. *Scripta Materialia* 2004;51:59–63. <https://doi.org/10.1016/j.scriptamat.2004.03.017>.
- [28] Bacci T, Borgioli F, Galvanetto E, Pradelli G. Glow-discharge nitriding of sintered stainless steels. *Surface and Coatings Technology* 2001;139:251–6. [https://doi.org/10.1016/S0257-8972\(01\)01010-6](https://doi.org/10.1016/S0257-8972(01)01010-6).
- [29] Welzel U, Ligot J, Lamparter P, Vermeulen AC, Mittemeijer EJ. Stress analysis of polycrystalline thin films and surface regions by X-ray diffraction. *Journal of Applied Crystallography* 2005;38:1–29. <https://doi.org/10.1107/S0021889804029516>.
- [30] Kröner E. Berechnung der elastischen Konstanten des Vielkristalls aus den Konstanten des Einkristalls. *Zeitschrift Für Physik* 1958;151:504–18. <https://doi.org/10.1007/BF01337948>.
- [31] Wang Z, Stoica AD, Ma D, Beese AM. Diffraction and single-crystal elastic constants of Inconel 625 at room and elevated temperatures determined by neutron diffraction. *Materials Science and Engineering A* 2016;674. <https://doi.org/10.1016/j.msea.2016.08.010>.
- [32] Noyan IC, Cohen JB. Residual stress – measurement by diffraction and interpretation. *Materials Research and Engineering* 1987.
- [33] Zeilinger A, Todt J, Krywka C, Müller M, Ecker W, Sartory B, et al. In-situ Observation of Cross-Sectional Microstructural Changes and Stress Distributions in Fracturing TiN Thin Film during Nanoindentation. *Scientific Reports* 2016;6. <https://doi.org/10.1038/srep22670>.
- [34] Scherrer P. Bestimmung der Größe und der inneren Struktur von Kolloidteilchen mittels Röntgenstrahlen. *Nachrichten von Der Gesellschaft Der Wissenschaften Zu Göttingen, Mathematisch-Physikalische Klasse* 1918;2:98–100. <https://doi.org/10.1007/978-3-662-33915-2>.
- [35] Langford JJ, Wilson AJC. Scherrer after Sixty Years: A Survey and Some New Results in the Determination of Crystallite Size. *Journal of Applied Crystallography* 1978;11:102–13. <https://doi.org/10.1107/S0021889878012844>.
- [36] Sravan Sashank S, Rajakumar S, Karthikeyan R, Nagaraju DS. Weldability, Mechanical Properties and Microstructure of Nickel Based Super Alloys: A review. *E3S Web of Conferences* 2020;184:1–6. <https://doi.org/10.1051/e3sconf/202018401040>.

- [37] Gamon A, Arrieta E, Gradl PR, Katsarelis C, Murr LE, Wicker RB, et al. Microstructure and hardness comparison of as-built inconel 625 alloy following various additive manufacturing processes. *Results in Materials* 2021;12:100239. <https://doi.org/10.1016/j.rinma.2021.100239>.
- [38] Wong H, Dawson K, Ravi GA, Howlett L, Jones RO, Sutcliffe CJ. Multi-Laser Powder Bed Fusion Benchmarking—Initial Trials with Inconel 625. *International Journal of Advanced Manufacturing Technology* 2019;105:2891–906. <https://doi.org/10.1007/s00170-019-04417-3>.
- [39] Cahoon JR, Broughton WH, Kutzak AR. The determination of yield strength from hardness measurements. *Metallurgical Transactions* 1971;2:1979–83. <https://doi.org/10.1007/BF02913433>.
- [40] Gu DD, Meiners W, Wissenbach K, Poprawe R. Laser additive manufacturing of metallic components: materials, processes and mechanisms. *International Materials Reviews* 2012;57:133–64. <https://doi.org/10.1179/1743280411Y.0000000014>.
- [41] Singh R, Gupta A, Tripathi O, Srivastava S, Singh B, Awasthi A, et al. Powder bed fusion process in additive manufacturing: An overview. *Materials Today: Proceedings* 2019;26:3058–70. <https://doi.org/10.1016/j.matpr.2020.02.635>.
- [42] Bhavar V, Kattire P, Patil V, Khot S, Gujar K, Singh R. A review on powder bed fusion technology of metal additive manufacturing. *Additive Manufacturing Handbook: Product Development for the Defense Industry* 2017:251–61. <https://doi.org/10.1201/9781315119106>.
- [43] Liverani E, Toschi S, Ceschini L, Fortunato A. Effect of selective laser melting (SLM) process parameters on microstructure and mechanical properties of 316L austenitic stainless steel. *Journal of Materials Processing Technology* 2017;249:255–63. <https://doi.org/10.1016/j.jmatprotec.2017.05.042>.
- [44] SLM Solutions Group AG. *Materialdatenblatt Fe-Alloy 316L (1.4404) n.d.:*4–8.
- [45] Oerlikon AM. Additive Manufacturing of 316L Stainless Steel. *International Journal of Recent Technology and Engineering* 2019;8:6825–9. <https://doi.org/10.35940/ijrte.d5199.118419>.
- [46] Valente EH, Nadimpalli VK, Andersen SA, Pedersen DB, Christiansen TL, Somers MAJ. Influence of atmosphere on microstructure and nitrogen content in AISI 316L fabricated by laser-based powder bed fusion. *European Society for Precision Engineering and Nanotechnology, Conference Proceedings - 19th International Conference and Exhibition, EUSPEN 2019* 2019:244–7.

- 
- [47] SLM Solutions Group AG. Material Data Sheet Ni-Alloy IN625 / 2.4856 / B446 2016:2–6.
- [48] EOS GmbH. IN625: Material data sheet Technical data 2015;49:1–6.
- [49] Wong K V., Hernandez A. A Review of Additive Manufacturing. ISRN Mechanical Engineering 2012;2012:1–10. <https://doi.org/10.5402/2012/208760>.
- [50] Chen J, Yang Y, Song C, Zhang M, Wu S, Wang D. Interfacial microstructure and mechanical properties of 316L /CuSn10 multi-material bimetallic structure fabricated by selective laser melting. Materials Science and Engineering A 2019;752:75–85. <https://doi.org/10.1016/j.msea.2019.02.097>.
- [51] Liu ZH, Zhang DQ, Sing SL, Chua CK, Loh LE. Interfacial characterization of SLM parts in multi-material processing: Metallurgical diffusion between 316L stainless steel and C18400 copper alloy. Materials Characterization 2014;94:116–25. <https://doi.org/10.1016/j.matchar.2014.05.001>.
- [52] Qian L, Li M, Zhou Z, Yang H, Shi X. Comparison of nano-indentation hardness to microhardness. Surface and Coatings Technology 2005;195:264–71. <https://doi.org/10.1016/j.surfcoat.2004.07.108>.
- [53] Nix WD, Gao H. Indentation size effects in crystalline materials: A law for strain gradient plasticity. Journal of the Mechanics and Physics of Solids 1998;46:411–25. [https://doi.org/10.1016/S0022-5096\(97\)00086-0](https://doi.org/10.1016/S0022-5096(97)00086-0).
- [54] Fröhlich F, Grau P, Grellmann W. Performance and analysis of recording microhardness tests. Physica Status Solidi (A) 1977;42:79–89. <https://doi.org/10.1002/pssa.2210420106>.
- [55] Mercelis P, Kruth J. Residual stresses in selective laser sintering and selective laser melting. Rapid Prototyping Journal 2006;12:254–65. <https://doi.org/10.1108/13552540610707013>.
- [56] Megahed M, Mindt HW, N'Dri N, Duan H, Desmaison O. Metal additive-manufacturing process and residual stress modeling. vol. 5. Integrating Materials and Manufacturing Innovation; 2016. <https://doi.org/10.1186/s40192-016-0047-2>.
- [57] Platl J, Bodner S, Hofer C, Landefeld A, Leitner H, Turk C, et al. Cracking mechanism in a laser powder bed fused cold-work tool steel: The role of residual stresses, microstructure and local elemental concentrations. Acta Materialia 2022;225:117570. <https://doi.org/10.1016/j.actamat.2021.117570>.

- [58] Mohr G, Altenburg SJ, Ulbricht A, Heinrich P, Baum D, Maierhofer C, et al. In-situ defect detection in laser powder bed fusion by using thermography and optical tomography—comparison to computed tomography. *Metals* 2020;10. <https://doi.org/10.3390/met10010103>.
- [59] Kempen K, Vrancken B, Buls S, Thijs L, Van Humbeeck J, Kruth JP. Selective Laser Melting of Crack-Free High Density M2 High Speed Steel Parts by Baseplate Preheating. *Journal of Manufacturing Science and Engineering, Transactions of the ASME* 2014;136. <https://doi.org/10.1115/1.4028513>.